Dissertation
submitted to the
Combined Faculties for the Natural Sciences and for Mathematics
of the Ruperto-Carola University of Heidelberg, Germany
for the degree of
Doctor of Natural Sciences

presented by
Dipl.-Phys. Florian Grussie
born in Landshut

Oral examination: 29th June 2016

Experimental studies of ion-neutral reactions under astrophysical conditions

Referees:

Dr. Holger Kreckel

Prof. Dr. André Schöning

Experimentelle Studien zu Ionen-Neutral-Reaktionen unter astrophysikalischen Bedingungen

Kollisionen zwischen Ionen und Neutralteilchen sind ausschlaggebend für die Gasphasensynthese von komplexen Molekülen im interstellaren Medium. Eine genaue Modellierung des astrochemischen Netzwerks ist abhängig von möglichst präzisen experimentellen Daten dieser Reaktionsraten und deren Verzweigungsverhältnissen. Für die meisten Ionen-Neutral-Reaktionen sind diese Ratenkoeffizienten unter astrophysikalischen Bedingungen völlig unbekannt. Um diese wichtige Gruppe von Reaktionen zu erforschen, werden im Rahmen dieser Arbeit zwei unterschiedliche experimentelle Ansätze vorgestellt. Eines der grundlegendsten und zugleich bedeutsamsten Ionen in der interstellaren Chemie ist H_3^+. Es ist davon auszugehen, dass die H_3^+-Ionen in interstellaren Wolken durch Kollisionen mit H_2 thermalisiert werden. Jedoch zeigten kürzlich astronomische Beobachtungen eine signifikante Abweichung ihrer Anregungstemperaturen. Um diesen Thermalisierungsprozess experimentell zu untersuchen, wurden $H_3^+ + H_2$ Reaktionsmessungen im thermischen Gleichgewicht unter Verwendung einer 22pol Falle am Max-Planck-Institut für Kernphysik durchgeführt. Für zukünftige Experimente zur Untersuchung von Reaktionen zwischen Atomen und Ionen am kryogenen Speicherring CSR wurde ein Strahlführungssystem entwickelt, das die Überlagerung von neutralen Atomen im Grundzustand mit dem im Ring gespeicherten, gekühlten Ionenstrahl ermöglicht.

Experimental studies of ion-neutral reactions under astrophysical conditions

Ion-neutral collisions are pivotal for the gas-phase synthesis of complex molecules in the interstellar medium. Accurate modeling of the astrochemical network relies on precise laboratory data of reaction rate coefficients and their branching ratios. For the majority of ion-neutral reactions, rate coefficients at astrophysical conditions are completely unknown. To gain an experimental insight of ion-neutral, gas-phase chemistry under interstellar conditions, two different experimental approaches are presented. One of the most fundamental ions for interstellar chemistry is H_3^+. This ion is assumed to be thermalized in collisions with H_2. However, recent astronomical observations of H_2 and H_3^+ in diffuse interstellar clouds revealed a significant difference in their excitation temperatures. In this work, 22 pole trap measurements, performed at the Max Planck Institute for Nuclear Physics (MPIK) in Heidelberg, of the $H_3^+ + H_2$ reaction at thermal equilibrium are presented and discussed. For future experiments on ion-atom reactions, an injection beamline for the Cyrogenic Storage Ring (CSR) was developed to perform merged-beams experiments on neutral ground-state atoms superimposed with the cooled, stored ions in the CSR.

Contents

1 Introduction **1**

I The nuclear spin equilibrium of H_3^+ in collisions with H_2 **5**

2 The triatomic hydrogen ion H_3^+ **7**

2.1 Brief historical overview 7

2.2 Theoretical background 10

2.3 Interstellar chemistry 15

2.3.1 The formation of H_3^+ 16

2.3.2 The destruction of H_3^+ 17

2.3.3 The thermalization of H_3^+ and abnormal excitation temperatures . . 20

3 Experimental setup **27**

3.1 Preparation of H_2 with defined nuclear spin ratios 28

3.2 Analysis of defined H_2 nuclear spin ratios 33

3.2.1 The Raman spectroscopy setup 33

3.3 The 22 pole ion trap setup 39

3.3.1 The storage ion source 40

3.3.2 The ion transport into the trap 41

3.3.3 The temperature-variable 22 pole trap 42

3.3.4 The mass selective quadrupole 44

3.3.5 The Daly-type detection system 44

3.3.6 The laser system 45

4 Laser induced reaction spectroscopy **47**

4.1 Laser induced reaction 47

4.2 22 pole trap conditions 49

4.3 22 pole trap measurement procedure 53

4.4 Signal intensities 54
4.5 Analysis 56
4.6 Discussion and Conclusion 63

II Neutral atom beam creation for merged beam studies at the CSR 69

5 Experimental apparatus for reaction studies of molecular ions with neutral atoms 71

6 Principles of ion beam transport 75
6.1 Motion of particles in linear approximation 76
6.2 Transfer matrix formalism 81
6.3 Transport of ion beams 83
6.4 Filamentation 88
6.5 Fringing field 90

7 The Cryogenic Storage Ring (CSR) 91
7.1 Concept of the vacuum system 92
7.2 Overview of experimental capabilities 94
7.3 The ring lattice 97

8 Development and design of a versatile transfer line for the CSR 101
8.1 Ion source platforms 103
8.2 Beam transport systems 105
8.2.1 300 kV beamline 107
8.2.2 60 kV beamline 112
8.3 Elements of the beamlines 116
8.3.1 Dipole magnets 118
8.3.2 Monitors 120
8.3.3 Electrostatic quadrupole triplet 125
8.3.4 90° deflector with a hole 133

9 Photodetachment setup **147**
9.1 Photodetachment efficiency 149
9.2 Laser system 151
9.2.1 Measurement of the laser profile 152
9.3 Photodetachment chamber 155
9.4 Beam cleaner 159

10 Final design of the CSR transfer line **163**
10.1 Vacuum simulations 163
10.2 Overview of the CSR transfer line 167

11 Test measurements **169**
11.1 Beam emittance measurement 171
11.1.1 Quadrupole variation method 171
11.1.2 Analysis 175
11.2 Photodetachment measurements 179
11.2.1 Measurement overview 179
11.2.2 Neutral flux measurement 181
11.2.3 Photodetachment efficiency 185

12 Summary and Perspectives **191**

A Statistical nuclear spin configurations of the reaction $H_3^+ + H_2$ **195**

B Estimated reaction rates inside the 22 pole trap **199**

C Transfer matrices in linear approximation **203**

D Ion-optical simulation of the 90° deflector without shielding tube **207**

References **209**

Chapter 1

Introduction

The space between the stars is filled with dilute matter, comprising mainly of hydrogen and helium. The interstellar medium (ISM), which is the birthplace of new stars and planets, has a highly inhomogeneous density distribution. With an average density of ~ 1 cm^{-3}, the ISM contains regions of denser concentrations of gas and dust particles, forming interstellar clouds. For molecular clouds the particle density ranges from 10 cm^{-3} to 10^6 cm^{-3}, of which $\sim 92.1\%$ is hydrogen and $\sim 7.8\%$ is helium, while the next most abundant nuclei, namely oxygen, carbon, neon, and nitrogen merely make up $\sim 0.1\%$. Typical cloud temperatures range between 10-100 K. Despite these extreme conditions, seemingly adverse to an active and rich chemistry, almost 200 molecules have been detected in the interstellar medium or circumstellar shells [1]. A stable population of these species in the ISM is maintained via the balancing of formation and destruction processes. Due to the low particle densities in interstellar clouds, reactions between three or more particles are unlikely, thus chemical processes are dominated by two-body reactions. Typically, neutral-neutral reactions are inhibited via an activation barrier, for which there is insufficient thermal energy available for the reaction to surmount. Reactions between anions and cations, while energetically favorable, are infrequent due to the relatively low abundance of negative ions in the interstellar medium. As a result, the dominant gas-phase processes in interstellar clouds tend to be exothermic ion-neutral reactions. These reactions are a key formation mechanisms in the chemical network of the ISM, leading to a diverse range of complex interstellar molecules. With the previous generation of observation platforms recently decommissioned, e.g. Herschel [2] and Spitzer [3], the next generation of high sensitivity platforms have emerged, e.g. SOFIA [4] and ALMA [5]. To interpret the vast information from the

astronomical observations, models of the interstellar chemical network and experimental studies are needed. A full-comprehension, accounting both for the presence and abundance of interstellar molecules, relies upon extensive laboratory studies in coincidence with astrophysical models.

In 1973, E. Herbst and W. Klemperer published a seminal work, modeling the chemistry of dense interstellar clouds [6]. At that time, virtually no experimental studies at astrophysically relevant temperatures were available, they relied on estimations for nearly all reaction rate coefficients. In this period, rate coefficients were typically measured at relatively high temperatures using flowing afterglows [7]. In this method, ionized molecules are transported in a carrier gas (usually helium) into a reaction region where they react with an injected gas via multiple collisions. Using the rate measurements of the mass-selected daughter products, as a function of the number density of the reactant gas, the reaction rate coefficients can be determined. In the subsequent years, this technique was further refined into what is now known as selected ion flow tube (SIFT) technique. In SIFT, a single ionic species is mass selected prior to merging into the reaction region [8]. Most experimental studies on ion-neutral collisions to date, have been performed using this technique. The resulting rate coefficients are measured at room temperatures and at relatively high pressures. To date, most ion-neutral rate coefficients used in astrophysical models are merely extrapolations of such room temperature measurements to astrophysical temperatures. Few rate coefficient measurements were performed at astrophysically relevant temperatures and most demonstrated a strong temperature dependence. For example, a previous measurement using a temperatures variable 22 pole trap investigating the reaction of CH^+ + H. This experiment measured an order of magnitude variation in the rate coefficient in the low temperature regime [9], highlighting the pitfalls in simply extrapolating room temperature rate coefficients to the low temperature regime. Despite the importance of these rate coefficients and lack of experimental data, there remains few rate coefficient studies at low temperatures. This is due in part to the challenge of replicating the extreme physical conditions of the ISM within the laboratory.

This work describes two unique experimental instruments and the corresponding experimental techniques to investigate gas-phase reactions at astrophysically relevant temperatures. Part I of this thesis will focus on the simplest stable polyatomic molecule, the triatomic hydrogen ion H_3^+. In a brief introduction, an historical overview of the H_3^+ ion is given and the main theoretical aspects are discussed.

The central role of H_3^+ in the astrochemical network is highlighted and its importance in the ISM is discussed. In a simplified model, the formation and destruction mechanism of H_3^+ in interstellar clouds is presented. During its lifetime, the H_3^+ ions are assumed to be thermalized via numerous collisions with H_2, which is supposed to be the most frequent bi-molecular reaction in the ISM. However, recent astronomical observations in the diffuse interstellar medium showed a significant discrepancy between the excitation temperatures of H_2 and H_3^+. To this end, the reaction $H_3^+ + H_2$ is investigated at interstellar conditions using a temperature-variable 22 pole trap. In these measurements, performed at thermal equilibrium, the resulting nuclear spin configuration of H_3^+ is probed via laser-induced reaction spectroscopy. The results obtained in these experiments are presented and analyzed.
The second part of this thesis describes the development and design of a versatile transfer line for the Cryogenic Storage Ring (CSR) at the Max Planck Institute for Nuclear Physics. To study cold ion-atom interstellar chemical reactions, an apparatus to merge cooled stored ions ($\sim$ 10 K) with a well-defined neutral atomic beam is presented. After introducing the principles of ion beam transport via electromagnetic fields, a linear transfer matrix formalism, which is used to describe the propagation through an ion-optical system, is discussed. Ion beam properties are defined to form the basis of the design of the ion-optical system of the CSR transfer line. After a brief overview of the CSR, discussing the experimental capabilities, the development of the CSR transfer line, consisting of two merged beamlines, is presented. Taking into account the experimental requirements, the ion-optical system of the CSR transfer line is designed and simulated. The individual elements utilized for the final design of the two beamlines are subsequently discussed in more detail. In this context, an electrostatic 90° deflector with a hole, that allows for fast switching ($\sim \mu$s) between the two beamlines, is designed, simulated and constructed. Another crucial component of the CSR transfer line is the photodetachment apparatus, which is designed in order to generate a well-defined neutral atom beam, that is subsequently merged to ions stored inside the CSR. After presenting and discussing the final layout of the CSR transfer line, first test-measurements are performed on the ion beam transport and photodetachment efficiency. Finally, the results are summarized and perspectives on future work are presented.

Part I

The nuclear spin equilibrium of H_3^+ in collisions with H_2

Chapter 2

The triatomic hydrogen ion H_3^+

The first part of this thesis will focus on the triatomic hydrogen ion H_3^+. This chapter gives a brief historical review of previous research on H_3^+ and highlights the role that this simplest stable polyatomic molecule plays in both physics and astronomy. To this end, the theoretical foundations which permits the discussion of spectroscopic properties of H_3^+ are presented, including the structure, quantum numbers and selection rules for electric dipole transitions of H_3^+. An introduction of the interstellar medium is presented, demonstrating the key role of H_3^+ in interstellar chemistry. A general outline of the formation, destruction and thermalization processes of H_3^+ in interstellar clouds is also given.

2.1 Brief historical overview

The first experimental evidence on the existence of H_3^+ was published by J. J. Thomson more than 100 years ago. In 1911, using a primitive mass spectrometer, an ion with a mass to charge ratio of 3:1 was detected in a hydrogen discharge [10, 11]. The

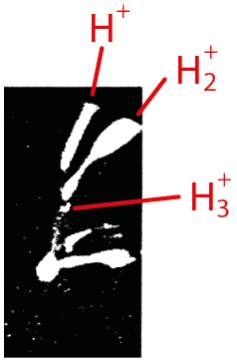

Figure 2.1: The picture shows the photographic plate on which H_3^+ was detected together with H^+ and H_2^+ by J. J. Thomson.

original photographic plate (an image of which is shown in Fig. 2.1) displays the H^+ and H_2^+ ions together with H_3^+, which is represented by the small dot. After excluding all other possibilities, Thomson labeled his discovery as H_3^+. Doubts still remained, however, and in subsequent work he referred to the molecule by X_3 [12, 13]. In a short publication in 1934, he re-described his discovery of H_3^+ as "heavy hydrogen" (HD^+) [14], after deuterium was discovered by H. C. Urey in 1932 [15].
However, in retrospect, his initial identification as H_3^+ was almost certainly correct. A. Dempster demonstrated in 1916, that the abundance of H_3^+ can be higher than H_2^+ in a hydrogen discharge [16], and in 1925 T. R. Hogness and E. G. Lunn investigated the relative concentration of H^+, H_2^+ and H_3^+ as a function of the gas pressure [17]. This publication discussed for the first time the formation of H_3^+ via the ion-neutral reaction

$$H_2 + H_2^+ \rightarrow H_3^+ + H. \tag{2.1}$$

In 1935, theoretical studies by C. A. Coulson predicted that H_3^+ has an equilateral triangle structure with the side length of 0.85 Å[18], a value similar to contemporary predictions. Subsequent theoretical studies by J. Hirschfelder and H. Erying presented arguments for a symmetric linear configuration of H_3^+ [19, 20, 21], triggered a heated debate. In 1937, Hirschfelder finally relented to Coulson's prediction and concluded that the triangular structure of H_3^+ was indeed more stable [22, 23]. With the advancement of computers, the equilateral triangular shape of H_3^+ in its ground state was confirmed in 1964 [25, 26, 27]. The experimental evidence was provided in 1978 in work by M. Gaillard et al. using Coulomb Explosion Imaging, as it is shown

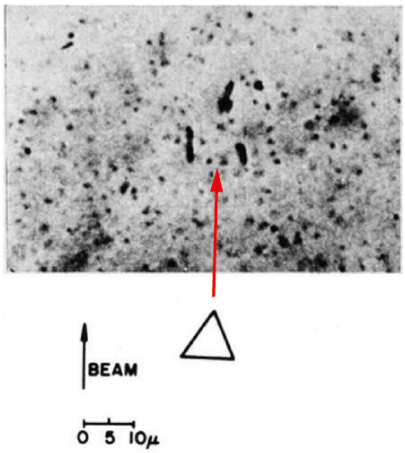

Figure 2.2: The picture illustrates the triangular shape of the H_3^+ ion, discovered by Coulomb Explosion Imaging [24].

in Fig. 2.2 [24]. In this experiment, H_3^+ ions were accelerated to energies in the MeV range and the two electrons of the H_3^+ ion were stripped off when passing through a thin carbon foil. The initial Coulomb potential energy is converted into kinetic energy and the three protons were detected after a distance of a few meters.
In 1961, the existence of H_3^+ in interstellar space was first postulated by D. W. Martin et al. [28], formed from the highly exothermic reaction between H_2^+ and H_2 (reaction 2.1). In the beginning of the 1970s, W. D. Watson [29], E. Herbst and W. Klemperer [6] established a deeper understanding of the chemical network of interstellar molecules, in which H_3^+ plays a central role.
In 1976, theoretical studies of G. D. Carney and R. N. Porter provided a prediction for the vibrational spectrum of H_3^+ with a high degree of accuracy [30]. These calculations and the development of tunable laser systems in the IR regime, paved the way for laboratory spectroscopy of H_3^+. The first experimental spectrum of H_3^+ was published in 1980 by T. Oka, almost 70 years after its initial discovery. Utilizing direct absorption spectroscopy in a liquid-nitrogen cooled multiple-reflection discharge cell, 15 absorption lines in the spectral range of 2950-2450 cm^{-1} of H_3^+ were obtained and assigned. This work was an important step in initiating systematic astronomical observations in the dense interstellar medium by T. Oka and T. R. Geballe in 1981 [33]. At that time, the technology available for astronomical infrared spectroscopy was insufficiently sensitive to detect interstellar H_3^+ [34]. It was this limitation that

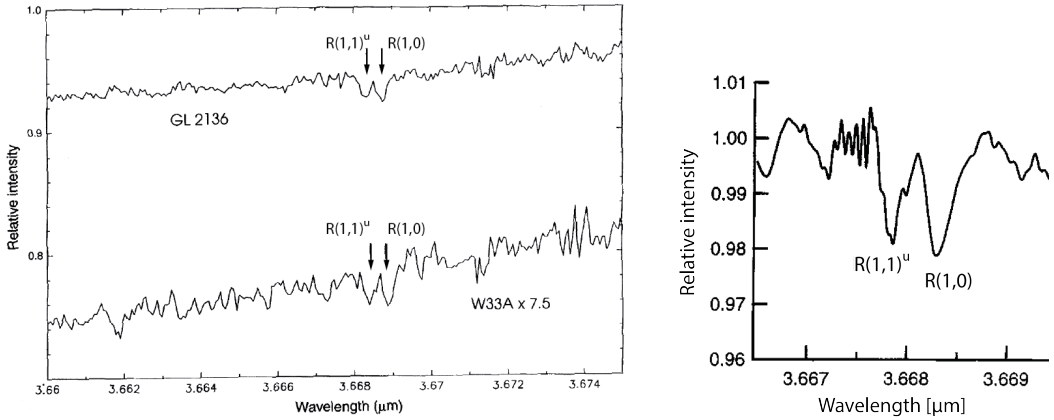

Figure 2.3: H_3^+ detected for the first time in interstellar space. The graph on the left-hand side (a) shows a spectrum of the dense interstellar medium GL2136 and W33A [31]. The detection of H_3^+ in the diffuse interstellar medium is shown in the spectrum (Cygnus OB2 No. 12) on the right hand-side (b) [32]. The transitions $R(1,1)^u$ and R(1,0) correspond to para- and ortho-H_3^+, respectively.

prevented the studies at UKIRT in the 1980s from publishing more than merely an upper limit for the H_3^+ column densities [35]. In the same year, the H_3^+ overtone band at 2 μm was detected in the southern auroral region of Jupiter by P. Drossart et al. [36]. Subsequent studies by Oka and Geballe, discovered H_3^+ infrared emission lines also in Jupiter and Saturn [37, 38]. Despite this ongoing interest and progress, it was not until the advent of a new generation of sensitive, high resolution, infrared spectrographs, that Geballe and Oka could uncover observational evidence of H_3^+ in the dense interstellar medium [31]. The spectra, taken in 1996, are shown in Fig. 2.3(a). Two years later, H_3^+ was detected even in the diffuse interstellar medium (see Fig. 2.3(b)) [32].

During this period of observational discovery, theoretical and experimental work on H_3^+ also made great progress. In 1996, L. Neale, S. Miller and J. Tennyson published a calculated line list comprising approximately three million transitions for H_3^+ energy levels up to 15000 cm^{-1} [39]. Since the first spectroscopic observations in the laboratory in 1980, Oka's experimental apparatus was continually improved. This setup yielded several hundred ($\sim$ 700) measured transitions of H_3^+, even into the visible spectral range [40]. Due to the reduction in oscillator strength for the higher-lying transitions, the direct absorption cell technique had reached its limit. To overcome this limitation, in 2004, the spectroscopic research on H_3^+, using a cryogenic 22 pole trap setup in combination with the laser induced reaction spectroscopy was presented [41]. This experimental technique (discussed in Sec. 4) forms the basis of the measurements presented in the first part of this thesis. This ultra-sensitive technique provided measurements on transitions up to 16700 cm^{-1} containing up to 9 vibrational quanta which are more than 6 orders of magnitude weaker than the fundamental band lines were obtained previously [42]. Recent theoretical calculations using a high accuracy potential energy surface for H_3^+ reproduce the measured spectrum to within tenths of cm^{-1} [43], making it one of the best-studied polyatomic molecules.

2.2 Theoretical background

The triatomic hydrogen ion H_3^+ contains three protons, which share two electrons equally. Therefore, it is the simplest stable polyatomic molecule and is often used as a benchmark system for quantum chemistry. A one dimensional presentation of the potential energy surface together with the vibrational energy levels of H_3^+ is il-

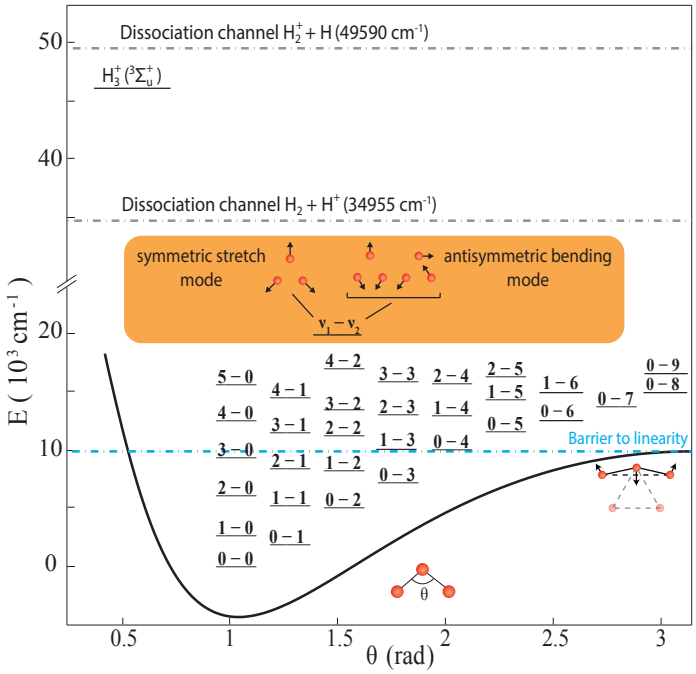

Figure 2.4: Vibrational energy levels overlaid with a one dimensional presentation of the H_3^+ potential energy surface, where θ represents the angle between the two $H-H$ bonds. The blue dashed line represents the barrier to linearity. The vibrational energy levels are labeled according to the schematic in the yellow box ($\nu_1 - \nu_2$). The dissociation channels are represented by the grey dashed lines, together with the theoretically predicted electronically excited state of H_3^+.

lustrated in Fig. 2.4, where θ represents the angle between the two H - H bonds. The minimum energy which is needed to achieve a linear configuration of H_3^+ (the so-called barrier to linearity), is represented by the blue dashed line. The vibrational ground state lies ~ 4362 cm^{-1} above the potential minimum [44]. According to theoretical predictions [45], the lowest electronically excited state of H_3^+ (triplet $^3\Sigma_u^+$) is bound, lying above the dissociation channel $H_3^+ \rightarrow H_2 + H^+$. Direct decay from the excited triplet state to this dissociation channel is prevented by symmetry restrictions. The next dissociation channel $H_3^+ \rightarrow H_2^+ + H$ lies 1.8 eV higher and is accessible to both singlet and triplet states of H_3^+ [46]. No sharp electronic spectrum is expected.

H_3^+ in its ground state has an equilateral triangular structure with a H - H bond length of 0.88 Å. The high degree of symmetry (D_{3h}) leads to an absence of a permanent dipole moment. Thus, H_3^+ has no pure rotational spectrum. However, a "forbidden" rotational spectrum is theoretically predicted due to spontaneous symmetry breaking [47], which can be described as an interaction between the rotational

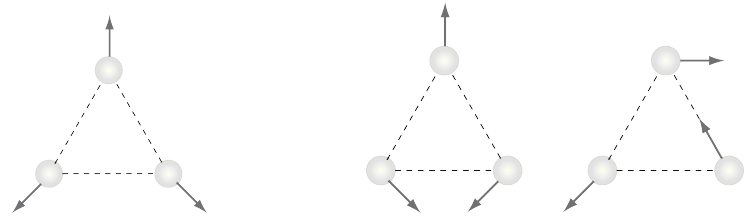

(a) Breathing mode ν_1 (b) Bending mode ν_2

Figure 2.5: The normal modes of vibration of H_3^+.

and the vibrational motion. While undergoing rotation, the centrifugal forces create a minute dipole moment, enabling rotational transitions [48]. These transitions are extremely weak and to date no pure rotational spectrum of H_3^+ has been observed. H_3^+ has three normal modes of vibration, as depicted in Fig. 2.5. The breathing mode ν_1 (shown in 2.5(a)), where the molecule expands and contracts as an equilateral triangle, is totally symmetric and infrared inactive. The doubly degenerated bending mode ν_2 (shown in Fig. 2.5(b)) is infrared active and forms the basis for spectroscopy of H_3^+. Any linear combination of these two bending mode components ν_2 have a vibrational angular momentum l [49]. The notation for the vibrational motion is given by C. M. Lindsay and B. J. McCall [50], which can be represented by a combination of the two normal modes $v_1\nu_1 + v_2\nu_2^l$. The quantum numbers v_1 and v_2 represent the number of quanta in the normal modes ν_1 and ν_2, respectively. The quantum number l is the projection of the total vibrational angular momentum onto the molecular axis (the normal of the molecular plane) and can have the values $l = -v_2, -v_2 + 2, ..., v_2 - 2, v_2$.

The total angular momentum (F) and the parity are good quantum numbers for any molecule. F can be split into the motional angular momentum, J, and the nuclear spin angular momentum, I, due to the weak spin-spin and spin-rotation interactions. For H_3^+, neither the projection (k) of J onto the molecular axis, nor l are good quantum numbers. Despite this, the strong coupling of the vibrational angular momentum to the rotation leads to the introduction of the Hougen quantum number [51],

$$G = |g| = |k - l| \,. \tag{2.2}$$

As mentioned before, H_3^+ consists of three protons, which are fermions ($I_p = \frac{1}{2}$). The nuclear spin of the protons can either be lined up to a total nuclear spin with $I = \frac{1}{2}$ or $I = \frac{3}{2}$. These two nuclear spin configurations are called para (for $I = \frac{1}{2}$) and ortho (I

$= \frac{3}{2}$), respectively, and can be regarded as two separate chemical species of H_3^+, due to the weakness of the nuclear magnetic interaction. A direct conversion between an ortho state (quadruply degenerate) and a para state (doubly degenerated) of H_3^+ is strictly forbidden. The quantum number g is related to the nuclear spin by

$$ortho - H_3^+ \longleftrightarrow g = 3n \tag{2.3}$$

$$para - H_3^+ \longleftrightarrow g = 3n \pm 1, \tag{2.4}$$

where n is an integer [52].

The rotational energy levels of H_3^+ are defined by the quantum numbers J and G. The lowest rotational energy levels in the vibrational ground state [1] of H_3^+, calculated by [39], are illustrated in Fig. 2.6. The ortho states are represented by the red solid lines and the para states are represented by the blue solid lines, consistent with Eq. 2.3 and 2.4. The Pauli exclusion principle forbids energy levels with $G = 0$ and even J, leading to the absence of a state with zero angular momentum $J = G = 0$ (indicated by grey dashed lines in Fig. 2.6). Therefore, the lowest rotational state of H_3^+ with $J = 1$, $G = 1$ is in para configuration. The next lowest level ($J = 1$, $G = 0$), which is in ortho configuration lies 22.84 cm^{-1} higher in energy.

[1] In this case is $G = |k|$.

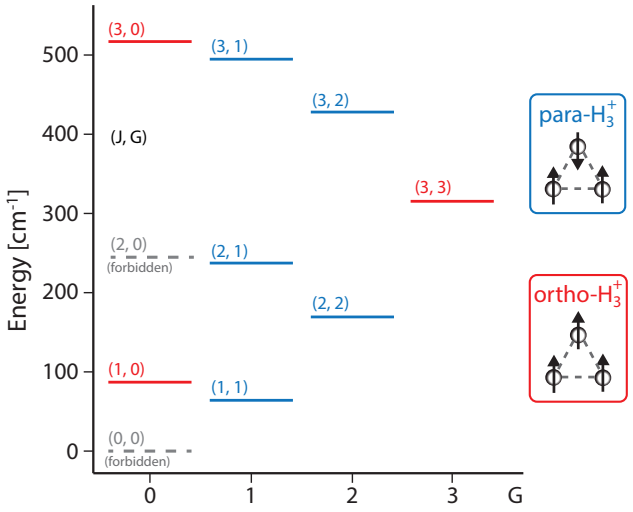

Figure 2.6: The lowest rotational energy levels in the vibrational ground state of H_3^+. The rotational states are represented by the solid lines (in blue for para states and red for ortho states) and labeled with the quantum numbers (J, G). The grey dashed lines indicate the energy levels, which are forbidden by the Pauli principle. The values for the energy levels are taken from [39].

The labeling of the rovibrational transitions, which are used in this work, follow the convention set by Lindsay and McCall [50]. As our experiment (see Chap. 4) generates H_3^+ in the lowest rotational states of the vibrational ground state, it is sufficient to label the transitions only by the final vibrational state,

$$v_1\nu_1 + v_2\nu_2^{|l|}\,, \tag{2.5}$$

and the branch symbol

$$^{\{n|t|\pm6|\pm9|\ldots\}}\{P|Q|R\}(J,G)^{\{u|l\}}_{\{u|l\}}\,, \tag{2.6}$$

where (J,G) represents the initial state and P, Q, R denotes ΔJ = -1, 0, +1, respectively. If the initial and/or final level resides in a doublet state (e.g. having the same values for both J and G), the right superscript (final state) and/or subscript (initial state) is labeled. The labels u and l indicate the upper or lower state of the doublet, respectively. The superscript on the left-hand side represents ΔG, where t is used for transitions with ΔG = +3 and n for ΔG = -3 or ΔG = 1 (if $G <$ 3). Larger changes in G are signified by their numerical values. For $\Delta G = 0$, the superscript is left blank.

For any electric dipole transitions, the selection rules for the total angular momentum $\Delta F = 0, \pm 1$ ($F = 0 \nleftrightarrow F = 0$) and the parity (+ $\leftrightarrow$ -) are rigorous [53]. The parity of a level of H_3^+ is given by $(-1)^k$ and leads to the selection rule $\Delta k = 2n + 1$, where k represents the projection of J onto the molecular axis and n is an integer. According to the conservation of the total nuclear spin, the selection rule $\Delta I = 0$ or $\Delta g = 3n$ forbids transitions between ortho and para states. As the total nuclear spin I and the motional angular momentum J are almost completely uncoupled ($F = J + I$), $\Delta J = 0, \pm 1$ ($J = 0 \nleftrightarrow J = 0$) are also a good selection rules. Thus the selection rules for the electric dipole transitions can be summarized in Tab. 2.1.

$\Delta k = 2n + 1$ (+ $\leftrightarrow$ -)
$\Delta I = 0$
$\Delta g = 3n$
$\Delta J = 0, \pm 1$
$J = 0 \nleftrightarrow J = 0$

Table 2.1: Selection rules for electric dipole transitions of H_3^+.

2.3 Interstellar chemistry

H_3^+ can be regarded as the engine of interstellar chemistry in molecular clouds. Fig. 2.7 illustrates some of the fundamental reactions with H_3^+ as a cornerstone. Although, H_3^+ is the most frequently produced interstellar molecular ion, its steady state concentration in interstellar clouds is low, owing to its high chemical reactivity. H_3^+ acts as universal proton donor and initiates the formation of larger molecules, e.g. water and hydrocarbons. The relatively small proton affinity of H_2 (4.377 eV) [54] [2] instigates the proton hop reaction $H_3^+ + X \rightarrow XH^+ + H_2$, where X is a neutral species. For example, in the formation of water (left reaction chain in Fig. 2.7), neutral atomic oxygen (O) is protonated by H_3^+ forming OH^+. In subsequent chain reactions with H_2, H_2O^+ and then H_3O^+ are formed. Finally, the H_3O^+ ion recombines with an electron and dissociates to form interstellar water.

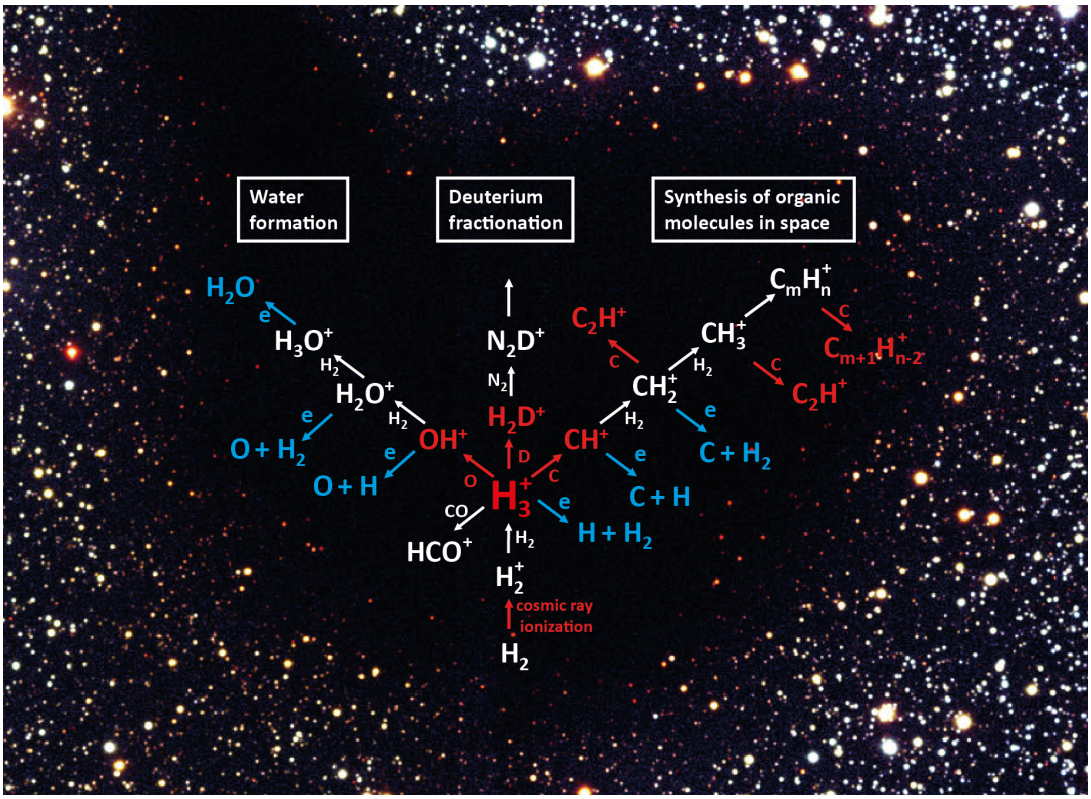

Figure 2.7: Simplified gas phase chemical network of ion-neutral reactions in the interstellar medium, highlighting the role of H_3^+ as the key ion of the interstellar medium. H_3^+ serves as universal proton donor, which enables the formation of large molecules. The background image shows the Bernard 68 molecular cloud (European Southern Observatory) [55].

[2] Species with a lower proton affinity than H_2 are listed in Tab. 4.1

2.3.1 The formation of H_3^+

In the interstellar medium, the pathway to H_3^+ formation begins with the ionization of H_2 via cosmic rays (c.r.)

$$H_2 + \text{c.r.} \rightarrow H_2^+ + e^- \,, \tag{2.7}$$

this reaction is then followed by the exothermic ion-neutral reaction

$$H_2^+ + H_2 \rightarrow H_3^+ + H \,. \tag{2.8}$$

This reaction is very efficient due to its relatively high exothermicity of 1.73 eV, which is given by the difference of the proton affinity in H_2 (4.38 eV) and H (2.65 eV) [54]. This reaction rate coefficient can be described by Langevin collision theory [56, 57]. In this framework the positive charge of H_2^+ polarizes H_2, inducing an attractive dipole moment. The Langevin rate coefficient k_L is given by

$$k_L = 2\pi q \sqrt{\frac{\alpha}{\mu}} \,, \tag{2.9}$$

where α describes the polarizability of H_2, q denotes the elementary charge and μ represents the reduced mass of the reaction complex. In practical units (α in Å^3, μ in amu), Eq. 2.9 can be rewritten as [58]

$$k_L = 2.342 \sqrt{\frac{\alpha}{\mu}} \cdot 10^{-9} \, \text{cm}^3\text{s}^{-1} \,. \tag{2.10}$$

Taking the polarizability $\alpha_{\text{H2}} = 0.787$ Å^3 for H_2 [59], the calculated rate coefficient of reaction 2.8 is $k_L = 2.08 \cdot 10^{-9}$ cm^{3}s^{-1}, which is in agreement with experimental studies [60, 61, 62].
Measurements of the cosmic ray ionization rate (ζ_2) of H_2 (reaction 2.7) from molecular cloud observations vary from $\sim 10^{-15}$ s^{-1} to 10^{-17} s^{-1} [63, 64], many orders of magnitude lower than the rate coefficient of reaction 2.8. As a result, the formation rate of H_3^+ is limited by the ionization rate ζ_2 and can be therefore represented as

$$\left[\frac{dn(H_3^+)}{dt}\right]_{\text{form}} = \zeta_2 n(H_2) \,, \tag{2.11}$$

where $n(H_2)$ denotes the H_2 density of the molecular cloud.

2.3.2 The destruction of H_3^+

Two processes are dominant in the destruction of H_3^+ in the interstellar medium, namely proton hop reactions and dissociative recombination (DR) reactions with electrons. The typical proton hop reaction

$$H_3^+ + X \rightarrow XH^+ + H_2\,, \tag{2.12}$$

where X is a neutral atom or molecule, is assumed to have a Langevin rate coefficient k_X, which is on the order of $\sim 10^{-10}$-10^{-9} cm^{3}s^{-1}. The destruction rate of H_3^+ due to proton hop reactions is then given by

$$\left[\frac{dn(H_3^+)}{dt}\right]_{\text{destr,hop}} = \sum_X k_X n(H_3^+) n(X)\,, \tag{2.13}$$

where $n(H_3^+)$ and $n(X)$ represents the number densities of H_3^+ and the neutral reaction partner X, respectively. In interstellar clouds, this process is dominated by the reactant CO [65], which has a polarizability of $\alpha = 1.953$ Å^3 [59], leading to a Langevin rate coefficient of $k_{CO} \approx 2.0 \cdot 10^{-9}$ cm^{3}s^{-1}. The destruction rate of H_3^+ induced by proton hop reactions (Eq. 2.13) can then be approximated by

$$\left[\frac{dn(H_3^+)}{dt}\right]_{\text{destr,hop}} \approx k_{\text{CO}} n(H_3^+) n(\text{CO})\,. \tag{2.14}$$

For simplicity and clarity, the second most frequent proton hop reaction (with atomic oxygen) is neglected here, which has a Langevin rate coefficient of $k_{\text{O}} = 0.8 \cdot 10^{-9}$ cm^{3}s^{-1}.

A second destruction mechanism, occurs when an electron recombines with H_3^+, denoted dissociative recombination (DR), i.e.

$$H_3^+ + e^- \rightarrow \begin{cases} H + H + H \\ H_2 + H \end{cases}\,. \tag{2.15}$$

The thermal DR rate coefficient k_e of H_3^+ was determined from storage ring measurements to be $\sim 2.6 \cdot 10^{-7}$ cm^{3}s^{-1} at interstellar temperatures [66], which is in agreement with theoretical studies [67, 68]. The destruction rate of H_3^+ due to DR

is given by

$$\left[\frac{dn(H_3^+)}{dt}\right]_{\text{destr,DR}} = k_e n(H_3^+) n(e)\,, \tag{2.16}$$

where, $n(e)$ and $n(H_3^+)$ represents the number density of the electrons and the H_3^+ ions, respectively. In the diffuse interstellar medium, $n(e)$ can be approximated by the number density of C^+ [69], since carbon has a lower ionization potential than hydrogen and thus is usually fully ionized by UV photons. Although the number density of hydrogen is many orders of magnitudes higher, the number of ionized hydrogen inside a molecular cloud is marginal, due to the self-shielding effect. Due to the high column density of hydrogen ($> 10^{14}$ cm^{-2}) [70], the UV absorption bands become optically thick, which prevent the photons from penetrating deeply into the interstellar cloud. Therefore, only the outer layer of an interstellar cloud contains ionized hydrogen, and as a result, it can be assumed that all electrons in diffuse clouds originate from the ionization of C by UV photons.

The total destruction rate of H_3^+ in interstellar molecular clouds can thus be approximated by

$$\left[\frac{dn(H_3^+)}{dt}\right]_{\text{destr}} \approx k_{CO} n(H_3^+) n(CO) + k_e n(H_3^+) n(C^+)\,. \tag{2.17}$$

Considering diffuse ($n(H) \sim 10^1$ - 10^3 cm^{-3}) and dense ($n(H) \sim 10^3$ - 10^6 cm^{-3}) clouds separately, the total destruction rate of H_3^+ can be simplified. In diffuse clouds, where the UV radiation penetrates the cloud and ionizes essentially all C atoms, the number density of electrons ranges from 10^{-4} to 10^{-1} cm^{-3}. Due to the longer range 1/r Coulomb potential, the DR rate coefficient of H_3^+ is ~ 100 larger than the Langevin charge induced-dipole $1/r^4$ potential rate coefficient k_{CO}. Therefore, the destruction rate of H_3^+ in diffuse clouds (Eq. 2.17) can be approximated by

$$\left[\frac{dn(H_3^+)}{dt}\right]_{\text{destr,diff}} \approx k_e n(H_3^+) n(e) \approx k_e n(H_3^+) n(C^+)\,. \tag{2.18}$$

In dense clouds, where molecules are abound (C is effectively converted to CO), thus the electron fraction is very small ($< 10^{-7}$)[71] the probability of DR diminishes. As a result, the destruction rate of H_3^+ in dense clouds (Eq. 2.17) can be approximated as

$$\left[\frac{dn(H_3^+)}{dt}\right]_{\text{destr,dense}} \approx k_{CO} n(H_3^+) n(CO)\,. \tag{2.19}$$

The steady-state number density of H_3^+ in diffuse and dense interstellar clouds can be estimated by equating the rates of formation (Eq. 2.11) and destruction (Eq. 2.18 & 2.19), which result in

$$n(H_3^+)_{\text{diff}} \approx \frac{\zeta_2}{k_e} \cdot \frac{n(H_2)}{n(e)} \approx \frac{\zeta_2}{k_e} \cdot \frac{n(H_2)}{n(C^+)} \tag{2.20}$$

$$n(H_3^+)_{\text{dense}} \approx \frac{\zeta_2}{k_{CO}} \cdot \frac{n(H_2)}{n(CO)} \,. \tag{2.21}$$

The number density of CO in dense clouds and the number density of electrons ($\approx n(C^+)$) in diffuse clouds are assumed to be directly proportional to the number density of the cloud $n(H)$. Therefore, the ratios $n(C^+)/n(H_2)$ from Eq. 2.20 and $n(CO)/n(H_2)$ from Eq. 2.21 are constant. As a result, the number density of H_3^+ in interstellar clouds is shown not to simply scale with the number density of the cloud, but to be essentially constant in diffuse and dense clouds, making H_3^+ a unique astrophysical tracer.

Using a relative carbon abundance of $n(C)/n(H_2) = 1.4 \cdot 10^{-4}$ in diffuse clouds [72, 73], a CO fraction of $n(CO)/n(H_2) = 1.5 \cdot 10^{-4}$ in dense clouds [71], the low temperature DR rate coefficient $k_e = 2.6 \cdot 10^{-7}$ cm^{3}s^{-1} [66], the Langevin rate coefficient $k_{CO} = 2.0 \cdot 10^{-9}$ cm^{3}s^{-1} and a lower limit for the cosmic ionization rate $\zeta_2 \approx 10^{-17}$ s^{-1} [63], the number density of H_3^+ in diffuse and dense clouds can be approximately given by

$$n(H_3^+)_{\text{diff}} \approx 2.7 \cdot 10^{-7}\,\text{cm}^{-3} \tag{2.22}$$

$$n(H_3^+)_{\text{dense}} \approx 3.3 \cdot 10^{-5}\,\text{cm}^{-3} \,. \tag{2.23}$$

This is succinctly summarized by T. Oka in a graphic, as shown in Fig. 2.8 [65]. The graphic shows the number densities $n(X)$ of H_2, CO, C^+ and H_3^+ dependent on the number density of a molecular cloud $n(H)$. It is remarkable that for dense and diffuse clouds, the number density of H_3^+ is independent of the number density of the cloud. This feature makes H_3^+ a unique astrophysical tool, which allows for estimation of the effective path length L of an interstellar cloud and the cosmic ionization rate ζ_2. The observed H_3^+ column density $N(H_3^+)$ can be approximated by $N(H_3^+) = n(H_3^+) \cdot L$. Using this relation in Eq. 2.20 and Eq. 2.21 can be used to determine the value of $\zeta_2 L$.

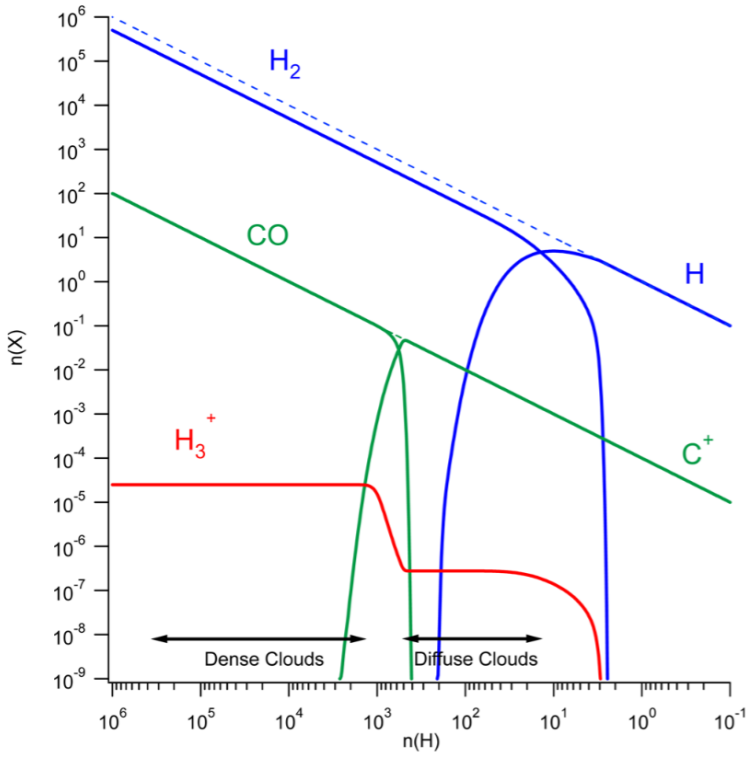

Figure 2.8: Schematic diagram (taken from [65]) showing the number densities n(X) of H_2, CO, C^+ and H_3^+ with respect to the number density of the interstellar cloud n(H). The number density of H_3^+ does not scale with the density of the interstellar cloud, dissimilarly to the number density of H_2 and CO.

2.3.3 The thermalization of H_3^+ and abnormal excitation temperatures

Interstellar chemistry is, due to its high abundance ($\sim 92.1\%$), hydrogen dominated. In diffuse and dense interstellar clouds, where molecular hydrogen (H_2) is prevalent, H_3^+ ions are thermalized in collisions with H_2,

$$H_3^+ + H_2 \rightarrow (H_5^+)^* \rightarrow H_3^+ + H_2\,. \tag{2.24}$$

In this thermalization process, the H_3^+ and H_2 form the unstable collision complex $(H_5^+)^*$, prior to dissociating back into H_3^+ and H_2. The lifetime of H_3^+ in the interstellar medium is in the order of $\sim$ 10 - 15 years (taking $n(\mathrm{CO}) = 1$ cm^{-3} and $n(\mathrm{C}) = 10^{-2}$ cm^{-3} in Eq. 2.18 and Eq. 2.19, respectively), during which the H_3^+ ions are thermalized in collisions with H_2. This thermalizing reaction has a relatively high Langevin rate coefficient of $k_{\mathrm{H2}} = 1.9 \cdot 10^{-9}$ cm^{3}s^{-1} (using a value for the polarizability of $\alpha_{\mathrm{H2}} = 0.787$ Å^3 for H_2 [59]). In diffuse interstellar clouds, with a H_2 number

density of ~ 50 cm^{-3}, reaction 2.24 occurs on average every 4 months. Under these circumstances, H_3^+ undergoes roughly 40 collisions with H_2 over its lifetime. In dense clouds, the number of collisions between H_3^+ and H_2 is several orders of magnitudes higher, due to the higher H_2 density.

Although the reactants and the products are the same, reaction 2.24 is indeed a chemical reaction, where the proton configuration may change. This reaction, which is assumed to be the most frequent bi-molecular reaction in the universe, has three different branching pathways

$$H_3^+ + \tilde{H}_2 \rightarrow H_3^+ + \tilde{H}_2 \tag{2.25}$$

$$H_3^+ + \tilde{H}_2 \rightarrow \tilde{H}_2H^+ + H_2 \tag{2.26}$$

$$H_3^+ + \tilde{H}_2 \rightarrow H_2\tilde{H}^+ + H\tilde{H}\,. \tag{2.27}$$

These pathways represent the possible rearrangements of the hydrogen atoms after scrambling via an $(H_5^+)^*$ collision complex. In these processes, $\tilde{H}$ indicates a proton, which originates from the neutral parent reactant H_2. In reaction 2.25 the configuration of the reaction partners H_3^+ and H_2 remain the same, known as the identity reaction. Reaction 2.26 is denoted as proton hop reaction, where a proton is transferred from the H_3^+ ion to the H_2 molecule. In the so-called exchange reaction 2.27, an H atom is exchanged between H_3^+ and H_2.

Both molecules have two possible nuclear spin configurations (para and ortho), which are associated with specific rotational states (as discussed for H_3^+ in Sec. 2.2). The nuclear spin configurations of H_2 are discussed in more detail in Sec. 3.1.

Theoretical studies introduced nuclear spin selection rules in chemical reactions, using group theory [74] and angular momentum algebra [75, 76]. These selection rules lead to restrictions in the resulting nuclear spin configurations of H_3^+ and H_2, dependent on the reaction pathway. For instance, a reaction between para-H_3^+ and para-H_2 will always form para-H_3^+ for reaction pathway 2.25 (identity) and 2.26 (proton hop), whereas an exchange reaction (2.27) can lead to ortho-H_3^+. In the case, where reaction 2.24 occurs frequently, and the available energy is sufficiently high to populate many rovibrational states, the nuclear spin selection rules lead to a statistical description for the reaction pathways 2.25, 2.26 and 2.27. The resulting nuclear spin configurations of the H_3^+ (o/p) + H_2 (o/p) complex are summarized in Tab. A.1 [76] (see Appendix A). If the abundance of H_2 is several orders of magnitude higher than of H_3^+, the total change in the ortho/para ratio of H_2 is negligible. The branching

Table 2.2: Branching fractions for the formation of ortho- and para-H_3^+ via the reaction pathways identity (2.25), proton hop (2.26) and exchange (2.27) [76].

reaction	identity		proton hop		exchange	
spin species	o-H_3^+	p-H_3^+	o-H_3^+	p-H_3^+	o-H_3^+	p-H_3^+
(o-H_3^+, o-H_2)	1	0	2/3	1/3	2/3	1/3
(o-H_3^+, p-H_2)	1	0	0	1	2/3	1/3
(p-H_3^+, o-H_2)	0	1	2/3	1/3	1/3	2/3
(p-H_3^+, p-H_2)	0	1	0	1	1/3	2/3

fractions for the formation of ortho- and para-H_3^+ via the reaction pathways 2.25, 2.26 and 2.27 can then be inferred from Tab. A.1, ignoring the nuclear spin configuration of the resultant H_2. The result is summarized in Tab. 2.2, where the rows represent the nuclear spin configuration of the reactant and the columns represent the nuclear spin configuration of the H_3^+ produced via the reaction pathways identity, proton hop and exchange. In a next step, the para fraction of H_3^+ (defined by $p_3 = [\text{p-}H_3^+]/[\text{p-}H_3^+ + \text{o-}H_3^+]$) can be derived as a function of the para fraction of H_2 (defined by $p_2 = [\text{p-}H_2]/[\text{p-}H_2 + \text{o-}H_2]$), using these branching fractions in the steady state approximation, as shown in [77]. The para fraction of H_3^+ is then given by

$$p_3 = \frac{k_H(\frac{1}{3} + \frac{2}{3}p_2) + \frac{1}{3}k_E}{k_H + \frac{2}{3}k_E}\,, \tag{2.28}$$

where k_H and k_E represent the rate constants of the proton hop reaction and the exchange reaction, respectively. Defining a parameter $\alpha = \frac{k_H}{k_E}$, Eq. 2.28 can be rewritten as

$$p_3 = \frac{\alpha + 2\alpha p_2 + 1}{3\alpha + 2}\,. \tag{2.29}$$

It is apparent from Eq. 2.29, that the ratio α is a crucial value in the resultant ortho/para ratio of H_3^+. As the statistical weights of the proton hop reaction and the exchange reaction is given by 3 and 6, respectively, the statistical limit for the branching ratio is $\alpha = 0.5$. In experimental studies, performed in a hydrogen discharge using pure para-H_2, the ortho/para ratio of H_3^+ was determined by spectroscopy. A value of $\alpha = 2.4 \pm 0.6$ was derived, where the hydrogenic plasma had a temperature of $\sim$ 400 K [75]. In a later experiment, where the setup was cooled by liquid nitrogen, α was found to be 1.6 ± 0.1 at 350 K and 0.5 ± 0.1 at 135 K [78].

In a low temperature regime (10 - 160 K), the nuclear spin selection rules, alone,

are insufficient to statistically describe the products from $H_3^+ + H_2$ reactions. The lower energy that is available limits the accessibility of higher energy levels. The development of a mircocanonical statistical model by Park and Light [79], using state-to-state reaction rate coefficients, also accounts for the conservation of the angular momentum, energy and parity. These reaction rate coefficients are computed based on the total energy of the reactant (kinetic temperature T_{kin} and rotational temperature T_{rot}) and the branching fractions of the three reaction pathways (2.25, 2.26, 2.27). The subscript of the reaction rate coefficients k_{ijkl} denotes the nuclear spins of the reactants and the products of the $H_3^+ + H_2$ reaction, e.g. k_{oppo} represents the rate coefficient of o-H_3^+ + p-H_2 → p-H_3^+ + o-H_2. The relative ratios for the nuclear spin configurations, which are derived from the state-to-state reaction rate coefficients assuming complete proton scrambling, are shown in Tab. A.3 (see Appendix) for 10 K, 80 K and the high temperature limit [79]. For high temperatures, it converges to the statistical model by T. Oka (compare Tab. A.2 and Tab. A.3). In case of the low temperature model, the para fraction of H_3^+ (p_3) in the steady state approximation (given by Eq. 2.28 for high temperature) changes to [80, 77]

$$p_3 = \frac{(k_{oopp} + k_{oopo})(1 - p_2) + k_{oppo}\, p_2}{(k_{oopp} + k_{oopo} + k_{poop} + k_{pooo})(1 - p_2) + (k_{oppo} + k_{ppoo})p_2}\,. \tag{2.30}$$

This model can be applied to the conditions of the interstellar medium.
In the low-temperature diffuse and dense clouds, H_3^+ populates only the two lowest rotational levels [80]. The para fraction of H_3^+ (p_3) can then be approximated by

$$p_3 = \frac{para - H_3^+}{total - H_3^+} \approx \frac{N(1,1)}{N(1,1) + N(1,0)}\,, \tag{2.31}$$

where $N(1,1)$ is the column density for the (J=1,G=1) state and $N(1,0)$ is the column density for the (J=1,G=0) state of H_3^+. The (1,0) state, which is in ortho configuration lies $\Delta E(H_3^+) = 22.84\ \mathrm{cm}^{-1}$ ($\hat{=}$ 32.86 K) higher in energy than the (1,1) state, which is in para configuration. Using the Boltzmann factor, the observation of their column densities $N(1,0)$ and $N(1,1)$ in cold molecular clouds can be used to determine the excitation temperature $T_{ex}(H_3^+)$ of H_3^+ by

$$\frac{N(1,0)}{N(1,1)} = \frac{g_o}{g_p} \exp\left\{\frac{-\Delta E(H_3^+)}{k\, T_{ex}(H_3^+)}\right\} = 2 \exp\left\{\frac{-32.86[K]}{T_{ex}(H_3^+)}\right\}\,, \tag{2.32}$$

where g_o and g_p represent the spin statistical weight $(2I + 1)$ of the ortho ($I_o = \frac{3}{2}$, $g_o = 4$) and the para ($I_p = \frac{1}{2}$, $g_p = 2$) state, respectively. The excitation temperature of a molecule in the interstellar medium is considered to be a defining characteristic parameter. It should be noted, that the excitation temperature is merely a convenient way to parameterize the level populations as a single number T_{ex}, although it is not necessarily equal to the kinetic temperature (T_{kin}) of the cloud. In principle, any atom or molecule with more than one populated level can provide information on the molecular cloud temperature.

The excitation temperature of H_2, $T_{ex}(H_2)$, observed in the interstellar medium by probing the relative intensities of the two lowest rotational levels of H_2 ($J = 0$ and $J = 1$), is commonly denoted as T_{01} [81]. Due to many reactive collisions of H_2 with protons, it is assumed that T_{01} reflects the kinetic temperature in diffuse interstellar clouds [82]. The level spacing (ΔE_{01}) between the first two rotational states of H_2 is 118.85 cm^{-1} ($\hat{=}$ 171 K), where the $J = 0$ state is in para configuration and $J = 1$ is an ortho state (discussed in Sec. 3.1). Since at least 99 % of the interstellar H_2 populates only the first two rotational states, the excitation temperature T_{01} can then be approximated by

$$\frac{N(1)}{N(0)} = \frac{g_1}{g_0} \exp\left\{\frac{-\Delta E_{01}}{k\,T_{01}}\right\} = 9 \exp\left\{\frac{-171[K]}{T_{01}}\right\}. \tag{2.33}$$

The statistical weights g_0 and g_1 are given by $(2J + 1)$ for para-H_2 states and $3(2J + 1)$ for ortho-H_2 states, resulting in a ratio of 9. The para fraction of H_2 (p_2) derived by astronomical observations can be approximated by

$$p_2 = \frac{para - H_2}{total - H_2} \approx \frac{N(0)}{N(0) + N(1)}. \tag{2.34}$$

The column densities of interstellar H_2 for $J = 0$ ($N(0)$) and for $J = 1$ ($N(1)$) have been determined for many molecular clouds [83, 84]. The excitation temperatures T_{01} of these clouds have been calculated using Eq. 2.33. The majority ranges from 50 K to 75 K, equivalent to a H_2 para fraction of $p_2 = 0.75$ - 0.55 (using Eq. 2.34). Recently, the column densities $N(1,0)$ and $N(1,1)$ of H_3^+ have been determined in some of the same sight lines. As a result, the para fraction of H_3^+ ranges from 0.55 to 0.7, according to Eq. 2.31. This implies that the excitation temperature $T_{ex}(H_3^+)$ ranges from 20 K to 40 K (using Eq. 2.32). To date, nine sight lines with measured H_2 column densities of diffuse molecular clouds have been also observed for H_3^+,

Table 2.3: Overview of astronomical observations of H_2 and H_3^+ in diffuse interstellar sight lines [83, 84, 64, 85, 86].

sight line	p_3	p_2	$T_{ex}(H_3^+)$ [K]	T_{01} [K]
ζ Per (HD 24398)	0.65±0.04	0.68±0.06	25±3	58±6
X Per (HD 24534)	0.66±0.05	0.69±0.03	25±4	57±3
HD 73882	0.67±0.04	0.76±0.05	23±3	51±4
HD 110432	0.60±0.02	0.57±0.03	30±2	68±3
HD 154368	0.69±0.06	0.76±0.07	22±4	51±6
λ Cep (HD 210839)	0.57±0.07	0.54±0.03	34±11	73±4
62 Tau (HD 27778)	0.61±0.04	0.70±0.05	29±4	56±5
χ^2 Ori (HD 41117)	0.61±0.12	0.66±0.07	29±13	60±7
9 Gem (HD 43384)	0.55±0.06	0.53±0.12	38±11	74±15

showing a significant discrepancy in the excitation temperature of H_3^+ ($T_{ex}(H_3^+)$) and H_2 (T_{01}) [64, 85, 86]. These observations are summarized in Tab. 2.3. The excitation temperature of H_3^+ is on average 33 K lower than the excitation temperature of H_2. This discovery was unexpected, since both species should thermalized to the kinetic cloud temperature by reactive collisions. The ortho and para populations of H_2 are predicted to be thermalized by collisions with protons [82]. In a similar manner, the ortho and para populations of H_3^+ should be brought into thermal equilibrium by reactive collisions with H_2 [87, 88, 89]. Fig. 2.9 shows the para fractions of H_2 and H_3^+ from the astronomical observations listed in Tab. 2.3, together with the para fractions at thermal equilibrium. While it is commonly accepted that the excitation temperature T_{01} accurately reflects the kinetic temperature of molecular clouds, the observed excitation temperatures of H_3^+ seem to be non-thermal. Consequently, the ortho and para populations of H_3^+ cannot be utilized as thermometer of interstellar molecular clouds.

This unexpected observation is still under discussion and raises the question whether the reactive collision $H_3^+ + H_2 \rightarrow H_3^+ + H_2$ has a non-thermal outcome. Therefore experimental studies at molecular cloud temperatures are required to examine this discrepancy in the interstellar medium. In the following chapters, an experimental apparatus and technique to study the nuclear spin equilibrium of H_3^+ in collisions with H_2 at interstellar conditions, is presented and discussed in detail.

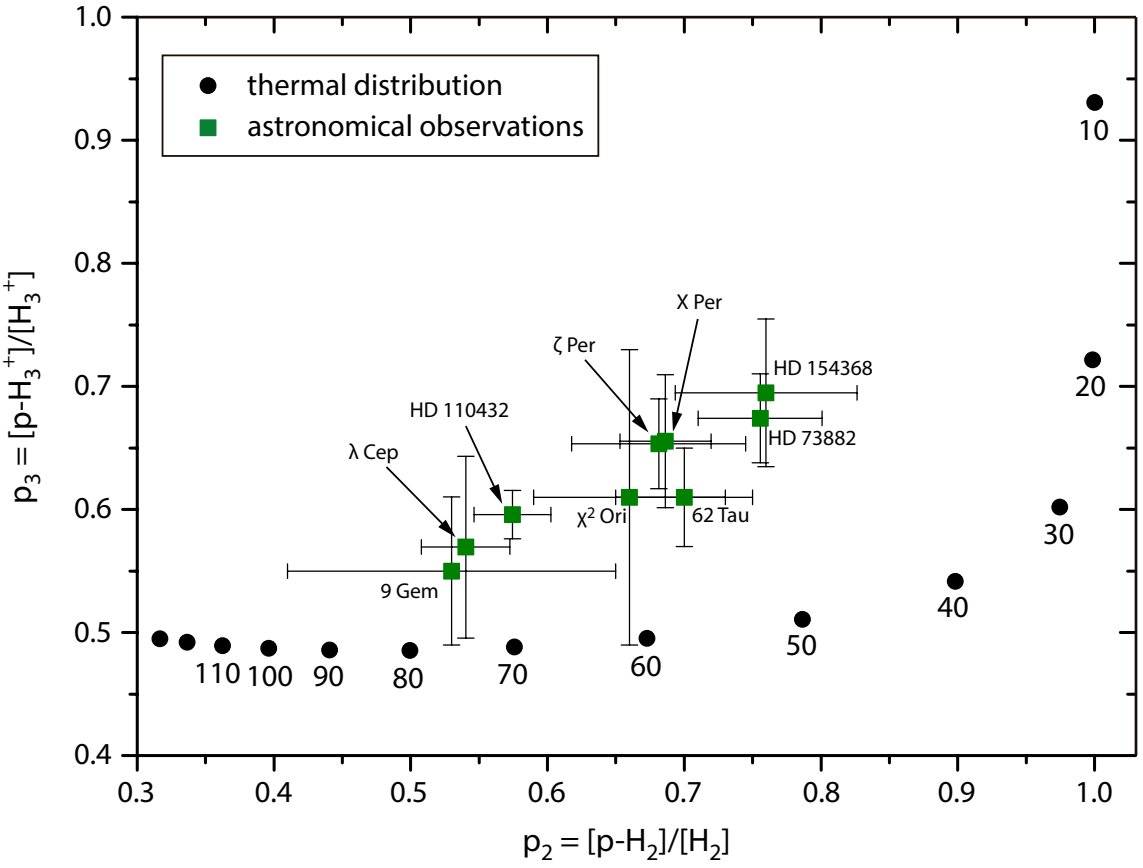

Figure 2.9: Graphical overview of the observed H_2 and H_3^+ para fraction in 9 sight lines. Each of the green squares represents one sight line (summarized in Tab. 2.3). The black solid circles indicate the para fractions of H_2 and H_3^+ at thermal equilibrium in steps of 10 K (the temperature is given by the number [K] at the circle).

Chapter 3

Experimental setup

Experimental measurements on the thermalization process of H_3^+ in collisions with H_2 at interstellar conditions, require that both reactants are in thermal equilibrium with respect to one another. To achieve this, the H_3^+ ions are stored in a well-defined, temperature regulated, stable environment and the merged H_2 reactant gas has a defined nuclear spin configuration, which matches the storage temperature conditions. After a set storage time, in which the H_3^+ ions undergo numerous collisions with H_2 molecules, the nuclear spin configuration of the H_3^+ ions are probed.
In this chapter an experimental system is introduced, that can create a well-defined ortho/para H_2 gas sample, which subsequently can be merged with stored H_3^+ ions in a thermally well-defined environment and probed via a laser after a set time period. Following that, a technique to determine the resulting nuclear spin configuration of H_3^+ is presented in Chap. 4.
Prior to studying the H_3^+ thermalization process in collisional reactions with H_2 at thermal equilibrium, a H_2 gas sample has to be manipulated and characterized by its nuclear spin configuration. To this end, a pure (>99%) para-H_2 sample is created using a para-hydrogen converter (described in Sec. 3.1). Via dilution of the pure sample with normal H_2 (which has a para/ortho ratio of 1/3), H_2 gas samples are formed with a specific para/ortho-H_2 ratio. Raman spectroscopy is then employed to confirm the para/ortho-H_2 ratio of the prepared samples, presented in Sec. 3.2.
As previously discussed in Sec. 2.3 and described in more detail in Sec. 3.1, each H_2 para/ortho ratio corresponds to a certain excitation temperature of H_2, denoted as T_{01}. For experimental measurements in thermal equilibrium, the environmental temperature is set to this equivalent excitation temperature of the prepared H_2 molecules. In this equilibrated environment the reactants of $H_3^+ + H_2$ are combined

and the reaction proceeds at a temperature $T = T_{01}$.
To provide a well-defined, temperature regulated environment for this ion-neutral reaction, a temperature-variable 22 pole trap [90] is utilized. A 22 pole trap (further detailed in Sec. 3.3) is similar in design to a linear radio-frequency (RF) quadrupole trap (the so-called linear Paul trap) [91], with the exception of the number of radial confinement electrodes. By applying an alternating potential to these electrodes, an effective field is formed in which the ions can be trapped. Using a quadrupole trap, the effective potential confining the ions radially scales with r^2 (where r denotes the radial displacement of a charged particle), effectively leading to a single field-free point at the axial center of the trap. By increasing the number of poles, the weak-field area around the axial center of a linear RF trap is expanded [92]. As the effective potential of multipole traps scales with r^{2n-2} [92], a 22 pole trap (composed of two sets of n=11 electrodes) possesses a nearly box-like effective potential, in which the ions move mostly unperturbed, with a very short ranged reflecting wall at the radial limits. This allows the storage of ions in combination with efficient buffer gas cooling down to very low ion temperatures ($\sim$ 10 K). Beyond the nearly field-free region, in proximity to the electrodes, the RF field induces a mircomotion to the stored particles [93]. Demonstrated in detailed numerical simulations by [58], the micromotion of the ions combined with the present gas (i.e. buffer gas) leads to an increase of the internal energy of the stored particles, commonly referred to as RF heating. Consequently, the ions are heated in proximity of the trap electrodes, while being thermalized in the field-free region via collisions with the buffer gas. The increase in the ion temperature caused by the RF heating depends on the mass of the stored ions and the buffer gas, the ion number density and in particular the trap geometry [92, 58]. In contrast to a quadrupole trap, the 22 pole trap permits the stored ions to move most of the time in a wide field-free region bordered with steep confining walls. Therefore, the stored ions can approach closer to the nominal trap temperature. For this reason, the 22 pole is an ideal tool for the investigation of ion-collision processes at cryogenic temperatures.

3.1 Preparation of H_2 with defined nuclear spin ratios

Molecular hydrogen (H_2) has two nuclear spin configurations, denoted para and ortho, respectively. In H_2 the nuclear spin (I) of the protons couple to a total nuclear spin of either 0 or 1. If the nuclear spin of both protons point in the same direction

($I = 1$), the H_2 is in the ortho configuration. If the nuclear spin of both protons point in opposite directions ($I = 0$), the H_2 is in para configuration.
The ortho hydrogen (o-H_2) has a spin triplet and symmetric nuclear spin wave functions ($|\uparrow\uparrow\rangle, |\downarrow\downarrow\rangle, |\uparrow\downarrow\rangle + |\downarrow\uparrow\rangle$). The para hydrogen (p-$H_2$) has an antisymmetric nuclear wave function ($|\uparrow\downarrow\rangle - |\downarrow\uparrow\rangle$). Considering H_2 in its electronic and vibrational ground state, where their corresponding wave functions are symmetric, the rotational wave function has to be antisymmetric for o-H_2 and symmetric for p-H_2. Therefore, p-H_2 cannot exist in rotational states with odd rotational quantum numbers J and o-H_2 cannot exist in rotational states with even rotational quantum numbers J.
In thermal equilibrium at high temperatures ($\gtrsim$ 250 K), 25% of H_2 is populated in a para state and 75% is populated in a ortho state, due to the state multiplicity of their nuclear spin. The rotational energy levels E_J of H_2 (in the electronic and vibrational ground state) can be approximated by a rigid rotor, corrected by a centrifugal distortion term [94], yielding

$$E_J = B_0 J(J+1) - D_0 J^2 (J+1)^2, \tag{3.1}$$

where the rotational constant $B_0 = 59.33289\ \mathrm{cm}^{-1}$ and the centrifugal distortion constant $D_0 = 0.045498\ \mathrm{cm}^{-1}$ is taken from [95]. The energy levels of the first four rotational states are shown in Fig. 3.1 (left).
The thermal population numbers N_J of the rotational energy levels E_J depend on

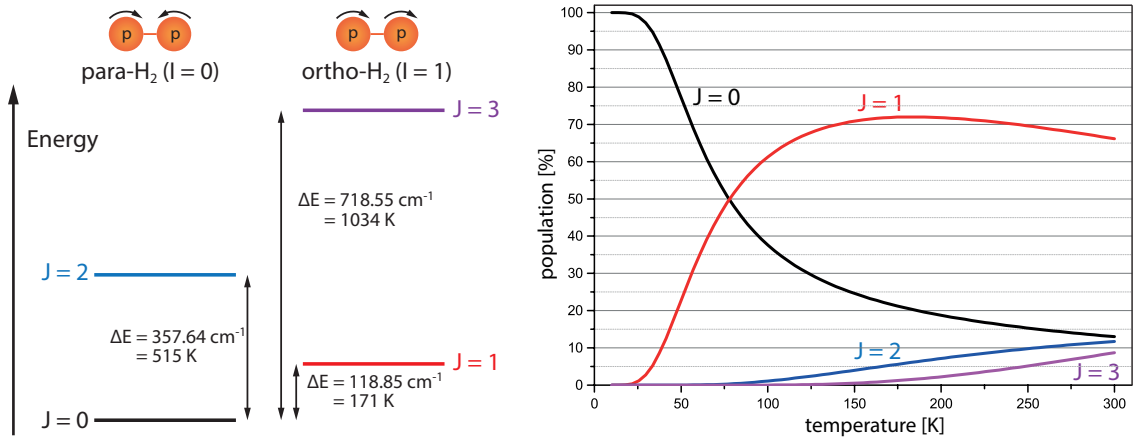

Figure 3.1: The sketch on the left-hand side side illustrates the lowest rotational energy levels in the vibrational ground state of H_2. The energy levels and their thermal population (Boltzmann-distribution), shown in the right graph, are calculated using the rotational constant $B_0 = 59.33289\ \mathrm{cm}^{-1}$ and $D_0 = 0.045498\ \mathrm{cm}^{-1}$, which are taken from [95].

the temperature T, the statistical weight g_J and the Boltzmann factor,

$$N_J = \frac{g_J}{Z} e^{\frac{-E_J}{k_B T}}, \tag{3.2}$$

where the partition function Z and the statistical weight g_J is given by

$$Z = \sum_{J=0}^{\infty} g_J e^{\frac{-E_J}{k_B T}}, \qquad g_J = \begin{cases} 2J+1 & \text{for para-H}_2 \\ 3(2J+1) & \text{for ortho-H}_2 \end{cases}. \tag{3.3}$$

The thermal populations of the rotational energy levels (up to $J = 11$) of H_2 in its electronic and vibrational ground state were calculated for temperatures up to 300 K, using Eq. 3.2. In this temperature range $> 99.5\%$ of H_2 populates the first four rotational states, which are shown in Fig. 3.1 (right). At a temperature of 100 K, already 99% of H_2 populates only the first two rotational states. In the steady state at 20 K, 99.8% of H_2 is in the para-state $J = 0$.
In Fig. 3.2, the para fraction of H_2 (p_2) in thermal equilibrium is plotted as a function of the temperature. The relative number densities of all calculated para states (even J) and ortho states (odd J) are summed up in dependence of the temperature, respectively. The p_2-value, defining the fraction of the number density n of

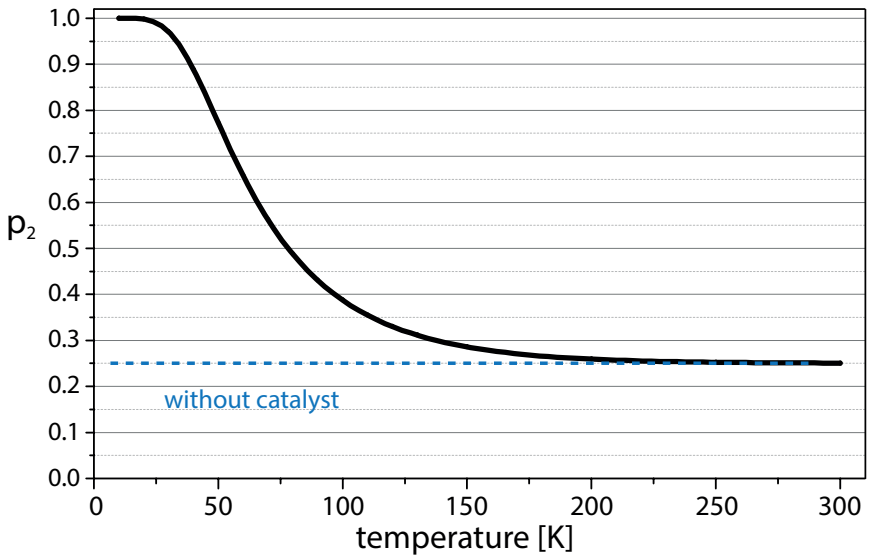

Figure 3.2: The graph illustrates the temperature dependence of the para fraction in H_2 (p_2) at thermal equilibrium.

H_2-molecules in the para configuration, is then given by

$$p_2 = \frac{n(p - H_2)}{n(p - H_2) + n(o - H_2)} \,. \tag{3.4}$$

Radiative transitions between the two nuclear spin configurations are strictly forbidden, due to the conservation of angular momentum. Therefore, a paramagnetic catalyst at low temperatures is needed to convert the nuclear spin on its solid surface and generate H_2 in a spin configuration with $p_2 > 0.25$.

The setup of para hydrogen converter

At the Max Planck Institute for Nuclear Physics in Heidelberg, a para hydrogen converter has been built [96]. The heart of the converter (shown in Fig. 3.3 (left)) is a copper container (shown in Fig. 3.3 (top right)), sitting on a 10 K cold head and housed in an ultra high vacuum (UHV) environment. The container is filled with a Fe_2O_3 powder (Fig. 3.3 (bottom right)), which serves as the paramagnetic catalyst. In order to achieve temperatures $\sim$ 10 K, the copper container is directly mounted on the second stage of the cold head (Leybold Coolpower 7/25). The temperature is monitored by two temperature dependent silicon diodes (Lakeshore DT-470-CU-13), attached to the top and the bottom of the container. The temperature can be regulated by using a heating foil, which is placed at the copper container. Normal H_2 gas is fed through the UHV chamber into the copper container, which is held at a temperature of $\sim$ 10 K. The H_2 molecules have to pass through the Fe_2O_3 powder to reach the outlet gas line at the other side of the container. They freeze out at the large surface of the powder, where their nuclear spin can relax into the energetically lowest state. By heating the copper container to a temperature of $\sim$ 20 K, the H_2 evaporates and is guided into a gas bottle. In order to prevent the p-H_2 gas from converting back at room temperature, the interior surface of the gas bottle is coated with teflon.
The experiment requires the production of H_2 samples, which have defined para fractions p_2. Rather than generating them directly via the para hydrogen converter at the corresponding temperature, it is more convenient to dilute the generated p-H_2 gas with n-H_2. To achieve this the n-H_2 gas line is directly connected to the p-H_2 gas line bypassing the copper container. The para fraction of the produced H_2 samples

can be estimated by

$$p_2 = \frac{n(p-H_2) + \frac{1}{4}n(n-H_2)}{n(p-H_2) + n(n-H_2)}\,, \tag{3.5}$$

where n represents the number densities of the respective species. De facto, in Eq. 3.5 the number densities can be approximated by the pressures of the respective H_2 gas, to estimate the p_2-value.

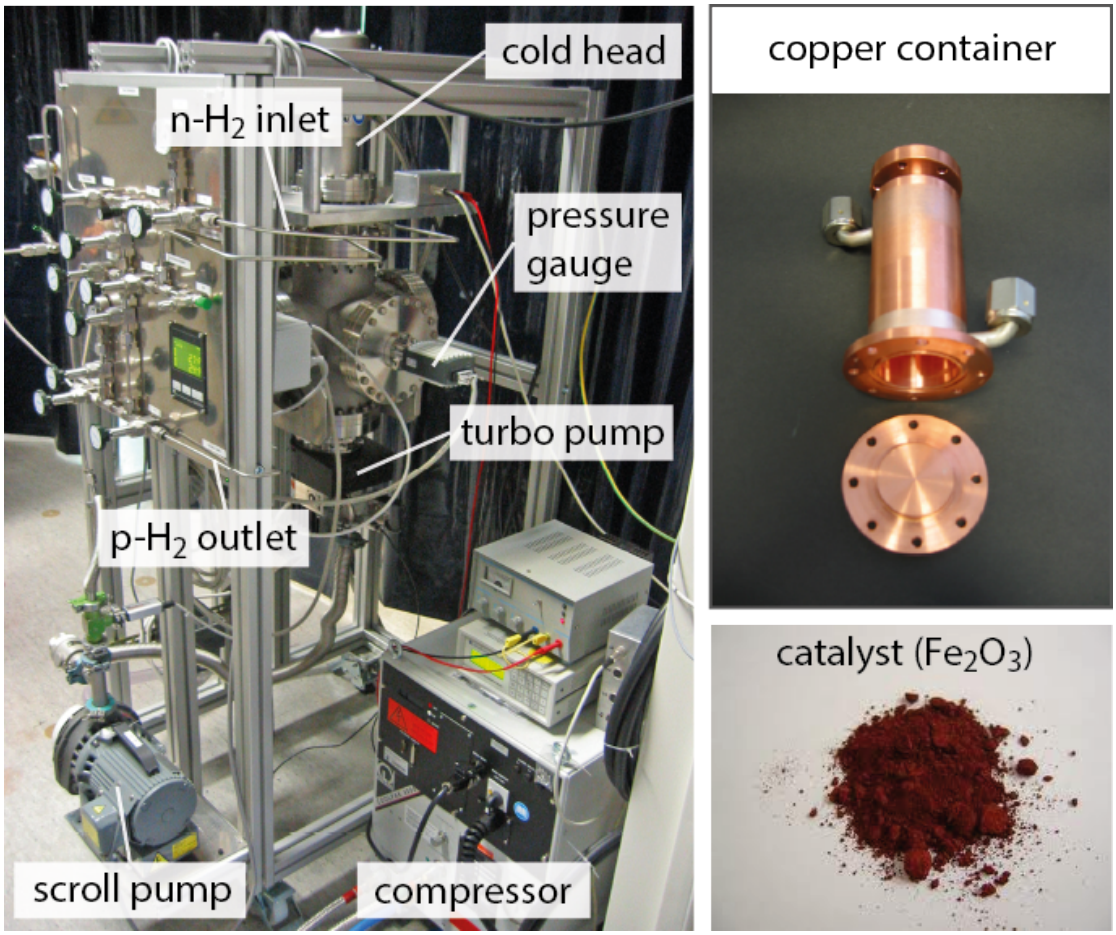

Figure 3.3: The left picture shows the setup of the para hydrogen converter. The cold head extends into the vacuum chamber, which is evacuated with a turbo pump to $\sim 10^{-9}$ mbar. The copper container, which is directly mounted on the cold head, is shown in the upper right picture. The gas line of the normal-H_2 gas (inlet) and the generated para-H_2 gas (outlet) is fed through the vacuum chamber and is attached to the copper container, where the H_2 gas has to pass through the paramagnetic catalyst. A sample of the catalyst which is located inside the copper container is shown in the lower left picture. The pictures are taken from [96].

3.2 Analysis of defined H_2 nuclear spin ratios

The prepared hydrogen samples are analyzed to confirm their para/ortho ratio. A sensitive noninvasive analytic tool, suitable for confirming the para/ortho ratio is Raman spectroscopy [94, 97]. Raman-scattering can be regarded as the inelastic scattering of a photon with a molecule, as illustrated in Fig. 3.4. The incoming photon ($E_{ph,i} = \frac{hc}{\lambda_i}$) excites a molecule, which is in an initial state $|i\rangle$, into a virtual state $|v\rangle$. The excited molecule subsequently emits a secondary photon ($E_{ph,f} = \frac{hc}{\lambda_f}$), leaving the molecule in a final state $|f\rangle$, according to the selection rule ΔJ = -2, 0, +2 for rotational states. The energy difference ΔE can appear in a ro-vibrational state of the molecule.

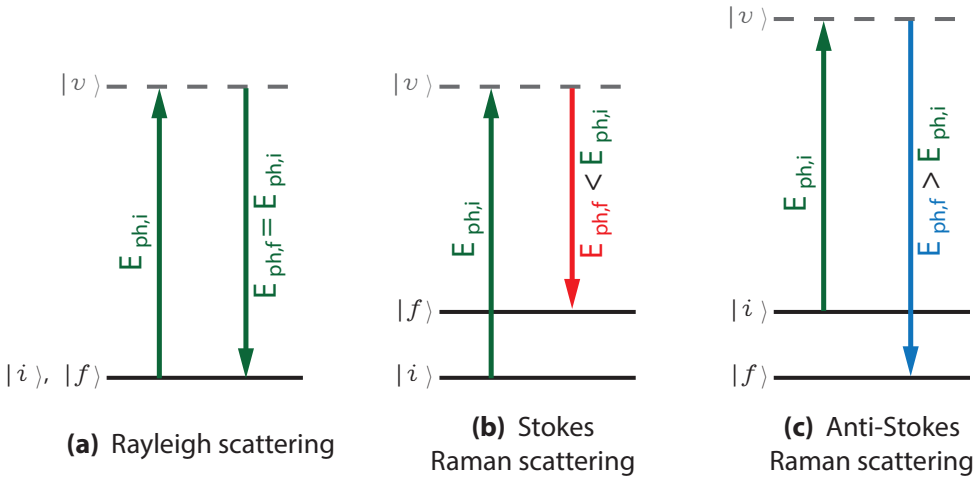

Figure 3.4: The schematic level diagram illustrates the scattering of a photon with a molecule. The molecule in the initial state $|i\rangle$ undergoes a transition via a virtual state $|v\rangle$ into the final state $|f\rangle$. (a) illustrates the Rayleigh scattering, where the initial and the final state of the molecule are identical. The Stokes Raman scattering (b) shows the case, where the final state of the molecule is higher in energy than the initial state. If the final state is lower than the initial state of the molecule, the transition is called Anti-Stokes (c). In all processes the energy is conserved.

3.2.1 The Raman spectroscopy setup

The Raman spectroscopy setup at the Max Planck Institute for Nuclear Physics in Heidelberg [96] is shown in Fig. 3.5. It consists of a frequency-doubled Nd:YAG continuous wave (cw) laser (InnoLight Diabolo), which has an output power of $\sim$ 500 mW at a wavelength of 532 nm. A set of high reflective mirrors guide the

laser beam through a glass cell (Bruker A131, anti-reflection coated), containing the H_2 gas test sample. An additional mirror (M4), which reflects the laser beam back, is placed behind the glass cell to increase the laser overlap with the H_2 molecules in the gas cell, as shown in Fig. 3.5. Two iris diaphragms prevent stray light from the laser and block the back reflected laser beam. Lens 1 and lens 2 (for the back reflection) bring the laser into focus at the center of the glass cell, where photons can interact with the stored H_2 molecules. A fraction of the secondary photons, which are emitted due to Raman scattering, are collected by lens 3, perpendicular to the laser beam. Lens 4 focuses the collected photons onto the entrance slit of a spectrometer (Acton SectraPro-300i). A stepping motor tilts the grating inside the spectrometer to scan the selected wavelength range. A photomultiplier tube (PMT), which is attached to the exit slit, detects the photons passing the spectrometer. The PMT (Hamamatsu R2256P) is actively cooled by a Peltier element to reduce electronical noise. An edge filter, which is placed between lens 3 and 4 suppresses the Rayleigh scattered photons at 532 nm. Additionally, the entire setup is housed in an anodized aluminum case to reduce the background signal due to ambient light. One of the two gas lines, which are attached to the glass cell, is connected to a scroll pump. After achieving a medium vacuum of $\sim 10^{-2}$ mbar inside the glass cell, a

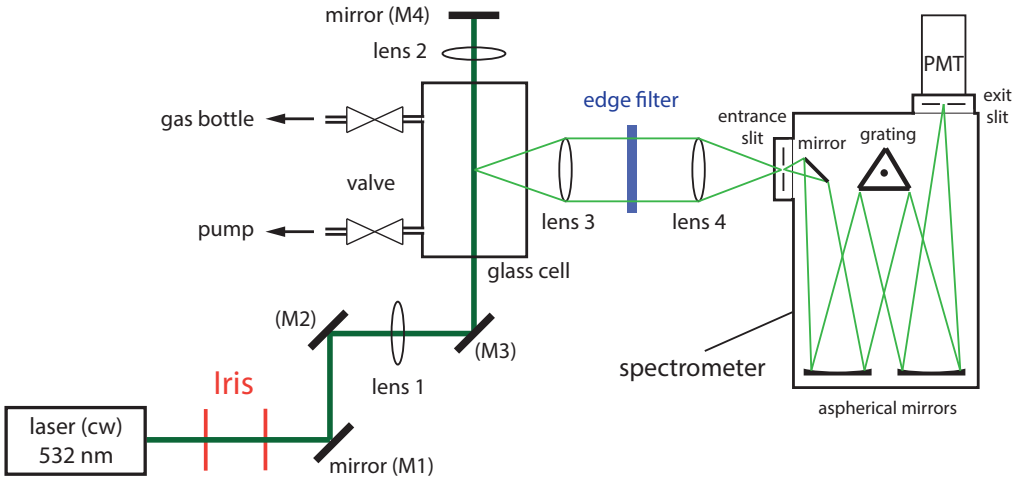

Figure 3.5: Sketch of the Raman spectroscopy setup: A laser beam (532 nm, cw) is guided and passed through a glass gas cell, using high reflectivity mirrors. The glass cell has two inlet gas lines, which can be closed by valves. One of gas lines is attached to the sample gas bottle, the other is connected to a scroll pump for evacuating the glass cell. The laser interacts via Raman scattering with molecules stored inside the glass cell. Subsequently, a spectrometer analyzes the secondary photons emitted by the sample gas (collected by lens 1 and 2). A photomultiplier tube (PMT) detects the photons, which pass the spectrometer.

gas sample of typically 0.5 - 0.7 bar is transferred via the other gas line and can be analyzed.

The para fraction of the produced H_2 gas samples is determined by analyzing the pure ($\Delta\nu = 0$) rotational Raman spectra $J \rightarrow J + 2$ (Stokes lines), as shown in Fig. 3.6. This example shows three Raman spectroscopy measurements on H_2 with different para fractions. The green color represents a Raman spectrum of n-H_2 with $p_2 = 0.25$ and the blue color denotes a para fraction of $p_2 = 0.52$ and the red color denotes $p_2 = 0.82$. The dots represent the detection signal of the PMT scanned in the wavelength range between 530 nm and 570 nm in steps of 0.05 nm. At every wavelength step the signal is integrated over 300 ms. The peaks of the Raman spectra are fitted by a Gaussian distribution, indicated by the solid lines in the same color of the corresponding dots. The broadening of the peaks in the Raman spectrum originate from the adjustment of the slits of the spectrometer, which is a compromise between higher signal and narrow peaks. The most relevant feature of the measured spectra, for this study, are the relative intensities of the Raman lines. The relative intensities reflect the mixture of the H_2 samples, whilst the central wavelength are merely used for transition identification. Therefore, the slits of the spectrometer are

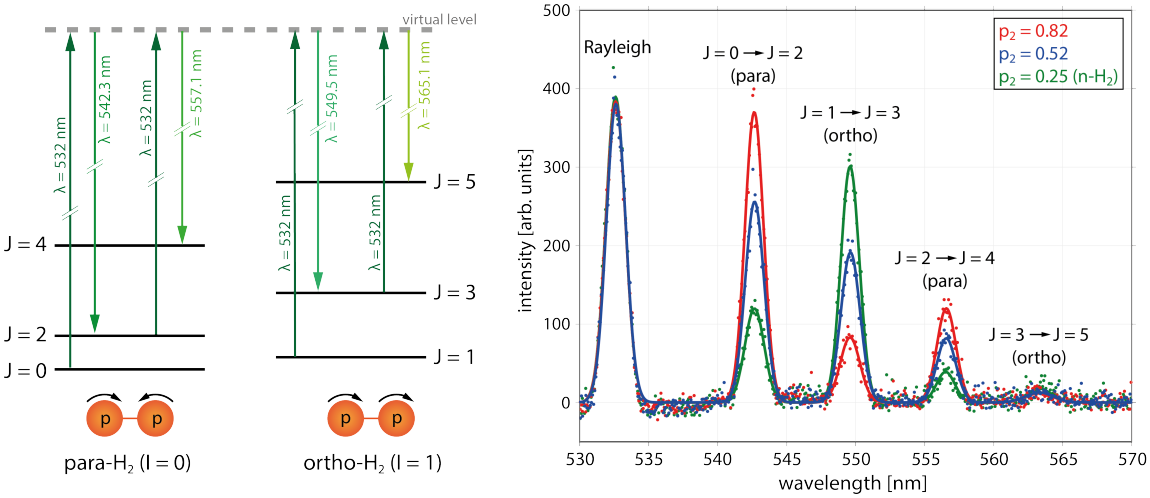

Figure 3.6: The sketch on the left side shows the six lowest rotational energy levels in the vibrational ground state of H_2. The green arrows indicate the Stoke transitions of the Raman scattering ($J \rightarrow J + 2$), which were scanned for the analysis of the para fraction in H_2. The graph on the right side illustrates Raman spectra of three H_2 gas samples with different para fractions ($p_2 = 0.82$ (red), $p_2 = 0.52$ (blue) and n-H_2 (green) with $p_2 = 0.25$). The dots represent the detection signal dependent on the wavelength of the emitted photons. The peaks of the Raman spectra are fitted by a Gaussian distribution, indicated by the solid lines in the same color of the corresponding dots. The Rayleigh peak is highly suppressed using an edge filter.

set to optimize the signal intensity, but with well separated peaks. The intensities I of the lines in the Raman spectrum are proportional to the population density N_i of the initial energy levels of the molecule, according to [98]

$$I = k_\nu \cdot \sigma \cdot \Omega \cdot N_i \cdot I_L, \tag{3.6}$$

where k_ν is a constant factor, σ describes the Raman cross section, the function Ω contains the geometrical optics of a setup and I_L is the photon density, interacting with the molecules. For an experimental setup, the Raman signal intensity I is converted into a measured signal S, within a time interval Δt:

$$S \propto Q_e(\lambda) \cdot I \cdot \Delta t, \tag{3.7}$$

where the quantum efficiency $Q_e(\lambda)$ of the detector depends on the wavelength λ. In order to eliminate the wavelength dependent influences on the signal (e.g. the spectrometer properties, the angle of the edge filter and the quantum efficiency of the PMT), each measurement on p_2-H_2 is taken relative to n-H_2. Therefore, a calibration spectrum of n-H_2 is obtained prior to each Raman spectrum measurement of a prepared H_2 sample. For the analysis, only the transition $J = 0 \rightarrow J = 2$ (p-H_2 state) and the transition $J = 1 \rightarrow J = 3$ (o-H_2 state) of the Raman spectra are used to determine the para fraction of the H_2 samples. As discussed in 3.1, n-H_2 consists of 75% o-H_2 and 25% p-H_2. The Raman signal intensity $I_o(n - H_2)$ of the $J = 1 \rightarrow J = 3$ transition of n-H_2 and the Raman signal intensity $I_p(n - H_2)$ of the $J = 0 \rightarrow J = 2$ transition of n-H_2 is normalized to the known fraction o(n-H_2) : p(n-H_2) of 3 : 1, which leads to the calibration factor c:

$$c = \frac{3}{1} \Big/ \frac{I_o(n - \mathrm{H_2})}{I_p(n - \mathrm{H_2})}. \tag{3.8}$$

The para fraction of the prepared H_2 gas samples (p_2) can be derived by the calibration of the Raman line intensities of their spectra, using the calibration factor c:

$$p_2 = \frac{I_p(\mathrm{H_2\,sample})}{I_p(\mathrm{H_2\,sample}) + I_o(\mathrm{H_2\,sample}) \cdot c}\,, \tag{3.9}$$

where I_p(H_2 sample) and I_o(H_2 sample) represent the Raman signal intensity of the transitions $J = 0 \rightarrow J = 2$ (p-H_2 state) and $J = 1 \rightarrow J = 3$ (o-H_2 state), respectively. The results of the six prepared H_2 gas samples, which were used for the

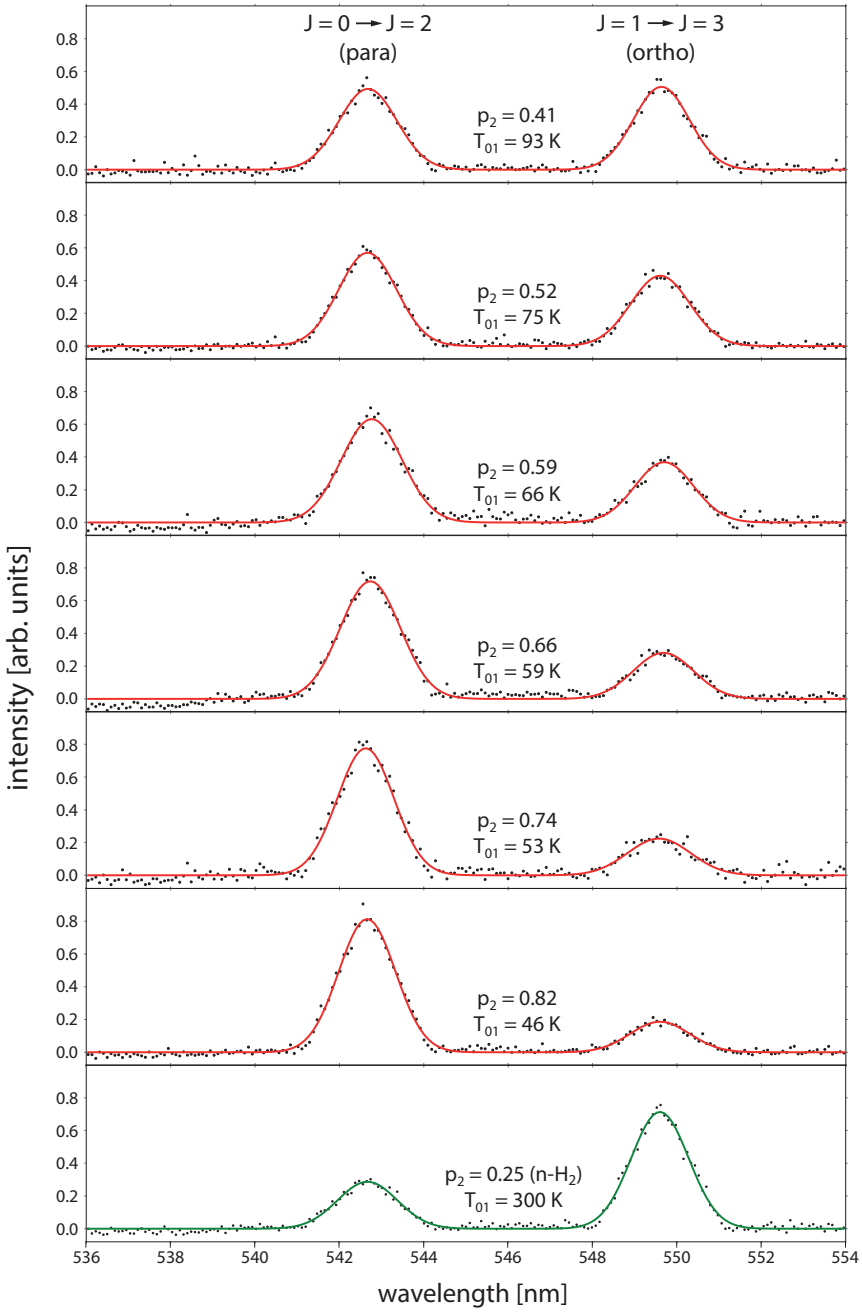

Figure 3.7: The diagrams illustrate the Raman spectrum, including the transition $J = 0 \rightarrow J = 2$ (para) and the transition $J = 1 \rightarrow J = 3$ (ortho), of six prepared p_2-H_2 gas samples and n-H_2. The black dots represent the normalized Raman signal intensities, which are not corrected by the calibration factor c. The peaks of the Raman spectra are fitted by a Gaussian distribution, indicated by the red lines (green line for the n-H_2 Raman spectrum). The p_2 values and the corresponding excitation temperature T_{01}, which are given in the diagrams, were averaged over the Raman spectra, which were taken before and after the experiment in the 22 pole trap.

experiment in the 22 pole trap, and a Raman spectrum of n-H_2 are depicted in 3.7. For each measurement the Raman spectra were scanned 3 times in wavelength steps of 0.05 nm with a signal integration time of $\Delta t = 300$ms. The measured signals, indicated by the black dots, are not corrected by the calibration factor c. For a better overview, the spectra are normalized and sorted by the para fraction of the H_2 gas samples. The trend in p_2 is clearly visible in the spectra. The red (green for n-H_2) line in the diagrams indicates the fitted Gaussian line profiles. A Raman spectrum of each sample was taken before and after the measurements in the 22 pole trap. Within these 4-5 days, a back-conversion of the p-H_2 in the gas samples appears, which decreases p_2 by ~ 0.04. Furthermore, the low Raman signal to noise ratio, mainly due to the relatively low pressure of the H_2 gas samples, accounts for the total uncertainty in p_2 of $\Delta p_2 = 0.05$. The average para fraction of the H_2 samples, calculated according to equation 3.9 (taking the calibration factor c (3.8) into account), as well as the corresponding excitation temperatures T_{01} are given in the diagrams.

3.3 The 22 pole ion trap setup

In the last two decades, 22 pole traps have become an established versatile research tool in the field of molecular physics. Since its development in the 1990s by D. Gerlich and co-workers [90, 92], the 22 pole trap has enabled precision spectroscopic measurements on molecular ions ranging from the fundamental (e.g. H_3^+ [41]) to the complex (e.g. biomolecules [99]). In addition, the 22 pole trap yielded time resolved cluster formation measurements [100] and photodetachment studies of anions [101]. The 22 pole trap setup at the Max Planck Institute for Nuclear Physics in Heidelberg was initially build as a cryogenic temperature-variable ion source for the Test Storage Ring (TSR) to investigate the temperature dependent dissociative recombination of

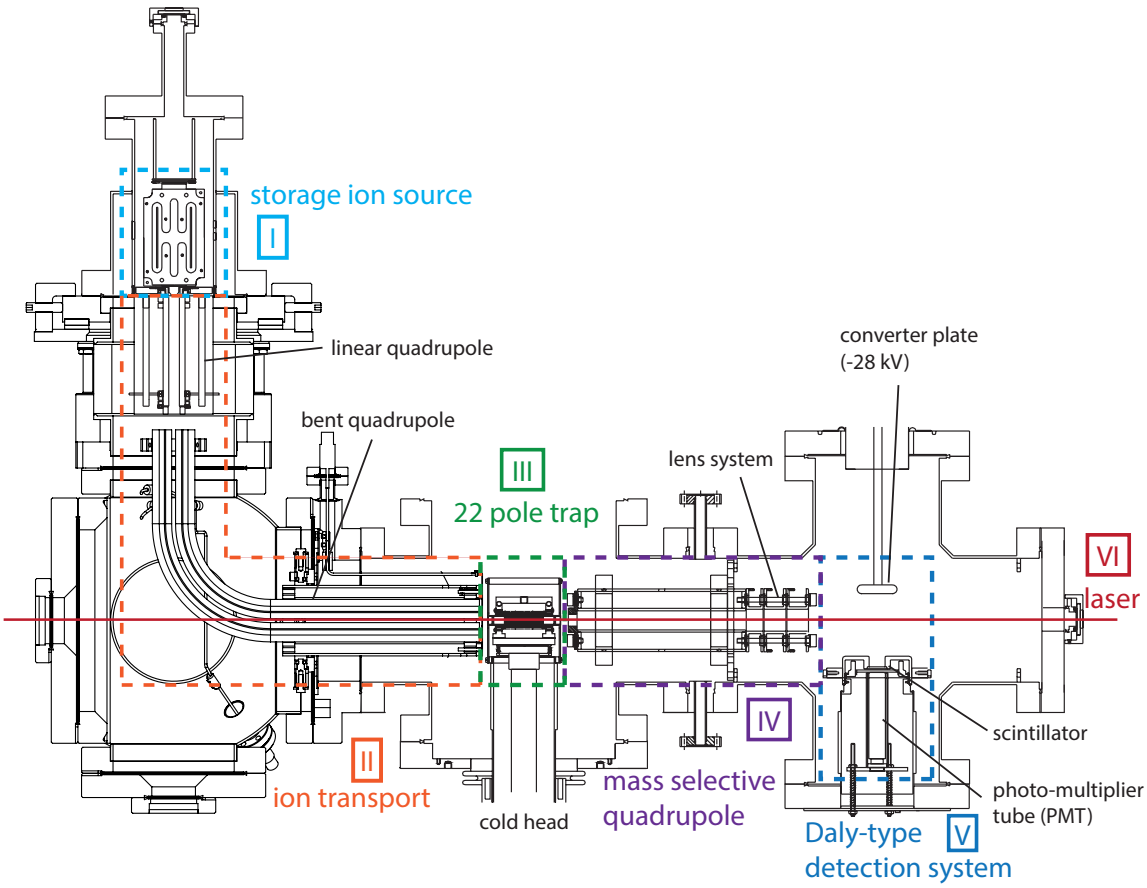

Figure 3.8: Schematic of the 22 pole trap setup. Ions are produced in the storage ion source (I), subsequently transported by a linear and a bent quadrupole (II) into the 22 pole trap (III), where the ions can be buffer-gas cooled and interact with a reactant gas and a laser field (VI). Finally, the ions are mass selected (IV) and detected by the Daly-type detection system (V).

H_3^+ with electrons [102]. The compact design also enabled the operation of the 22 pole trap as a stand-alone device for high resolution spectroscopy using laser induced chemical reactions [41].
The experimental setup is embedded in an ultra-high vacuum (UHV) system, achieving base pressures in the order of 10^{-9} mbar. The setup can be divided into six parts, as shown in Fig. 3.8:

I The radio-frequency storage ion source

II The ion transport into the trap

III The temperature-variable 22 pole trap

IV The mass selective quadrupole

V The Daly-type detection system

VI The laser system

3.3.1 The storage ion source

In this setup the H_3^+ ions are produced in a Teloy-type storage ion source [103]. The RF storage source consists of a stack of eight molybdenum plates (50 mm x 80 mm), which are electrically insulated from one another by ruby pearls (see Fig. 3.9). These eight plates possess double H-shaped cutouts (see Fig. 3.8 (I)), which create the volume in which the H_3^+ ions are produced. Above one of the side arms of the double H-shaped structure a rhenium filament is placed, which serves as an electron emitter. These electrons are accelerated by the negative potential of the filament and guided by a repeller into the source volume. A fraction of the H_2-gas is ionized via electron impact:

$$H_2 + e^- \rightarrow H_2^+ + 2e^-. \tag{3.10}$$

These H_2^+ ions can now react with H_2 to form H_3^+,

$$H_2 + H_2^+ \rightarrow H_3^+ + H + 1.7 \text{ eV}. \tag{3.11}$$

The two endplates are held at a constant voltage, confining the ions inside the source. The axial confinement of the ions is created by the plate electrode B1 at the back and the ring electrode B0 at the front of the source (shown in Fig. 3.9). Each of the eight

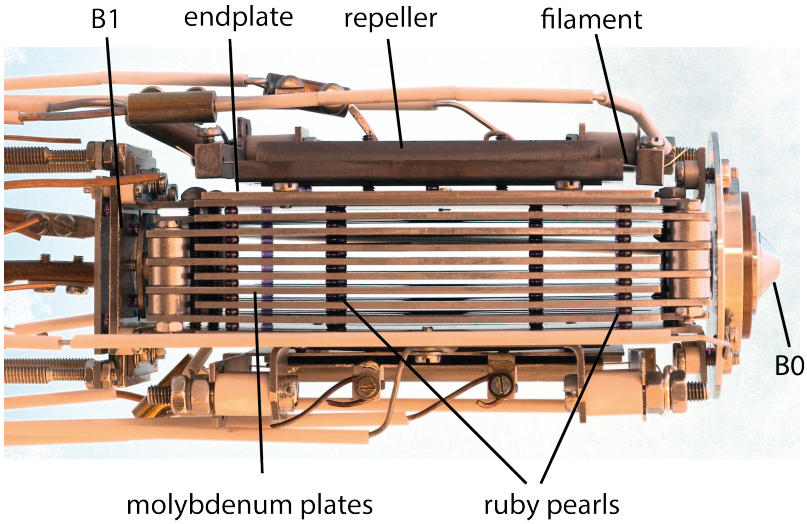

Figure 3.9: Side view of the storage ion source: The picture shows the stack of the molybdenum plates insulated from each other by ruby pearls. The filament is surrounded by the repeller. The ring electrode B0 is used to extract the ions from the source.

plates of the stack are supplied with a RF voltage of 16 MHz with an amplitude of 34 V. The resulting effective potential allows to store the ions inside the source, while H_3^+ is constantly produced. Due to collisions with the parent gas H_2, the H_3^+ ions result in internal temperatures of 400 - 500 K and a smaller energy spread during the source storage time [104]. The hot filament prevents a further cooling of the H_3^+ ions inside the source. Ion bunches are extracted applying a voltage pulse to the ring electrode B0 (d_i = 3 mm). The kinetic energy of the ions leaving the source is defined by the applied source DC potential of 0.5 V.

3.3.2 The ion transport into the trap

After ion production, the ions are transported into the 22 pole trap via first a linear and then a bent quadrupole. The linear quadrupole (see Fig. 3.10(a)) guides the ions by using a radio-frequency of 9.4 MHz at a voltage amplitude of 21 V to the bent quadrupole (see Fig. 3.10(b)). The linear quadrupole, which is directly mounted after the source, has a length of 90 mm and an inner radius of 4.3 mm.
A circular plate at the entrance, following the small aperture of the source (B0), limits the H_2-gas flow from the source. This first differential pumping section reduces the H_2-gas pressure by more than an order of magnitude, using a turbomolecular pump (Leybold Turbovac 361) underneath the bent quadrupole. Afterwards, the ions pass the bent quadrupole (see Fig. 3.10(b)), which is operated at a radio-frequency of

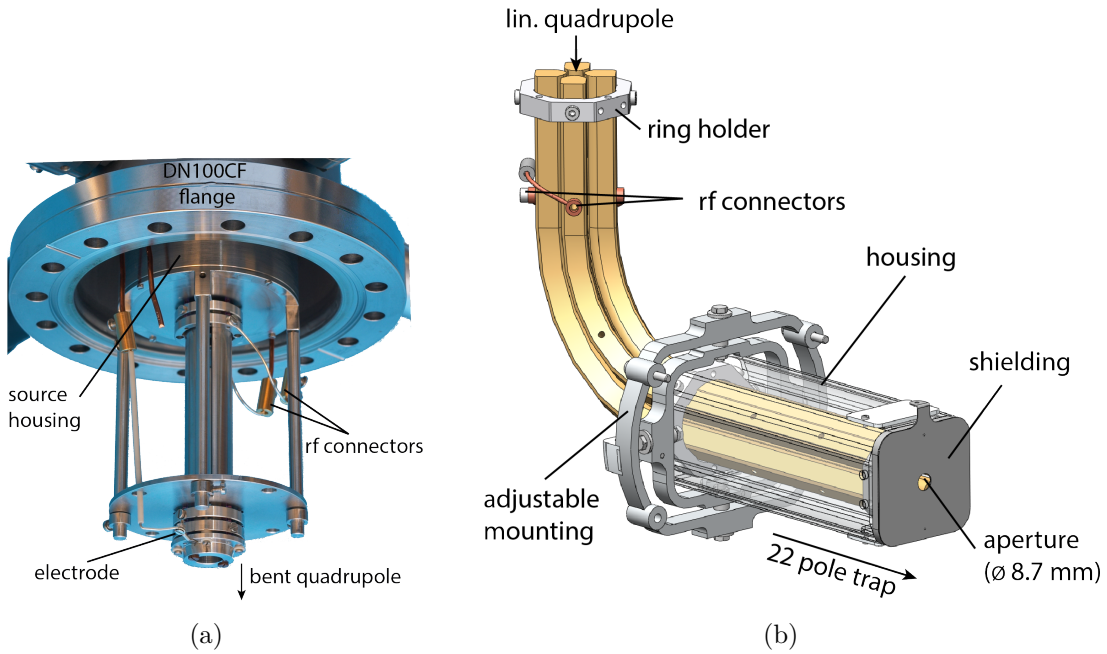

Figure 3.10: The left picture shows a photograph of the linear quadrupole, mounted directly at the exit of the source. In the right picture, a CAD drawing of the bent quadrupole is depicted.

11.1 MHz with an amplitude of 5 V. This section was implemented into the setup to create a second stage of differential pumping. The last section of the quadrupole is encased by a housing with a small aperture (d = 8.7 mm) at the exit. According to vacuum simulations and measurements the pressure (created by H_2 leaking from the source) improves by another factor of roughly 10. As a result the pressure difference between the source vacuum chamber and the trap vacuum chamber is greater than two orders of magnitude.

3.3.3 The temperature-variable 22 pole trap

The heart of the setup is the temperature-variable 22 pole ion trap (see Fig. 3.11), designed by D. Gerlich and co-workers [92]. It consists of two sets of 11 stainless steel rods, each with a radius of 1 mm and a length of 40 mm. The rods are alternately embedded in one of the side plates in a circle with a radius of 5 mm. Via each of these side plates a radio-frequency voltage of 17.7 MHz with an amplitude of 22 V is applied to the rods. To maintain thermal isolation, the electrical connection is inductively coupled via two coaxial coils to interrupt the thermal connection. The

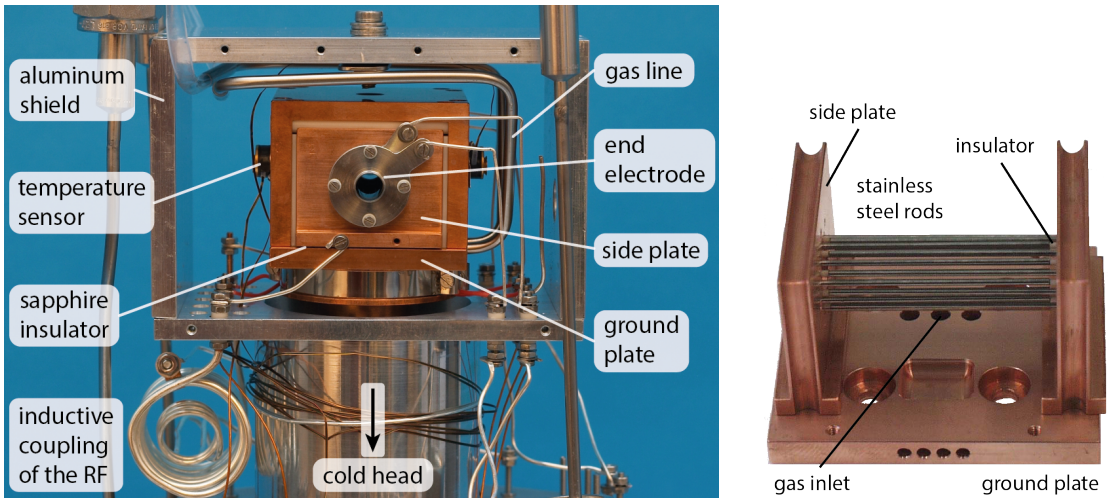

(a) (b)

Figure 3.11: The 22 pole ion trap: The left picture shows a photograph of the 22 pole trap in axial direction. In the right picture a side view is shown.

side plates are insulated by sapphire stripes to maintain high thermal conductivity to the copper housing. The 22 pole trap, due to its high pole order, provides a nearly box-shaped radial potential containing a large field free area in the center of the trap [92]. Two ring electrode pairs at the entrance and the exit of the trap at a DC voltage of 1 V confine the ions in axial direction during the storage time. Over the course of trap loading the entrance electrodes are switched to a negative potential. The exit electrodes are switched to a negative potential to extract the H_3^+ ions. The entire housing of the trap is made up of bulk copper plates and is directly mounted on the second stage of a cold head (Leybold Coolpower 2/10), which has a cooling power of 2 W at 10 K. The first stage of the cold head (with a cooling power of 12 W at 35 K) is connected to the aluminum shield, which surrounds the trap minimizing heat transfer induced by black body radiation. This structure allows nominal trap temperatures down to 10 K. Two kapton heating foils (placed underneath the ground plate) are utilized to set a variable and stable temperature of up to $\sim$ 100 K. The temperature is monitored by a temperature dependent silicon diode (Lakeshore DT-470-CU-11A) on each of the side plates of the trap. The gas lines are attached to drill holes inside the ground plate, which allows the gas to cool prior to entering the trap volume. Helium is used as a buffer gas, hydrogen as a reactant gas and argon as a probing gas (discussed in chapter 4).

3.3.4 The mass selective quadrupole

After ion extracting, it is necessary to differentiate by mass. Therefore a quadrupole with a commercial RF power supply (Extrel 150 QC) at a fixed frequency of 1.2 MHz is used. The direct current and the alternating current of the RF is varied simultaneously to select a certain mass-to-charge ratio [105]. Changing the quadrupole voltages at a fixed V_{dc} / V_{ac} ratio permits only a certain ion species to pass through. After mass selection a lens system focus the ions before reaching the detection system.

3.3.5 The Daly-type detection system

The experimental technique requires a detection system which is very sensitive for single ion counting and has a large dynamic range. The central axis of the 22 pole trap is ideally kept clear, allowing for a laser to be merged co-linear to the path of both the stored and extracted ions. This configuration is advantageous as it permits to couple the setup to the storage ring to act as a cold source. The Daly-type detection system [106] consists of an aluminum converter plate in combination with a scintillator and a photomultiplier tube (PMT) (see Fig. 3.12). Positively charged ions, which have passed the mass selective quadrupole, are attracted to the converter plate held at a negative voltage. Due to the plate's high electric potential of -28 kV, the ions are accelerated to the surface of the aluminum plate, where upon impact on average more than 4 secondary electrons [107] are ejected. These electrons are then accelerated away from the negative plate onto a grounded aluminum-coated scintillator, where several photons are created. A PMT (Hamamatsu R4124) sitting outside of the vacuum chamber detects the photons. The scintillator is coated with an aluminum layer to reduce counts arising from the laser reflections and ambient light, while allowing energetic electrons to pass through. The sputtering process to coat the plastic scintillator with an aluminum layer of about 150 nm thickness is technically challenging. As a result the aluminum layer is not perfectly homogeneous, so that a fraction of the environmental light still reaches the the PMT. To further reduce dark counts due to photons an optical filter glass covers the PMT in addition. Despite the comparatively low quantum efficiency of a PMT, the Daly-type detection system has a detection efficiency close to unity, due to the high number of photons per ion created.

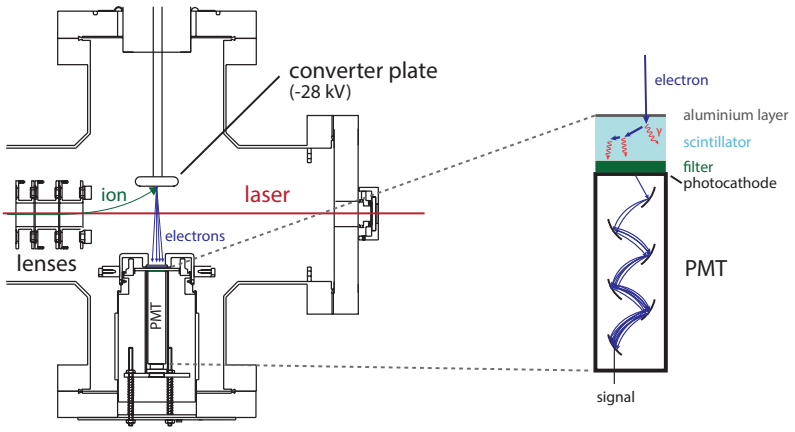

Figure 3.12: Functional principle of the Daly-type detection system.

3.3.6 The laser system

A home-built diode laser system (cw) was used to probe the H_3^+ ions in the 22 pole trap. The laser diode (Toptica LD-1370-0010-AR-1), which is tunable from 1330 to 1400 nm (7519 - 7143 cm^{-1}), is mounted on a Peltier element to control and stabilize the temperature. An external cavity, using a grating (900 lines/mm) in littrow configuration [108] leads to a stable operation (with a typical laser power of 15 mW) and spectral linewidths smaller than 1 MHz (~ 3 x 10^{-5} cm^{-1}), which is more than 2 orders of magnitudes smaller than the Doppler broadened transition linewidths in our measurements. A beam sampler in the laser path (shown in Fig. 3.13) splits 2% of the laser power towards the monitoring units. The power as well as the wavelength of the laser is continuously monitored during each measurement. The anamorphic prism pair transforms the laser profile from an elliptic to a round shape. Previous experiments and simulations demonstrated an inhomogeneous distribution of the ions stored in a 22 pole trap [101, 58]. Therefore it is essential to fix the laser path to assure that the laser beam always merges the same volume inside the 22 pole trap. The laser path is carefully aligned for each measurement by using a fluorescing alignment disc (FAD) and an iris diaphragm, one of each before and after the trap setup. The FADs having a central hole of 1.5 mm diameter are used for the alignment of the laser path. For the experiments the FADs are flipped out and the iris diaphragm limits the size of the beam to 2.5 mm diameter. At the entrance and the exit of the 22 pole trap setup the laser travels through a view port (fused silica) with 91% transmission for this wavelength range. After the alignment the laser power is checked on each side of the 22 pole trap setup (position 2 and 3,

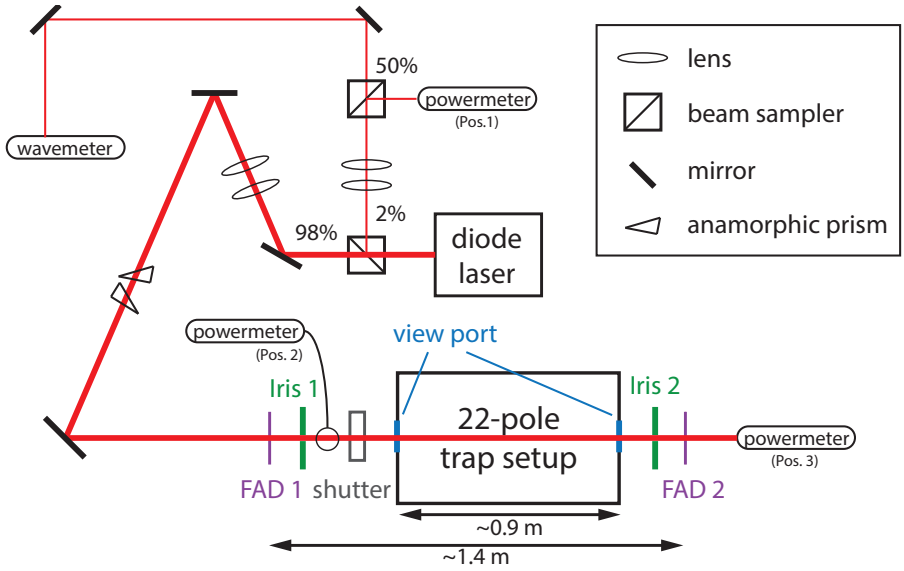

Figure 3.13: Schematic of the laser system

shown in Fig. 3.13) to determine the laser power, that is deposit inside the 22 pole trap. The measurement procedure (details see chapter 4) requires a long trap storage time, where the laser is blocked for most of the time. For this purpose a mechanical shutter is placed between the laser and the 22 pole trap. The laser interaction time (where the laser is not blocked) is too short to monitor the laser after passing the trap. Therefore the power meter (Coherent FieldMaster-GS with an optical sensor LM-2-IR) is placed at position 1 during the experiment. A beam splitter enables to monitor the wavelength of the laser at the same time. The wavemeter (EXFO WA-1500) is calibrated by Doppler-free Li spectroscopy (^{6}Li D_2 line, $2^2S_{1/2} \rightarrow 2^2S_{3/2}$, 14903.632 cm^{-1} [109]), resulting in an absolute uncertainty of 0.005 cm^{-1}.

Chapter 4

Laser induced reaction spectroscopy

This chapter discusses the technique of the laser induced reaction spectroscopy, which has been utilized to probe the H_3^+ ions stored in the 22 pole trap. Furthermore, the measuring procedure to obtain ro-vibrational transitions of H_3^+ is explained. The conditions inside the trap, which are required to perform the experiment are discussed in detail. The relative signals of the probed transitions are analyzed, resulting in the determination of the para fraction of thermalized H_3^+ in collisions with H_2. The analysis of this experiment is explained in detail, followed by a discussion of the results.

4.1 Laser induced reaction

The laser induced reaction (LIR) spectroscopy [110, 111, 41] is superior to conventional absorption spectroscopy methods in that it yields a higher degree of sensitivity. This allows for probing weak transitions with high precision, performed on a relatively small number of ions, which are stored in a trap. This method exploits the change in the chemical composition of an ion cloud via laser interaction. Inside the 22 pole trap, a well-defined cold ion cloud (in this case H_3^+) is exposed to a probing gas, which does not react with the stored ions due to an energy barrier. The chemical reaction can then be driven by a specific induced excitation of the reactant, overcoming this reaction barrier. As a result of this laser-induced reaction, an ion species is formed, which is distinguishable in its mass-to-charge ratio. Afterwards, the charged products of this reaction are extracted towards a mass-selective ion counting detector system (described in Sec. 3.3).
H_3^+ acts as an almost universal proton donor, due to the low proton affinity of H_2. The

Table 4.1: List of species, which have a lower proton affinity than H_2. The values of the proton affinity are taken from [54].

species X	proton affinity $E_{PA}(X)$ [eV]	$E_{PA}(H_2) - E_{PA}(X)$ [eV]	[cm^{-1}]
H_2	4.377		
O_2	4.363	0.013	108.67
Ar	3.827	0.550	4438.80
N	3.547	0.830	6695.82
F	3.525	0.852	6871.37
F_2	3.441	0.936	7548.48
Ne	2.060	2.316	18683.10
He	1.843	2.534	20438.56

few exceptions, which have an even lower proton affinity [54] are listed in Tab. 4.1. One of these species can be used as the probing reactant for H_3^+ to perform a laser induced proton hop reaction. In this study, argon has been the probing gas in the endothermic reaction

$$H_3^+ + Ar \Longleftrightarrow ArH^+ + H_2 - 0.55\,eV. \tag{4.1}$$

This chemical reaction enables to obtain transitions from ground state H_3^+ to energy levels beyond 0.55 eV ($\widehat{=}$ 4438.8 cm^{-1}). Hence, the excitation of two or more vibrational quanta of H_3^+ (see Fig. 2.4) is needed to enable the formation of ArH^+ in reaction 4.1. In recent years this scheme was successfully applied to investigate the rovibrational spectrum of H_3^+. It has been shown that the high sensitivity of this technique allows to observe transitions from the two lowest rotational states of the vibrational ground state to final levels, which are at least six orders of magnitude weaker than the fundamental. The measured transitions involved up to nine vibrational quanta [42].

In this study, the technique of the LIR spectroscopy was used to probe the relative populations of the three lowest rotational states in the vibrational ground state. The theoretical values for low overtone transitions is assumed to be quite accurate. The well known transitions to the vibrational overtone band $3\nu_2^1 \leftarrow 0$ which were used in this work are illustrated in Fig. 4.1 together with their theoretical predicted Einstein A_{if} coefficients [39]. The energy levels (J,G)=(1,1) and (2,2) correspond to para states of H_3^+, whereas the energy level (1,0) represents the ortho configuration.

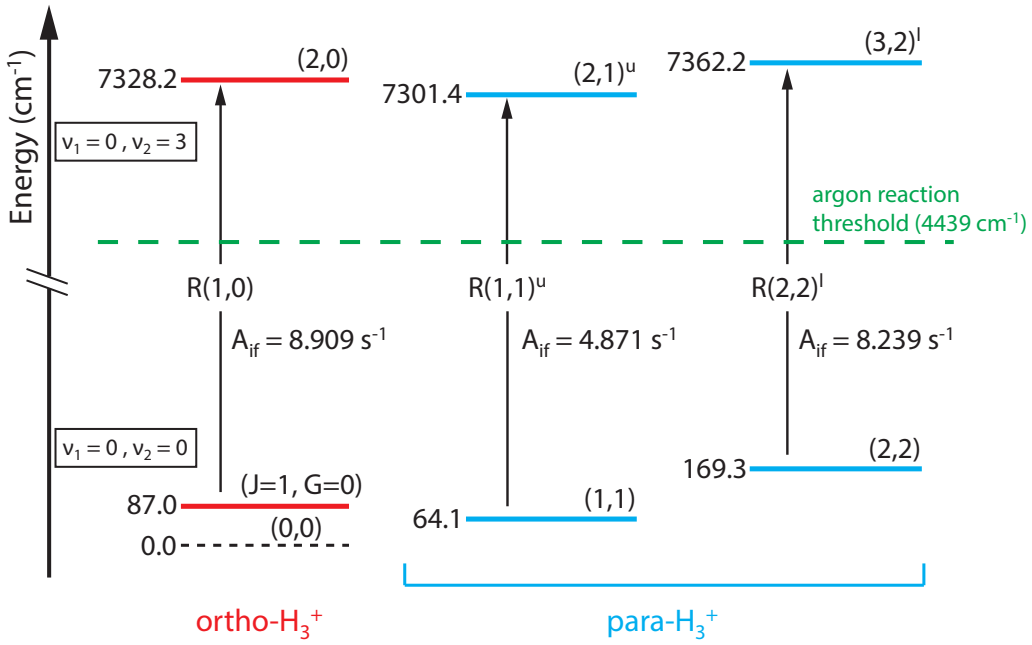

Figure 4.1: Energy diagram of H_3^+, which illustrates the probed transitions from the vibrational ground-state to the vibrational overtone $3\nu_2^1$. The three lowest rotational states in the vibrational ground state were probed by LIR spectroscopy, where two of these states represent para-H_3^+ and the other one ortho-H_3^+. The green dashed line indicates the reaction barrier of the proton hop reaction with argon. The Einstein A_{if} coefficients are taken from [39].

The relative signals of these transitions can be used to derive the populations of the initial states (discussed in Sec. 4.4) and allow the determination of the para fraction of H_3^+ (p_3).

4.2 22 pole trap conditions

The temperature of the 22 pole trap can be stabilized to a constant value between 10 and 100 K, as described in Sec. 3.3. For this experiment the lower limit of the trap temperature is determined by the vapor pressure of the probing gas argon. As a consequence of the required gas pressure inside the trap, the operating temperature is restricted to a lower limit of $\sim$ 40 K. At the beginning of each experiment the trap temperature is carefully set and stabilized to the requested value, which is given by the excitation temperature of the prepared H_2 sample according to its para fraction. The preparation and the analysis of the H_2 gas samples are previously discussed in detail in Sec. 3.1 and 3.2, respectively. The determined para fraction p_2 and excita-

tion temperature T_{01} of each H_2 gas sample are presented in Fig. 3.7.
Approximately 500 H_3^+ ions are stored inside the 22 pole trap during each measurement cycle. Their kinetic energy as well as their internal states are cooled via buffer gas cooling to the nominal trap temperature, which is set to T_{01}. In thermal equilibrium, the population numbers $N_{(J,G)}$ of the rotational energy levels $E_{(J,G)}$ of H_3^+ at a temperature T is given by the Boltzmann factor,

$$N_{(J,G)} = \frac{g_{(J,G)}}{Z}\, e^{\frac{-E_{(J,G)}}{k_B T}}, \tag{4.2}$$

where the partition function Z and the statistical weight $g_{(J,G)}$ is given by

$$Z = \sum_{J=0}^{\infty} g_{(J,G)}\, e^{\frac{-E_{(J,G)}}{k_B T}}, \qquad g_{(J,G)} = \begin{cases} 2(2J+1) & \text{for para-}H_3^+ \\ 4(2J+1) & \text{for ortho-}H_3^+ \end{cases}. \tag{4.3}$$

The thermal populations of the lowest 15 rotational energy levels, up to (J,G) = (6,0), of H_3^+ in its electronic and vibrational ground state were calculated using Eq. 4.2, for temperatures up to 100 K. The energy levels $E_{(J,G)}$ in this calculation are taken from theoretical predictions by Neale et al. [39]. Fig. 4.2 illustrates the five lowest allowed rotational energy levels (left) and their calculated thermal populations for temperatures ranging from 5 to 100 K (right). In this range, these states hold $\geq 99\%$ of the population for H_3^+.
As described in the previous section, the three lowest energy levels of H_3^+ in the

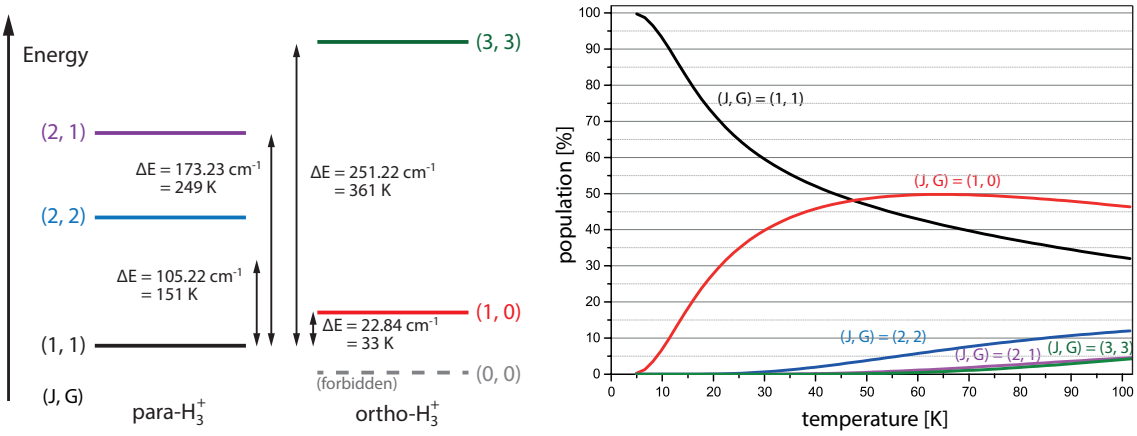

Figure 4.2: The sketch on the left side illustrates the five lowest allowed rotational energy levels in the vibrational ground state of H_3^+. The energy levels (values taken from [39]) and their thermal populations (calculated via Eq. 4.2) are shown in the right graph.

temperature regime of 40 - 100 K are probed. At temperatures of 40 K, 99.8% of the H_3^+ ions lie within these three states. With increasing temperature, the population fraction within these states falls, e.g. 90.7% at 100 K. In this regime, the higher energy levels influence the determination of the para fraction (p_3) only by $\leq 1.2\%$.
The experiment requires a stable number density for all neutral gases in every measurement. He, H_2 and Ar, are continuously fed into the 22 pole trap volume and merged with the stored H_3^+ ions. The prior gas species in the trap is helium which acts as buffer gas, cooling via frequent collisions the internal states of the H_3^+ ions to the nominal trap temperature. A fast buffer cooling ($\sim$ ms) requires a relatively high He density inside the trap. The prepared H_2 molecules serve as the reactant gas in the investigated reactive collision $H_3^+ + H_2 \rightarrow H_3^+ + H_2$, as outlined in Sec. 2.3.3. Argon acts as the probing gas in the LIR spectroscopy technique, as described in the previous section.
The typical gas pressures of each species, inside the trap volume, are listed in Tab. 4.2. A cold cathode pressure gauge (Pfeiffer IKR270) [112], placed on the outer vacuum chamber of the 22 pole trap, measures the room temperature gas pressure surrounding the trap. This gauge provides an estimation of the gas pressures inside the 22 pole trap, calculated using the gas-species scaling factor, gas conductance and the trap temperature (described in more detail in Appendix B). The calculated pressure for each gas species is denoted in the second column of Tab. 4.2. These gas pressures are converted to number densities approximated by the ideal gas law, shown in third column. In addition, the number density of N_2 and H_2 can be approximated via measurement of reactive collisions in the trap. In the case of N_2 (residual gas), the destruction of H_3^+ proceeds via the exothermic proton hop reaction $H_3^+ + N_2 \rightarrow NH^+ + H_2$, where the Langevin rate coefficient (k_L) can be calculated using Eq. 2.10 ($\alpha_{N2} = 1.71$ Å^3 [59]). The measured lifetime ($\tau_{H_3^+}$) of the stored H_3^+ ions of ~ 5 s allows to determine the N_2 number density $n(N_2)$ to

$$n(N_2) = \frac{1}{k_L \cdot \tau_{H_3^+}} \approx 1.1 \cdot 10^8 \, \mathrm{cm}^{-3} \, . \tag{4.4}$$

As previously discussed in Sec. 3.3.1, the H_3^+ ions are produced in a hot ion source, and thus they are internally excited. As energetically permitted by the chemical equation 4.1, the thermally excited H_3^+ react with the present Ar to ArH^+ when entering the trap. Cooled down by He buffer gas, the back reaction of Eq. 4.1, $ArH^+ + H_2 \rightarrow H_3^+ + Ar$, proceeds at a lifetime τ_{ArH^+}, which depends on the H_2 number

gas species	pressure in main chamber [mbar]	number density in trap, pressure derived [cm^{-3}]	number density in trap, lifetime derived [cm^{-3}]	collisions with H_3^+
N_2	$< 2.7 \cdot 10^{-9}$	$< 3 \cdot 10^8$	$1.1 \cdot 10^8$	0.1
He	$9.1 \cdot 10^{-4}$	$1 \cdot 10^{14}$		$4 \cdot 10^5$
Ar	$5.4 \cdot 10^{-6}$	$5.9 \cdot 10^{11}$		550
H_2	$1.5 \cdot 10^{-6}$	$1.6 \cdot 10^{11}$	$6.6 \cdot 10^{10}$	60 - 160

Table 4.2: List of gas species and their estimated number densities inside the trap volume. The estimated gas pressures inside the trap are derived from a pressure gauge placed on the outer vacuum chamber of the 22 pole trap. These gas pressures are then converted to number densities approximated by the ideal gas law. The fourth column denotes the calculated number densities of N_2 and H_2 according to Eq. 4.4 and 4.5, respectively. Therefore, the calculated Langevin rate coefficient and the lifetime of a chemical reaction were used. The average number of collisions per H_3^+ ion during the trap storage time (500 ms) is given in the last column, approximated by 4.6 using the Langevin rate coefficients in reaction with H_3^+. The values for the polarizability of the gas species to calculate the Langevin rate coefficients are taken from [59].

density inside the trap volume. For each measurement performed, the H_2 number density is set carefully in order to create an ArH^+ lifetime of $\tau_{ArH^+} \approx 10$ ms. The Langevin rate coefficient (k_L) can be calculated, using a H_2 polarizability of $\alpha_{H2} = 0.787$ Å^3 [59], yielding an estimated H_2 number density $n(H_2)$ of

$$n(H_2) = \frac{1}{k_L \cdot \tau_{ArH^+}} \approx 6.6 \cdot 10^{10}\,\mathrm{cm}^{-3}\,. \tag{4.5}$$

The number of collisions per H_3^+ ion within the trap storage time (N_{col}) can then be determined by

$$N_{col} = k_L \cdot n \cdot t_{storage}\,, \tag{4.6}$$

where k_L represents the calculated Langevin rate coefficient and n denotes the number density of the gas species colliding with H_3^+ during the trap storage time $t_{storage}$. In Tab. 4.2, the (average) number of collisions with an H_3^+ ion are calculated according to Eq. 4.6 for the given number densities of the gas species during the trap storage time ($t_{storage} = 500$ ms).

4.3 22 pole trap measurement procedure

This section presents the procedure in which H_3^+ ions, undergoing reactive collisions with H_2, are probed under thermal equilibrium conditions. The measurement cycle, over a single trap filling, is illustrated schematically in Fig. 4.3. The ions in the trap are stored for 500 ms, during which time they interact with the neutral gas species. The scheme, shown in Fig. 4.3, is separated into five phases. At first, the H_3^+ ions are guided into the 22 pole trap, as previously described in Sec. 3.3. Since the H_3^+ ions are produced in a hot ion source they are thermally excited when reaching the trap. As a result, $\sim$ 60 % of the excited H_3^+ ions react promptly with Ar forming ArH^+. Within the first few ms, the H_3^+ ions are cooled, via collisions with the helium buffer gas, down to their lowest rotational states in the vibrational ground state. Despite this rapid cooling, in Fig. 4.3 approximately 60 ms are needed prior to the disappearance of the ArH^+ signal into the background noise (phase II), for the given H_2 number density. This time period is governed by the back reaction of Eq. 4.1, i.e. $ArH^+ + H_2 \rightarrow H_3^+ + Ar$. The rate of ArH^+ ion back-conversion is directly correlated to the H_2 number density inside the trap. While a higher H_2 number density decreases the ArH^+ lifetime (in phase II), it also depletes the amplitude of

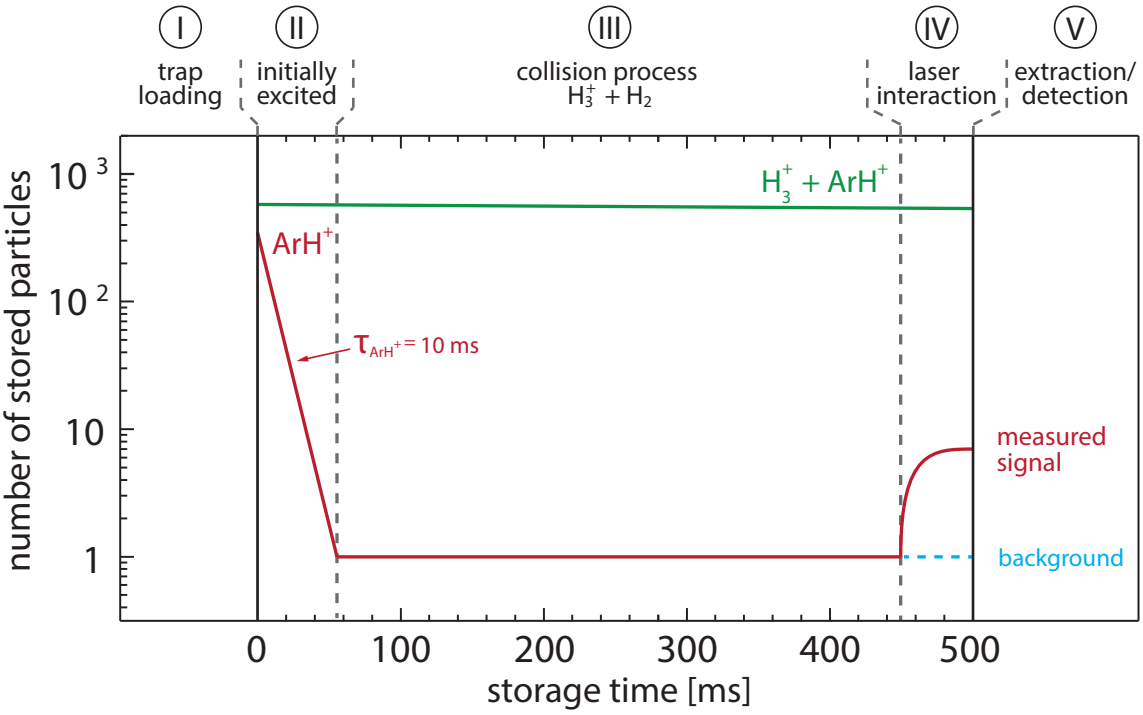

Figure 4.3: Scheme of the measuring procedure inside the 22 pole trap.

the measured signal (phase IV) due once again to the competitive reaction 4.1. The intensity of the measured signal is discussed in detail in the next section. For this study, the optimal ArH^+ lifetime was found to be 10 ms.
In phase III, it can be assumed that all H_3^+ ions stored in the trap populates only the lowest rotational states of the vibrational ground state. The H_3^+ ions interact in reactive collisions with the prepared H_2 gas samples, according to the reactions pathways described in Sec. 2.3, Eq. 2.25 - 2.27. In order to probe the H_3^+ populations afterwards, a tunable cw-laser beam is passed axially through the 22 pole trap during the last 50 ms of trap storage (phase IV). If the laser photons have the right wavelength, H_3^+ ions can be excited by absorbing a photon and a laser induced ArH^+ signal is generated via reaction 4.1. After a laser interaction time of $\tau_{LIT} =$ 50 ms, an equilibrium between laser excitation and ArH^+ decay ($\tau_{ArH^+} \approx 10$ ms) in reaction 4.1 is established. All ions are then extracted from the trap, mass selected and counted by a single ion detector system, as described in Sec. 3.3.

4.4 Signal intensities

This section discusses the ArH^+ signal intensities, which are measured in the experiment. Phase IV in Fig. 4.3 represents the laser interaction time (τ_{LIT}) in which the ArH^+ signal is created. As previously described, laser photons (ν_L) excite H_3^+ ions that are stored in the trap. These H_3^+ ions overcome the reaction barrier in reaction 4.1 and form ArH^+ ions. This process competes with the exothermic back reaction $ArH^+ + H_2 \rightarrow H_3^+ + Ar$, which is characterized by the ArH^+ lifetime (τ_{ArH^+}). The number of ArH^+ ions (N_{ArH^+}) that are formed in this time period is then given by the differential equation

$$\frac{dN_{ArH^+}}{d\tau_{LIT}} = k_{(J,G)}(\nu_L)\, N_{H_3^+} - \frac{1}{\tau_{ArH^+}} N_{ArH^+}\,, \tag{4.7}$$

where $k_{(J,G)}(\nu_L)$ denotes the formation rate of ArH^+ per H_3^+ ion. Based on the relatively high lifetime of the stored H_3^+ ions ($\sim$ 5 s) compared against the laser interaction time ($\tau_{LIT} = 50$ ms), the number of H_3^+ ions ($N_{H_3^+}$) can be assumed to be constant within the time period τ_{LIT}. The differential equation 4.7 can then be solved to give

$$N_{ArH^+} = k_{(J,G)}(\nu_L)\, N_{H_3^+}\, \tau_{ArH^+}\, (1 - e^{-\tau_{LIT}/\tau_{ArH^+}})\,. \tag{4.8}$$

The ArH^+ lifetime τ_{ArH^+} is set ~ 10 ms for all measurements in this study. Consequentially, the term $e^{-\tau_{LIT}/\tau_{ArH^+}} \approx 6.4{\cdot}10^{-3}$ in Eq. 4.8 can be neglected, leading to

$$N_{ArH^+} = k_{(J,G)}(\nu_L)\, N_{H_3^+}\, \tau_{ArH^+}\,. \tag{4.9}$$

The formation rate $k_{(J,G)}(\nu_L)$, which depends on the population of the initial H_3^+ state (J,G), is given by

$$k_{(J,G)}(\nu_L) = \int f_{(J,G)}(\nu-\nu_0)\, B_{lu}\, \rho(\nu-\nu_L) d\nu\,, \tag{4.10}$$

where $f_{(J,G)}(\nu-\nu_0)$ denotes the fraction of H_3^+ ions interacting with a laser beam that possess a spectral energy density $\rho(\nu-\nu_L)$. The Einstein B_{lu} coefficient describes the strength of the transition. The fraction $f_{(J,G)}(\nu-\nu_0)$, where ν_0 represents the frequency of the transition, contains the population $p_{(J,G)}$ of the initial H_3^+ state (J,G) and the geometrical overlap of the laser beam with the ion cloud stored inside the 22 pole trap. This overlap can be approximated by the ratio of the laser cross section and the trap cross section, $A_L/A_{trap} \approx 5\%$. As the ion distribution inside the trap cannot be considered as homogeneous due to space charge effects and the influence of the axially confining ring electrodes [58, 101], the actual overlap is not exactly defined. Therefore it is crucial to fix a reliable laser path for all measurements (as described in Sec. 3.3.6), in order to keep the overlap consistent which allows for relative normalization in the experiment. The fraction $f_{(J,G)}(\nu-\nu_0)$, which is also affected by the laser frequency due to the Doppler effect, can be described by

$$f_{(J,G)}(\nu-\nu_0) = p_{(J,G)}\, C e^{-(\nu-\nu_0)^2/2\sigma_D^2}\, \frac{A_L}{A_{trap}}\,, \tag{4.11}$$

using the normalization constant $C = \frac{1}{\sqrt{2\pi}\sigma_D}$. The Doppler width σ_D is given by the standard deviation

$$\sigma_D = \sqrt{\frac{k_B T}{mc^2}}\nu_0\,, \tag{4.12}$$

where m denotes the mass of H_3^+, k_B the Boltzmann constant, T the temperature and ν_0 the center frequency. As previously described in Sec. 3.3.6, the laser bandwidth is negligible compared to the Doppler broadening of the probed transitions. Therefore, the spectral energy density $\rho(\nu-\nu_L)$ can be approximated by $\delta(\nu-\nu_L)\frac{P_L}{A_L c}$, where

Table 4.3: List of the transitions in order to probe the three lowest rotational levels in the vibrational ground state. The Einstein B_{lu} coefficients are derived from the theoretically predicted Einstein A_{ul} coefficients [39], using Eq. 4.15.

transition label	transition frequency [cm^{-1}]	nuclear spin configuration	A_{ul} [s^{-1}]	J_l	J_u	B_{lu} [cm^3/Js^2]
R(1,0)	7241.256	ortho	8.909	1	2	$2.348 \cdot 10^{21}$
$R(1,1)^u$	7237.291	para	4.871	1	2	$1.286 \cdot 10^{21}$
$R(2,2)^l$	7192.899	para	8.239	2	3	$1.861 \cdot 10^{21}$

P_L denotes the laser power. As a result, Eq. 4.10 can be rearranged to give

$$k_{(J,G)}(\nu_L) = \frac{p_{(J,G)}\, B_{lu}\, P_L}{A_{trap} c}\, C\, e^{-(\nu_L-\nu_0)^2/2\sigma_D^2}\,, \tag{4.13}$$

which can be used in Eq. 4.9 leading to

$$N_{ArH^+} = \frac{N_{H_3^+}\, \tau_{ArH^+}\, p_{(J,G)}\, B_{lu}\, P_L}{A_{trap} c}\, C\, e^{-(\nu_L-\nu_0)^2/2\sigma_D^2}\,. \tag{4.14}$$

The calculated line list, published by L. Neale, S. Miller and J. Tennyson provides also the Einstein A_{ul} coefficients for all transitions [39]. These can be converted into Einstein B_{lu} coefficients by

$$B_{lu} = \frac{g_u}{g_l}\frac{c^3 A_{ul}}{8\pi h \nu_0^3}\,, \tag{4.15}$$

where g_l and g_u denote the rotational degeneracy of the lower and the upper energy level, respectively, according to $g = 2J + 1$. The transitions, which were scanned in order to determine the relative populations of the lowest rotational levels in H_3^+ are listed in Tab. 4.3.

4.5 Analysis

The para fraction of the H_3^+ ions, which collide reactively with the prepared p_2-H_2 molecules at the corresponding excitation temperature T_{01}, is determined by probing the relative populations of the three lowest states in H_3^+. The utilized transitions are shown in Fig. 4.1 and listed in Tab. 4.3. The resulting ArH^+ signal as a function of the laser frequency can be described by Eq. 4.14, in which the scaled signal of the Gaussian line profiles reflect the relative populations in H_3^+. The transitions

R(1,1)^u and R(2,2)^l represent the two lowest para states, whereas R(1,0) represents the lowest ortho state in H_3^+. As previously discussed in 4.2, these three states represent between 99.8% and 90.7% of the population in H_3^+, dependent on their internal temperature (see Eq. 4.2). Therefore, a calibration factor $f(T)$ is calculated which accounts for the minor deviation in the resulting para fraction. The para fraction (p_3) of H_3^+ can then be given by

$$p_3 = \frac{A_{ArH^+}[R(1,1)] + A_{ArH^+}[R(2,2)]}{A_{ArH^+}[R(1,0)] + A_{ArH^+}[R(1,1)] + A_{ArH^+}[R(2,2)]} \cdot f(T)\,, \tag{4.16}$$

where A_{ArH^+} represents the measured ArH^+ yield scaled by the laser power P_L, the ArH^+ lifetime τ_{ArH^+}, the number of stored H_3^+ ions $N_{H_3^+}$, and the Einstein B_{lu} coefficient.

A detailed discussion of the analysis of the H_3^+ para fraction p_3 will be given on the example of the measurements using the H_2 gas sample having a para fraction of p_2 = 0.66. The same method is applied to all measurements discussed in this chapter. The temperature of the trap is cooled down to a constant value T_{trap}, which is a few Kelvin lower than the excitation temperature T_{01}. As previously described in Chap. 3, the RF heating [58] will add to a slightly higher temperature of the stored ions. In previous experiments and preliminary test-measurements, an increase of the ion temperature in order of ∼5-10 K was observed (compared to the nominal trap temperature). In the measurements using a H_2 para fraction of $p_2 = 0.66$, which corresponds to $T_{01} = 60$ K, the trap temperature is set to 54K.

The measurement cycle which is shown in Fig. 4.3 illustrates the procedure inside the 22 pole trap per trap-filling. For each wavelength step, the measurement cycle is repeated 100 times. For the first 10 trap fillings, the number of H_3^+ ions ($N_{H_3^+}$) are determined while the laser beam is blocked during the whole cycle. For the next 10 trap fillings, the number of the ArH^+ ions (N_{ArH^+}) are counted while the laser interacts with the stored ions within the last 50 ms of the cycle. This is repeated 5 times prior to shift the laser frequency to the next step, which results in 50 cycles measuring H_3^+ and 50 cycles measuring ArH^+ per wavelength step. The wavelength of the laser is scanned in steps of 0.003 cm^{-1} over the three transitions. The power P_L as well as the wavelength ν_L of the laser is monitored for each measurement cycle, as described in Sec. 3.3.6. Each scan contains 40 - 50 wavelength steps. With at least two scans, the measurement requires $\gtrsim$ 2.5 hours per transition, in which the experimental conditions in the trap have to be stable. Therefore, a reliable prepara-

tion of the trap settings is necessary, as outlined in Sec. 4.2. In order to verify that, the trap temperature and the gas pressure is monitored during the measurements. The ArH^+ lifetime τ_{ArH^+} is adjusted to a constant value of ∼10 ms, that is checked before and after each scan.

The natural line width of the transitions (< 1 kHz) and the line width of the laser (< 1 MHz) are orders of magnitudes smaller than the temperature induced Doppler width (> 260 MHz). Therefore, the measured Gaussian line profiles reflect the kinetic temperature of the stored H_3^+ ions according to Eq. 4.12. The resulting line profiles of the three transitions, labeled by R(1,0), R(1,1)^u and R(2,2)^l, are illustrated in Fig. 4.4, where the ArH^+ yield is normalized to the laser power and the number of H_3^+ ions stored inside the 22 pole trap for each wavelength step. The Gaussian fits of the line profiles are indicated by the red lines, where σ_D denotes its Doppler width. The calculated kinetic temperature T_{kin} of the H_3^+ ions using Eq. 4.12 is shown in Tab. 4.4, together with a selection of the fit parameters including their uncertainties. The stated ArH^+ lifetimes, which were measured separately before and after each scan, are yet to be factored. Due to the weaker signal-to-noise ratio of the line profiles for transition R(1,1)^u and R(2,2)^l, their fit parameters have larger relative uncertainties. For this reason, the strongest line R(1,0) provides the most accurate measurement of T_{kin} which is equal to 62±3 K. The rotational temperature T_{rot} in H_3^+ is determined by the relative populations of the two para states. For this purpose, the ArH^+ yield in the transition line R(1,1)^u and R(2,2)^l are both scaled by their ArH^+ lifetimes (given in Tab. 4.4) and by their Einstein B_{lu} coefficients (given in Tab. 4.3). Using Eq. 4.2, the rotational temperature is calculated to T_{rot} = 69±4 K. The factor $f(T)$ in Eq. 4.16 accounts for the deviation in the calculated

Table 4.4: Resulting parameters of the Gaussian fit applied to the line profiles of transition R(1,0), R(1,1)^u and R(2,2)^l. The kinetic temperatures T_{kin} are calculated from the Doppler width σ_D via Eq. 4.12. The amplitude and the area of the Gaussian line profiles are yet to be scaled by the ArH^+ lifetime τ_{ArH^+} and the Einstein B_{lu} coefficient.

	R(1,0)	R(1,1)^u	R(2,2)^l
τ_{ArH^+} [ms]	9.91 ± 0.04	9.97 ± 0.13	9.94 ± 0.06
amplitude	3.21 ± 0.07	1.49 ± 0.08	0.39 ± 0.05
area	(8.07 ± 0.18)·10^{-2}	(3.70 ± 0.23)·10^{-2}	(1.09 ± 0.16)·10^{-2}
σ_D [cm^{-1}]	(1.003 ± 0.021)·10^{-2}	(0.992 ± 0.059)·10^{-2}	(1.105 ± 0.165)·10^{-2}
T_{kin} [K]	62 ± 3	61 ± 7	77 ± 24

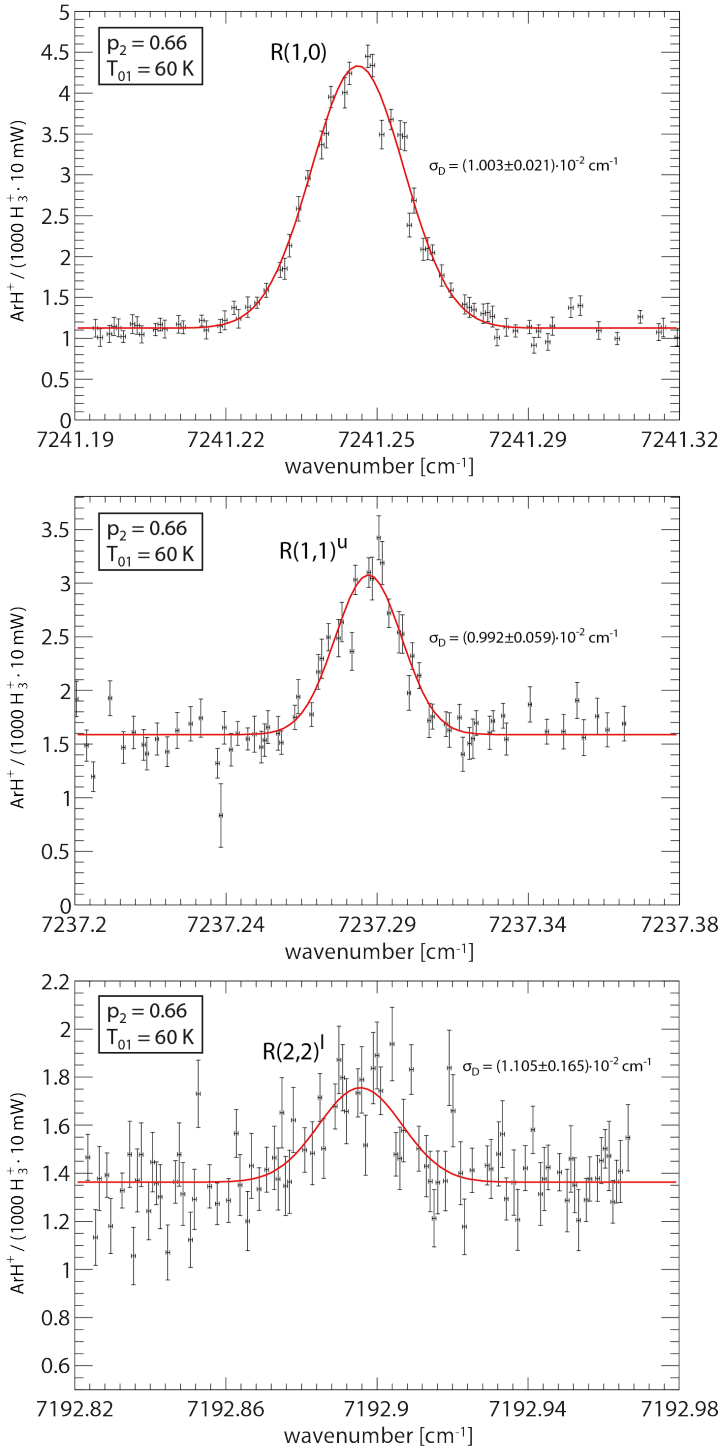

Figure 4.4: The diagrams illustrate the ArH^+ yield as function of the laser frequency using transition R(1,0), R(1,1)^u and R(2,2)^l. The ArH^+ yield is normalized to the laser power and the number of H_3^+ ions stored inside the 22 pole trap for each wavelength step. The normalization to the ArH^+ lifetime and to the Einstein B_{lu} coefficient is not included. The red lines indicate Gaussian fits, where σ_D denotes its Doppler width. A selection of the fit parameters including their uncertainties are listed in Tab. 4.4.

para fraction p_3 due to higher populated states in H_3^+, which were not probed in this measurement. Assuming that the rotational populations are in equilibrium among the same nuclear spin configurations, the calibration factor $f(T)$ is defined by T_{rot}. The calculated value for $f(T)$ in this measurement (T_{rot} = 69±4 K) corrects the H_3^+ para fraction by a factor of 1.008±0.001. The para fraction of H_3^+ can then be calculated by Eq. 4.16, in which A_{ArH^+} represents the normalized ArH^+ yield. Therefore, the ArH^+ yield listed in Tab. 4.4 has to be normalized to their Einstein B_{lu} coefficient and their ArH^+ lifetime, in order to derive the relative populations of the probed states. From these relative populations, the H_3^+ para fraction can be calculated to p_3 = 0.502±0.015.

An additional source of error, which has not been considered so far, takes place during the laser interaction time (phase IV in Fig. 4.3) of the measurement. Within this 50 ms, the back reaction of the ArH^+ signal, $ArH^+ + H_2 \rightarrow H_3^+ + Ar$, potentially changes the relative populations in H_3^+. In this time period, a steady state in reaction 4.1 is established, in which permanently ArH^+ is generated by LIR and destroyed by reactions with H_2 (p_2). For all measured transitions, this effect leads to a depletion of the probed state. If, for example, a stored H_3^+ ion in the ortho state (1,0) reacts with Ar to ArH^+, the probability that the back reaction with H_2 (p_2) forms again ortho-H_3^+ is given by (2/3 - 2/3 p_2) according to the spin selection rules [113, 114]. The probability to form para-H_3^+ in this back reaction is given by (1/3 + 2/3 p_2), which influences the relative populations of the stored H_3^+ ions. The maximum ArH^+ formation rate, measured while scanning the strongest transition R(1,0) was 1600 s^{-1}. During the laser interaction time of 50 ms, 1600 $s^{-1} \cdot 50$ ms = 80 ArH^+ ions are formed in total. Statistically, ∼62.5 of these ArH^+ ions are converted into para-H_3^+ and ∼17.5 react back to ortho-H_3^+ for the given H_2 para fraction of p_2 = 0.66. This change in the population of H_3^+ is significant compared to the total number of stored H_3^+ ions (∼ 500). Using the determined H_3^+ para fraction p_3 = 0.502, the absolute number of H_3^+ ions in ortho and in para configuration at the end of the measurement cycle can be calculated. Assuming 500 H_3^+ ions, detected after the measurement cycle, statistically 249 of them populate an ortho state. The derived rotational temperature (T_{rot} = 69 K) allows to calculate the population in the (1,0) state to ∼244 H_3^+ ions, using Eq. 4.2. The absolute number of H_3^+ ions in the (1,0) state, before a laser is passing the trap and induces the change in the populations, would then be ∼306.5. This possible influence of the laser interaction demonstrates the worst case scenario, because during the laser interaction time, also

the $H_3^+ + H_2$ collisions shift the populations back towards equilibrium. For this reason, this calculated worst case scenario does not introduce a scaling factor, but an increased uncertainty in the measured H_3^+ para fraction p_3.
This model applies similarly to the measured line profiles for the para states. Although, as the ArH^+ formation rate during the laser interaction time is lower, the laser induced population change is smaller for the para states. The model thus leads only to an increase in the lower uncertainty bound of the measured H_3^+ para fraction, resulting in $p_3 = (0.502^{+0.015}_{-0.049})$.
The line profiles of all measurements are shown in Fig. 4.5, sorted by the para fraction (p_2) of the used H_2 gas samples. The ArH^+ yield is scaled by the laser power and the number of H_3^+ ions stored inside the 22 pole trap. For a better comparison, the amplitude of the strongest transition R(1,0) is normalized to 1. The Gaussian fits of the line profiles probing the two para H_3^+ states are represented by the blue lines. The relative populations in these para states provide the determination of the rotational temperature T_{rot} of the stored H_3^+ ions, as previously discussed. The Gaussian fit of the line profile R(1,0), which represents the ortho H_3^+ state, is indicated by the red line. This Gaussian line shape provides the most accurate evaluation of the kinetic temperature T_{kin} of the H_3^+ ions. As demonstrated for the measurement using the H_2 probing gas with $p_2 = 0.66$, the measured line profiles, which are shown in Fig. 4.5, are analyzed similarly. The H_3^+ para fraction p_3 is derived via Eq. 4.16, using the ArH^+ yield normalized to the laser power, the number of stored H_3^+ ions, the ArH^+ lifetime and the Einstein B_{lu} coefficient. The results (p_3^{exp}) are summarized in Tab. 4.5, together with the determined temperatures. T_{01} represents the calculated excitation temperature of H_2 having a para fraction of p_2 (discussed in Sec. 3.2). The stated trap temperature T_{trap} is measured by a sensor attached to the housing of the 22 pole trap (details in Sec. 3.3). The kinetic temperature T_{kin} is inferred from the Doppler width of the transition line R(1,0) using Eq. 4.12. The rotational temperature T_{rot} is derived from the relative populations of the probed para H_3^+ states using Eq. 4.2. Supposing that T_{01} ,T_{kin} and T_{rot} are equal, the experiment can be considered as performed in thermal equilibrium (as intended). Overall, the measured temperatures are in mutual agreement given their uncertainties. The impact of deviations in these temperatures can be described by the model based on Park and Light [79], discussed in Sec. 2.3.3. The theoretical predicted para fraction in H_3^+ is then given by Eq. 2.30, in which the state-to-state reaction rate coefficients are computed for the measured kinetic and rotational temperatures [77]. In this

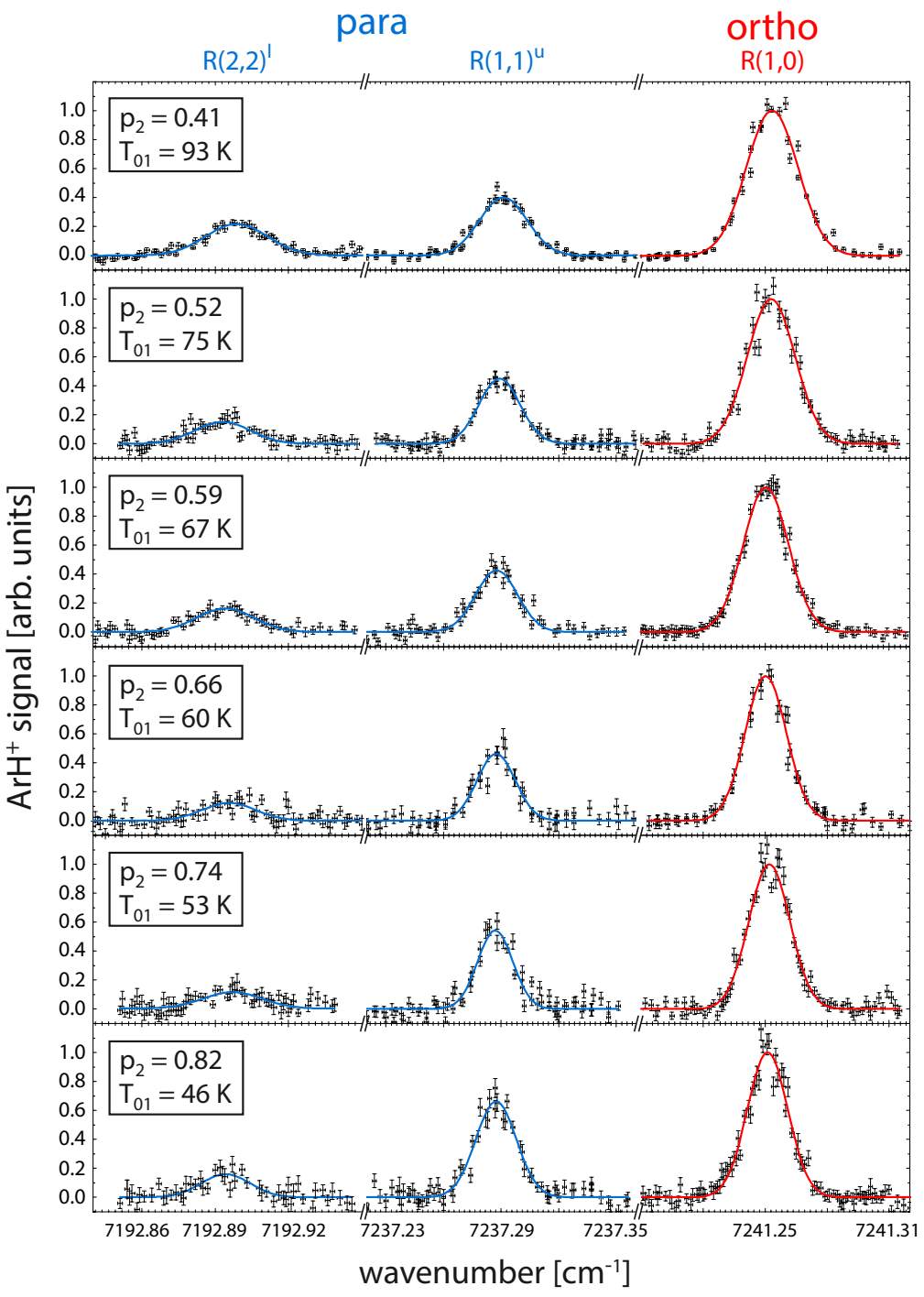

Figure 4.5: The diagrams illustrate the ArH^+ signal as function of the laser frequency. The ArH^+ signal is scaled by the laser power and the number of H_3^+ ions stored inside the 22 pole trap for each wavelength step. In order to provide a better comparison, the amplitude in the line profile R(1,0) is normalized to 1 for each experiment. The Gaussian fits are indicated by the blue (para states) and the red (ortho state) lines.

Table 4.5: Measured para H_3^+ fraction (p_3^{exp}) in comparison with theoretical predicted values (p_3^{theory}), which are calculated based on the Park and Ligt model [79] accounting for the kinetic and rotational temperature of the stored H_3^+ ions (T_{kin}, T_{rot}). T_{trap} represents the measured trap temperature using a sensor attached to the housing of the trap. The para fraction of the probing gas H_2 is denoted by p_2 and T_{01} represents the calculated excitation temperature for these H_2 gas samples.

p_2	T_{01} [K]	T_{trap} [K]	T_{kin} [K]	T_{rot} [K]	p_3^{exp}	p_3^{theory}
0.41±0.05	93±11	87±1	96±4	100±4	$0.501^{+0.009}_{-0.030}$	0.493
0.52±0.05	75±7	71±1	82±4	77±3	$0.506^{+0.011}_{-0.037}$	0.500
0.59±0.05	67±5	64±1	74±3	83±4	$0.506^{+0.011}_{-0.044}$	0.504
0.66±0.05	60±5	54±1	62±3	69±4	$0.502^{+0.015}_{-0.049}$	0.501
0.74±0.05	53±4	48±1	62±3	62±3	$0.528^{+0.015}_{-0.055}$	0.506
0.82±0.05	46±4	44±1	60±5	66±4	$0.581^{+0.012}_{-0.067}$	0.546

chemical model, values for α and S^{id} are adopted from [78] as 0.5 and 0.1, respectively. As described previously in Sec. 2.3.3, α describes the branching ratio between the proton hop (Eq. 2.26) and exchange (Eq. 2.27) reaction, and S^{id} denotes the identity (Eq. 2.25) branching fraction. From these calculations, performed by K. Crabtree [115], theoretical para fractions of H_3^+, denoted by p_3^{theory} in Tab. 4.5, are derived for a given set of experimental conditions.

Theoretical predictions and experimental results have been found in good agreement within the errorbars, as shown in Tab. 4.5 and Fig. 4.6. The lower uncertainty bound of the measured para fraction p_3^{exp} hints towards an overestimation, showing that the calculated model for the laser induced population change is representative of the worst case scenario.

4.6 Discussion and Conclusion

In this work, the reactive collision $H_3^+ + H_2 \rightarrow H_3^+ + H_2$, which is assumed to represent the thermalization process undergone by H_3^+ in interstellar molecular clouds (as discussed in Sec. 2.3.3), has been investigated under thermal equilibrium conditions. The resulting nuclear spin of the H_3^+ product after collisions with H_2, were determined from probing of the H_3^+ populations of the three lowest rotational levels. These results are depicted in Fig. 4.6, together with theoretical predictions and the astronomical observations (as outlined in Sec. 2.3.3), where the H_3^+ para faction p_3

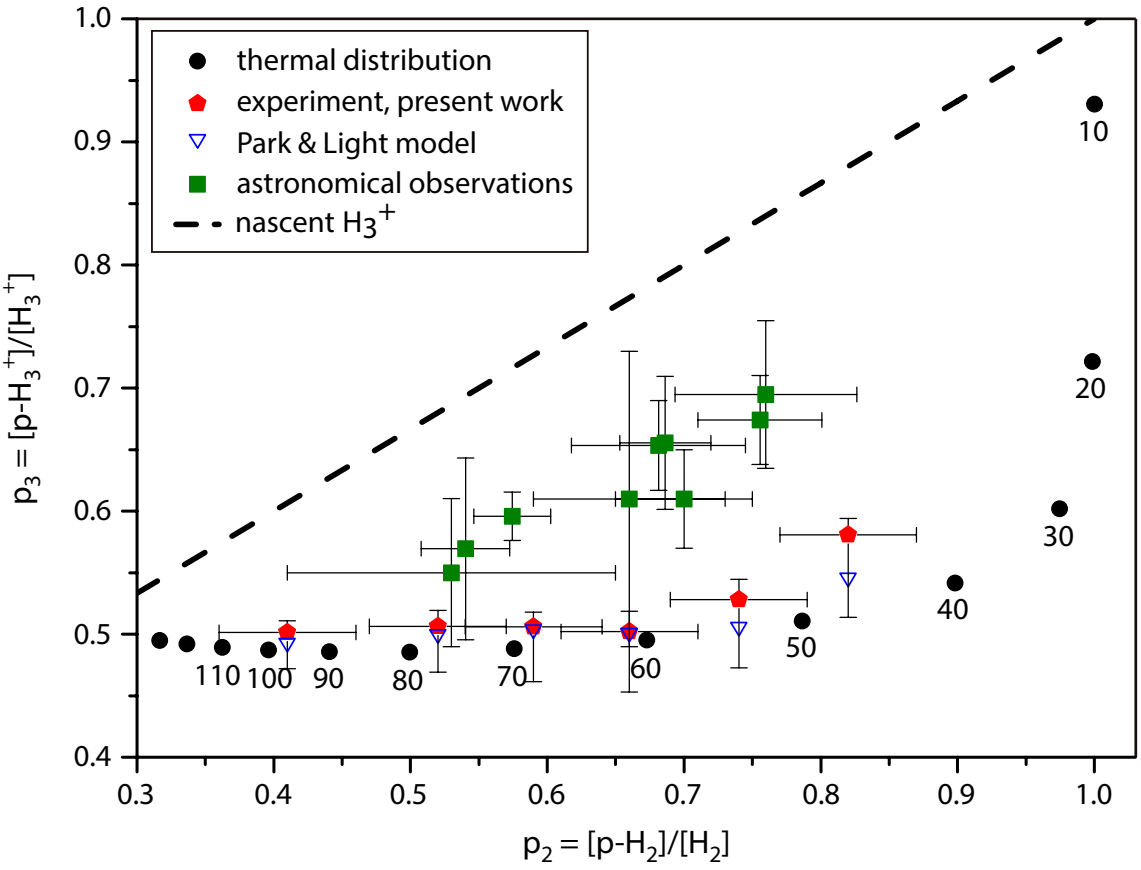

Figure 4.6: Plot of the measured H_2 and H_3^+ para fraction (listed in Tab. 4.5), indicated by the red dots. The black solid circles show the para fractions of H_2 and H_3^+ under thermal equilibrium conditions, in steps of 10 K (the labeled temperature is given in [K]). The blue triangles represent the calculated para fraction of H_3^+ based on Park and Light theory. The green squares represent astronomical observations, as discussed in Sec. 2.3.3. Finally, the dashed black line represents the nascent para H_3^+ fraction.

is presented relative to the H_2 para faction p_2 [116]. The red pentagons represent the measured para fraction, derived in this study (as listed in Tab. 4.5). Model calculations, based on the Park and Light model [79], using the experimental conditions of this work as input parameters, are denoted by the blue triangles. The black solid circles show the para fractions of H_3^+ as a function of H_2 under thermal equilibrium conditions, in 10 K steps. The astronomical observations (listed in Tab. 2.3) are indicated by the green squares. The black dashed line represents the calculated nascent para H_3^+ fraction formed in diffuse molecular clouds via reaction $H_2^+ + H_2$. Using nuclear spin selection rules [74, 76], the nascent H_3^+ para fraction can be determined as $p_3 = \frac{1}{3} + \frac{2}{3}p_2$ [80].

The experimental results show that in equilibrium the nuclear spin of H_3^+ from colli-

sions with H_2 lies close to thermal predictions. The theoretical values (blue triangles), which account for the slightly higher kinetic and rotational temperatures of the H_3^+ ions, are similarly found to be in good agreement with measurements. This result demonstrates, that the H_3^+ product of the reaction $H_3^+ + H_2 \rightarrow H_3^+ + H_2$ is thermal, thus can be described by the Park and Light model.

Despite the good agreement between experimental measurements and theoretical models, a discrepancy remains between with astronomical observations along diffuse sight lines. The para fractions of H_3^+ and H_2, observed within the same diffuse molecular clouds, are inconsistent with with both simple thermal equilibrium conditions and the presented experimental measurements. The observed H_3^+ ions show a systematically higher para fraction relative to the observed H_2 para fraction than that given by models or experimental measurements. These values are lying between the nascent H_3^+ para fraction curve and thermal equilibrium conditions. Thus giving the impression, that the number of collisions between H_3^+ and H_2 in diffuse molecular clouds is insufficient to bring the two species into equilibrium. Observed clouds appear to reside in an intermediate stage, where H_3^+ ions created along the nascent H_3^+ curve have yet to reach steady state.

In Sec. 2.3.3, it was discussed how, in diffuse interstellar clouds, H_3^+ undergoes $\sim$ 40 collisions with H_2 during its lifetime. This number of collisions may be sufficient for thermalization, but this number relies on accuracy of the collisional rate coefficient for $H_3^+ + H_2$ (k_{H_2}) and the dissociative recombination (DR) rate coefficient k_e. In diffuse interstellar clouds, according to Eq. 2.16, k_e represents the dominant destruction process of H_3^+. Whereas, k_{H_2} represents the thermalization process of H_3^+ during collisions with H_2. A lifetime can be determined, for both mechanisms, from the reciprocal of their rates, yielding $\tau_\mathrm{life} = (k_\mathrm{e} n(\mathrm{e}))^{-1}$ for the DR process and $\tau_\mathrm{therm} = (k_{\mathrm{H}_2} n(\mathrm{H}_2))^{-1}$ for the thermalization process, where $n(H_2)$ and $n(\mathrm{e})$ denote the number density of H_2 and electrons, respectively. The number of reactive collisions N_{rc} with H_2 per H_3^+ lifetime can thus be estimated using

$$N_{rc} = \frac{\tau_\mathrm{life}}{\tau_\mathrm{therm}} = \frac{k_{H_2}}{k_\mathrm{e}} \frac{n(H_2)}{n(\mathrm{e})} \,. \tag{4.17}$$

In this estimation, the rate coefficient k_{H_2} can be approximated by the Langevin rate coefficient; $k_{H_2} = 1.9 \cdot 10^{-9}$ cm^{3}s^{-1}, while the DR rate coefficient; $k_\mathrm{e} = 2.6 \cdot 10^{-7}$ cm^{3}s^{-1} [66] and a $n(H_2)/n(\mathrm{e})$ ratio of $5{\cdot}10^3$ is used, resulting in $N_{rc} \sim 40$. It should be noted that these values possess large uncertainties and could have a

temperature dependence. From this simple model, it is clear that the number of reactive collisions (N_{rc}) is directly proportional to the reaction rate coefficient k_{H_2}. Thus, if a reaction rate coefficient of $\sim 3{\cdot}10^{-10}$ cm^{3}s^{-1}, as presented in reaction studies of the deuterated reaction counterpart [117], was substituted into Eq. 4.17, this would reduce the estimated number of collisions to $N_{rc} \sim 6$. This few collisions, might be insufficient to fully thermalize the H_3^+ ions [80]. However, a more recent experimental measurement of this reaction rate, yielded a result that was found to be consistent with the Langevin rate coefficient [118].

A second potential influence on the H_3^+ para fraction p_3 in molecular clouds, that could account for the discrepancy between observation and measurements, would be a DR rate coefficient for H_3^+ that possesses a nuclear spin dependence. Assuming a different DR rate coefficient, k_e(o) and k_e(p) for ortho- and para-H_3^+, respectively,

$$\text{ortho}{-}H_3^+ + e^- \xrightarrow{k_e(o)} H + H + H,\ H_2 + H \tag{4.18}$$

$$\text{para}{-}H_3^+ + e^- \xrightarrow{k_e(p)} H + H + H,\ H_2 + H, \tag{4.19}$$

the DR destruction process would lead to a preferential depletion of one nuclear spin configuration. The astronomically observed H_3^+ para fraction could thus be explained by the faster destruction process of ortho-H_3^+, k_e(o) > k_e(p). However, theoretical calculations predict DR rate coefficients which are contrary to this hypothesis. These calculations of k_e(o) and k_e(p), demonstrated that at low temperatures (T < 200 K) k_e(p) > k_e(o), thus para-H_3^+ is in fact destroyed faster by an order of magnitude [68]. Recent flowing afterglow studies, scanning a temperature regime between 60 and 300 K, verified the overall trend of these calculations [119]. This preferential depletion of para-H_3^+ in diffuse molecular clouds, should decrease the astronomically observed p_3 and thus raises even more questions.

A time-dependent theory of the chemistry in diffuse interstellar clouds, with a focus on the ortho and para configuration of H_2 and H_3^+, has been recently published [86]. This model is incompatible with the astronomical observations, if the ratio for the ortho/para DR rate coefficients, k_e(o):k_e(p) is smaller than 1:5, which disagree the flowing afterglow experiments [119]. For the model to accurately reproduce astrophysical observations, k_e(o) should be approximately equal to k_e(p). While previous DR rate coefficient measurements, performed at storage rings, showed only a slight enhancement in the para-H_3^+ DR rate coefficient [120, 121], the internal temperature of these H_3^+ ions, stored in a room-temperature storage ring, has been

measured to be >100 K [121]. This higher internal temperature could potentially account for the difference between the two results.

The time-dependent model shows only a minor effect on the ortho/para ratio in diffuse clouds, for the variation of the density or the chemical age. Another parameter that has a strong influence on the model is the cosmic ray ionization rate ζ_2, which limits the formation rate of H_3^+ in molecular clouds (discussed in Sec. 2.3.1). An increase of ζ_2 to 10^{-15} s^{-1}, which is the upper limit for cosmic ray ionization rate observed in molecular clouds [63], provides the best agreement with the astronomical observations.

It is clear, that further measurements and improved astrophysical models are required to provide a full understanding of the nuclear spin discrepancy of H_2 and H_3^+ in diffuse interstellar clouds. An accurate total DR rate coefficient k_e of H_3^+, as well as its nuclear spin dependency (k_e(p), k_e(o)) at low temperatures is required.

The thermalization reaction $H_3^+ + H_2$ could be investigated as a function of their collision frequency, in order to investigate the thermalization process. This study could be conducted using a 22 pole trap, utilizing a similar procedure as discussed in this work, but by varying the H_2 number density or the trap storage time. An accurate measurement of the reaction rate coefficient k_{H_2} for this thermalization reaction is very difficult, as both the reactants and the products are indistinguishable. Therefore, further studies on its deuterated counterparts are essential.

Part II

Neutral atom beam creation for merged beam studies at the CSR

Chapter 5

Experimental apparatus for reaction studies of molecular ions with neutral atoms

As presented in the first part of this work, the 22 pole trap is a versatile tool for the investigation of ion-neutral reactions in the gas phase at astrophysically relevant temperatures. While robust in its own right, the 22 pole trap is limited in that it can only probe reactions, which involve neutrals that do not freeze out at low temperatures and are freely available in the gas phase. Most experimental studies on ion-neutral collisions are performed with molecular neutrals, this is mainly due to the challenge in producing sufficient cold neutral atoms (excluding noble gases). Therefore, few experiments measuring reaction rate coefficients of ion-atom collisions at astrophysical relevant temperatures have been performed to date.
In one such experiment, the thermal rate coefficient for the reaction CH^+ + H was measured in a 22 pole trap, where H atoms were extracted from a H_2 parent gas using a discharge tube [9]. The H atoms were then precooled via collisions with a cryogenic surface prior to guiding them into the trap volume. The subsequent slow H atom beam is then merged axially with the trapped CH^+ ions in the 22 pole trap. This setup provided measurements of low energy reactions between CH^+ ions and hydrogen or deuterium atoms in a temperature range of ∼10 to 100 K.
In a similar experiment, the thermal rate coefficient for the reaction D_3^+ + C was investigated. The D_3^+ ions were stored in a temperature variable (80-600 K) ring electrode trap [122]. Despite the low temperature of the D_3^+ ions, carbon atom beam, produced via high-temperature vaporization of a carbon rod, is estimated to have

a translational temperature of 1000 K or higher [123], temperatures which are not astrophysically relevant.

In the aforementioned setups, where the ions are translationally and internally cooled in a cryogenic trap, the reaction temperature is predominately determined by the translational energy of the incident neutral atom beam. One method to mitigate this effect, is the merged beams technique. In this technique, two fast beams are superimposed with near matched velocities, enabling the study of low center-of-mass energy reactions, while maintaining fast beams in the laboratory reference frame [124, 125].

Astrophysically relevant experiments require that the parent reactants are both translationally (in the center-of-mass reference frame) and internally cold. Thus, experimental measurements involving well-defined, internally relaxed, ground state particles are often favorable. A relatively simple method to produce a fast neutral atom beam is via charge exchange [126] or collisional electron detachment [127] in a gas cell. In both methods, a charged atomic beam is passed through a gas cell. In the case of charge exchange, fast positively charged atoms (A^+) are neutralized by the electron transfer reaction $A^+ + B \rightarrow A + B^+$, where B represents the gas species in the gas cell. In the collisional electron detachment technique, fast negatively charged atoms are neutralized via electron stripping in collisions with the cell gas. Although these are both convenient methods, the final quantum state of the resultant neutral atoms is ambiguous. If energetically allowed, the resultant neutral atom may be excited, due to numerous collisions with the cell gas.

One method for the preparation of fast neutral ion beams in their ground state is via photodetachment [128, 129]. In this method, a negatively charged atomic beam is overlapped with a laser beam, where the energy ($E_\gamma = h\nu$) of the laser photons is greater than the binding energy of the outermost electron of the negative atom, yielding: $X^- + h\nu \rightarrow X + e^-$. Since the outer electron of a negatively charged atom is bound only by polarization forces, its binding energy is relatively small. As a result, most negatively charged atomic species have only a single bound state [130]. For single-photon electron detachment, the photon energy determines the possible final states of the neutral atoms. Any photon energy, which is higher than the electron affinity of the atomic anion but with insufficient energy to reach a higher excited state of the neutral species, guarantees the production of ground term neutral atoms, exclusively.

This technique forms the bases for merged-beams measurements on ion-atom reac-

tions with astrophysical impact and has been successfully applied in previous experiments, e.g. [131]. In that experiment, the associative detachment reaction H^- + H $\rightarrow$ H_2 + e^- for a temperature range between 30 and 3000 K was investigated [132]. The H^- ions are accelerated to 10 keV, after their production in a duoplasmatron source. Since H^- ions have a single bound state [133], they exist only in the ground state independent of the source temperature. This H^- ion beam is crossed by a high power (1.4 kW) laser system, continuous wave (cw), at a wavelength of 975 nm ($\hat{=}$1.25 eV). This photon energy is sufficient for the electron photodetachment process, as H^- has an electron affinity of $\sim$0.75 eV [133]. Approximately 7.5% of the H^- ion beam is converted into a neutral H atom beam, which has the same velocity than the parent beam. In this particular case, this method results in a self merged-beams measurement, where both reactants are in their ground state. By mismatching their relative velocities using a tunable electrostatic field, experimental thermal rate coefficients were measured in a large temperature range (30-3000 K).
In recent measurements using a similar setup, the thermal rate coefficients of reaction H_3^+ + C [123] and reaction H_3^+ + O [134] were studied. As the outer electron of C^- and O^- is bound by 1.262 eV [135] and 1.461 eV [136], respectively, the 975 nm laser is insufficient for their electron detachment. Therefore, a cw high power (2 kW) laser at a wavelength of 808 nm ($\hat{=}$1.53 eV) was used for the production of the neutral C and O atoms. The neutral atom beam is subsequently merged in a separate beamline section with H_3^+ ions. These measurements provided the determination of the thermal rate coefficient in the temperature regime of $\sim$70-10000 K [123]. A major drawback, however, was the high internal temperature of the H_3^+ ion ($\sim$2200-3400 K), due to their method of production in a duoplasmatron source. The internal excitation and as a result the molecular structure of the H_3^+ ions leads to a somewhat ambiguous effect on the measured reaction rate coefficients. Therefore, these measurements' astrophysical relevance is arguable.
The second part of this thesis presents the design and construction of a new experimental setup for studying gas phase ion-neutral reactions under astrophysically relevant conditions. Experiments will be conducted in the Cryogenic Storage Ring (CSR) at the Max Planck Institute for Nuclear Physics. Conditions inside the experimental chambers of the CSR can replicate those found in interstellar clouds, making it ideal for such experimental studies. The operating principles and experimental properties of the CSR are briefly outlined in Chap. 7. For the injection of ions into the CSR and subsequent merging with a fast neutral beam, a versatile design

for the injection transfer line of the CSR was required. The concept, design and construction of this beamline are detailed in Chap. 8. To meet the experimental requirements, the demands placed on the CSR transfer line are discussed. To this end, the design and simulations of the vacuum system and the ion-optical elements of the transfer line are presented. For the transfer line of the CSR, two beamlines are merged using an electrostatic 90° deflector with a hole. A photodetachment section is implemented in the transfer line in order to generate neutral atoms (H, D, C, O) in their ground state. These neutral atoms are then merged with stored ions in a straight section of the CSR to perform ion-neutral collision experiments at matched velocities. The implementation of this setup, utilizing photodetachment of negative ion beams (H^-, D^-, C^-, O^-) by a high power laser beam, will be discussed in detail in Chap. 9.

In Chap. 11, first photodetachment and ion beam measurements are presented and analyzed. The photodetachment efficiency was benchmarked using a C^- and O^- parent. These measurements were obtained for laser powers up to 2 kW and kinetic energies of the anions ranging from 10 keV to 35 keV. In a second measurement, a method to non-destructively determine the transverse emittance of an ion beam, that is transported by the transfer line, is demonstrated. Chap. 12 provides a summary of the CSR transfer line and fast neutral beam generation for perspective merged-beams experiments, with a particular emphasis on astrophysics.

Chapter 6

Principles of ion beam transport

This chapter will discuss the principles of ion beam transport via electromagnetic fields. A coordinate system is introduced in order to describe the motion of a charged particle relative to the central path. Starting from first principles, the equations of motion governing the flight of a charged particle path traversing an electromagnetic field is derived. Taking the example of a particle transported via a magnetic field, the equations of motion are solved using a linear approximation. This linear approximation includes ion optical effects such as drift, deflection, and focusing but neglects higher order terms that account for aberration effects.
A matrix formalism is then used to characterize the particle trajectory guided through a linear ion-optical beam transport system. For ion beams, which contain a large number of particles, it is convenient to characterize the bulk-beam properties in terms of its phase space distribution. The beam's phase space is the particle distribution defined by the individual particles spatial coordinate and angle of the ion trajectory relative to the central path. Using this framework, the beam emittance is defined and the twiss parameters are introduced to aim in the characterization of particle beams. For completeness, the influence of non-linear ion-optical effects on the phase space distribution of a particle beam are briefly discussed, a more detailed discussion of which can be found in [137, 138].
Since the CSR facility (see Chap. 7) is limited to kinetic energies of 300 keV per charge unit, it is sufficient to limit the discussion of the ion beam transport to non-relativistic ions, e.g., a 300 keV proton possess a Lorentz factor γ of ≈ 1.00032 ($\approx$2.54% the speed of light).

6.1 Motion of particles in linear approximation

An ion beam contains a large number of charged particles, which are guided along a predefined path via electromagnetic fields created by ion-optical elements. The motion of a particle, which can be approximated by a point mass, is commonly described relative to the central path [137]. Thus, a particle trajectory can then be described by

$$\mathbf{r}(s) = \mathbf{r_0}(s) + x(s)\mathbf{u_x}(s) + y(s)\mathbf{u_y}(s), \tag{6.1}$$

where an orthogonal coordinate system moves along the central path $\mathbf{r_0}(s)$. In this coordinate system, the s-axis always points tangential to the central trajectory, x and y represent the horizontal and vertical axis, and $\mathbf{u_x}(s)$ and $\mathbf{u_y}(s)$ their corresponding unit vectors, respectively. The functions $x(s)$ and $y(s)$ denote the deviation of a particle from $\mathbf{r_0}(s)$. This approach provides a reasonable basis for describing ion-optics via a linear approximation, assuming small deviations of $x(s)$ and $y(s)$ relative to the central path and a small angular deviation.
The force acting on the charged particle in an electromagnetic field is given by the Lorentz force,

$$\mathbf{F_L} = q(\mathbf{E} + \mathbf{v} \times \mathbf{B}), \tag{6.2}$$

where q denotes the electrical charge of a particle, moving in an electric ($\mathbf{E}$) and magnetic ($\mathbf{B}$) field with the velocity $\mathbf{v}$.
From Eq. 6.2, the equations of motion of a charged particle in an electromagnetic field can be derived. Here, as an example, the equations of motion of a charged particle solely due to the influence magnetic field is derived. The derivation of the motion of a particle in an electric field can be similarly determined. From Eq. 6.2, the motion of a particle affected due to a magnetic field is given as

$$\mathbf{F_L} = \frac{d\mathbf{p}}{dt} = q\mathbf{v} \times \mathbf{B}, \tag{6.3}$$

where $\mathbf{p}$ denotes the momentum of the particle. Fig. 6.1 schematically shows the trajectory of a charged particle in presence of a magnetic field, described by an orthogonal coordinate system moving along the central path with the local radius ρ_0. The deflection of a particle, that has a small displacement x in x-direction relative to the central path, can be described by the radius $(\rho_0 + x)$ of the local curvature induced by the magnetic field. Since the velocity v_s of the particle can be linearly approximated by $v_s \approx v_z$, the centrifugal force F_C acting on this particle can be

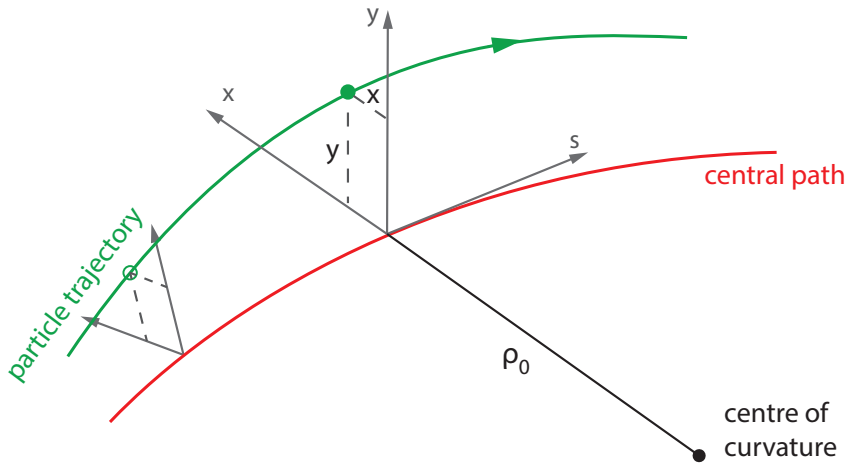

Figure 6.1: Sketch of a particle propagating through a magnetic field. The green solid line represents the trajectory of a random particle from an ion beam relative to the central path, indicated by the red solid line. The orthogonal coordinate system moves along the central path and defines the the particle trajectory relative to the central path, having a curvature radius ρ_0.

derived by

$$F_C = \frac{m v_s^2}{\rho_0 + x}\,, \tag{6.4}$$

where m and v_s represent the particle mass and velocity, respectively. In this co-propagating reference system (Eq. 6.1), the motion of a particle, e.g. in the x-z-plane, can be rewritten using Eq. 6.3 and Eq. 6.4, leading to

$$\ddot{x} = \frac{v_s^2}{\rho_0 + x} - \frac{q}{m}(v_z B_y - v_y B_z)\,. \tag{6.5}$$

Since the velocity v_s of the particle is linearly approximated by $v_s \approx v_z$, Eq. 6.5 can be simplified to

$$\ddot{x} = \frac{v_s^2}{\rho_0 + x} - \frac{q}{p} v_s^2 B_y\,, \tag{6.6}$$

where p denotes the total momentum of the particle. Series expanding Eq. 6.6, and taking only the first order terms, yields

$$\ddot{x} = \frac{v_s^2}{\rho_0}\left(1 - \frac{x}{\rho_0}\right) - \frac{q}{p} v_s^2 B_y\,. \tag{6.7}$$

Using the relations

$$\frac{d}{dt} = \frac{ds}{dt}\frac{d}{ds} = v_s\frac{d}{ds}\,, \tag{6.8}$$

$$\frac{d^2}{dt^2} = v_s^2\frac{d^2}{ds^2}\,, \tag{6.9}$$

the time-dependence of Eq. 6.7 can be re-written in terms of displacement. Using Eq. 6.8 and 6.9 in Eq. 6.7, the equation of motion can be given by

$$\frac{d^2x}{ds^2} = x'' = \frac{1}{\rho_0}\left(1 - \frac{x}{\rho_0}\right) - \frac{q}{p}B_y\,. \tag{6.10}$$

Assuming only small deviations of the particle trajectory, relative to the deflection radius ρ_0, the magnetic field term can be expanded around the central path using the Taylor expansion,

$$B_y(x) = B_0 + \frac{\partial B_y}{\partial x}x + \frac{1}{2!}\frac{\partial^2 B_y}{\partial x^2}x^2 + \frac{1}{3!}\frac{\partial^3 B_y}{\partial x^3}x^3 + \cdots\,. \tag{6.11}$$

Multiplying both sides by $\frac{q}{p}$ gives

$$\frac{q}{p}B_y(x) = \frac{q}{p}B_0 + \frac{q}{p}\frac{\partial B_y}{\partial x}x + \frac{q}{p}\frac{1}{2!}\frac{\partial^2 B_y}{\partial x^2}x^2 + \frac{q}{p}\frac{1}{3!}\frac{\partial^3 B_y}{\partial x^3}x^3 + \cdots \tag{6.12}$$

$$\equiv \frac{1}{\rho_0} + kx + \frac{1}{2}mx^2 + \frac{1}{6}ox^3 + \cdots\,. \tag{6.13}$$

In this magnetic field Taylor expansion, each term represents a multipole component,

Multipole	Term	Magnetic	Electrostatic	Effect
Dipole	$\frac{1}{\rho_0}$	$\frac{q}{p}B_0$	$\frac{q}{2E_{kin}}E_0$	Deflection
Quadrupole	k	$\frac{q}{p}\frac{\partial B_y}{\partial x}$	$\frac{q}{2E_{kin}}\frac{\partial E_x}{\partial x}$	Focusing
Sextupole	m	$\frac{q}{p}\frac{\partial^2 B_y}{\partial x^2}$	$\frac{q}{2E_{kin}}\frac{\partial^2 E_x}{\partial x^2}$	2nd order correction
Octupole	o	$\frac{q}{p}\frac{\partial^3 B_y}{\partial x^3}$	$\frac{q}{2E_{kin}}\frac{\partial^3 E_x}{\partial x^3}$	3rd order correction

Table 6.1: The four lowest order multipole terms of a magnetic and electrostatic field around the central path.

each of which has a different effect on the particle beam, detailed in Tab. 6.1. A similar approach can be used in the case of a charged particle guided by an electrostatic field yielding the electrostatic term contributions, also shown in Tab. 6.1. In linear approximation (of Eq. 6.13) and with the substitution $K_x(s) = \frac{1}{\rho_0^2} + k(s)$, Eq. 6.10 can be rewritten as

$$x''(s) + K_x(s)x(s) = \frac{\delta}{\rho_0}\,, \tag{6.14}$$

where $\delta = \Delta p/p_0$ is the momentum deviation to the central particle with the momentum p_0. This approach, including all approximations, which have been discussed for the motion of the particle in x-direction, can be similarly applied to the motion in the y-direction, with the exception that there is no centrifugal force contribution. The equation of motion is thus given as

$$y''(s) + K_y(s)y(s) = 0\,. \tag{6.15}$$

For mono-energetic particles ($\delta = 0$), the equations of motion (Eq. 6.14 and Eq. 6.15) have the same structure and are given by

$$u''(s) + K(s)u(s) = 0\,. \tag{6.16}$$

The general solution of the homogeneous differential equation can be given by linear combinations of a pair of linearly independent solutions ($C(s)$, $S(s)$), that satisfy the differential equation, leading to

$$u(s) = u_0 C(s) + u_0' S(s)\,, \tag{6.17}$$

$$u'(s) = u_0 C'(s) + u_0' S'(s)\,, \tag{6.18}$$

where u_0 and u_0' are arbitrary initial parameters of the particle trajectory [138]. The functions $C(s)$ and $S(s)$ are cos-like or sin-like solutions, which satisfy the following initial conditions:

$$C(0) = 1\,, \quad C'(0) = 0\,, \tag{6.19}$$

$$S(0) = 0\,, \quad S'(0) = 1\,. \tag{6.20}$$

If the particles are not mono-energetic ($\delta \neq 0$), an ion-optical element which deflects the particle in the horizontal (x) plane leads to the inhomogeneous differential equation Eq.6.14. The general solution of which, can be given as a linear combination of the homogeneous solution (given by Eq. 6.17) and a particular solution for the inhomogeneous equation, given by $\delta d_x(s)$, where $d_x(s)$ denotes the dispersion function [137]. The dispersion function must satisfy the initial conditions:

$$d_x(0) = 0\,, \tag{6.21}$$

$$d_x'(0) = 0\,. \tag{6.22}$$

Assuming that K is constant within an ion-optical element, the principal solutions for $C(s)$, $S(s)$ and $d_x(s)$, for $K > 0$ (focusing), are given by [137]

$$C(s) = \cos\left(\sqrt{K}s\right)\,, \tag{6.23}$$

$$S(s) = \frac{1}{\sqrt{K}}\sin\left(\sqrt{K}s\right)\,, \tag{6.24}$$

$$d_x(s) = \frac{1}{\rho_0 K}\left[1 - \cos\left(\sqrt{K}s\right)\right]\,. \tag{6.25}$$

For $K = 0$, representing a drift section,

$$C(s) = 1\,, \tag{6.26}$$

$$S(s) = s\,, \tag{6.27}$$

$$d_x(s) = 0\,, \tag{6.28}$$

and for $K < 0$ (defocusing),

$$C(s) = \cosh\left(\sqrt{|K|}s\right)\,, \tag{6.29}$$

$$S(s) = \frac{1}{\sqrt{|K|}}\sinh\left(\sqrt{|K|}s\right)\,, \tag{6.30}$$

$$d_x(s) = \frac{1}{\rho_0|K|}\left[\cosh\left(\sqrt{|K|}s\right) - 1\right]\,. \tag{6.31}$$

These equations describe the transversal motion of particles in magnetic and electrostatic fields in linear approximation. The variation in the longitudinal displacement of a particle relative to the reference particle (which moves along the central path) is given by $l = -v_0(t - t_0)$. t denotes the time of flight of an arbitrary particle relative

to the time of flight (t_0) of the reference particle in a reference plane. Consequently, $(t - t_0) > 0$, which is tantamount to a temporal delay of the arbitrary particle, indicates that the particle is spatially located behind the reference particle.
In linear approximation, only deflecting ion-optical elements can lead to such a longitudinal displacement, resulting from the difference between the inner and the outer path of a curvature. This effect is important to describe the longitudinal variation of particles in bunched ion beams. For continuous ion beams, which are guided through static ion-optics, the longitudinal extend can be neglected.

6.2 Transfer matrix formalism

The transversal coordinates x, x', y and y' can be combined with l and δ to form a 6-vector $\mathbf{x}$;

$$\mathbf{x}(s) = \begin{pmatrix} x \\ x' \\ y \\ y' \\ l \\ \delta \end{pmatrix} = \begin{pmatrix} \text{horizontal displacement} \\ \text{horizontal divergence} \\ \text{vertical displacement} \\ \text{vertical divergence} \\ \text{longitudinal displacement} \\ \text{momentum deviation} \end{pmatrix}. \tag{6.32}$$

To describe the propagation of this vector through an ion-optical element, a matrix formalism is introduced. The effect of each ion-optical element, in a linear approximation, on a particle trajectory can be represented by a first order 6×6 transfer matrix R [137]. In general, this transfer matrix is given by

$$R = \begin{pmatrix} (x|x) & (x|x') & (x|y) & (x|y') & (x|l) & (x|\delta) \\ (x'|x) & (x'|x') & (x'|y) & (x'|y') & (x'|l) & (x'|\delta) \\ (y|x) & (y|x') & (y|y) & (y|y') & (y|l) & (y|\delta) \\ (y'|x) & (y'|x') & (y'|y) & (y'|y') & (y'|l) & (y'|\delta) \\ (l|x) & (l|x') & (l|y) & (l|y') & (l|l) & (l|\delta) \\ (\delta|x) & (\delta|x') & (\delta|y) & (\delta|y') & (\delta|l) & (\delta|\delta) \end{pmatrix}. \tag{6.33}$$

For ion-optics, in which the horizontal and the vertical motion of a particle are independent of each other, the xy-coupled elements in R are 0. For such transfer matrices without xy-coupled elements, the transverse sections of R can be separated as two 2×2 sub-matrices R_u. The sub-matrices R_u, representing the matrix elements of R

that couple to either the x or the y-components of a particle trajectory, are determined by the characteristic solutions $C(s)$, $S(s)$, $C'(s)$ and $S'(s)$ of the differential equations Eq. 6.17 and Eq. 6.18, which were presented in the previous section. R_u is then given by

$$R_u = \begin{pmatrix} C_u & S_u \\ C'_u & S'_u \end{pmatrix} = \begin{pmatrix} (u|u) & (u|u') \\ (u'|u) & (u'|u') \end{pmatrix} . \tag{6.34}$$

Using the matrix formalism, Eq. 6.17 and 6.18 can be expressed as

$$\begin{pmatrix} u(s) \\ u'(s) \end{pmatrix} = \begin{pmatrix} C_u(s) & S_u(s) \\ C'_u(s) & S'_u(s) \end{pmatrix} \cdot \begin{pmatrix} u(s_0) \\ u'(s_0) \end{pmatrix} , \tag{6.35}$$

where the initial transversal coordinates $u(s_0)$ and $u'(s_0)$ of a particle are transformed to $u(s)$ and $u'(s)$ via the matrix R_u. Taking the simple example of a drift section, where $K = 0$ and $\rho_0 \to \infty$, the characteristic solutions of the matrix elements are shown in Eq. 6.26 - 6.28, the transfer matrix for a drift section with the length L is given by

$$R_{\text{Drift}} = \begin{pmatrix} 1 & L & 0 & 0 & 0 & 0 \\ 0 & 1 & 0 & 0 & 0 & 0 \\ 0 & 0 & 1 & L & 0 & 0 \\ 0 & 0 & 0 & 1 & 0 & 0 \\ 0 & 0 & 0 & 0 & 1 & L/\gamma^2 \\ 0 & 0 & 0 & 0 & 0 & 1 \end{pmatrix} . \tag{6.36}$$

The ion-optical transfer matrices, implemented in the final transfer-line design, are summarized in Appendix C. A linear beam transport system, consisting of a sequence of ion-optical elements, can then be fully characterized by the multiplication of their transfer matrices. The transfer matrix of the transport system (R_T) is then determined by

$$R_T = R_n \cdot R_{n-1} \cdots R_2 \cdot R_1 , \tag{6.37}$$

where R_i (i=1..n) represents the transfer matrix of an ion-optical element.

6.3 Transport of ion beams

As previously discussed, in a linear approximation, the transport of the particle through an ion-optical system (R_T) can be determined by

$$\mathbf{x}(s) = R_T\,\mathbf{x}(0)\,. \tag{6.38}$$

However, an ion beam is formed by the superposition of a large number of single particle trajectories. In Fig. 6.2, the horizontal trajectory of a single particle is presented schematically, as a component of an ion beam. An ion-optical transport system, consisting of drift sections and horizontally focusing quadrupoles, guides

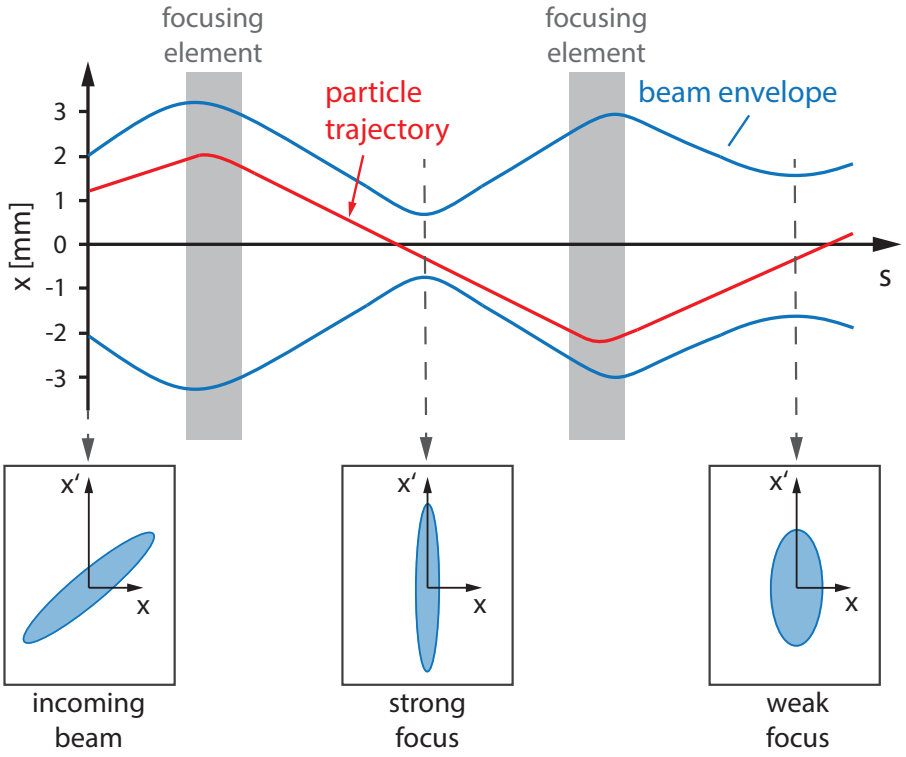

Figure 6.2: Illustration of a single particle's horizontal trajectory (red solid line) as a component of an ion beam, propagating through an ion-optical transport system. The blue solid line indicates the beam envelope as a function of the position s along the central path. The ion-optical system (drift - quadrupole - drift - quadrupole - drift) transports the ion beam (including the single particle) along the path s. Two focusing elements, which are indicated by the grey areas, focus a horizontally diverging ion beam. The three boxes show schematically the phase space ellipse (horizontal) of the incoming beam (diverging), in the first focus and the second focus. This sequence indicates the transformation of the phase space ellipse at different locations of the ion beam.

the particle along the path s. The horizontal position $x(s)$, which is given relative to the central path, can be calculated as a function of s via Eq. 6.38. Since it is impractical to determine the trajectory of each individual particle, a formalism representing the entire ion beam is required. An ion beam can be characterized by the intensity distribution of the single particle trajectories $\mathbf{x}(s)$, called the phase space density $\rho(\mathbf{x}) = \rho(x, x', y, y', l, \delta)$. Assuming that the horizontal (x, x'), vertical (y, y') and longitudinal (l, δ)) coordinates are uncorrelated, the phase space density can be separated in two-dimensional distributions: $\rho(x, x', y, y', l, \delta) = \rho(x, x')\rho(y, y')\rho(l, \delta)$. These distributions are usually represented by an ellipse. This phase space ellipse can be represented by a 2×2-matrix, the so-called σ-matrix [137]. The horizontal σ-matrix is given by

$$\sigma_x = \begin{pmatrix} \sigma_{11} & \sigma_{12} \\ \sigma_{21} & \sigma_{22} \end{pmatrix} , \tag{6.39}$$

where $\sigma_{12} = \sigma_{21}$. A physical representation of the elements of the σ-matrix are denoted in Fig. 6.3. The equation of the phase space ellipse is given by

$$\mathbf{X}^T \sigma_x^{-1} \mathbf{X} = 1 , \tag{6.40}$$

where $\mathbf{X}$ denotes the vector from the point of origin to the edge of the ellipse [137],

$$\mathbf{X}^T = (x, x') , \quad \mathbf{X} = \begin{pmatrix} x \\ x' \end{pmatrix} . \tag{6.41}$$

The inverse matrix σ_x^{-1} is determined by

$$\sigma_x^{-1} = \frac{1}{\det(\sigma_x)} \begin{pmatrix} \sigma_{22} & -\sigma_{12} \\ -\sigma_{12} & \sigma_{11} \end{pmatrix} . \tag{6.42}$$

Using Eq. 6.42 in Eq. 6.40 leads to the equation of the phase space

$$\sigma_{22} x^2 - 2\sigma_{12} x x' + \sigma_{11} x'^2 = \det(\sigma_x) = \epsilon_x^2 , \tag{6.43}$$

where ϵ_x denotes the emittance, which is a measure of the beam quality. The value of ϵ_x times π defines the area A_x of the phase space ellipse, according to

$$A_x = \pi \epsilon_x = \pi \sqrt{\det(\sigma_x)} = \pi \sqrt{\sigma_{11}\sigma_{22} - \sigma_{12}^2} . \tag{6.44}$$

As the particle trajectories are not necessarily distributed homogeneously in phase space, the ellipse parameters are better defined with respect to the phase space density distribution $\rho(x, x')$. A realistic model for $\rho(x, x')$ is given by the Gaussian distribution

$$\rho(\mathbf{x}) = \frac{1}{2\pi\epsilon_x^{1\sigma}} \exp\left(-\frac{1}{2}\mathbf{x}^T \sigma_x^{-1}\mathbf{x}\right) , \tag{6.45}$$

where $\mathbf{x}$ represents arbitrary phase space coordinates. $\epsilon_x^{1\sigma}$ denotes the 1σ-emittance

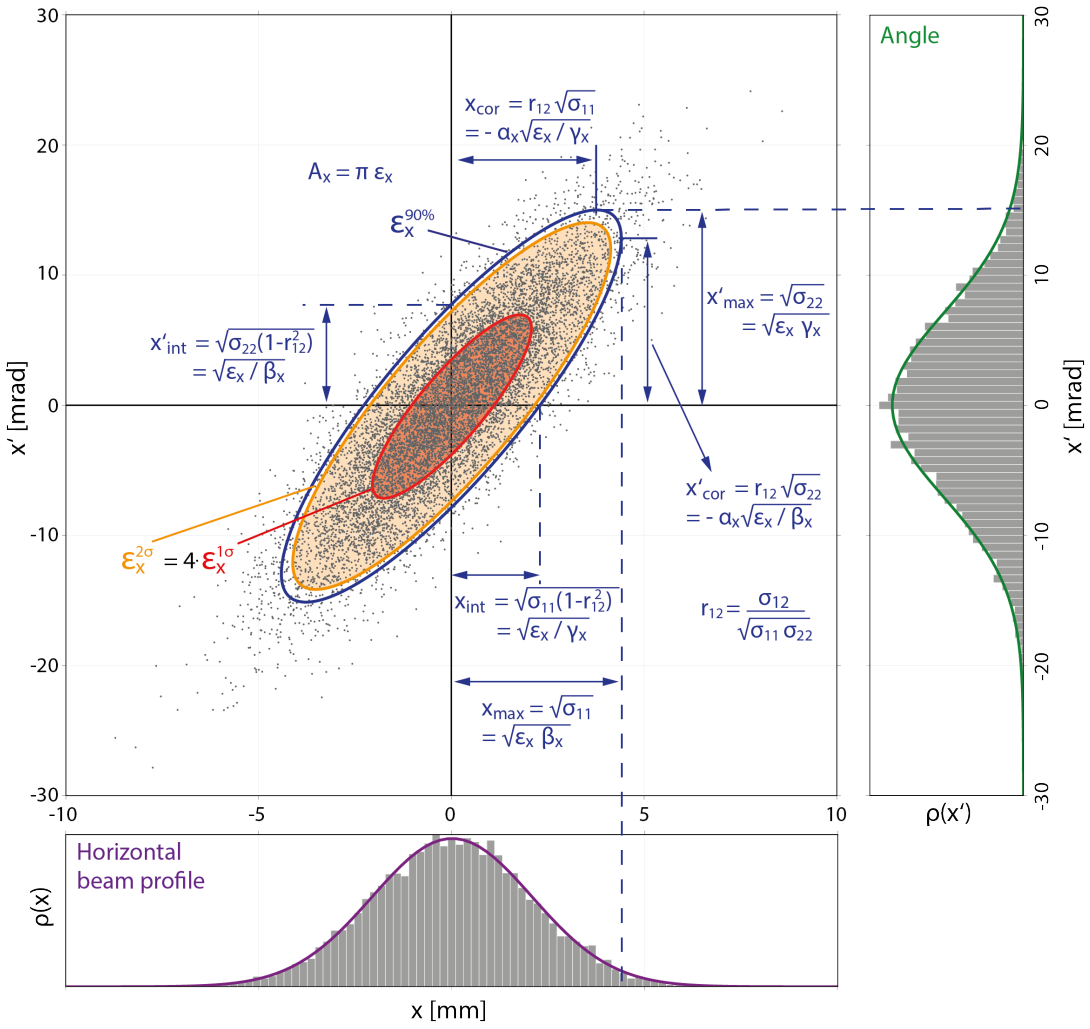

Figure 6.3: Phase space of a diverging ion beam. The phase space distribution $\rho(x, x')$ of the ion beam can be represented by a Gaussian function, according to Eq. 6.45). The grey dots represent single particles, whereas their density distributions of x and x' are shown in the graph below and at the right side, respectively. Phase space ellipses are fitted for one standard deviation (red ellipse), two standard deviations (orange ellipse) and the blue ellipse indicates the area, that includes 90% of all particles. The relation to the σ-matrix elements (Eq. 6.39) and the twiss parameters (Eq. 6.49) are here illustrated for $\epsilon_x^{90\%}$.

of the particle beam, which is represented by the phase space coordinates $\mathbf{X}$ in Eq. 6.40. The density distribution can be represented by elliptic contour lines, as demonstrated in Fig. 6.3, where the phase space of a diverging ion beam is illustrated. The grey dots represent the single particles. The diagram below and on the right side show the Gaussian distributions of $\rho(x)$ and $\rho(x')$, respectively. The one-dimensional density distribution $\rho(x)$, representing the horizontal beam profile, is given by the projection of the density distribution $\rho(x, x')$ onto the x-axis, according to

$$\rho(x) = \int \rho(x, x') dx' \,. \tag{6.46}$$

Using Gaussian density distributions, the phase space ellipse presented in Eq. 6.40, edges the area of the 1σ-emittance. This area is indicated by the red ellipse in Fig. 6.3. The orange phase space ellipse, which can be represented by

$$\mathbf{X}^T \sigma_x^{-1} \mathbf{X} = 4 \,, \tag{6.47}$$

denotes the 2σ-emittance, which leads, according to Eq. 6.44 to the simple relation

$$\epsilon_x^{2\sigma} = 4\epsilon_x^{1\sigma} = 4\sqrt{\det(\sigma_x)} = 4\sqrt{\sigma_{11}\sigma_{22} - \sigma_{12}^2} \,. \tag{6.48}$$

Apart from using the standard deviation, it is also convenient to define the beam emittance by the percentage fraction of the included particles. This approach has the advantage, in that it provides a value for the emittance, that is independent on the density distribution $\rho(x, x')$. As an example, the emittance $\epsilon_x^{90\%}$, that considers 90% of all particles within the phase space ellipse is represented by the blue solid line in Fig. 6.3.
Using the so-called twiss parameters α, β and γ [139], the phase space matrix (Eq. 6.39) can be rewritten to

$$\sigma = \epsilon \cdot \begin{pmatrix} \beta & -\alpha \\ -\alpha & \gamma \end{pmatrix} \,. \tag{6.49}$$

The betatron function $\beta_x(s)$, which gives a representation of the horizontal beam amplitude $x_{max}(s)$ along the central path, is correlated to the beam envelope via

$$x_{max}(s) = \sqrt{\epsilon_x \beta_x(s)} \,, \tag{6.50}$$

where x_{max} is the maximum beam radius for a given emittance ϵ_x (see Fig. 6.3). The parameter $\alpha(s)$ represents the derivative of $\beta(s)$ as a function of s; $\alpha(s) = -\beta'(s)/2$.

Thus, α is equal to 0 for a beam waist, represented by an upright phase space ellipse, as shown in Fig. 6.2. The twiss parameter γ is defined by

$$\gamma = \frac{1+\alpha^2}{\beta}\,, \tag{6.51}$$

which allows to determine the maximum divergence of a beam, using a defined emittance ϵ_x, via

$$x'_{max} = \sqrt{\epsilon_x \gamma_x}\,. \tag{6.52}$$

The twiss parameters are ideal to describe the ion beam transport, as they are independent of the phase space area. Eq. 6.43 of the phase space can be also represented using the twiss parameter, leading to the Courant-Snyder ellipse [139],

$$\gamma(s)x^2(s) + 2\alpha(s)x(s)x'(s) + \beta(s)x'^2(s) = \epsilon_x\,. \tag{6.53}$$

According to Liouville's theorem, the phase space density does not change when only conservative forces are involved [138]. Therefore, the emittance ϵ stays constant along a transfer line, using only linear ion-optics (e.g. drifts, deflectors, quadrupoles). These elements determine the phase space ellipse, but do not alter the area:

$$\epsilon_x = \gamma(s)x^2(s) + 2\alpha(s)x(s)x'(s) + \beta(s)x'^2(s) \tag{6.54}$$

$$= \gamma(s_0)x^2(s_0) + 2\alpha(s_0)x(s_0)x'(s_0) + \beta(s_0)x'^2(s_0)\,. \tag{6.55}$$

From Eq. 6.35, the transport equation using the twiss parameter is given by

$$\begin{pmatrix} \beta(s) \\ \alpha(s) \\ \gamma(s) \end{pmatrix} = \begin{pmatrix} C^2 & -2SC & S^2 \\ -CC' & S'C + SC' & -SS' \\ C'^2 & -2S'C' & S'^2 \end{pmatrix} \cdot \begin{pmatrix} \beta(s_0) \\ \alpha(s_0) \\ \gamma(s_0) \end{pmatrix}\,. \tag{6.56}$$

To better illustrate the twiss parameter formalism, the example of a drift section (characterized in Eq. 6.26 - 6.28) is given by,

$$\begin{pmatrix} \beta(s) \\ \alpha(s) \\ \gamma(s) \end{pmatrix} = \begin{pmatrix} 1 & -2s & s^2 \\ 0 & 1 & -s \\ 0 & 0 & 1 \end{pmatrix} \cdot \begin{pmatrix} \beta_0 \\ \alpha_0 \\ \gamma_0 \end{pmatrix}\,, \tag{6.57}$$

where s denotes the length of the drift. Fig. 6.4 shows schematically the evolution of the twiss parameter α, β and γ as function of the drift length s. Starting with

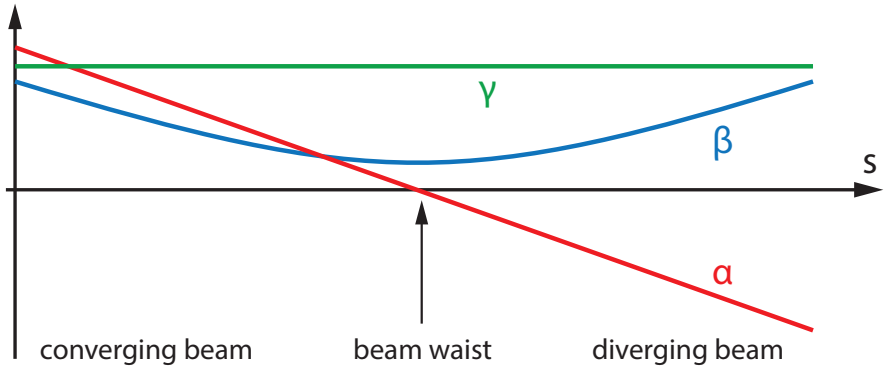

Figure 6.4: Schematic of the evolution of the twiss parameter α (red line), β (blue line) and γ (green line) within a drift section.

a converging beam, the betatron function decreases and $\alpha > 0$. At the focal point, where the beam forms a waist, $\alpha = 0$. Beyond this beam waist, the betatron function increases and $\alpha < 0$. As the drift angle does not change, the twiss parameter γ stays constant within a drift section.

6.4 Filamentation

Ion-optical elements, which possess significant non-linear field contributions, introduce aberrations in the beam. In the example of a sextupole, field aberrations quadratically increase with the transversal displacement of a particle (relative to the central path). Therefore, the focal strength depends on the amplitude of the beam. Consequently, the transport via a non-linear ion-optic leads to a distortion of the phase space distribution, called filamentation. Liouville's theorem states that the total phase space area is conserved, but as the phase space undergoes filamentation, the ellipse fit of the resulting deformed phase space distribution can lead to an increase of the effective emittance.
In Fig. 6.5, a negative ion beam ($E_{kin} = 20$keV) is focused via an einzel lens. The initial Gaussian phase space distribution of the ion beam is shown in diagram 1. The area bounded by the red ellipse encompasses 90% of all particles. While passing an einzel lens, the non-linear field components introduce a filamentation of the phase space. This effect is shown in the diagrams 2-4, which illustrate the phase space distribution of the beam at the stated positions. So that the phase space ellipses continue to contain 90% of the particles, their area must increase. As a result, the initial effective emittance $\epsilon_x^{90\%}(1) \approx 142$ mm mrad, increases to $\epsilon_x^{90\%}(2) \approx 199$ mm

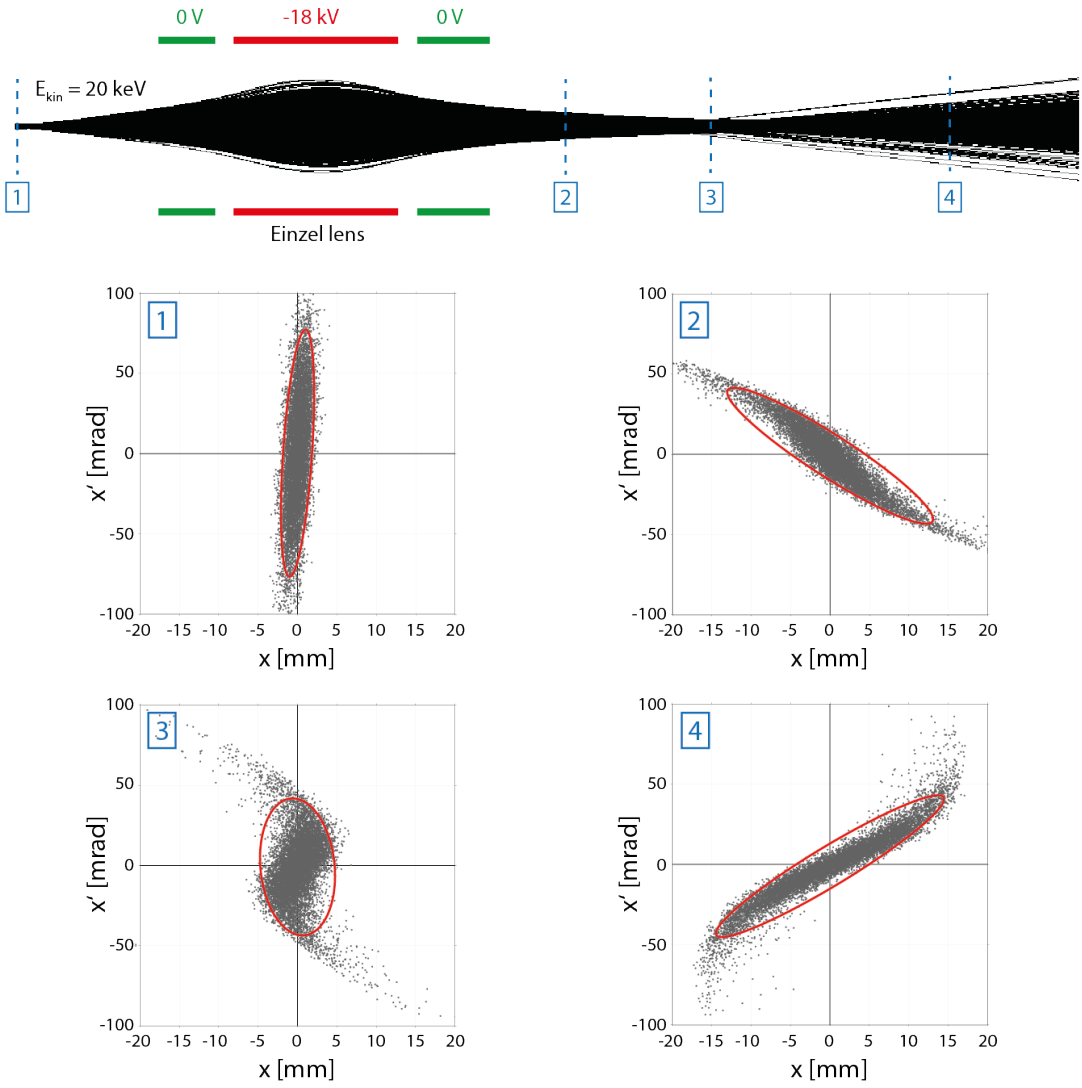

Figure 6.5: Simulation of a negative ion beam, undergoing focusing via an einzel lens. Due to the non-linear field components, the phase space distribution of the ion beam is deformed after passing the einzel lens. The phase space filamentation is shown for three other positions (2-4). For each phase space distribution, the phase space ellipse that comprises 90% of all particles is fitted (red line).

mrad, $\epsilon_x^{90\%}(3) \approx 202$ mm mrad and $\epsilon_x^{90\%}(4) \approx 204$ mm mrad for position 2,3 and 4, respectively.

This demonstrated effect leads to distortion of the trajectory in phase space, but does not necessarily lead to unstable beam transport, as long as the accumulation of this distortion is finite. However, the increased emittance can lead to beam losses, dependent on aperture sizes and the cross-section of the beam pipe utilized.

6.5 Fringing field

In section 6.1, the equation of motion for a particle traversing a field of constant strength (K) was derived (Eq. 6.16). In reality, ion-optical elements are never perfect and possess fringing fields which extend past the electrode volume, as illustrated in Fig. 6.6. In this example, the one-dimensional field profile along the central path consists of a superposition of a constant field and a fringing field, where the field strength decreases towards ground from its edges extending beyond its geometrical length. The resulting magnetic or electric field can be approximated by a box-like field profile with an effective length L_{eff}, called hard edge model. In the example of a dipole magnet, where the field distribution is substituted by an equivalent box-like distribution of the strength B_0, the effective length L_{eff} is defined as [137]

$$L_{\text{eff}} = \frac{1}{B_0} \int_{-\infty}^{\infty} B(s) ds \,. \tag{6.58}$$

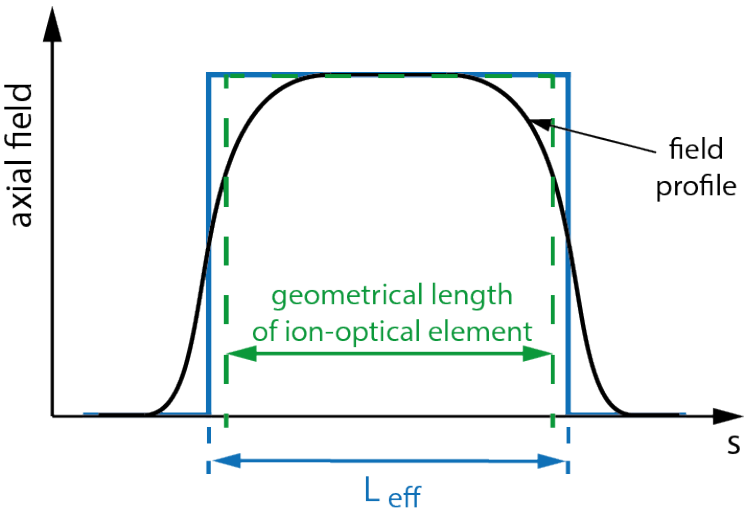

Figure 6.6: One-dimensional field profile of an ion-optical element along the central path s (indicated by the black line). The field profile extends beyond the geometrical length of the ion-optical element, indicated by the green dashed line. The field is approximated by a box-like field profile, which has an effective length L_{eff} (indicated by the blue line).

Chapter 7

The Cryogenic Storage Ring (CSR)

The Cryogenic Storage Ring (CSR), located at the Max Planck Institute for Nuclear Physics, is a fully electrostatic storage ring, designed for the stable storage of positive or negative ions at kinetic energies ranging between 20 and 300 keV per charge unit. Using only electrostatic elements inside the CSR permits the storage of charged particles independent of their mass. Therefore, the CSR allows the investigation of large molecules, clusters and biomolecules. The inner vacuum chambers of the CSR can be cooled down to cryogenic temperatures below 10 K. This low temperature minimizes the environmental black-body radiation to which the stored particles are exposed. Conveniently, the cold vacuum chambers act as a cryopump, enabling residual gas pressures $< 10^{-13}$ mbar RTE (room temperature equivalent). Often, the lifetime of stored particles is limited by the electron capture process and the electron stripping process, caused by collisions with the residual gas inside the CSR. Thus, it is preferential to minimize the residual gas pressure. The first cold commissioning phase of the CSR (March - July 2015) successfully demonstrated a temperature of $\leqslant 6$ K for all inner vacuum chambers, measured by temperature sensors. During this test phase, various ionic species (ranging from positively charged atoms and molecules to negatively charged clusters) were stored inside the CSR at kinetic energies between 60 and 90 keV. The measured lifetime of the stored particles ranged from a few hundred seconds to ~ 2600 s. These cold environments and long storage times, enable stored molecular ions which possess a permanent dipole moment to radiatively cool into their rovibrational ground states. It is these aforementioned properties, that make the CSR a unique experimental tool for the research of large molecules, highly charged ions and astrophysical reactions.

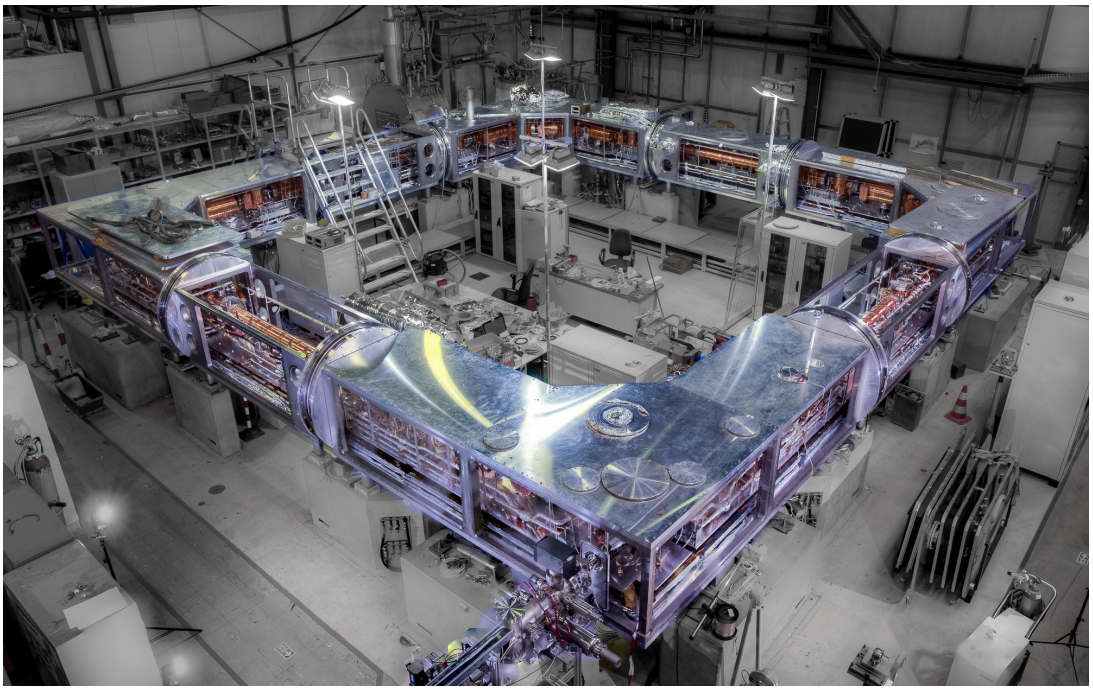

Figure 7.1: Photograph of the Cryogenic Storage Ring (credit C. Föhr).

7.1 Concept of the vacuum system

The internal structure of the CSR is designed to minimize the heat transfer from the external environment, in order to achieve <10 K at the inner experimental vacuum chambers. It is within these experimental chambers that the ions are stored. The CSR relies on a cryostat to deliver cryogenic helium for the cooling circuits. This cryostat (Linde, based on type L140) has two cooling stages, which are attached to the 2K and the 5K helium line, respectively. The cooling power of the first stage is rated to provide 10 W at 1.8 K or 21 W at 2 K. The second cooling stage has a cooling power of 600 W in a temperature range of 5-80 K [140]. In Fig. 7.2, the design and concept of the vacuum system and the thermal segmentation is demonstrated. The left picture shows a photograph of a cross section of a CSR chamber, whereas the right picture highlights the thermal segmentation. The vacuum system of the CSR comprises of an isolation vacuum ($<10^{-5}$ mbar), which subsequently houses an extremely high vacuum ($<10^{-13}$ mbar), denoted as experimental vacuum. The experimental vacuum comprises of stainless steel chambers, that are wrapped in thin copper sheets to provide a high thermal conductivity. These vacuum chambers are connected to the 2K helium line, using braided copper cables. The second cooling

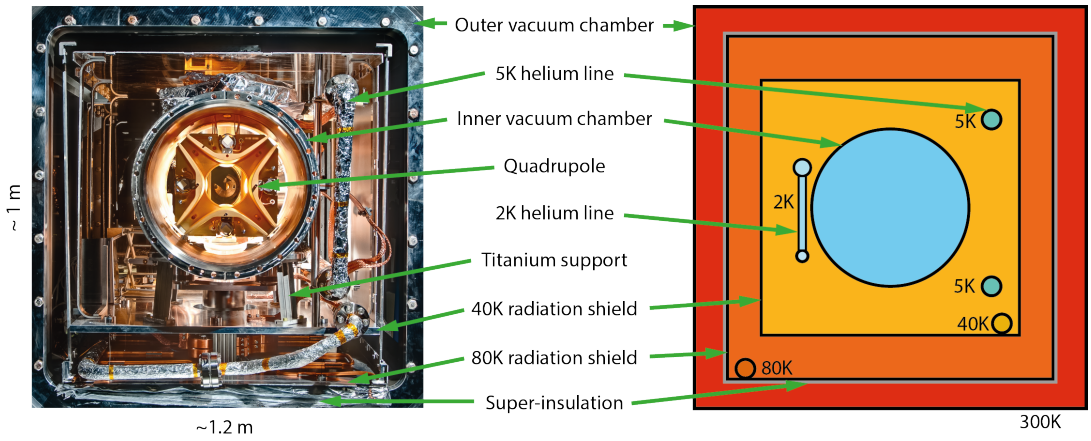

Figure 7.2: Cross section of a CSR chamber, looking along the stored beam path. The left picture shows a photograph of the structure of the CSR chamber. The right picture indicates a simplified schematic of this structure, divided into thermal segments.

stage of the cryostat, connected to the 5K helium line, cools internal components, e.g. the amplifiers for the detection systems. After two circulations inside the CSR, this helium line is attached to an aluminum shield, which is called 40K radiation shield. This shield surrounds the inner vacuum chambers of the CSR and the two helium line systems. A second aluminum shield, the so-called 80K radiation shield, is wrapped in a multilayer superinsulation foil (Coolcat 2 NW), surrounding the 40K radiation shield. These shields are directly attached to the 5K helium line, each after two circulations inside the CSR, respectively. Since the outer vacuum chamber is at room temperature, these two radiation shields reduce the transport of the thermal radiation to the inner vacuum chambers. To minimize the heat flow via conduction, the inner vacuum chambers are supported by titanium plates. As heat flow is proportional to the cross sectional area of the conductor, the titanium supports are corrugated to maintain rigidity, while minimizing the permitted plate thickness. High voltages are applied to the ion-optics via electrical wires which are fed through the isolation vacuum. As these copper wires tend to be good thermal conductors, they are thermally anchored to the 40K-shield and the inner vacuum chamber using sapphire plates. Detailed calculations of the heat transport due to black-body radiation and conductance are presented in [140].

To achieve residual gas pressures of $<10^{-13}$ mbar (RTE), a sequential pumping scheme is required. First, the vacuum chambers are baked out at ∼600 K and pumped by turbopumps in tandem with the activated NEG (Non-Evaporable Getter) strips (SAES Getters, type ST707) to pressures in the region of 10^{-11} mbar. NEG

strips provide pumping in the form of chemically binding the residual gas molecules, e.g. H_2, CO and N_2. Finally, the entire inner vacuum chamber is cooled to <10 K, at which point most chemical elements condensate on the chamber surface. The residual gas contains then mainly H_2, which can be cryo-pumped using liquid helium at the 2K-cold units [141].

7.2 Overview of experimental capabilities

As illustrated in Fig. 7.3, the ion-optical elements of the CSR possess an 8-fold symmetry. In each of the four corners, the stored ion beam is deflected by 90° using a combination of two 39° deflectors with two 6° cylindrical deflectors. The particles in the CSR are stored on an orbit of approximately 35 m, focused by electrostatic quadrupole doublet elements. The segment of 2.8 m between these quadrupole doublets defines the four straight sections of the CSR, each of which is reserved for an experiment. Anticlockwise from the beam injection, the first straight section is dedicated for ion-neutral reaction measurements, where the stored ion beam is merged with a neutral atom beam, representing the focus for this part of the thesis.
The second straight section houses the electron cooler and target [142, 143], where a geometrically well defined electron beam with a narrow energy distribution, is merged with the stored ion beam at low relative velocities. The phase space of the stored particles is then cooled by Coulomb interaction with the electron beam. Since the electron beam has a much higher number density than the stored ion beam, the transverse and longitudinal ion temperature tends towards the temperature of the electron beam. The design of the electron cooler aims for electron beam energies down to 1 eV, which provides phase space cooling of stored ion beams up to mass 160 amu per charge state [144]. Additionally, the velocity of the electron beam can be precisely detuned, relative to the velocity of the stored particles, this allows the electron beam to serve as electron target. Stored positive molecular ions can thus recombine with an electron of the merged electron beam. The created neutral fragments are subsequently detected by a neutral imaging detector (NICE) [145] as a function of the relative velocities. This technique allows the determination of energy-resolved electron recombination rate coefficients [121]. Since the electron cooler is in the test assembly phase, and not yet installed into the CSR, this section of the CSR has been temporarily transformed into a laser section. Laser experiments permit the probing of the energy level population for the stored ions, using a tunable

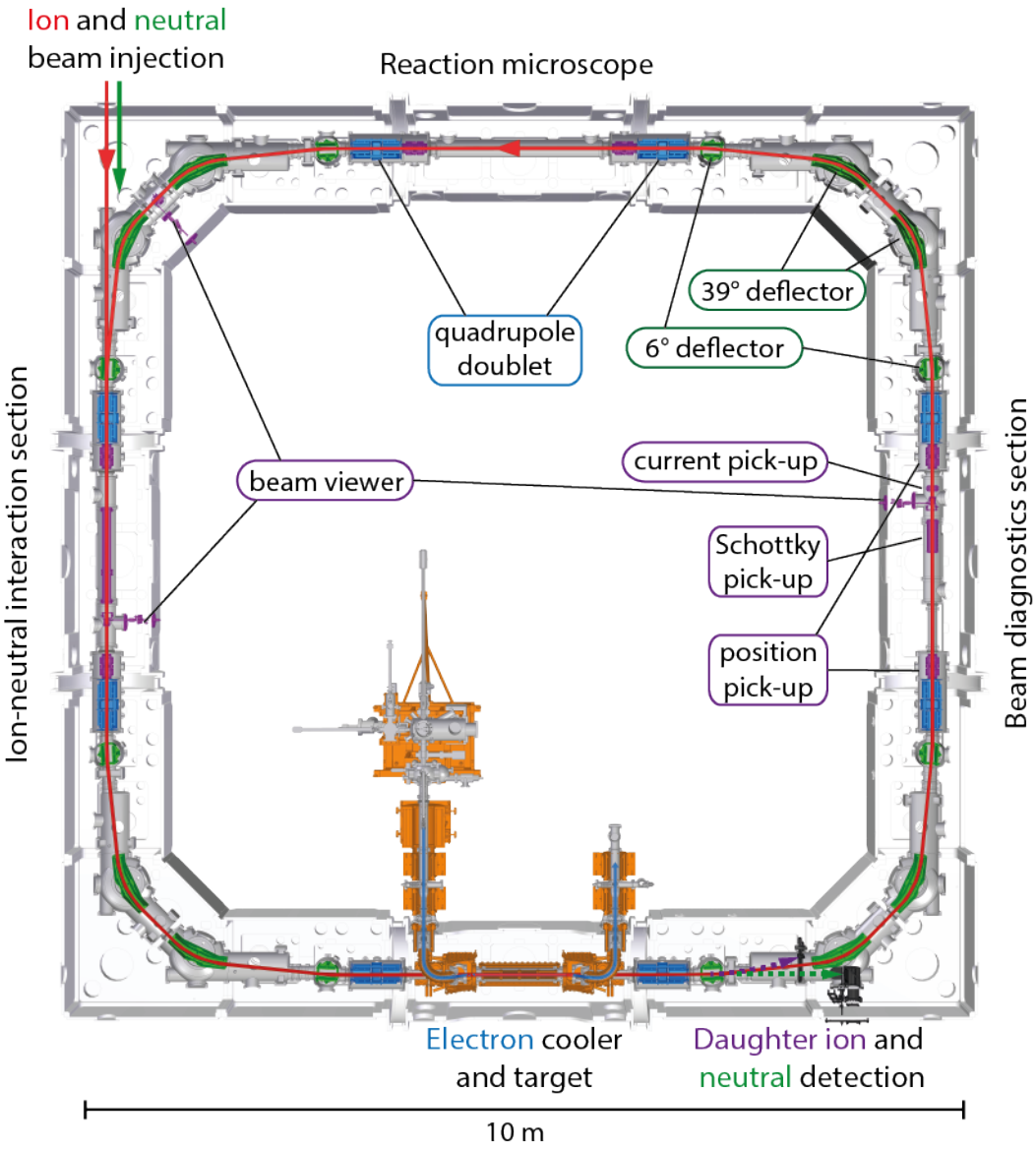

Figure 7.3: Schematic overview of the CSR. The four straight sections, between the quadrupole doublets (blue), are occupied by experimental setups. The deflecting ion-optical elements (6° and 39° deflector) are indicated in green. The quadrupole doublets, which focus the stored ion beam, are shown in blue. The beam diagnostics (the beam viewer, the Schottky, current and position pick-ups) are indicated by the purple elements.

laser system. Due to the success of these measurements, the electron cooler will be retrofitted to accommodate the laser section to preserve this laser capability for future experiments. The charged daughter products, which are generated in that section, can be detected by a movable single particle counter (COMPACT) [146].
The third section is entirely dedicated for beam diagnostics, consisting of three different pick-up modules [147, 143] and a beam viewer [148]. The beam viewers, which consists of an aluminum converter plate and a combination of a MCP and a phosphor screen, are destructive diagnostics. Therefore, the three beam viewers can only provide feedback for the settings of the ion-optical elements during the first turn in the CSR. The pick-ups are non-destructive diagnostic tools, which allow to capacitively measure certain beam properties. The most sensitive module, the Schottky pick-up, is used for the first verification of stored particles. In addition to a sensitive measurement of the number of stored particles, the Schottky pick-up also provides the determination of their momentum spread. This measurement allows to identify any contamination of stored particles, possessing the same kinetic energy but a different mass. Additionally, the energy spread of the stored beam serves as diagnostics for the efficiency of the electron cooler. The measurement of the Schottky signal as a function of time reflects the lifetime of the stored ions [143]. The current pick-up provides the determination of the absolute ion beam current ranging from 1 nA to 1 mA [147]. The position pick-up modules allow the determination of the position of the beam center relative to the center of the pick-up electrode. Since most experiments inside the CSR benefit from an accurate determination of the beam position, three of the straight sections are equipped with pick-up electrodes. As the measurement of the beam position alone is insufficient for the operation of electron cooler, this straight section will be equipped by beam profile scanners.
The fourth straight section is designated for a reaction microscope [149], which allows the investigation of collision processes, using Cold Target Recoil Ion Momentum Spectroscopy (COLTRIMS) [150]. In this technique, a cold supersonic gas jet is injected perpendicular to the stored ion beam. A simultaneous measurement of the momentum vectors of the various reaction products allow the experimental investigation of collision-induced many-particles reactions. The design of this experimental section of the CSR is currently under development.

7.3 The ring lattice

As presented previously in Fig. 7.3, the CSR lattice consists of electrostatic ion-optical elements, consisting of both quadrupole doublets and cylindrical deflectors. The focusing CSR quadrupoles have a length of 0.2 m and are separated by 0.15 m within a doublet. The 90° bend in each corner is divided in two 6° deflectors with a bending radius of 2 m and two 39° deflectors with a bending radius of 1 m. The 1.1 m separation between the two deflectors yields a straight line clearance of ∼0.1 m, which enables the injection of either an ion or neutral beam. This clearance also provides the detection of neutral fragments, that are generated in experiments, by placing various detectors in appropriate positions. During the injection of an ion beam into the CSR, the 6° deflector, in the first corner, is switched to ground. In order to store the ion beam after the injection, the voltages for the 6° deflector are switched fast (ns) relative to the revolution time of the stored ions (μs).
A storage ring is a closed periodic ion-optical system, which has to fulfill the initial and end condition: $\beta(s) = \beta(s + L_{lat})$, where L_{lat} represents the circumference of the storage ring. For a given periodic lattice and quadrupole strengths, fulfilling this requirement, the betatron function $\beta(s)$ is unique. Using the transfer matrices

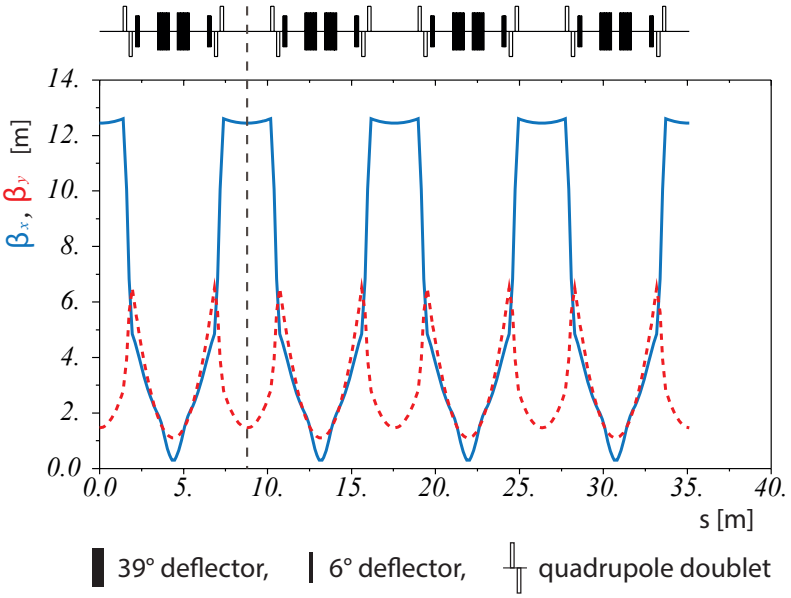

Figure 7.4: Simulated horizontal and vertical betatron functions β_x (blue solid line) and β_y (red dashed line) for the standard operating mode of the CSR, adopted from [151]. The grey dashed line indicates the position of the center of a straight section inside the CSR.

program, Methodical Accelerator Design (MAD 8) [152], the CSR lattice was simulated in a linear approximation [151]. For the standard operating mode of the CSR, providing stable ion storage and a relatively large beam acceptance, the quadrupole strengths in a doublet are determined to K_o = 5.5 m^{-2} and K_i = -6.9 m^{-2}. The resulting horizontal (x) and vertical (y) betatron functions β_x and β_y are shown in Fig. 7.4 [151]. This representation of the periodic CSR lattice starts in the center of a straight section of the CSR. At this position, the twiss parameters are calculated to be $\alpha_x = \alpha_y = 0$ (beam waist), β_x = 12.3 m and β_y = 1.2 m.
As the MAD 8 calculation only accounts for linear ion-optic effects, each electrostatic element of the ring was also simulated using the finite element program TOSCA (Opera3D) [153]. From the geometrical models of the ion-optical elements, TOSCA enables the tracking of individual particles. This simulation provides information on the ring acceptance of the CSR, which is limited by the field quality in the quadrupoles. The ring acceptance is defined as the maximal beam emittance that is stored. In Fig. 7.5, the maximum phase space ellipses, calculated using TOSCA in both the horizontal and vertical, which allow for a stable ion storage, are shown. The horizontal acceptance was determined to $A_x(\epsilon_y \to 0)$ = 120 mm mrad and the vertical acceptance $A_y(\epsilon_x \to 0)$ = 180 mm mrad.

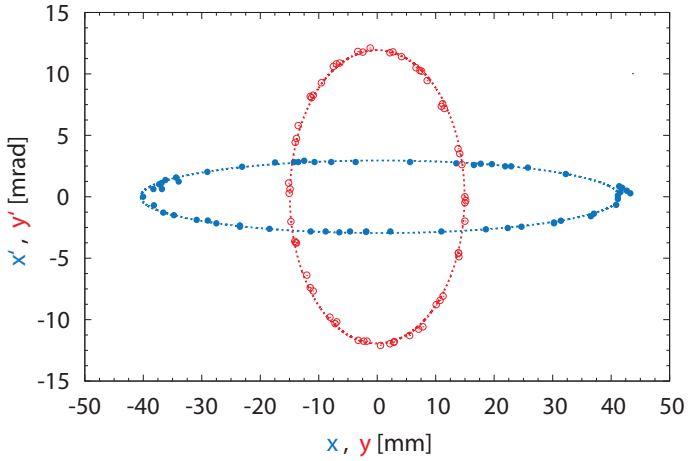

Figure 7.5: Simulation of a single particle tracked through the CSR lattice. In the center of a straight section of the CSR, the phase space coordinates of the orbiting particle is detected, forming a phase space ellipse. The maximum phase space for a stable ion storage defines the ring acceptance. The horizontal representation of the maximum phase space for $\epsilon_y \to 0$, shown in blue, leads to the horizontal acceptance A_x = 120 mm mrad. In red, the maximum phase space for $\epsilon_x \to 0$ represents the vertical acceptance A_x = 180 mm mrad [151].

Using the particle tracking simulation program G4beamline [154] together with the field maps generated in TOSCA, the values of the betatron functions in the center of a straight CSR section were determined to $\beta_x = 12.4$ m and $\beta_y = 1.4$ m [151]. The twiss parameters of a ring lattice are called machine parameters. These parameters have to be matched by the injected beam to preserve beam stability and phase space density. A mismatch leads to filamentation in the stored ion beam. For this reason, the ion-optical design of a transfer line has to consider for these machine parameters. The phase space matching of the injected beam takes place in the center of the straight section of the CSR, where the machine parameters are given by

$$\begin{aligned} \beta_x &= 12.4\,\mathrm{m}\,, \\ \beta_y &= 1.4\,\mathrm{m}\,, \\ \alpha_x &= 0\,, \\ \alpha_y &= 0\,. \end{aligned}$$

Chapter 8

Development and design of a versatile transfer line for the CSR

In Chap. 7, the capability of the CSR to store both positive and negative ions with energy to charge ratios up to 300 keV per charge unit in a cryogenic environment was discussed. In this section, the transfer beamline, which couples the ion source platforms to the CSR, is introduced. To minimize both the thermal and residual-gas load, conducted into the CSR from the transfer beamline, the transfer line must adhere to strict design and operating criteria. The final transfer line must be suitably versatile so that its optical elements are capable of efficiently transporting and delivering an ion beam that is:

- mass-filtered
- provide ion currents in the range from nA to mA
- either negatively or positively charged
- with kinetic energies of up to 300 keV per charge unit
- matching the machine twiss parameter of the storage ring

One of the experimental reactions planned in the CSR is the measurement of ion-neutral reaction rate coefficients, thus the transfer line must also be capable of first injecting and storing an ion beam, then relatively quickly switch to a second ion source platform, photodetach this second ion beam and subsequently merge the generated neutral particle beam with the prepared stored ions. To facilitate the investigation of low temperature ion-neutral reactions, relevant to astrochemistry, the

center-of-mass collision energy needs to be as low as a few meV. To this end, the transfer beamline must also permit the tuning of the neutral mean-particle energies with a precision in the range of a few electron volts, while suitably tailoring the angular beam spread via emittance cuts.
In experimental studies, where the ion and neutral species differ in mass, it is convenient to utilize separate ion sources, each with a distinct mass analyzing magnet, before finally merging the two beams in the storage ring. Such a system is beneficial in that;

- the sources and respective analyzing magnet parameters can be held constant, thus enabling stable ion generation and mass filtering
- the remaining electrostatic elements can be quickly ($\sim \mu$s) and reliably scaled to the beam energy for transport
- such a system allows for fast switching ($\sim \mu$s) between the two beams using relatively simple merging optical elements.

The kinetic energies required for two velocity-matched particle beams scale with the ratio of their masses. Therefore, the two ion source platforms do not necessarily require the same capabilities. The two ion source platforms are designed for potentials up to 300 kV and 60 kV, respectively. To maximize the absolute velocity in merged-beams experiments, the heavier particle species will be produced on the 300kV ion source platform. To quickly switch between the low (60kV platform) and high (300kV platform) energy beams, with minimal introduction of beam aberrations, a custom 90° cylindrical deflector was designed, simulated and constructed (Sec. 8.3.4).
To fulfill the aforementioned ion transfer conditions, the entire transfer beamline, both the high energy and the low energy sections, were simulated using the MAD X ion-optics transfer matrix program [155]. This program was used to optimize the number, position and size of the ion-optical elements (see Sec. 8.2). More extensive simulations, which also accounted for secondary effects such as for beam aberrations and fringing field effects, were then subsequently conducted using the SIMION ion optics package [156] (see Sec. 8.3). To maintain a maximum pressure in the order of 10^{-11} mbar in front of the CSR, the transfer beamline vacuum pressure was simulated using the VakTrak simulation software [157] and the injection chamber design optimized (see Sec. 10.1).
As this simulation, design, re-simulation and re-design process is a highly iterative

process to match the ion-optics, the vacuum conditions and the construction, only the final design of the transfer line will be presented here.

8.1 Ion source platforms

To generate either positively or negatively charged ion beams with kinetic energies up to 300 keV per charge unit, a custom ion source platform was designed and constructed. A large, 5 m × 5 m, platform area (as shown in Fig. 8.1(a)) was chosen so that a number of independent ion sources could be simultaneously housed in the platform, while providing sufficient clearance to maintain electric potentials up to ±300 kV. Each source sits on a potential, approximately 20 kV, above that of the source platform. After initial shaping, guiding and mass-filtering of the produced ions, as shown in Fig. 8.1(b), the ions are then accelerated out of the platform to their final kinetic energy, via an acceleration stage [158].
Prior to starting with the design of a complete transfer beamline, a section consisting of magnetic elements, taken from the former injection line of the Test Storage Ring (TSR), were assembled in front of the 300 kV platform. This section consists of two 45° bending magnets paired with two magnetic quadrupole doublets. These elements where chosen due to their immediate availability (including their power supply units) and the mass selecting properties provided by the 45° magnets. The initial structural conditions of the CSR facility are illustrated in Fig. 8.2.

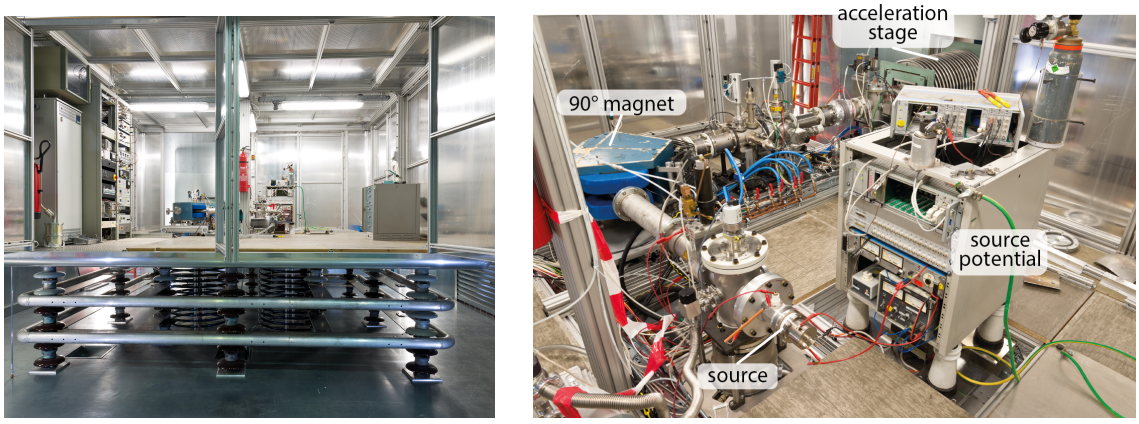

(a) (b)

Figure 8.1: Photographs of the 300 kV ion source platform. The left picture (a) shows the insulated 300 kV ion source platform, which is housed by an enclosed cage. The right picture shows the preliminary beamline on the source platform.

For the low energy platform, a maximum potential of 60 kV was selected. This potential was deemed sufficiently high to fulfill experimental requirements, whilst maintaining a relatively simple source setup. Since ion-neutral reaction studies rely on velocity-matched particle beams, the kinetic energy of the overlapping ions scale with their masses. Therefore, the heavier parent reactant in such reactions can be formed on the 300 kV platform to facilitate this.
Both platforms are envisaged to house a variety of ion sources. The high voltage

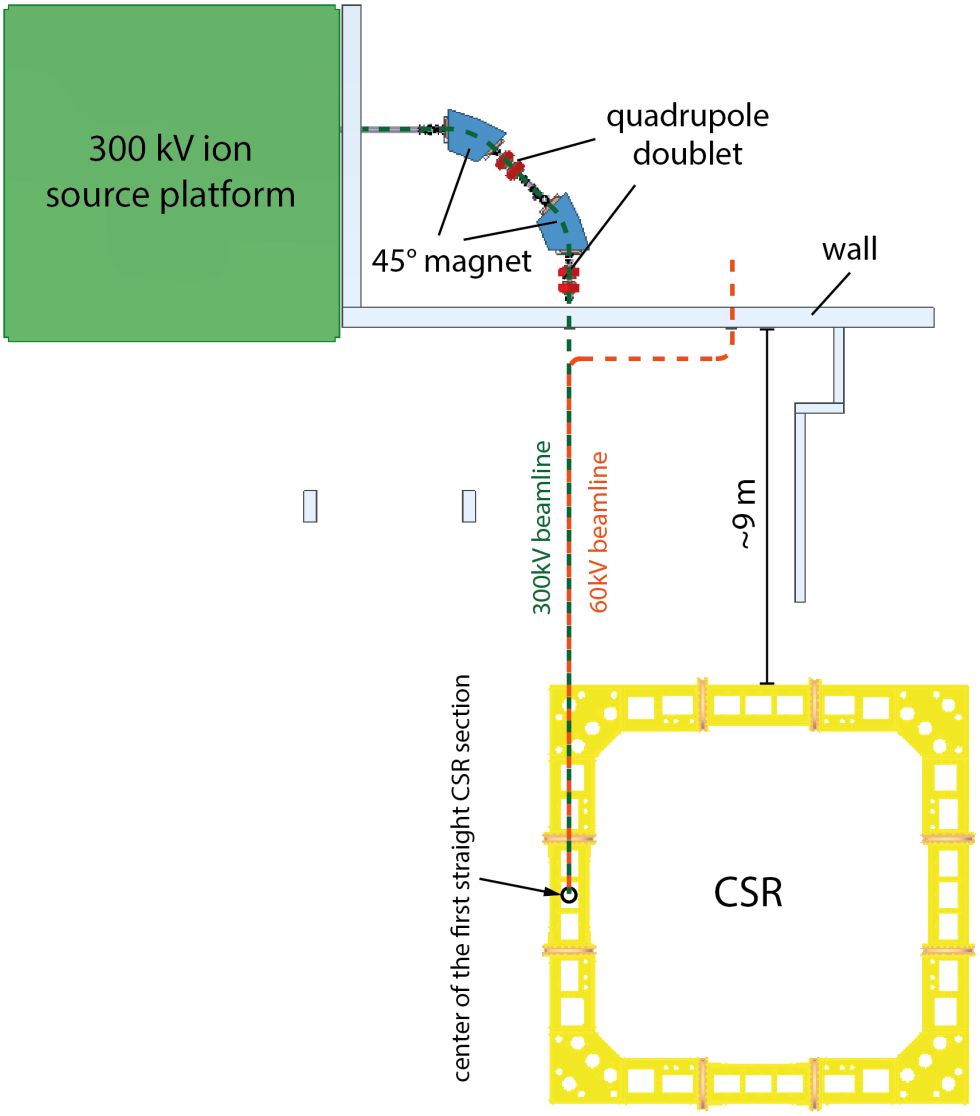

Figure 8.2: Overview of the initial structural conditions of the CSR facility. The planned ion beam paths to the center of the first straight CSR section are indicated by the dashed lines. The green dashed line denotes the path of the 300kV beamline. The path along the 60kV beamline is represented by the orange dashed line.

platform, as mentioned previously, is capable of housing a number of sources simultaneously, while the low voltage platform should be designed in a way that its source can be exchanged relatively quickly. A few of the sources currently designated or under development are:

- Metal Ion Sputter Source (MISS)
- Duoplasmatron Source
- Penning Source
- Electron Cyclotron Resonance (ECR) Source
- Supersonic Expansion Source
- Laser Vaporization (LVAP) Source
- Electrospray Ionization (ESI) Source
- Electron Beam Ion Trap (EBIT)
- 22pole Trap (see Sec. 3.3).

8.2 Beam transport systems

The designs for the CSR transfer line were calculated using the ion-optics transfer matrix program MAD X (Methodical Accelerator Design) [155]. In these simulations, the ion-optical elements are described by first order transfer matrices, as discussed in Sec. 6.2. The transport matrices of the ion-optical elements utilized in the final design for the CSR transfer line are presented in Appendix C. The final design is the result of an iterative process in order to optimize the type, number, locations and size of ion-optical elements and monitors, while still meeting the stringent requirements demanded of the transfer line. The most critical requirements of the transfer line are:

- Delivery of a well- defined mass selected ion beam
- Transporting ion beams with kinetic energies of up to 300 keV per charge unit
- The ion-optical elements do not exceed a maximum voltage of 10 kV

- Merging two beamlines
- Fit to existing infrastructure and space restrictions (see Fig. 8.2)
- Neutral beam generation via photodetachment section (∼3 m) of either beamline
- Fast switching (μs) ion-optics in the merged part of the transfer line
- Differential pumping sections to fulfill the vacuum requirements
- Matching the machine twiss parameter of the storage ring

Overall, the inherent properties of electrostatic ion-optical elements are preferential for the transport system of the CSR, with the exception of the mass selecting dipole magnets (Sec. 8.3.1). Electrostatic ion-optics possess some superior traits when compared to magnetic elements, e.g. they are capable of fast switching of their field strengths without hysteresis, an essential feature for the CSR transfer line. Thus changing the ion species of the source, while maintaining the kinetic energy, requires no adjustment of the electrostatic elements.
The ion-optical elements, which are utilized in the final design of the transfer line are discussed in detail in Sec. 8.3. A maximum of 10 kV was chosen for all ion-optical elements of the transfer line. In this regime, there are significant gains in terms of required plate clearance (to avoid electrical breakdown), cost and complexity of the ion-optical elements, relative to higher potentials. The required field strength of an electrostatic element of a certain length, allows the required voltages to transport both a 60 keV/q and 300 keV/q ion beam, discussed further in Sec. 8.3.3.
In order to merge the 60 kV and 300 kV beamline, a μs fast-switching 90° deflector with a hole was designed (see Sec. 8.3.4 for further information). The 90 degree deflector is designed as such that when both the inner and outer electrodes are grounded, an ion beam from the 300 kV platform can pass straight through the hole in the outer electrode, into the injection beamline. In this configuration the deflector acts as a drift section. When both electrode potentials are switched on, a beam with the correct energy-to-charge ratio from the 60kV beamline, is deflected by 90 degrees and merged into the injection beamline.
The beam envelope $u_{max}(s)$, can be related to the betatron function $\beta(s)$ and the emittance ϵ by $u_{max}(s) = \sqrt{\epsilon\beta(s)}$, as defined in Sec. 6.3. Therefore, for a given emittance, the aperture clearance and beam pipe diameters can limit the beam transfer.

The ideal positions of necessary constrictions (e.g. apertures, slits or differential pumping sections) should be calculated with respect to the beamline's betatron function $\beta(s)$.
Several monitors must also be implemented in the design of the transfer line in order to analyze the current, position or shape of the ion beam (see Sec. 8.3.2). It is convenient to position these monitors in a beam waist, where $\beta(s)$ has a local minimum (i.e. $\alpha = 0$). This simplifies the practical tuning of the ion-optical elements, when guiding ion beams in the laboratory environment.
During injection of the ion beam into the CSR, it is important to match the twiss parameter of the injected ion beam to the machine parameters, as discussed in Sec. 7.3. A mismatch can lead to a filamentation of the phase space distribution, which increases the effective emittance of the stored ion beam [137]. Unlike a single pass beamline, where the ion beam passes the ion-optical elements once, small non-linear field contributions are compounded in storage rings, due to the high number of revolutions.

8.2.1 300 kV beamline

The 300 kV ion source platform is currently undergoing development to include a series of advanced sources. For the preliminary source design, used during the first experimental measurements at the CSR, the twiss parameters of a beam emerging from the accelerator stage of the 300kV platform were calculated as $\beta_x = 0.28$ m, $\beta_y = 0.45$ m, $\alpha_x = \alpha_y = 0$ ($s = 0$ in Fig. 8.3) [159].
These twiss parameters are then used in the MAD X simulation for the final ion-optical design of the 300kV beamline. After the optimization process of the size, position and number of utilized ion-optical elements and monitors, with special compensation for the beamline requirements, the final ion-optical design and resulting betatron functions β_x(s) and β_y(s) of the 300kV beamline are shown in Fig. 8.3. In this figure, two 45° dipole magnets (represented by the blue boxes) provide the charge-to-mass separation of the ion beam (discussed further in Sec. 8.3.1). After passing the first magnet, the ion beam is focused by a quadrupole doublet, QP1, which forms a beam waist at monitor 1. Similarly, the quadrupole doublet, QP2, focuses the ion beam onto monitor 2, which is positioned prior to merging of the two beamlines via a 90° deflector with hole (see Sec. 8.3.4). For the 300kV beamline, the ion beam nominally passes the grounded 90° deflector, through the hole of its

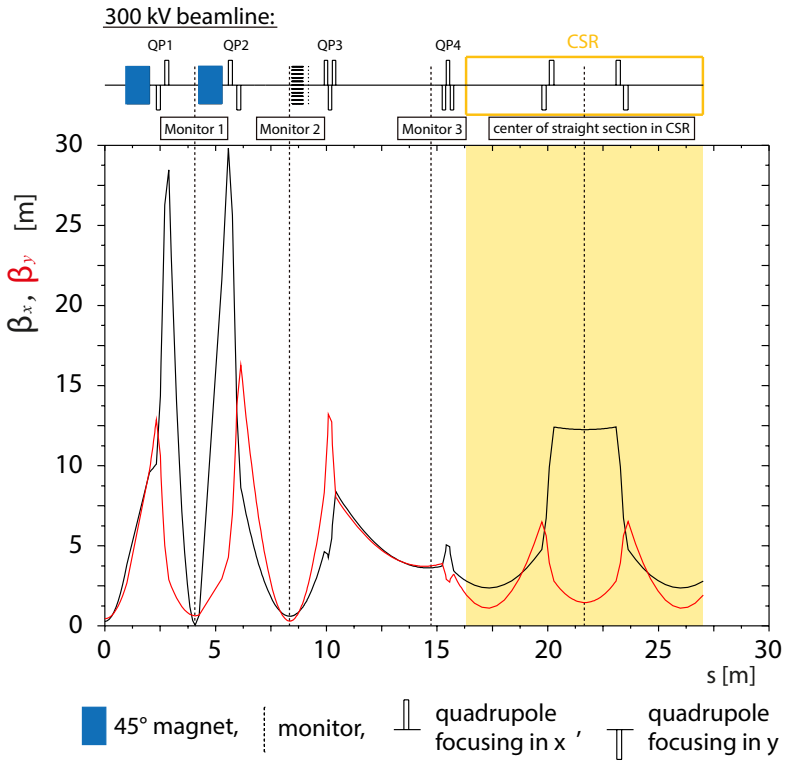

Figure 8.3: Horizontal (x) and vertical (y) betatron function of the 300 kV beamline, simulated via MAD X. In this configuration the 90° deflector is grounded and acts as a drift section. The CSR is highlighted by the yellow area.

outer electrode, in this instance the merging section acts as a drift. In Fig. 8.3, the location of its projection onto the 300kV beamline is represented by a green box. The subsequent elements are then shared by both the 300kV and the 60kV beamline. The quadrupole triplet, QP3, focuses the beam onto monitor 3. The distance between QP3 and QP4 of ∼4.5 m, is kept free of ion optics, for the eventual integration of the photodetachment section (discussed in Chap. 9). In this section, the ion beam is circularly symmetric, preferential for optimizing the ion beam transmission, when the beam is collimated by a pair of round apertures.

The quadrupole triplet QP4 is tuned in order to match the machine parameters of the CSR (discussed in Sec. 7.3). The quadrupole doublets inside the CSR during standard operation are set to K_o = 5.5 m^{-2} and K_i = -6.9 m^{-2}. The twiss parameters of the injected beam are tuned to match the ring parameters at the center of straight section (i.e. β_x = 12.4 m, β_y = 1.4 m and $\alpha_x = \alpha_x = 0$). The strength, K, of the quadrupoles in this simulation are optimized to generate a beam waist (α_x = 0 and $\alpha_y = 0$) at the monitor positions prior to matching the machine parameters in

Quadrupole	QP1 (doublet)	QP2 (doublet)	QP3 (triplet)	QP4 (triplet)
K [m^{-2}]	-10.5 / 11.4	10.0 / -9.9	8.9 / -22.6 / 14.2	-9.5 / 18.1 / -10.0

Table 8.1: Required quadrupole strengths (K) for the ion beam transport in the 300 kV beamline. The labeling corresponds to Fig. 8.3. A positive (negative) quadrupole strength indicates horizontal (vertical) focusing.

Twiss parameter	β_x [m]	β_y [m]	α_x	α_y
Initial	0.28	0.45	0	0
Monitor 1	0.05	0.64	$-2{\cdot}10^{-4}$	$2{\cdot}10^{-5}$
Monitor 2	0.61	0.30	$4{\cdot}10^{-8}$	$1{\cdot}10^{-8}$
Monitor 3	3.63	3.73	$-4{\cdot}10^{-3}$	$-4{\cdot}10^{-2}$
Center of straight section of the CSR	12.26 (12.4)	1.46 (1.4)	$-6{\cdot}10^{-4}$ (0)	$-5{\cdot}10^{-4}$ (0)

Table 8.2: Calculated twiss parameters of the 300kV beamline at the position of the monitors and in the center of the straight section of the CSR. The labeling corresponds to Fig. 8.3. The CSR machine parameters in the center of a straight section are given in brackets.

the center of the straight section in the CSR. These quadrupole strengths are listed in Tab. 8.1. The resulting twiss parameters at the position of the monitors and in the center of the straight CSR section are summarized in Tab. 8.2. The beam waists achieved, at the monitor positions are evident from the values of α_x and α_y. The twiss parameters of the ion beam are in good agreement with the matched machine parameters in the center of a straight section in the CSR. The relatively small difference between the betatron functions, lead to only a minor increase in the effective emittance, which can be calculated for a perfect beam waist ($\alpha_x = \alpha_y = 0$). If the machine parameter β_{CSR} is greater than the twiss parameter β_{beam} of the injected ion beam, the effective phase space ellipse satisfies

$$u'_{\mathrm{max}} = \sqrt{\frac{\epsilon_{\mathrm{beam}}}{\beta_{\mathrm{beam}}}} = \sqrt{\frac{\epsilon_{\mathrm{CSR}}}{\beta_{\mathrm{CSR}}}}\,, \tag{8.1}$$

where u'_{max} is the maximum angle in either the x or y direction, leading to an effective emittance of the stored ion beam ϵ_{CSR} of

$$\epsilon_{\mathrm{CSR}} = \frac{\beta_{\mathrm{CSR}}}{\beta_{\mathrm{beam}}} \epsilon_{\mathrm{beam}} \,. \tag{8.2}$$

For $\beta_{\mathrm{beam}} > \beta_{\mathrm{CSR}}$, the effective phase space ellipse expands to

$$u_{\mathrm{max}} = \sqrt{\epsilon_{\mathrm{beam}} \beta_{\mathrm{beam}}} = \sqrt{\epsilon_{\mathrm{CSR}} \beta_{\mathrm{CSR}}} \,, \tag{8.3}$$

where u_{max} is the maximum beam width in either the x or y direction, yielding

$$\epsilon_{\mathrm{CSR}} = \frac{\beta_{\mathrm{beam}}}{\beta_{\mathrm{CSR}}} \epsilon_{\mathrm{beam}} \,. \tag{8.4}$$

The horizontal and vertical phase space ellipse of the injected ion beam (twiss parameters are listed in Tab. 8.2), that have an emittance of $\epsilon_{\mathrm{beam}} = 30$ mm mrad are represented by the blue lines in Fig. 8.4. The effective phase space ellipses are indicated by the red lines. The increased horizontal and vertical emittances $\epsilon_{x,\mathrm{CSR}}$ and $\epsilon_{y,\mathrm{CSR}}$, which are induced by the mismatch to the machine parameters, are calculated using Eq. 8.2 and Eq. 8.4, respectively. As a result, the emittance of the

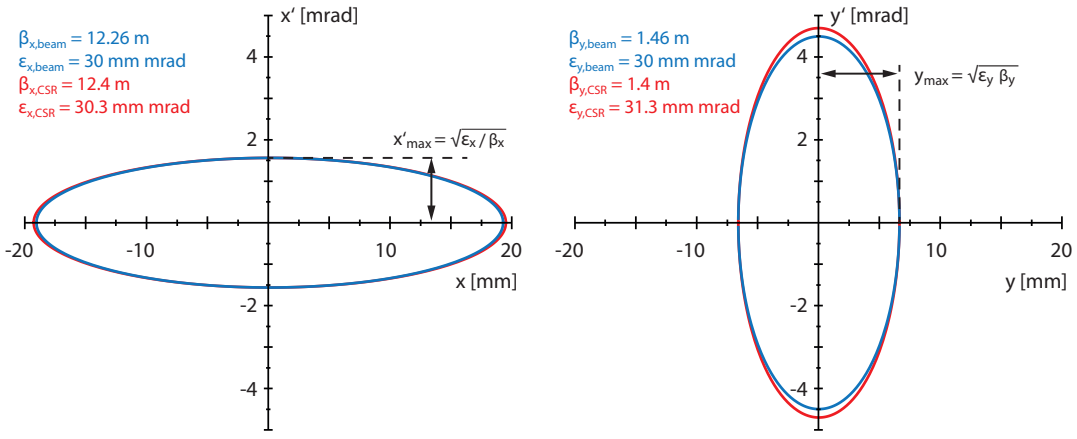

Figure 8.4: The blue lines indicate the horizontal (x) and vertical (y) phase space ellipse of an injected ion beam with an emittance of $\epsilon_{\mathrm{x,beam}} = \epsilon_{\mathrm{y,beam}} = 30$ mm mrad, in the center of a straight section of the CSR, representing the twiss parameters $\beta_{x,\mathrm{beam}} = 12.26$ m and $\beta_{y,\mathrm{beam}} = 1.46$ m ($\alpha_{\mathrm{x,y}} = 0$). The mismatch of the machine parameters ($\beta_{x,\mathrm{CSR}} = 12.4$ m, $\beta_{y,\mathrm{CSR}} = 1.4$ m) leads to the effective emittances $\epsilon_{x,\mathrm{CSR}}$ and $\epsilon_{y,\mathrm{CSR}}$, which are determined by Eq. 8.2 and Eq. 8.4, respectively. These resulting phase space ellipses are indicated by the red lines.

stored ion beam is increased horizontally by a factor $\frac{12.4}{12.26} \approx 1.01$, and vertically by a factor $\frac{1.46}{1.4} \approx 1.04$. These estimations assume a perfect match of the twiss parameters α_x and α_y, while mismatching β_x and β_y. An additional mismatch in α would cause a greater filamentation effect, leading to a major increase in the effective emittance [137].

The betatron functions $\beta(s)$ along the beamline (shown in Fig. 8.3) contains information of the beam size, dependent on the beam emittance, as discussed in Sec. 6.3. According to Eq. 6.50, the size of the beam envelope can be calculated using $u_{max}(s) = \sqrt{\epsilon\beta(s)}$. Assuming a beam emittance of $\epsilon_x = \epsilon_y = 30$ mm mrad, the horizontal (x) and vertical (y) beam width as a function of the propagation along the 300kV beamline is shown in Fig. 8.5. Both the horizontal and vertical beam size reach a maximum within the second quadrupole doublet (QP2). For an ion beam with an emittance of $\epsilon_{x,y} = 30$ mm mrad, the maximum horizontal and vertical beam

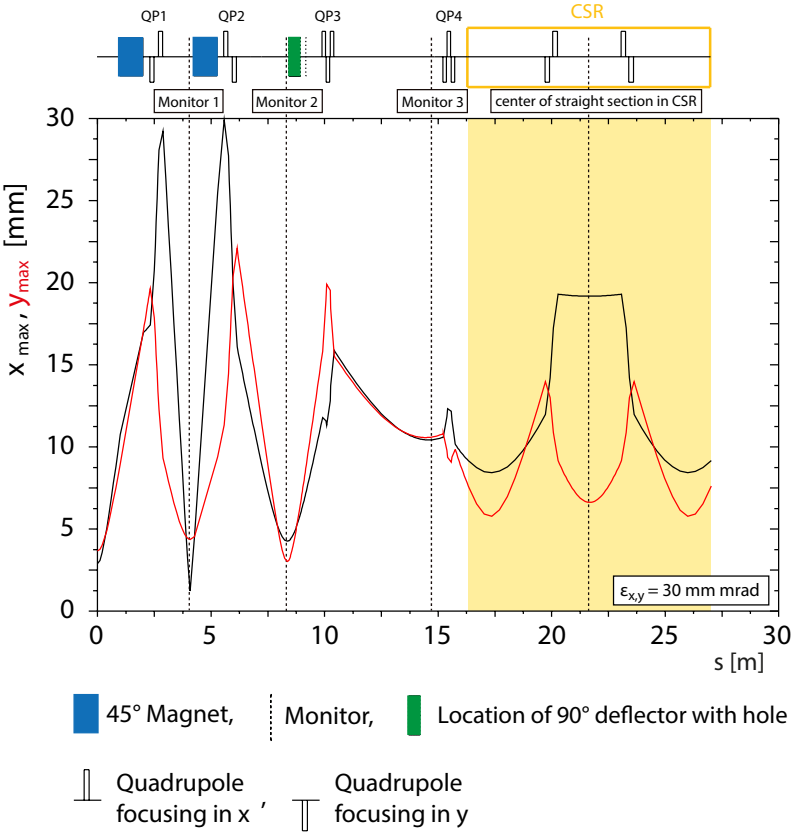

Figure 8.5: Horizontal (x) and vertical (y) beam size along the 300 kV beamline, assuming a beam emittance of $\epsilon_x = \epsilon_y = 30$ mm mrad. The beam widths, $x_{\max}$ and $y_{\max}$, as a function of the path s along beamline are calculated via Eq. 6.50 using the betatron functions β_x(s) and β_y(s) shown in Fig. 8.3.

width is calculated as $x_{\max} \approx 30$ mm and $y_{\max} \approx 22$ mm, respectively.
The maximum emittance, where an ion beam is transported loss-free into the CSR, the so-called acceptance of the beamline, can be calculated similarly. As the geometry of quadrupole doublet QP2 represents the bottleneck for the ion beam transport of the 300kV beamline, the acceptance ($A_{x,300\text{kV}}$, $A_{y,300\text{kV}}$) is defined by its pipe dimensions and the betatron functions in this location. The pipe aperture of QP2 has an inner radius of $r_p = 35$ mm, in which the betatron functions have a peak value of $\beta_{\text{x,max}}(\text{QP2}) \approx 30$ m and $\beta_{\text{y,max}}(\text{QP2}) \approx 17$ m. Using Eq. 6.50, the horizontal and vertical geometrical acceptance of the 300kV beamline is given by

$$A_{x,300\text{kV}} = \frac{r_p^2}{\beta_{\text{x,max}}(\text{QP2})} \approx 41\,\text{mm mrad}\,, \tag{8.5}$$

$$A_{y,300\text{kV}} = \frac{r_p^2}{\beta_{\text{y,max}}(\text{QP2})} \approx 72\,\text{mm mrad}\,. \tag{8.6}$$

In the ion-optical simulation, the design of the 300kV beamline was optimized to match the twiss parameters at the respecting monitors and the machine parameters of the CSR, while accounting for ion beam transmission. The large acceptance of the CSR ($A_{x,\text{CSR}} = 120$ mm mrad, $A_{y,\text{CSR}} = 180$ mm mrad), presented in Sec. 7.3, allows for a mismatching of the transported ion beams to the CSR machine parameters. Dependent on the initial emittance of the ion beam, which is generated on the source platform, and the extent of its mismatch to the CSR machine parameters, the ion beam with an increased phase space can be still stored loss-free in the CSR. The expanded phase space of the stored ion beam, caused by mismatching, can be afterwards compressed using the CSR electron cooler [143].

8.2.2 60 kV beamline

A second beamline, which is designed for the alternative injection of an ion beam into the CSR, begins with an ion source platform, which can maintain electric potentials of up to ±60 kV. This 60 kV beamline has to fulfill the same requirements, that are discussed in the previous Sec. 8.2 for the 300kV beamline. The path of the ion beam along the 60kV beamline is indicated in Fig. 8.2 by the orange dashed line. For the MAD X simulations of the ion beam transport along the 60kV beamline, it is convenient to assume that the ion source output is a circularly symmetric beam (due to the cylindrical symmetry of most ion sources). The ion-optical element, which is usually attached as a part of the ion source (i.e. einzel lens), can generate a beam

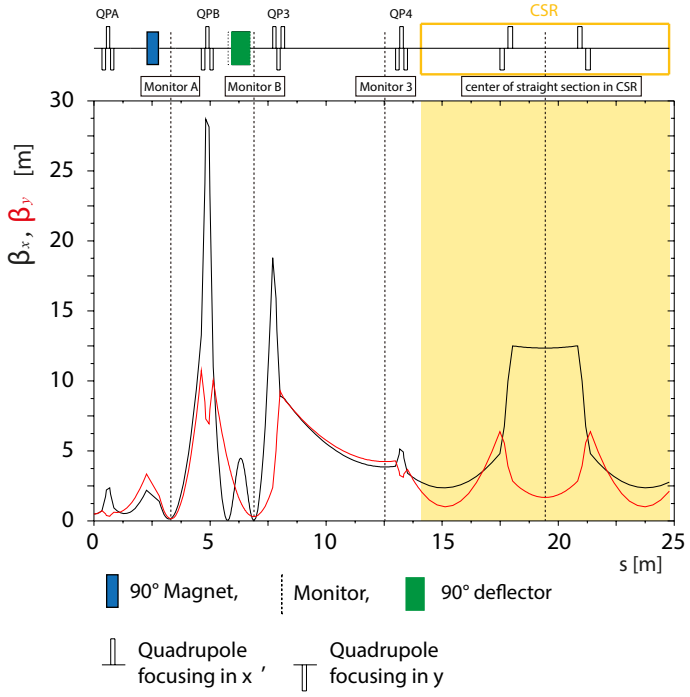

Figure 8.6: Horizontal (x) and vertical (y) betatron function of the 60 kV beamline, simulated via MAD X. The location of the CSR is marked by the yellow area.

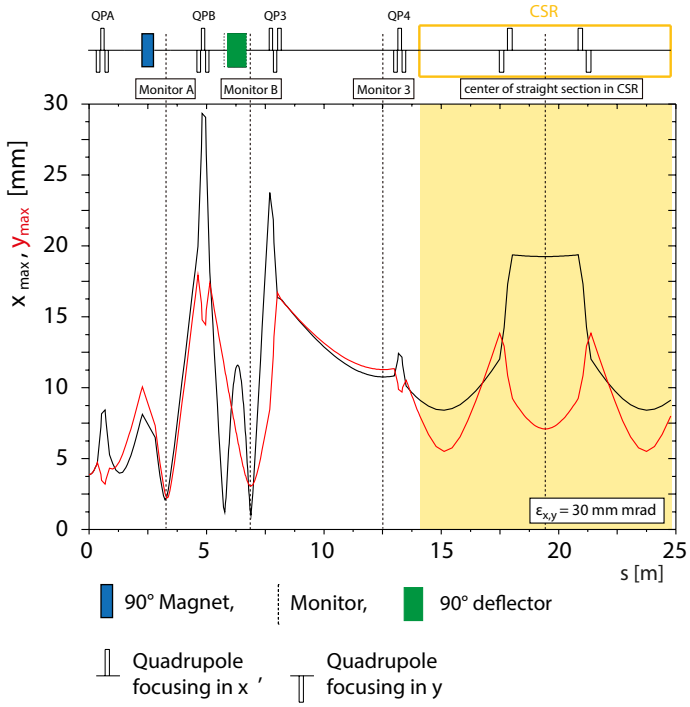

Figure 8.7: Horizontal (x) and vertical (y) beam size along the 60 kV beamline, assuming a beam emittance of $\epsilon_x = \epsilon_y = 30$ mm mrad. The beam widths, $x_{\max}$ and $y_{\max}$, as a function of the path s along beamline are calculated via Eq. 6.50 using the betatron functions β_x(s) and β_y(s) shown in Fig. 8.6.

waist at a position s_0 after extraction. Therefore, the starting twiss parameters for the MAD X simulations are selected so that $\beta_x = \beta_y = 0.5$ m and $\alpha_x = \alpha_y = 0$.
The final ion-optical design of the 60kV beamline consists a double-focusing 90° dipole magnet, which provides the mass separation of the ion beam (discussed in Sec. 8.3.1), a cylindrical 90° deflector with a hole to merge the two beamline (discussed in Sec. 8.3.4) and four electrostatic quadrupole triplets, focusing the ion beam (discussed in Sec. 8.3.3). The resulting betatron functions β_x(s) and β_y(s), together with the ion-optical concept, are shown in Fig. 8.6. The strength of the first quadrupole triplet (QPA) is optimized to create a beam waist at monitor A, which is located at a distance of twice the radius of the 90° magnet. Subsequently, the quadrupole triplet QPB focuses the ion beam onto monitor B, which is placed after the 90° deflector. The position of the cylindrical 90° deflector, which focuses

Quadrupole	K [m^{-2}]
QPA	-30.0 / 43.0 / -23.5
QPB	-19.9 / 35.5 / -17.2
QP3	23.2 / -20.3 / 0.9
QP4	-8.7 / 17.6 / -10.2

Table 8.3: Required quadrupole strengths (K) for the ion beam transport in the 60 kV beamline. The labeling of the quadrupole triplets corresponds to Fig. 8.6. A positive (negative) quadrupole strength indicates a horizontal (vertical) focusing.

Twiss parameter	β_x [m]	β_y [m]	α_x	α_y
Initial	0.5	0.5	0	0
Monitor A	0.64	0.38	$-4{\cdot}10^{-1}$	$1{\cdot}10^{-1}$
Monitor B	0.04	0.31	$1{\cdot}10^{-7}$	$6{\cdot}10^{-7}$
Monitor 3	3.86	4.24	$-4{\cdot}10^{-7}$	$2{\cdot}10^{-7}$
Center of straight section of the CSR	12.35 (12.4)	1.68 (1.4)	$-8{\cdot}10^{-4}$ (0)	$-6{\cdot}10^{-4}$ (0)

Table 8.4: Calculated twiss parameters of the 60kV beamline at the position of the monitors and in the center of the straight section of the CSR. The labeling corresponds to Fig. 8.6. The CSR machine parameters in the center of a straight section are given in brackets.

the ion beam horizontally, is indicated by the green box in Fig. 8.6. Beyond this point, the ion-optical elements (QP3 and QP4) and monitor 3 is shared with the 300kV beamline (discussed in the previous Sec. 8.2.1). The quadrupole triplet QP3 creates a beam focus at the position of monitor 3. Finally, the strength of quadrupole triplet QP4, which is located in front of the CSR, is optimized in order to match the machine parameters (β_x = 12.4 m, β_y = 1.4 m and $\alpha_x = \alpha_x = 0$) in the center of a straight CSR section. The quadrupole strengths, which are required in this beamline simulation, to optimize the ion beam transport are listed in Tab. 8.3. The resulting twiss parameters of the ion beam at the starting position, at the positions of the monitors and in the center of the first straight CSR section are summarized in Tab. 8.4. The small values of α_x and α_y (≈ 0) demonstrate the prevalence of a beam waist at the dedicated positions.

According to Eq. 6.50, the horizontal and vertical beam width can be calculated for any given beam emittance as a function of β_x and β_y, respectively. Assuming a beam emittance $\epsilon_{\mathrm{x,beam}} = \epsilon_{\mathrm{y,beam}}$ = 30 mm mrad, the the horizontal and vertical beam widths ($x_{\max}$, $y_{\max}$) are illustrated in Fig. 8.7 along the beam path (s). The maximum beam size is located in quadrupole triplet QPB, where the ion beam horizontally attains a beam width of $x_{\max} \approx 29$ mm, and vertically a beam width of $y_{\max} \approx 18$ mm.

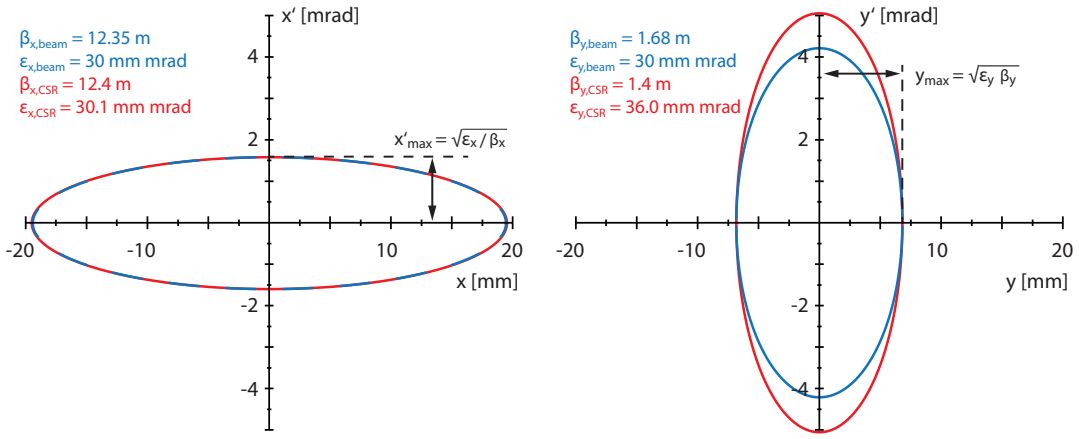

Figure 8.8: The blue lines indicate the horizontal (x) and vertical (y) phase space ellipse of an injected ion beam with an emittance of $\epsilon_{\mathrm{x,beam}} = \epsilon_{\mathrm{y,beam}}$ = 30 mm mrad, in the center of a straight section of the CSR, representing the twiss parameter $\beta_{x,\mathrm{beam}}$ = 12.35 m and $\beta_{y,\mathrm{beam}}$ = 1.68 m ($\alpha_{\mathrm{x,y}} = 0$). The mismatch of the machine parameters ($\beta_{x,\mathrm{CSR}}$ = 12.4 m, $\beta_{y,\mathrm{CSR}}$ = 1.4 m) leads to the effective emittances $\epsilon_{x,\mathrm{CSR}}$ and $\epsilon_{y,\mathrm{CSR}}$, which are determined by Eq. 8.2 and Eq. 8.4, respectively. These resulting phase space ellipses are indicated by the red lines.

Similarly to that previously discussed for the 300kV beamline, the matching of the beam's twiss parameter to the machine parameter is in relatively good agreement. Again, due to the small mismatch in the betatron functions β_x and β_y, can be calculated via Eq. 8.2 and Eq. 8.4, respectively. The horizontal and vertical phase space ellipses of an injected ion beam with an emittance of $\epsilon_{\mathrm{x,beam}} = \epsilon_{\mathrm{y,beam}} = 30$ mm mrad and of the stored ion beam with the effective emittances $\epsilon_{\mathrm{x,CSR}}$ and $\epsilon_{\mathrm{y,CSR}}$ are shown in Fig. 8.8. Using the calculated twiss parameters (see Tab. 8.4) and machine parameters in Eq. 8.2 and Eq. 8.4, the beam emittance is increased horizontally by a factor of $\frac{12.4}{12.35} = 1.004$, and vertically by a factor of $\frac{1.68}{1.4} = 1.2$.
In the ion-optical design of the 60kV beamline, which is shown in Fig. 8.6, the maximal emittance that is transported through this beamline, is limited by the dimensions of the quadrupole triplet QPB. In this electrostatic quadrupole design (discussed in Sec. 8.3.3), the electrodes are separated by a distance of 60 mm. The maximum horizontal and vertical value of the betatron function, inside the quadrupole lens, is given by $\beta_{\mathrm{x,max}}(\mathrm{QPB}) \approx 29$ m and $\beta_{\mathrm{y,max}}(\mathrm{QPB}) \approx 11$ m. Similarly to Eq. 8.5 and Eq. 8.5, the acceptance of the 60kV beamline can be estimated to

$$A_{x,60\mathrm{kV}} = \frac{r_e^2}{\beta_{\mathrm{x,max}}(\mathrm{QPB})} \approx 31\,\mathrm{mm\,mrad}\,, \tag{8.7}$$

$$A_{y,60\mathrm{kV}} = \frac{r_e^2}{\beta_{\mathrm{y,max}}(\mathrm{QPB})} \approx 82\,\mathrm{mm\,mrad}\,, \tag{8.8}$$

where r_e denotes the maximum beam width of 30 mm, which is transmitted through the quadrupole triplet QPB.
In this ion-optical simulation of the 60kV beamline, the number, size and positions of the ion-optical elements and the beam monitor positions were optimized for ion beam transport and for matching the beam's twiss parameters to the CSR machine parameters. As demonstrated in Fig. 8.6 and Tab. 8.4, the twiss parameter of the transported beam can be matched in good agreement with the CSR machine parameters, while creating a beam waist at the respecting monitors.

8.3 Elements of the beamlines

The layout of the CSR transfer line, as simulated in Sec. 8.2 using MAD X, is illustrated in Fig. 8.9. The ion path along each of the two beamlines, i.e. the 60kV (see Fig. 8.6) and the 300kV beamline (see Fig. 8.3), are represented by an

orange and green dashed line, respectively. In this overview, the positions of the dipole magnets are indicated by the blue areas, the quadrupoles are represented by red lines and the monitors are depicted as black dashed lines. The monitors and the quadrupoles are labeled using the same nomenclature as that in the MAD X simulations.

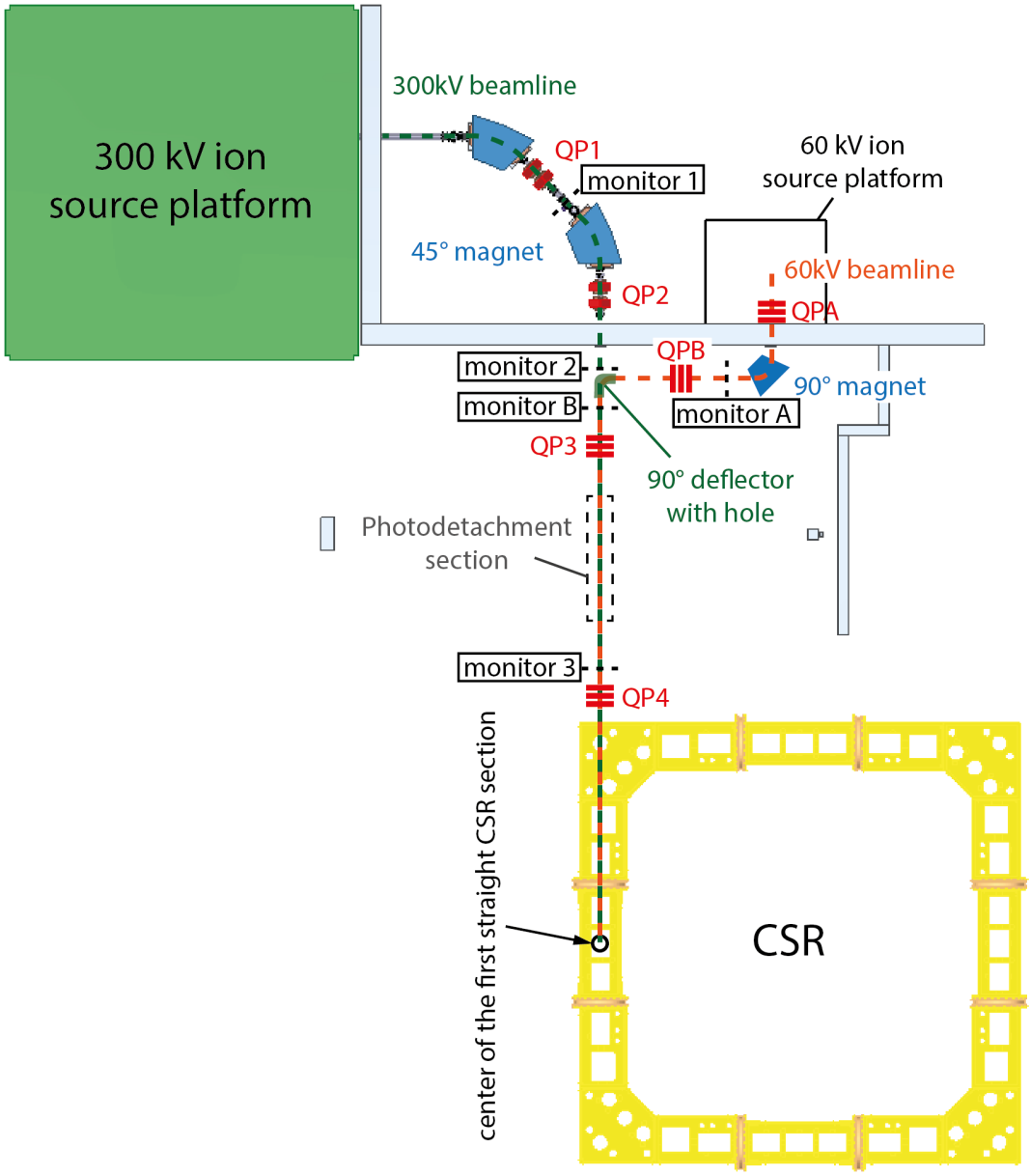

Figure 8.9: Schematic overview of the CSR transfer line, as calculated in Sec. 8.2 using MAD X. The positions of the ion-optical elements of the two beamlines are indicated by blue area: dipole magnet, red line: quadrupole, black dashed line: monitor. The labeling of the elements has the same nomenclature as that in the MAD X simulations.

This section discusses in detail the elements which are utilized for the final design of the CSR transfer line. This includes the dipole magnets, which filter the desired ion species, the monitors for beam diagnostics, the focusing electrostatic quadrupoles and the electrostatic 90° deflector with a hole to merge the two beamlines.

8.3.1 Dipole magnets

As the CSR is capable of storing ions irrespective of mass, it is necessary for the transfer line to first mass-filter the ion beam prior to injection. In general, most ion sources produce impure ion beams, i.e. a mixture of varying charge states and masses. These ion beam impurities, which are mainly due to contamination of the source (e.g. residual gas, impure surface), have to be filtered from the extracted beam prior to conducting experiments. In the CSR transfer line, dipole magnets are used in order to select a specific ion species by its mass-to-charge ratio.
The 90° dipole magnet, which is integrated in the 60kV beamline, has a bending radius of 0.35 m and a gap of 50 mm. The pole faces of this double-focusing magnet are rotated by 26.5° with respect to the ion beam trajectory. These factors have been taken into account in the previous MAD X calculations. For a mono-energetic beam traversing a homogeneous magnetic field B, the ions follow a curved path of a radius ρ. This path radius is related to the charge (q) and mass (m) of the ion, derived from equating the Lorentz force and the centrifugal force, leading to

$$m = \frac{(B\rho)^2 q^2}{2E_{\mathrm{kin}}}\,, \tag{8.9}$$

where E_{kin} denotes the kinetic energy of the ion. All ions with suitable charge-to-mass ratios, which are still transported through the magnet volume, can be further discriminated via slits, ideally positioned in the beam focuses before and after the magnet.
As the maximum field of this 90° magnet is limited to $B_{\mathrm{max}} = 0.95$ T (i.e yielding a maximum rigidity $(B\rho) \approx 0.33$ Tm), the highest ion mass that can be guided along the central path of the magnet, can be calculated from Eq. 8.9. For a maximum applied potential of 60 kV on the ion source platform, singly charged ions with masses up to ∼89 amu can be transported. In Fig. 8.10(a), the mass limit of the 90° magnet is shown for a singly charged ion as a function of its kinetic energy, according to Eq. 8.9.
An ion beam, which is generated on the 300kV platform, is guided by two 45° dipole

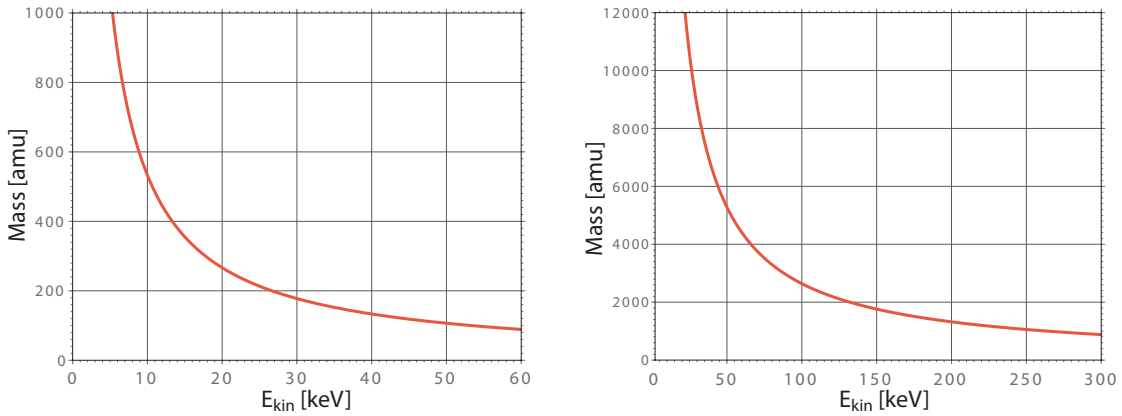

(a) (b)

Figure 8.10: Calculated mass limit for the two beamlines as a function of the kinetic energy (E_{kin}) of singly charged ions: Diagram (a) shows the mass limit of the 90° dipole magnet in the 60kV beamline. In diagram (b), the mass limit for the two 45° magnets in the 300kV beamline is depicted.

magnets, each with a bending radius of 1.3 m. Within the 50 mm magnet gap, a maximum field of $B_{\text{max}} = 1.8$ T can be applied, giving the maximum rigidity of $(B\rho) = 2.34$ Tm. Thus, the mass limit for transporting singly charged ions can be depicted by Fig. 8.10(b) as a function of the kinetic energy E_{kin}. For singly charged ions, possessing the maximum kinetic energy of 300 keV, the 45° magnets provide the transport of masses up to 880 amu. This mass range is sufficient for experiments involving atomic and molecular ions, or clusters.

For experimental studies investigating heavier particles, e.g. bio-molecules, which have a mass of several 1000 amu, the 300kV beamline can be upgraded by an electrostatic 90° deflector. Both of the 45° dipole magnets possess a straight line port, through which ions can be passed after zeroing the magnetic field. An electrostatic 90° deflector can thus be used to bypass the 45° magnets in order to guide the ions irrespective of mass. In this mode of operation, the ion beam would need to undergo mass-discrimination on the 300kV ion source platform, prior to the acceleration stage.

8.3.2 Monitors

Beam diagnostics are essential for the efficient guiding of ion beams. They are needed to tune the ion-optical elements and thus optimize the beam transport in the transfer line. For this reason, various monitors are utilized to measure the current, transversal position and profile of the ion beam propagating along the beamlines. These beam monitors have to be sensitive for both positively and negatively charged ion beams (pA - mA) with kinetic energies ranging from ∼20 keV to 300 keV.

Faraday cup

A Faraday cup is a relatively simple and robust diagnostic tool, which allows the measurement of absolute ion beam currents, independent on the particle's mass and kinetic energy. As demonstrated in Fig. 8.11, charged ions impinge onto a metal surface (target) and captures or deposit an electron from the bulk target, dependent on the charge state of the ions. The resulting current can then be measured using an ammeter. In order to achieve a high detection accuracy, the secondary electrons that are generated at the target surface have to be recaptured in the target cup. In this Faraday cup design, the secondary electrons are deflected back onto the target cup using a repeller cup. Via this destructive detection technique, in which the beam's charge is measured as a function of time, ion beam currents can be detected down to pA (dependent on the electronics and design of the cup).

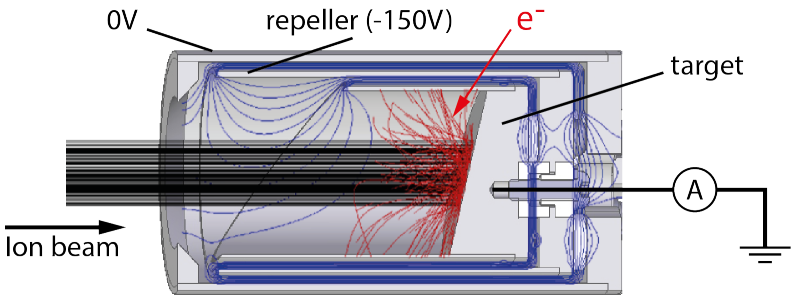

Figure 8.11: Operating principle of a Faraday cup. A positively or negatively charged ion beam (black) impacts on a metal surface, capturing or depositing an electron from the bulk target, which is connected to ground via an ammeter. The secondary electrons (red), which are created by the particle impact, have to be recaptured by the target cup (attached to the bulk target) in order to ensure an accurate current measurement. Therefore, these electrons are prevented from escaping the target cup by applying a negative potential to the repeller.

As Faraday cups are destructive monitors, they are mounted on a pneumatic feedthrough, which moves the cup into the beam path. In combination with horizontal and vertical slits at the entrance of a Faraday cup, the measured transmission of an ion beam as a function of the slits' distance and position contains information of the size and position of the ion beam. Furthermore, slits limiting the horizontal displacement of an ion beam, are placed in the focus after a dipole magnet to limit the transported ion species after the mass-to-charge separation. For this reason, movable slits are placed in each focal point after a dipole magnet in the two beamlines.
To measure the ion beam current along the CSR transfer line, a Faraday cup is placed on the 300kV ion source platform, at monitor A, monitor B and close to monitor 3 (see Fig. 8.9). Parallel to the position of monitor 3, the ion beam can be deflected into a Faraday cup by applying a voltage to an electrostatic parallel plate deflector (discussed in Sec. 9.4).

Beam Profile Monitor

The measurement of a beam profile allows the determination of the size, position relative to the central path and spatial distribution of a particle beam. For the CSR transfer line, a Beam Profile Monitor (BPM)[1], where a rotating wire scans the horizontal and vertical profile of a beam, is placed at several positions. In the 300kV beamline, a BPM is utilized for monitor 1 and monitor 2 (see Fig. 8.9). For the 60kV beamline, a BPM is positioned in the horizontal beam waist in front of the 90° deflector (see Fig. 8.6).
Fig. 8.12(a) shows a photograph of the BPM viewed along the beam axis. The molybdenum wire, which is formed into a 1/8-turn (45°) helix, is mounted on a rotating bar. The rotational axis of this bar is co-linear with the axis of the helix [160]. This special configuration allows the rotating wire to scan the horizontal and vertical beam profiles separately. The supporting bar of the wire is tilted by 45° relative to the beam axis. The rotational motion of the supporting bar creates then an approximately linear motion of the wire in first the x- and then the y-plane.
The signal of this beam profile monitor is generated by secondary electrons, which are ejected from the rotating wire due to particle impact. These electrons, which are collected by an insulated shield surrounding the inner vacuum pipe (shown in Fig. 8.12(a)), are generating the signal. After amplification, the signal can be displayed

[1]National Electrostatics Corporation, Model BPM80

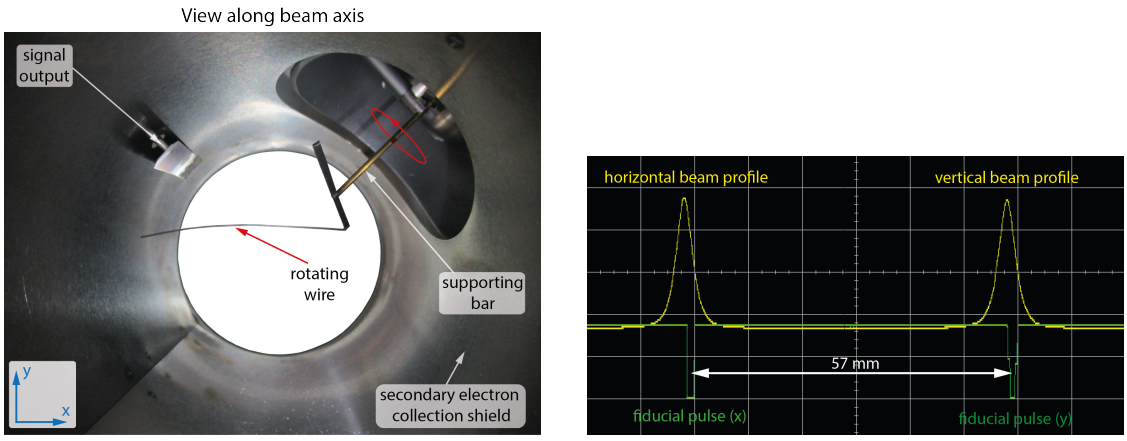

(a) (b)

Figure 8.12: The left picture (a) shows a photograph of a BPM, viewed along the beam direction. A helically shaped wire is mounted on a grounded bar, which rotates. The rotational axis is tilted by 45° relative to the central axis. As the wire moves through a particle beam, secondary electrons are ejected as a function of the wire position. These secondary electrons are collected by an insulated shield, which surrounds the inner vacuum pipe. For the signal output, this shield is contacted via the pin of an electrical feedthrough. The right picture (b) illustrates the amplified signal (yellow line) of the measured secondary electrons, which were generated by an ion beam with a current of ∼4 μA (D^-, 30 keV), displayed on an oscilloscope. The two fiducial pulses (green line) are generated, when the rotating wire passes the horizontal (x) and the vertical (y) axis.

using an oscilloscope as shown in Fig. 8.12(b). The yellow line shows the measured horizontal (x) and vertical (y) profile of a D^- beam with a kinetic energy of 30 keV and a current of ∼4 μA. The beam position relative to the central path is given by the fiducial signals, which are generated by mechanical contacts, inducing an electronic pulse. These pulses, which indicate the position of the wire inside the vacuum pipe, are created when the wire passes the horizontal (x) and the vertical (y) axis. The spatial distance between these pulses is given by the diameter of the helix (d_h = 57 mm for this BPM model). As the supporting bar rotates with a constant angular velocity (driven by a small electromotor), the wire crosses the beam (horizontally and vertically) as a function of the time. The beam profile signals, which are then detected in units of the time, can be converted into a spatial displacement relative to the horizontal and vertical axis. By measuring the time difference (Δt) between the fiducial pulses, the scaling factor is given by d_h/Δt.

The beam profile monitor BPM80 is designed for the profiling of beam's with diameters of up to 25 mm and beam current densities down to 10 nA cm^{-2} [161]. Due to the magnetic coupling of the rotational movement, this device is suitable for

operation at ultra high vacuum, in the order of 10^{-9} mbar.
The secondary electron yield which is generated via particle impacts onto the rotating wire, depends on both the kinetic energy and mass of the particles in a beam. It is for this reason, that the BPM cannnot provide a (direct) quantitative measurement of the ion beam current. Despite this limitation, one of the advantages of this monitor, is that it can non-destructively measure the beam profile. During the beam profile measurement, only a minute fraction of the particle beam impacts onto the 0.5 mm diameter rotating wire. This permits simultaneous measurement of a beam characteristics during propagating along a transfer line; e.g. for the 300kV beamline, the profile of an ion beam can be recorded at monitor 1 and 2, while simultaneously measuring the current at monitor B (see Fig. 8.9).

Beam viewer

The beam viewer, which is implemented in the CSR transfer line at the position of monitor 3 (see Fig. 8.9), can record beam profiles for a wide dynamic range of beam currents and energies [162, 148]. In Fig. 8.13, a CAD drawing of the beam viewer is shown, illustrating its operation principle. A particle beam impinges on an aluminum plate, which is mounted at an angle of 45° relative to the beam axis on a movable pneumatic feedthrough. Secondary electrons are ejected from the aluminum surfaces, which are accelerated in the electrostatic field between the plate and the grid placed in front of it. The aluminum plate holds a potential of -5 kV, which is covered by the grounded grid, so that the electrons travel with a kinetic energy of 5 keV towards a micro-channel plate (MCP) / phosphor screen combination. This combination is mounted plane parallel and centered relative to the aluminum plate, imaging the spatial distribution of the electron cloud generated at the aluminum plate. The MCP (40 mm in diameter) creates an electron cascade avalanche, which multiplies the number of electrons by several orders of magnitude. The front of the MCP is grounded to avoid a deflection of the ion beam prior to impact on the aluminum plate. A +2 kV potential is applied to the rear of the MCP, which is the acceleration voltage of the secondary electrons. These secondary electrons are then accelerated onto a phosphor screen (+5 kV), which is attached to the rear of the MCP. The phosphor screen converts the electrons into photons, which are detected by a camera outside the vacuum chamber. The camera images the phosphor screen at a 45° angle, which generates in the final analysis an image of the ion beam profile

with a spatial resolution of about 1 mm [162].

This monitor for the CSR transfer line has a high sensitivity over a large detection range (1 - 10^{12} particles/s) [148]. Using a phosphor screen with a relatively slow decay time, this destructive measurement allows also the detection of pulsed ion beams. This feature is essential for the use of ion sources, which are only operating in pulsed mode (e.g. 22 pole trap, supersonic expansion source).

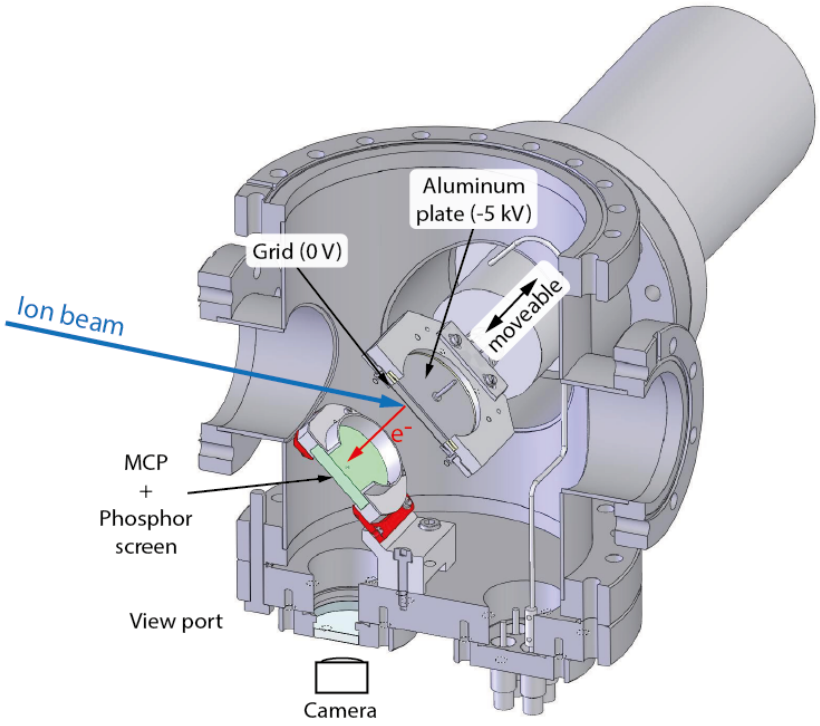

Figure 8.13: CAD drawing of the beam viewer. An aluminum plate at a potential of -5kV, which is covered by ground potential grid, can be moved into the beam axis. An ion beam impacts on the aluminum plate, which is tilted by 45° relative to the beam axis. The secondary electrons, emitted from the aluminum surface, are accelerated in the electrostatic field between aluminum plate (-5 kV) and grid (0 V) onto a MCP. This MCP is mounted plane parallel and centered relative to the aluminum plate. In order to not affect the transported ion beam, the front of the MCP is grounded. The electrons, emitted by the aluminum plate, impact with an kinetic energy of 5 keV onto the MCP, creating further secondary electrons. Applying a positive potential of +2 kV at the MCP's back, the number of electrons are gained by several orders of magnitude. A phosphor screen (+5 kV), directly attached to the MCP's back, converts these electrons into photons, which are recorded by a camera.

8.3.3 Electrostatic quadrupole triplet

An ideal electrostatic quadrupole lens consists of four identical infinitely long hyperbolic electrodes, each placed equidistant from the central path. The voltages applied to the electrodes are equal in magnitude with an alternating sign. The resulting potential distribution between the electrodes is defined by

$$\Phi(x, y) = \frac{U_0}{R_0^2}(x^2 - y^2)\,, \tag{8.10}$$

where U_0 denotes the voltage applied to the electrodes and R_0 represents the bore radius (half distance between the opposing electrode tips). The force acting on a charged particle, moving in the electric field, $\mathbf{E} = -\nabla\Phi$, is determined by the Lorentz force, as discussed in Sec. 6.1. Similar to the approach used for a particle influenced by a magnetic field, as previously demonstrated in Sec. 6.1, the homogeneous differential equations:

$$x''(s) + \frac{qU_0}{E_{\text{kin}}R_0^2}x(s) = 0\,, \tag{8.11}$$

$$y''(s) - \frac{qU_0}{E_{\text{kin}}R_0^2}y(s) = 0\,, \tag{8.12}$$

can be derived from Eq. 8.10. Where q and E_{kin} denotes the electrical charge and the kinetic energy of a particle, respectively. Using the quadrupole strength, K,

$$K = \frac{qU_0}{E_{\text{kin}}R_0^2}\,, \tag{8.13}$$

the differential Eq. 8.11 and Eq. 8.12 can be reduced to Eq. 6.16. The solutions, given by Eq. 6.23 - 6.30, define the linear transport matrix elements of the quadrupole lens. The resulting transport matrices, which are used for the MAD X simulations in Sec. 8.2, are given in Appendix C.

For the ease of fabrication, the hyperbolic electrode shape of electrostatic quadrupole lenses are often approximated by simpler cylindrical rods. The electrostatic quadruple lenses, which are implemented in the CSR transfer line to focus the ion beam, follow these design principle, and have been developed and built at the University of Frankfurt [163]. These electrodes are formed from thin sheet metal (stainless steel), mechanically pressed to form a cylindrical surface with shunts, as depicted in Fig. 8.14(a). The transfer line quadrupole triplets contain three quadrupole lenses, each

with a length of $L = 15$ cm and separated by 3 cm (see Fig. 8.14(b)). In the center of this 3 cm gap and at a distance of 1.5 cm to the entrance and exit of the triplet, grounded shield plates with an aperture of 5.5 cm in diameter are placed, reducing the fringing field. The bore radius of these quadrupole lenses is $R_0 = 3$ cm.
The quadrupole strengths required, which are derived from the simulations of the 300kV beamline and the 60kV beamline in Sec. 8.2, are summarized in Tab. 8.1 and Tab. 8.3, respectively. Using Eq. 8.13, the electrode voltages of the quadrupole lenses, needed to generate these quadrupole strengths K, can be calculated for a given ion charge state, q, and the kinetic energy E_{kin}. The maximal quadrupole strength, calculated in the ion-optical design of the 60kV beamline (lens in the quadrupole triplet QPA), is $K = 43.0\ \mathrm{m}^{-2}$. For an ion beam, traversing the maximum acceleration voltage of 60 kV, the electrode voltage required on the quadrupole lens is calculated to 2.3 kV, using Eq. 8.13. Similarly for the 300kV beamline, a maximal quadrupole strength of $K = 22.6\ \mathrm{m}^{-2}$ is calculated for the middle lens of quadrupole triplet QP3 (see Tab. 8.1). The required potential applied to the electrodes of this quadrupole lens is calculated to $U_0 = 6.1$ kV, in order to focus an ion beam, which is accelerated by the maximum voltage of 300 kV from its ion source platform. As a result, the required limit for the power supplies of up to ± 10 kV is sufficient for the ion-optical design of the CSR transfer line.

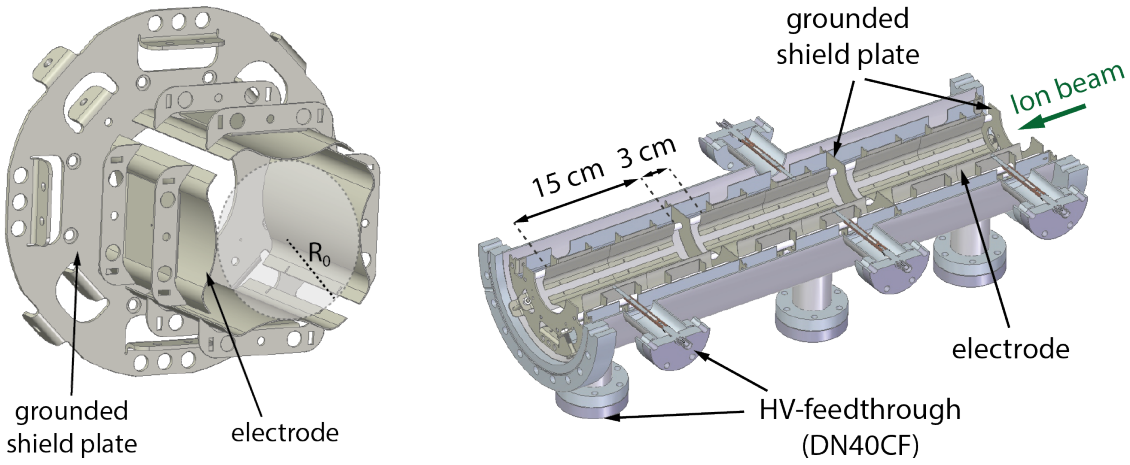

Figure 8.14: Electrostatic quadrupole lens, used for the CSR transfer line. The left picture (a) illustrates the electrode configuration of the quadrupole lens, designed and built at the University of Frankfurt [163]. Approximated by a cylindrical surface with shunts, the electrodes of a quadrupole lens are separated by a bore radius $R_0 = 3$ cm. The drawing on the right (b) illustrates the quadrupole triplet that is installed in its vacuum chamber.

For this quadrupole triplet, designed to fit a DN160 vacuum pipe, a custom vacuum chamber was designed and constructed for the CSR transfer line. As the available space for the elements in the CSR transfer line is restricted, a compact design was favorable. The vacuum chamber designed for the quadrupole triplet has a length of 0.57 m, matching the triplet length. As depicted in Fig. 8.14(b), the electrodes are laterally connected to HV-feedthroughs (mounted on DN40CF ports). In normal operation, the opposing electrodes of a quadrupole have a matching potential applied. Thus, for the first and last lens, opposite electrode pairs are electrically connected. To permit some degree of beam steering within the triplet, the four electrodes of the middle quadrupole lens are supplied independent from each other. Applying asymmetric voltages enables some flexibility in steering the beam as it passes the triplet. The quadrupole assembly was electrically tested in vacuum and successfully held a potential ±10 kV.

Ion-optical simulation

As the designed electrodes of the quadrupole lenses differ from the ideal hyperbolic shape, the SIMION ion optics package [156] was used to simulate the electric fields of the real quadrupole lens. Charged particles were tracked through the quadrupole triplet and the horizontal and vertical phase space distributions of the traversing ion beam at various positions along the central path recorded. These phase space distributions are fitted by ellipses, containing a certain fraction of the particles in the beam. These phase space ellipses contain the beam's twiss parameters, according to Eq. 6.53, as discussed in Sec. 6.3. To examine the validity of the linear approximation of an ideal quadrupole lens, the twiss parameters derived in the SIMION simulation are compared to those of the MAD X simulation, used in Sec. 8.2.
In these MAD X simulations, the ion-optical elements are represented using the hard edge model, where the field effecting the particles' trajectory is approximated by a constant with an effective length L_{eff} along the central path, as discussed in Sec. 6.5. To determine the effective length of the quadrupole lens, the electric field (E_x, E_y), transverse to the beam path, is recorded over the particle flight path s for various displacements (x,y) relative to the central path. The resulting electric field E_x (horizontal displacement of 2 mm) as a function of the flight path s is depicted by the black solid line in Fig. 8.15. The effective length L_{eff} of the quadrupole lens is given

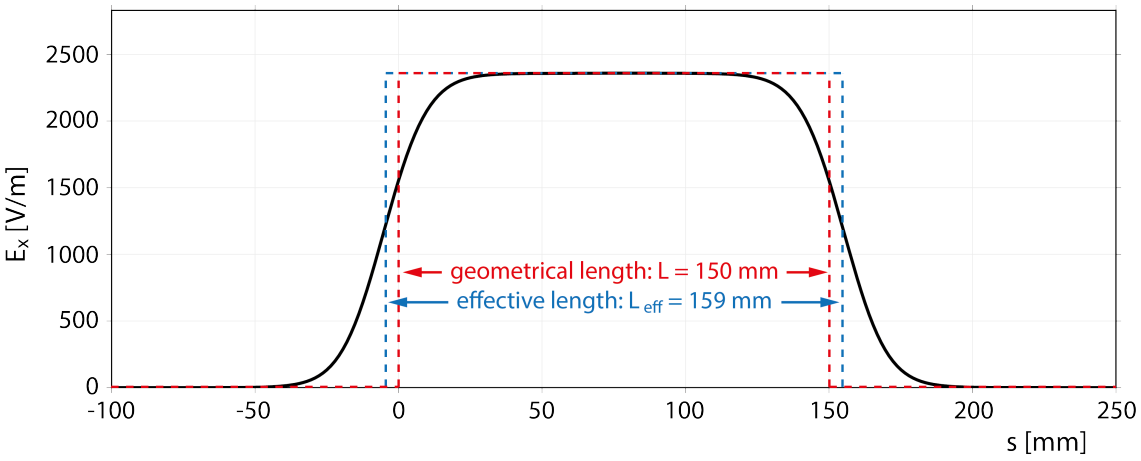

Figure 8.15: Horizontal electric field E_x, which is experienced by a particle passing the quadrupole lens along the beamline path s with a horizontal displacement of 2 mm. The position and geometrical length of the electrodes of the quadrupole lens is indicated by the dashed red line. A potential of ± 500 V is applied to the electrodes, creating the electric field inside the quadrupole lens. The resulting electric field E_x as a function of the flight path s is depicted by the black solid line. The effective length L_{eff} of the electrodes, indicated by the blue dashed line, is derived from Eq. 8.14.

by

$$L_{\text{eff}} = \frac{1}{E_0} \int_{-\infty}^{\infty} E(s) ds \,, \tag{8.14}$$

where E_0 denotes the electric field in the center of the quadrupole lens. The relative position and the geometrical length (150 mm) of the quadrupole's electrodes is indicated by the red dashed line in Fig. 8.15. The blue dashed line represents the effective length L_{eff} using the hard edge model, which is calculated from simulations using Eq. 8.14, leading to a relative increase of 9 mm, when compared to its geometrical length. This effective electrode length of 159 mm in tandem with the resultant reduced drift length, has been taken into account in the MAD X simulations, previously presented in Sec. 8.2.

To assess the validity of the linear approximation of an ideal quadrupole lens in the previous MAD X simulations, an ion beam focused by the real quadrupole triplet geometry was simulated using SIMION. In this simulation, the trajectory of 10000 negatively charged particles, with a kinetic energy of $E_{\text{kin}} = 10$ keV, are traced. Starting with the same initial ion beam conditions in both the horizontal and vertical plane, where the x, y positions and x′,y′ angular co-ordinates, are both mapped to a Gaussian distribution. The starting horizontal (x) and vertical (y) phase space distribution for the simulated ion beam is shown in Fig. 8.16. The fitted phase space

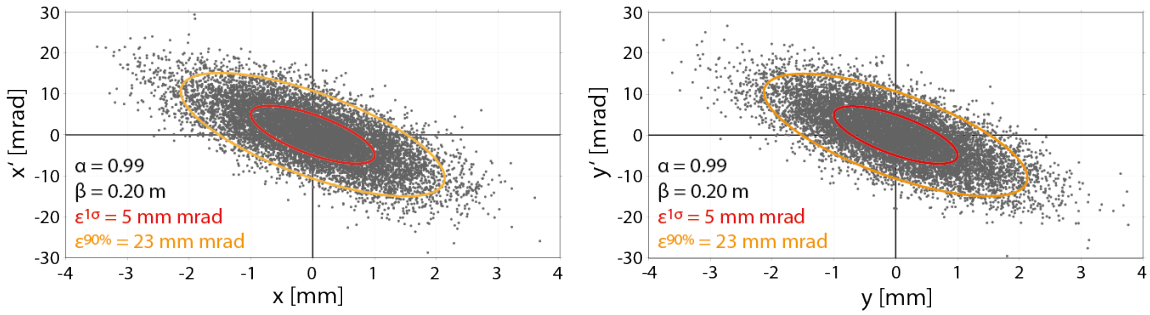

Figure 8.16: Initial phase space distributions of the ion beam used in the SIMION simulation of the quadrupole triplet. The grey dots represent single particles in the ion beam, which possess a both a spatial and angular Gaussian distribution x,y and x′,y′, respectively. The red ellipse represents the 1σ-emittance of the simulated ion beam. The phase space ellipse that includes 90% of all particles is indicated by the orange solid line ($\epsilon^{90\%} = 23$ mm mrad).

ellipses match Eq. 6.53, using the twiss parameters $\alpha = 0.99$ and $\beta = 0.2$ m, where the red and orange ellipse represents the emittance $\epsilon^{1\sigma}$ and $\epsilon^{90\%}$, respectively.
In Fig. 8.17, a simulation of the ion-optical system, transporting a negatively charged ion beam, is presented. Starting with a drift section of 0.57 m, a diverging ion beam is focused using the quadrupole triplet. The first and third quadrupole lens in this triplet focuses the beam horizontally via a potential of ±220 V and ±280 V, respectively. Using Eq. 8.13, the strength K of these quadrupoles is calculated as 24.4 m^{-2} and 31.1 m^{-2}. The center quadrupole lens element, which focuses the ion beam vertically, is supplied by a potential of ±400 V, corresponding to a quadrupole strength of -44.4 m^{-2}. In this simulation the ions' x (horizontal), y (vertical) and z (longitudinal) position coordinates, relative to the central path, and the corresponding velocities are recorded at various positions (A - F), illustrated in Fig. 8.17. For each of these positions, the horizontal and vertical phase space distributions are then determined and fitted by a 1σ phase space ellipse (red line) and an ellipse containing 90% of the particles (orange line).
As one would expect, throughout the first drift section, the horizontal and vertical twiss parameters of the beam remain equal. In the first quadrupole lens, the beam is focused horizontally and defocused vertically. This leads to a vertical spatial expansion of the beam, as indicated in the phase space distribution at position A. As the polarity of the second quadrupole lens is inverted, the ion beam then undergoes vertically focusing, before finally undergoing a second stage of horizontal focusing. The net effect of these three focusing / defocusing stages is that the beam converges horizontally and vertically after passing the quadrupole triplet (with independent

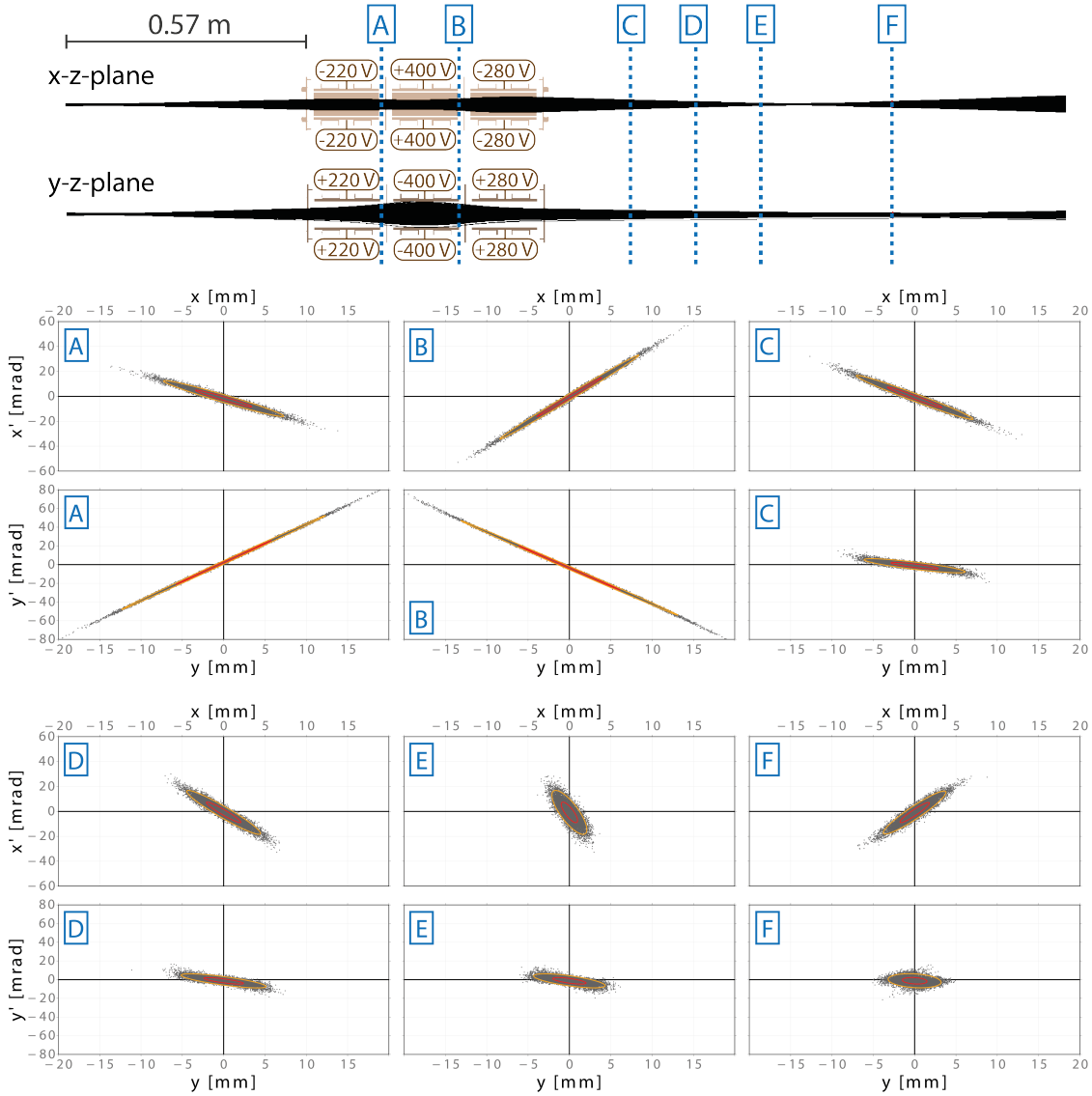

Figure 8.17: Simulation of a negatively charged ion beam with an kinetic energy of 10 keV, focused by the quadrupole triplet in the CSR transfer line. The initial phase space distribution of the beam is shown in Fig. 8.16, with the twiss parameters $\alpha = 0.99$, $\beta = 0.2$ m and an emittance $\epsilon^{90\%} \approx 23$ mm mrad. The diagrams A - F illustrate the horizontal (x) and vertical (y) phase space distributions recorded at the corresponding positions. The fitted red and orange ellipses represent the emittance $\epsilon^{1\sigma}$ and $\epsilon^{90\%}$, respectively.

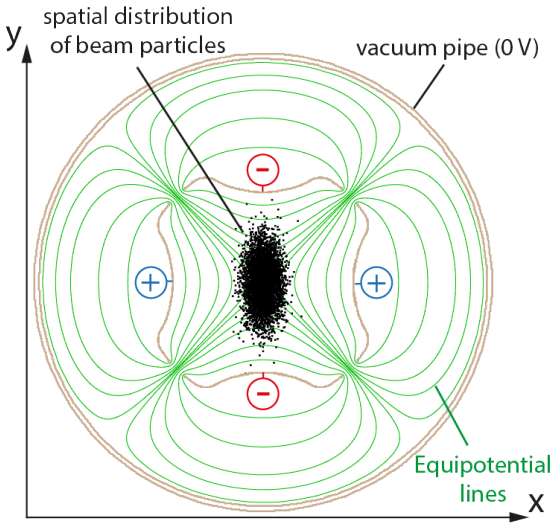

Figure 8.18: Spatial distribution of the negatively charged ion beam inside the center quadrupole lens of the simulation shown in Fig. 8.17. The green lines represent the potential field lines, focusing the beam in vertical direction.

focal lengths). In the subsequent drift section, the phase space distributions of the recorded particles are shown at distances of 0.21 m (C), 0.36 (D), 0.51 m (E) and 0.81 m (F) after the quadrupole triplet.

In these phase space distributions, there is no evidence of filamentation in the horizontal axis, but the same is not true in the vertical. There are minor vertical aberrations, due to the higher degree of spatial expansion inside the quadrupole lens. In Fig. 8.18, the spatial distribution inside the center quadrupole lens is illustrated. In this figure it can be seen that a portion of the ion beam is into close proximity with the electrodes in the vertical direction, where the linear approximation of the electric quadrupole field no longer holds. As the effective emittance is a useful measure of the beam transport quality (see Sec. 6.4), it can be shown that the effective emittance remains constant over the ion-optical system ($\epsilon^{1\sigma} \approx 5$ mm mrad and $\epsilon^{90\%} \approx 23$ mm mrad). This indicates that the beam aberrations are not detrimental to the overall single pass beam transport. The resulting twiss parameters of the fitted phase space ellipses, according to Eq. 6.53, are listed in Tab. 8.5. To compare these results to the linear approach of the transfer matrix formalism, the identical ion-optical system simulated via SIMION, is calculated using MAD X.

Starting with the same initial twiss parameters ($\alpha = 0.99$, $\beta = 0.2$ m), the resulting horizontal and vertical betatron functions are shown in Fig. 8.19. In this simulation, the effective length of a quadrupole lens ($L_{\text{eff}} = 159$ mm) and the cal-

culated quadrupole strengths K, using Eq. 8.13, are used. At the positions A - F, highlighted in Fig. 8.19, the twiss parameters of the propagating ion beam are determined. In Tab. 8.5, the resulting twiss parameters, derived from both MADX and SIMION simulations, are listed. In Fig. 8.19, the values of β_x and β_y, derived at the corresponding positions via the SIMION simulation, are indicated by black and red circles, respectively. The results of the horizontal betatron function match in good agreement. In the vertical plane, the simulations agree within small deviations. These deviations indicate the expected non-linear field effect toward the electrodes of the quadrupole lens, as observed in the previous SIMION simulation. However, these simulations revealed in the example of an ion beam with an emittance of $\epsilon^{90\%}$ $\approx$ 23 mm mrad, that the ion beam transport through this quadrupole triplet can be represented in linear approximation with adequate accuracy.

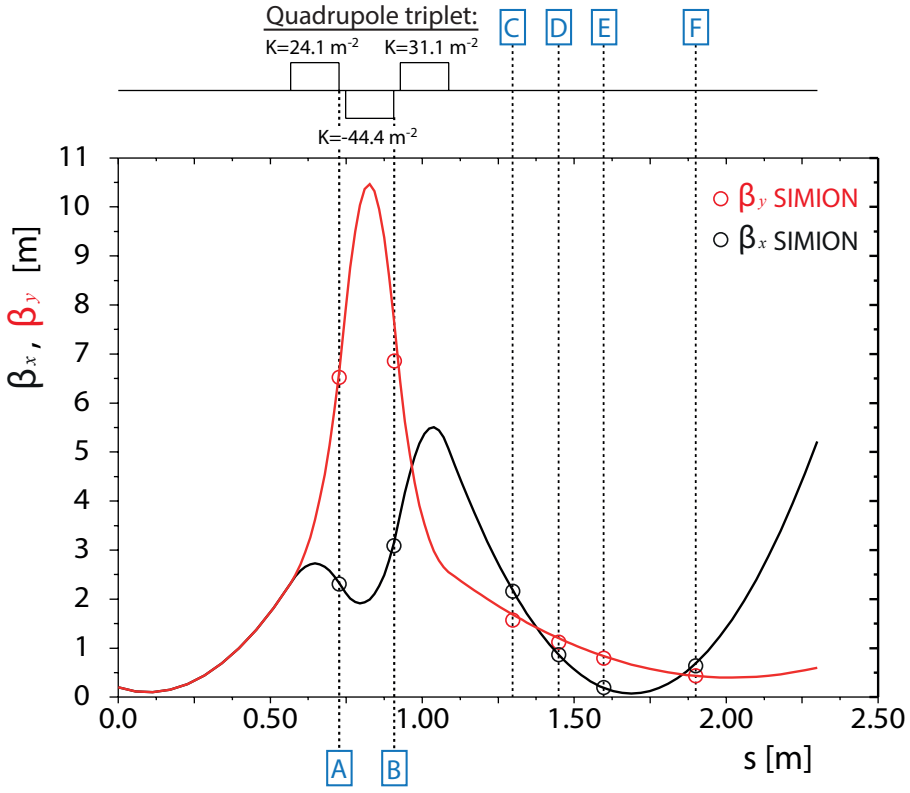

Figure 8.19: MAD X simulation of the betatron functions of an ion beam transported through a quadrupole triplet using linear transport matrices. The black and red open circles indicate β_x and β_y, respectively, derived from the SIMION simulations at the positions A - F, as shown in Fig. 8.17.

Position	initial	A	B	C	D	E	F
α_x (Simion)	0.99	4.47	-12.35	5.31	3.26	1.27	-2.72
α_x (MAD X)	0.99	4.77	-13.22	5.38	3.31	1.25	-2.90
β_x (Simion) [m]	0.2	2.31	3.09	2.16	0.86	0.19	0.64
β_x (MAD X) [m]	0.2	2.33	3.15	2.17	0.86	0.19	0.68
α_y (Simion)	0.99	-26.60	26.41	1.67	1.32	0.95	0.21
α_y (MAD X)	0.99	-27.79	30.89	1.79	1.42	1.04	0.29
β_y (Simion) [m]	0.2	6.52	6.86	1.57	1.12	0.79	0.43
β_y (MAD X) [m]	0.2	6.65	7.69	1.68	1.20	0.83	0.43

Table 8.5: Comparison of the resulting twiss parameters, at the positions A - F (see Fig. 8.17 and Fig. 8.19), that are derived from the SIMION and the MAD X simulations of an ion beam, propagating through the quadrupole triplet in the CSR transfer line.

8.3.4 90° deflector with a hole

To merge the 60kV and 300kV beamlines prior to injection into the CSR, an electrostatic cylindrical 90° deflector with a hole was designed, simulated and constructed. An electrostatic element has a number of advantages to a magnetic deflector in that it allows for fast switching (μs) between the 60kV and 300kV beamline. Due to space restrictions, a compact deflector design is desirable. Therefore, the concept of two separate electrostatic deflectors, similar to the ion deflection of the CSR (as discussed in Sec. 7.2), is less than preferable. When grounded, a cylindrical deflector with a hole in the outer electrode allows ions, that are produced on the 300kV ion source platform, to pass the deflector. When a potential is applied to the electrodes of the deflector, the ion beam transported by the 60kV beamline can be merged into the 300kV beamline. The deflector was designed so that with a maximum voltage of ±10 kV, an ion beam with a kinetic energy of up 60 keV per charge unit will be deflected by 90°.

In the case of an ideal cylindrical deflector, the radial electrostatic potential $U(r)$ between the coaxial electrodes is given by [164]

$$U(r) = \frac{1}{\ln(\frac{r_o}{r_i})} \left[(U_o - U_i) \ln(r) + (U_i \ln(r_o) - U_o \ln(r_i)) \right] , \tag{8.15}$$

where r_o and r_i represents the radius of the outer and the inner electrode, respectively and U_o and U_i denote the applied potentials to the outer and the inner electrode of the cylindrical deflector. The reference particle with a kinetic energy E_{kin} and charge q is guided along the central path, with a radius $\rho_0 = (r_o + r_i)/2$. Assuming that a reference particle with a constant kinetic energy traversing the electrostatic deflector, of which the central path potential is zero, leading to the condition $\mathrm{U}(\rho) = 0$. From these assumptions, the electric field $E(\rho_0)$ along the central path can be derived from Eq. 8.15, forming

$$E(\rho_0) = \frac{U(r_e)}{\rho_0 \ln(\frac{\rho_0}{r_e})}\,, \tag{8.16}$$

where r_e is the radius of either the inner or the outer electrode, held at a potential $U(r_e)$. Equating the centrifugal force and the Lorentz force for a reference particle the relationship

$$\frac{2E_{\text{kin}}}{\rho_0} = qE(\rho_0) \tag{8.17}$$

can be derived, where E_{kin} and q denotes the kinetic energy and charge of the reference particle. Using Eq. 8.16 in Eq. 8.17, the required voltages for the deflector's electrodes can be calculated, using

$$U(r_e) = \frac{2E_{\text{kin}} \ln(\frac{\rho_0}{r_e})}{q}\,. \tag{8.18}$$

Particles which deviate from the reference particle's kinetic energy, are guided by the electrostatic deflector along different paths. From Eq. 8.17, it is evident that the deflection radius is proportional to the kinetic energy, so that particles with a higher kinetic energy undergo a smaller angular deflection when passing the deflector. It is for this reason that such devices can also be utilized as a kinetic energy analyzer of charged particles [164].

On entering the deflector, a horizontal displacement of the incident particle, with respect to the reference path, leads to either a deceleration or acceleration of the particle, dependent on whether the displacement is towards the outer or inner electrode, respectively. As a result of this acceleration, these particles do not undertake perfectly circular trajectories.

In an ideal cylindrical electrostatic deflector, where the height of the electrodes are infinite, the deflector does not introduce any vertical deflection, thus the vertical movement of a charged particle is solely due to drift. In a real sector deflector, where the plate height is finite, the electric field near the vertical electrodes bound-

aries is no longer uniform. This inhomogeneous field induces an undesirable coupling of the horizontal and vertical movement, in which the horizontal deflection strength depends on the vertical position of the transported particles. Thus to preserve the vertical field in the vicinity of the central path of the deflector, the height of the electrodes should be adjusted relative to their distance. The radial field of a real electrostatic deflector consists not only of the sector field component, defined in Eq. 8.16, but also fringing field components (see Sec. 6.5), which can extend beyond the sector volume. Thus, the deflection angle of an ion beam can not simply be determined by the geometrical angle of the bent electrodes. The fringing field effect, which can be limited by apertures placed at the entrance and exit of the deflector, leads to an increase effective deflection angle of the guided ion beam. The resulting influence of the fringing fields on the deflection angle is dependent on the geometry of the apparatus, i.e. aperture size and distance relative to the deflector's electrodes. Throughout the design process of an electrostatic deflector, an iterative optimization procedure of design, simulation, and subsequent design refining, is needed to attain the desired deflection angle.

Prior to designing a deflector, a practical electrode geometry (e.g. height, radii and separation) and the outer electrode hole size, through which the 300 kV ion beam must pass, has to be considered. To estimate the hole size and plate separation required to transmit a beam from the 300kV platform unhindered, the beam diameter at this position was calculated. Starting with a beamline acceptance of $A_{x,300\mathrm{kV}} \approx 41$ mm mrad and $A_{y,300\mathrm{kV}} \approx 72$ mm mrad, calculated from Eq. 8.5 and Eq. 8.6 in Sec. 8.2.1, and using the derived maximum betatron function of $\beta_{\mathrm{x,max}}(90°) = 0.9$ m and $\beta_{\mathrm{y,max}}(90°) = 1.0$ m, a maximum beam radius can be calculated from:

$$x_{\max}(90°) = \sqrt{\beta_{\mathrm{x,max}}(90°) \cdot A_{x,300\mathrm{kV}}} \approx 6.1\,\mathrm{mm}\,, \tag{8.19}$$

$$y_{\max}(90°) = \sqrt{\beta_{\mathrm{y,max}}(90°) \cdot A_{y,300\mathrm{kV}}} \approx 8.5\,\mathrm{mm}\,. \tag{8.20}$$

To account for possible misalignment, steering error or higher order effects of the real transported ion beam, a suitably large hole size, with a radius of 15 mm, was selected for the outer electrode of the 90° deflector to allow transported beams a significant margin of error.

The minimum plate separation required to transport a beam from the 60kV platform can be similarly calculated from the 60kV beamline betatron function (see Fig. 8.6). From these preliminary calculations and the previously discussed requirements (e.g.

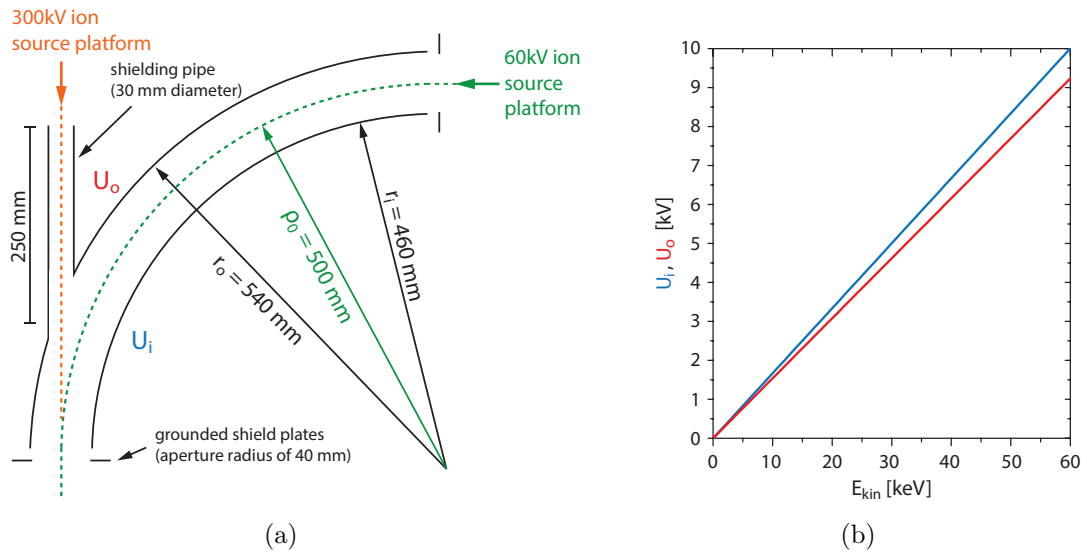

(a) (b)

Figure 8.20: The left-hand picture illustrates the concept of the 90° with a hole. When the electrodes are grounded, the central path of the ions, generated on the 300kV ion source platform, is represented by the orange dashed line. The green dashed line denotes the central path of ions from the 60kV beamline, when the correct potentials are applied to the inner and outer plate. The graph on the right-hand side (b) displays the absolute values of the required electrode potentials for the designed 90° deflector, calculated via Eq.8.18. The required potentials are depicted as a function of the kinetic energy of singly charged ions. For positively charged ions, the inner electrode has a negative potential U_i (blue line) and the outer electrode has a positive potential U_o (red line).

maximum voltage of ±10 kV), an initial concept a 90° deflector with a hole was formulated. Early simulations of the 90° deflector with a hole uncovered that such a design would lead to large deviations of the potential field inside the deflector. To suppress these deviations, the concept of mounting a shielding tube around the outer electrode hole, which would held at the same potential as the outer electrode, was considered (see Fig. 8.20(a)).

In the final design of this deflector, the inner and outer electrode sweep radii were chosen to be $r_i = 460$ mm and $r_o = 540$ mm, respectively, defining a central path radius of $\rho_0 = 500$ mm, as depicted in Fig. 8.20(a). Inserting these dimensions in Eq. 8.18, the potentials required to guide a singly-charged negative particle with a kinetic energy of $E_{\text{kin}} = 60$ keV, were calculated as $U_i = +10$ kV for the inner electrode and $U_o = -9.2$ kV for the outer electrode. Fig. 8.20(b) shows the calculated electrode potentials (absolute values), that are required for the transport of singly charged particles as a function of the kinetic energy.

The grounded shield plates with an aperture radius of 40 mm, which limit the fring-

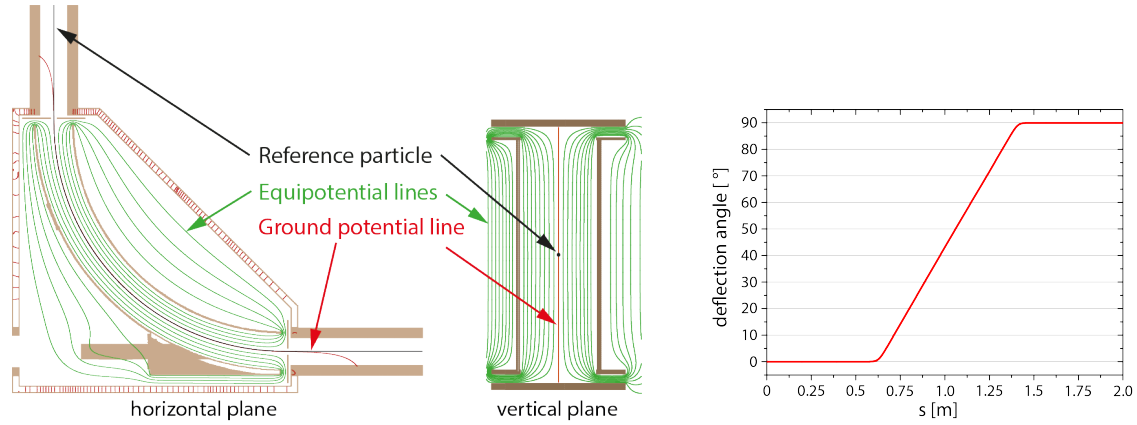

(a) (b)

Figure 8.21: The left (a) picture shows the distribution of the equipotential lines inside the deflector, represented by the green lines. Applying the electrode potentials according to Eq. 8.15, the course of the ground potential line (red line) match with the central path. Towards the grounded shield plates, the potential lines deviate from the uniform distribution. In combination with this fringing field, the reference particle (black line) is deflected by 90° in the horizontal plane. In the right diagram (b), this deflection angle is shown as a function of the flight path s.

ing field, are placed at a distance of 15 mm from the entrance and the exit of the deflector. In the resulting fringing fields, the reference particle is deflected by an additional angle of 1.7°. Therefore, the 90° deflector requires cylindrical plates forming a geometrical angle of only 88.3°. To mitigate the negative influence of the 30 mm diameter hole in the outer electrode, a shielding tube with a length of ∼250 mm is attached.

To validate the ion-optical characteristics of this 90° deflector design, including a hole, SIMION simulations of the system are performed and compared to the linear approximations used in the MAD X simulations discussed previously in Sec. 8.2.

Ion-optical simulation

The final concept and design of the 90° deflector with a hole, as discussed previously, was simulated using SIMION [156]. To assess the deflector properties, two distinct simulations were performed. In a first simulation, a reference particle was guided via the electrostatic field of the deflector along the central path. Applying the electrode potentials according to Eq. 8.15, a singly negatively charged particle with a kinetic energy of 60 keV is tracked through the deflector, as shown in Fig. 8.21(a). The equipotential lines, shown in green, illustrate the geometric potential distribution

and thus the electric field, set up in the deflector. From Fig. 8.21(a), the uniform distribution of the field lines, with the exception of the intermediate region between the sector field and field free space, demonstrate the uniformity of the potential field within the deflector. The grounded shield plates, which book-end the electrodes at a distance of 15 mm, limit the fringing field. The electric field of the deflector, which is composed of the sector field, generated by 88.3° electrodes and the fringing field, deflects the simulated reference particle (black line) horizontally by 90°. The resulting deflection angle as a function of the flight path s, is shown in Fig. 8.21(b). This diagram indicates, that the change in deflection angle is linear throughout the deflector and thus remains unperturbed when passing by the location of the hole in the outer electrode. Thus, the trajectory of the reference particle is unaffected by the influence of the hole, its effect suppressed by the shielding tube (held at potential of the outer electrode).

In a second simulation, an ion beam with a kinetic energy of 60 keV is transported by the 90° deflector, shown in Fig. 8.22. In this simulation, a bulk ion beam, consisting of 10000 singly-charged negative particles, are created $\sim$ 270 mm in front of the deflector, with the initial twiss parameter: $\alpha_x = \alpha_y = 1.0$ and $\beta_x = \beta_y = 0.2$ m. The horizontal and vertical distribution in x,y and x′,y′ are both mapped to a Gaussian distribution, resulting in a beam emittance of $\epsilon^{1\sigma} \approx 5$ mm mrad ($\epsilon^{90\%} \approx 23$ mm mrad), similar to Fig. 8.16. Relative to the central path, the x (horizontal), y (vertical) and z (longitudinal) coordinates and their velocities are recorded at various positions (A - E). For each of these positions, the horizontal and vertical phase space distributions are then determined and fitted by a 1σ phase space ellipse (red line) and an ellipse containing 90% of the particles (orange line).

After a drift length of 95 mm, this simulated ion beam creates a horizontal and vertical focal point in a distance of $\sim$175 mm in front of the deflector (see position A in Fig. 8.22). This horizontal and vertical beam waist in position A is marked by the upright phase space ellipses. Drifting for another $\sim$175 mm, the ion beam is guided via the 90° deflector. In the subsequent drift section after the deflector, the phase space distributions of the beam particles are recorded at distances of 75 mm (B), 175 mm (C), 325 mm (D) and 510 mm (E), as shown in Fig. 8.22. The fitted 1σ (red line) and 90% (orange line) phase space ellipses of these phase space distributions result in the twiss parameters α_x, α_y and β_x, β_y, according to Eq. 6.53. The resulting twiss parameters are listed in Tab. 8.6.

As a cylindrical deflector acts vertically as a drift section, the simulated ion beam

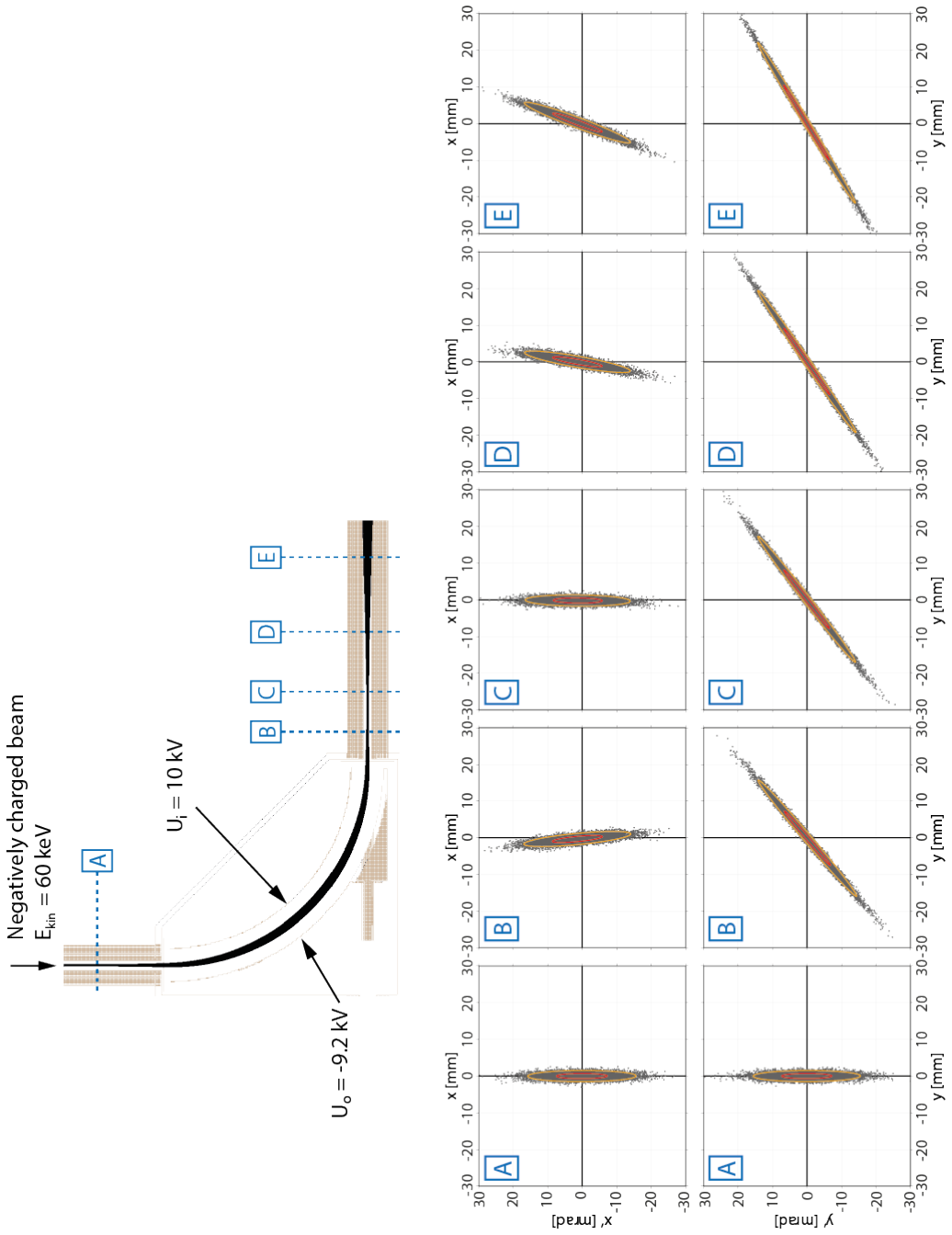

Figure 8.22: Ion-optical simulation of an ion beam that is transported via the electrostatic 90° deflector, shown in Fig. 8.20(a) (including the dimensions). The hole in the outer electrode of the deflector is shield by a tube, which hold the same potential than the outer electrode. In this simulation, negatively charged particles with a kinetic energy of 60 keV are tracked through the deflector. Starting at a distance of ∼270 mm to the deflector's entrance, the Gaussian distributed phase space of the simulated ion beam yields an emittance of $\epsilon^{90\%} \approx 23$ mm mrad. The initial horizontal and vertical twiss parameters are $\alpha_x = \alpha_y = 1.00$ and $\beta_x = \beta_y = 0.2$ m. At various positions (A - E) along the central path, indicated by the blue dashed line, the phase space distributions are recorded and fitted by ellipses, representing $\epsilon^{1\sigma}$ (red line) and $\epsilon^{90\%}$ (orange line).

Position	initial	A	B	C	D	E
α_x (MAD X)	1.00	0.03	0.93	-0.10	-1.64	-3.55
α_x (Simion with shielding tube)	1.00	0.02	0.90	-0.10	-1.62	-3.52
α_x (Simion w/o shielding tube)	1.00	0.04	0.95	0.03	-1.42	-3.13
β_x (MAD X) [m]	0.20	0.10	0.18	0.10	0.36	1.32
β_x (Simion with shielding tube) [m]	0.20	0.10	0.18	0.10	0.36	1.32
β_x (Simion w/o shielding tube) [m]	0.20	0.10	0.21	0.11	0.32	1.15
α_y (MAD X)	1.00	0.01	-9.94	-10.91	-12.37	-14.16
α_y (Simion with shielding tube)	1.00	0.02	-9.50	-10.22	-11.65	-13.23
α_y (Simion w/o shielding tube)	1.00	0.02	-8.52	-9.35	-10.49	-11.72
β_y (MAD X) [m]	0.20	0.10	10.61	12.54	16.16	21.03
β_y (Simion with shielding tube) [m]	0.20	0.10	10.30	12.45	15.91	20.51
β_y (Simion w/o shielding tube) [m]	0.20	0.10	10.03	11.92	14.94	18.83

Table 8.6: Comparison of the resulting twiss parameters in the simulations of the 90° deflector, using MAD X and SIMION. In the MAD X simulation, the ion beam transport in an ideal cylindrical 90° deflector is calculated in linear approximation. In SIMION, the geometrical model of the 90° deflector with a hole is simulated with shielding tube (see Fig. 8.22) and without shielding tube (see Fig. D.1). For each simulation, the twiss parameters of the transported ion beam are determined at the same positions along the central path.

is not confined vertically. After passing position A, the ion beam diverges vertically, as it is apparent in the recorded phase space distributions shown in Fig. 8.22. The fitted vertical phase space ellipses, which represent a constant number of particles, show an increasing beam size $y_{\max}$ with a constant $y'_{\max}$, while propagating along the beam path.

In the horizontal plane, where the ion beam is deflected by 90°, the radial electrostatic field of the deflector focuses the ion beam horizontally. After passing position A, where the ion beam has a focal point, the beam diverges along a drift length of ∼175 mm. At this distance to the entrance and exit of this 90° deflector, the horizontal beam profile is mapped, as demonstrated in Appendix C. As position A and position C are both located ∼175 mm away from the entrance and the exit of the deflector, respectively, the horizontal phase space distributions are similar. At both positions, the upright phase space ellipses indicate a horizontal beam waist and

an identical beam size, as shown in Fig. 8.22.
For both, the horizontal and vertical phase space distributions, there is no evidence of filamentation. The area of the fitted phase space ellipses, which represent the effective beam emittance (as discussed in Sec. 6.3), remain constant over the ion-optical system. These resulting effective emittances, which are useful to evaluate the beam transport quality (see Sec. 6.4), is determined to $\epsilon^{1\sigma} \approx 5$ mm mrad and $\epsilon^{90\%} \approx 23$ mm mrad for all positions (A - E).
Prior to comparing these results to the linear approximation of the transport matrix formalism, used for the ion-optical simulation of the 60kV beamline (Sec. 8.2.2), the benefit of the shielding tube attached to the outer electrode of the 90° deflector is analyzed. Using the framework of the previous simulation including beam parameters, the 90° deflector with hole is simulated without a shielding tube. In this simulation, shown in Appendix D, the horizontal and vertical phase space distributions of the propagating ion beam are recorded at the same positions A - E. The absence of the shielding tube, attached to the hole in the outer electrode, does not result in beam aberrations. For these simulated beam parameters, there is no evidence of non-linear field components. For both, the vertical and horizontal plane, the resulting effective emittance remains constant along the beam path.
However, the field perturbations, due to the hole in the outer electrode of the deflector, leads to a horizontal displacement of the beam position and an induced focusing effect in both, the horizontal and vertical plane. As shown in Fig. D.1, the beam's horizontal phase space distribution (position B - E) is shifted after passing the deflector. This shift is due to the shallower deflection angle induced by the hole in the outer plate of the cylindrical deflector. This angular difference of 5 mrad could be compensated by an adjustment of the applied voltages on the deflector electrodes, or by an increase of the electrodes' length. Both approaches could produce a 90° deflection of the guided ion beam, but a horizontal displacement of the beam's spatial center will remain. Therefore, only with an additional ion-optical steering element (e.g. parallel plate deflector), placed at the deflector's exit, can compensate for this effect.
Moreover, the hole in the outer electrode of the deflector leads to an additional focusing effect in horizontal and vertical direction. The resulting twiss parameters, derived from the simulation of the 90° deflector with and without shielding tube, are listed in Tab. 8.6. The simulation of the deflector without a shielding tube yields smaller absolute values for the twiss parameters α_x, α_y and β_x, β_y, highlighting its

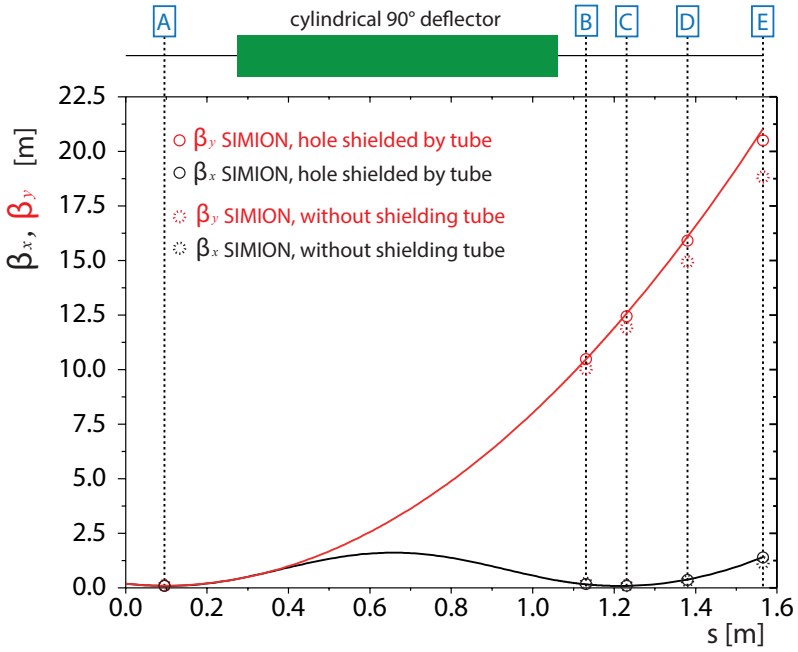

Figure 8.23: MAD X simulation of an ideal electrostatic 90° deflector using linear transport matrices. The black and red open circles indicate β_x and β_y, respectively, derived from the SIMION simulations of the 90° deflector with hole at the same positions (A - E).

focusing effects. Due to the hole geometry, the magnitude of the field distortion is xy-coupled.

As a consequence of these results, the concept of the shielding tube attached to the hole of the outer electrode is preferred over that without shielding. To assess the validity of the linear approximation for an ideal 90° deflector, as used in the previous MAD X simulations in Sec. 8.2.2, SIMION ion transport simulations of a geometric 90° deflector are compared to that obtained from MAD X. The beam transport of the identical ion-optical system is calculated via linear transport matrices (see Appendix C) using MAD X. Using the same initial twiss parameters, $\alpha_x = \alpha_y = 1.00$ and $\beta_x = \beta_y = 0.2$ m, the resulting horizontal and vertical betatron functions (β_x and β_y), along the central path s, is shown in Fig. 8.23. At the same positions (A - E), in which the phase space distributions of the beam were recorded in the SIMION simulations (see Fig. 8.22 and Fig. D.1), the calculated twiss parameters of the MAD X simulation are summarized in Tab. 8.6. The values of β_x and β_y, which were derived from the SIMION simulations at the corresponding positions, are presented in Fig. 8.23 by black and red circles. The resulting values β_x and β_y, extracted from the SIMION simulation of the 90° deflector with the shielding tube attached to the hole at the outer electrode, are indicated by the solid line circles and

show a good agreement with the MAD X simulation. The small deviations in the twiss parameters indicate, that the focusing effect, induced by the hole in the outer plate, is not entirely suppressed by the shielding tube. The dashed circles in Fig. 8.23 represent β_x and β_y, extracted from the SIMION simulation of the 90° deflector without a shielding tube. In this diagram, the induced focusing effect due to the hole in the outer electrode and the influence of the shielding tube is demonstrated. In this example of the ion beam transport via the custom designed 90° deflector, the linear approximation of an ideal cylindrical 90° deflector describes the beam transport in an adequate accuracy.

Construction

Leading from the insights gained from the simulations in previous section, this section discusses the physical design and construction of the 90° deflector, including its vacuum chamber. Briefly recapping on the beamline requirements; these components should be capable of maintaining ±10 kV potential and facilitate residual gas pressures in the order of 10^{-8} mbar.
In Fig. 8.24, the final construction drawings and photographs of the cylindrical 90° deflector are shown. The electrodes of the deflector and the grounded shield plates are both produced from A2-stainless steel due in part to its high mechanical rigidity, low out-gassing coefficient and relatively low magnetic permeability. For the most part, the electrodes are cold rolled from 3 mm thick sheet metal forming two concentric cylindrical sectors. The outer surface of the inner electrode has a radius of 460 mm, while the inner surface of the outer electrode has a radius of 540 mm. To maintain plate rigidity and alignment, a pair of guiding plates for each electrode, each with a recessed track in which the electrode can slot into, are clamped to the top and bottom of the corresponding electrode via metal rods, as shown in Fig. 8.24(b). Each electrode sweeps an angular sector of 88.3°. The inner electrode is composed of sheet metal in its entirety, while the outer electrodes is a composite of sheet metal sector (58°) and a bulk, machined part which houses the shielding tube. For this deflector section, a solid stainless steel cube was milled to form the fixture of the shielding tube. This bulk part has a hole with diameter of 60 mm in its center, which is precision machined to fit the outer diameter of the shielding tube, shown in Fig. 8.24(b). The shielding tube, which reduces the hole size to 30 mm, is machined to match the inner radius of the outer electrode, forming a smooth continuous surface.

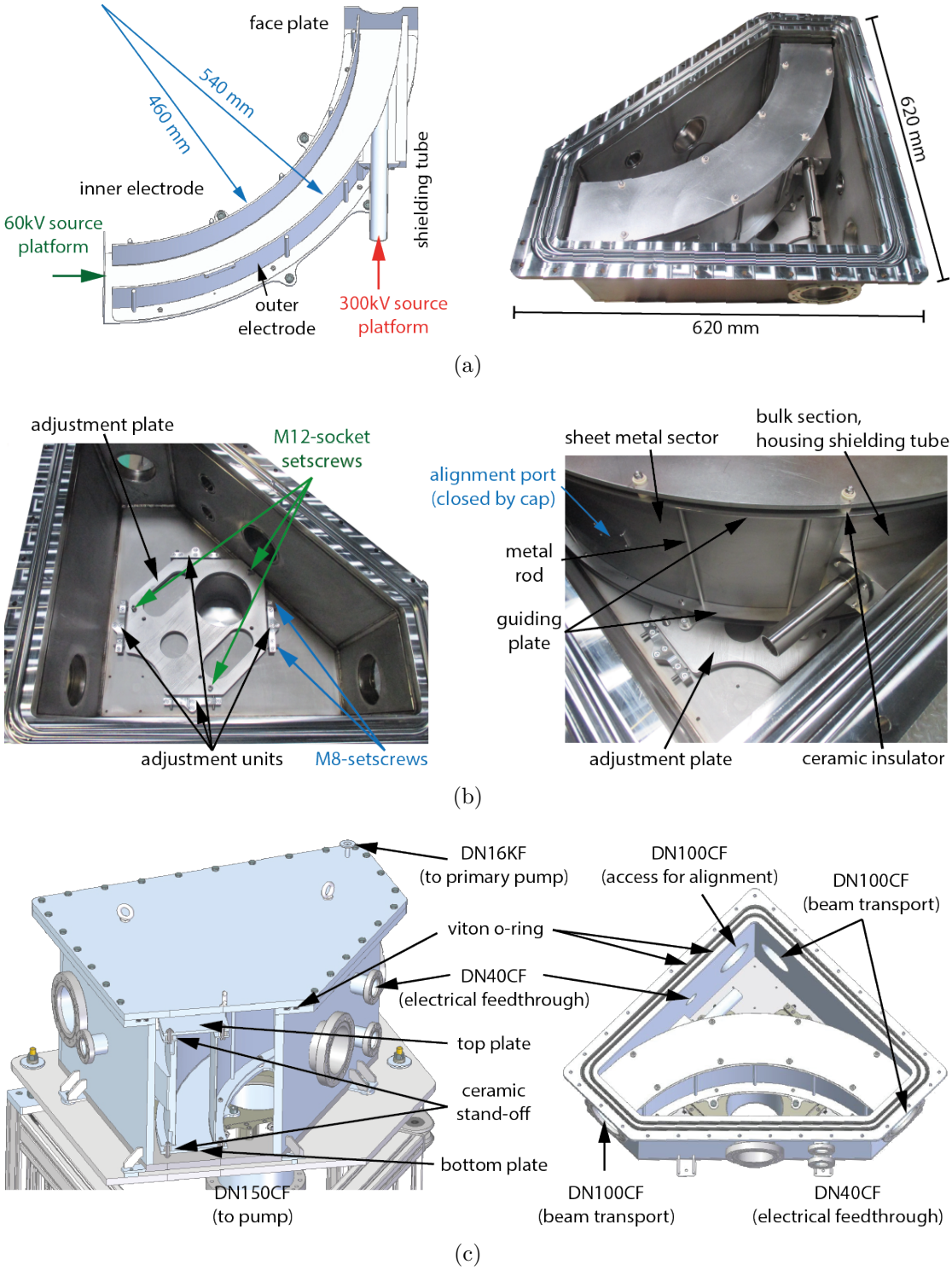

Figure 8.24: Construction drawings and photographs of the 90° deflector.

The dimensions of this geometry are given in Fig. 8.20(a) and Fig. 8.24(b). In the sheet metal sector of the outer electrode, an alignment port is implemented, which is closed by a cap. The cap forms a smooth surface together with the outer electrode, when its closed. For the alignment of the 90° deflector relative to the two beamlines, this port is needed to access both axes. The clearance of the port is 20 mm × 20 mm in its straight line projection.

The inner and the outer electrode assembly are both sitting on a grounded metal plate, electrically isolated, using a combination of two nested ceramic stand-offs and a pair of ceramic washers (Al_2O_3), shown in Fig. 8.24(c). In the same manner, the upper end of the electrodes are affixed. This construction of the top and bottom plate supports and aligns the concentric deflector electrodes. The length of these 6 mm thick top and bottom plate exceeds the electrodes' length by ∼15 mm at the entrance and exit of the deflector, respectively. At both ends, a face plate with an aperture radius of 40 mm is mounted to the top and bottom plate (see Fig. 8.24(a), left-hand side).

This rigid assembly, in which all parts are machined to a precision with a tolerance of 0.3 mm, is housed by a custom vacuum chamber. This vacuum chamber, shown in Fig. 8.24(b), right-hand side, is constructed from stainless steel plates with a thickness of 15 mm in an angular shape. The vacuum chamber, which has a side length of 620 mm, is equipped with several CF-ports namely utilized for beam transport, pumping, electrical feedthroughs, monitoring and access. The geometric position, size and layout of these ports are depicted in Fig. 8.24(c).

The lid of the chamber is sealed using a viton o-ring (7 mm in diameter). Due to the higher leak rate of o-ring sealings compared against copper gaskets, a second o-ring with a pump section in between was implemented (see Fig. 8.24(c)), in order to reliably achieve residual gas pressures of 10^{-8} mbar inside this chamber. Therefore, two grooves are milled in the upper plate of the chamber, housing the o-rings. Welded to the lid, a small tube with an inner diameter of 3.5 mm reaches in between these o-rings. Thus, a vacuum pump attached to the KF16 port of this tube, can evacuate the volume between the o-rings. This method can reduce the leak rate of the inner o-ring sealing significantly.

At the bottom of the vacuum chamber an adjustment plate is mounted, which enables the horizontal and vertical alignment of the 90° deflector, relative to the chamber. This plate sits on three M12-socket setscrews, which allows a vertical alignment of ±8 mm in position and ∼3° in angle. The horizontal translation stage allows for

displacements of ±5.5 mm and rotations of ∼4°, using the M8-setscrews at the four adjustment units fixed to the bottom plate (see Fig. 8.24(b), left-hand side).
The beam ports were sealed using blank flanges and the complete assembly was tested in isolation. A TMP (Edwards nEXT400D) backing pumped by a scroll pump (Edwards nXDS10i) maintained an UHV-environment $< 1 \cdot 10^{-8}$ mbar. Using SHV10-feedtroughs on DN40CF flanges, the 90° deflector was tested to hold ±10 kV applied at the electrodes.

Chapter 9

Photodetachment setup

To perform merged-beams experiments on ion-neutral reactions at the CSR, first a fast neutral atomic beam is required. Generated in the CSR transfer line, an atom beam can be directly merged with stored, cooled ions in the CSR. To this end, a photodetachment (PD) setup, in which a laser beam neutralizes a portion of an anion beam, was designed and constructed. This section, integrated into the CSR transfer line, is positioned after the merging of the 60kV and 300kV beamline via the 90° deflector with a hole (see Sec. 8.3.4). This location is advantageous, as it permits the photodetachment of negative ion beams from either ion source platform.

As discussed in Chap. 5, the investigation of astrophysically relevant reactions often requires the production of ground-state neutral atoms, which are merged to the cold, well-defined, ion beam. One method for the preparation of fast, neutral, ground-state, atoms is via the photodetachment process. In this process, a photon interacts with a negatively charged atom (X^-). This anion can be neutralized if the electron affinity (EA) of X^- is smaller than the photon energy ($E_\gamma = h\nu$). For single-photon electron detachment; $X^- + h\nu \rightarrow X + e^-$, the possible final states of the neutral atom X are determined by the excess photon energy, $E_\gamma - \mathrm{EA}$. Using a photon energy, higher the electron binding energy, but insufficient to excite the daughter atom, X, to a higher state, allows the production of neutral atoms in their ground state term.

Hydrogen (H), carbon (C), and oxygen (O) are three of the four most abundant elements in the universe (the fourth being helium, which forms only meta-stable anions). To generate a sufficiently intense neutral beam from their negatively charged counterpart via photodetachment, a suitable laser system must first be chosen. The electron affinity of these elements are given by $E_{\mathrm{EA}}(\mathrm{H}) = 0.754$ eV, $E_{\mathrm{EA}}(\mathrm{C}) = 1.262$ eV and

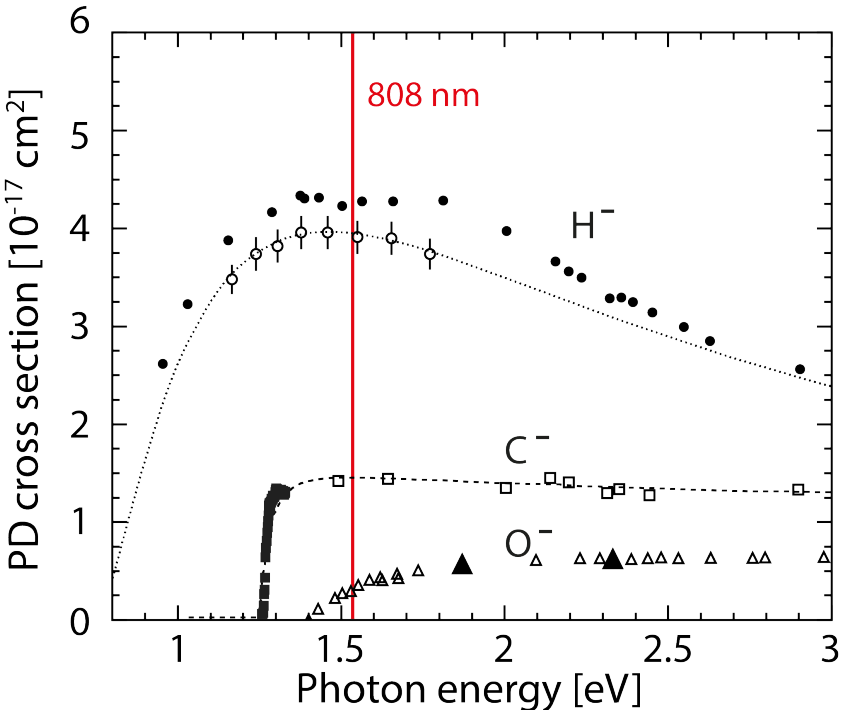

Figure 9.1: Photodetachment (PD) cross sections for H^-, C^- and O^- as a function of the photon energy [166]. The solid and open circles represent measured H^- PD cross sections [167, 168], and the dotted line indicates the calculated cross section for H^- [169]. The solid and open squares denote the measured C^- PD cross sections [170, 171], whereas the predicted cross section is represented by the dashed line [171]. The solid and open triangles denote the measured PD cross sections for O^- [172, 173]. The red solid line represents the laser wavelength of the utilized laser diode system.

$E_{\mathrm{EA}}(\mathrm{O}) = 1.461$ eV [165], respectively. High-power (∼kW), direct-diode laser stacks, operating in the infrared regime, > 800 nm, suitable for the efficient photodetachment of most anion beams [166], are readily available. In this work, a 2 kW diode laser system, operating at a wavelength of 808 nm (corresponding to $E_\gamma = 1.53$ eV) is employed, capable of efficiently photodetaching H^-, C^- and O^- beams, without the need of an additional amplification stages, amplification stages, e.g. external cavities.

In Fig. 9.1, the absolute photodetachment cross sections for H^-, C^- and O^- are shown as a function of the photon energy. The red line highlights the laser wavelength used in the presented photodetachment setup. This 808 nm laser system operates in the broad maxima regime of H^- and C^-, thus tuned to the relatively high PD cross sections in this region. While the photon energy is higher that the photodetachment threshold of O^-, the photon energy is below the PD cross section maximum.

In this chapter, the PD setup is introduced and discussed in detail. In Sec. 9.1, the expected PD efficiency for anions crossing a laser field at an angle is estimated. The high power laser system, utilized in this work, is introduced and laser profile measurements characterizing the beam quality are presented. Finally, the design and construction of the PD section in the CSR transfer line is shown. The main part of this PD section is the laser-interaction region, where the laser beam is merged to the anions transported along the transfer line. As only a fraction of this beam is neutralized in the laser field, a beam cleaner was designed, simulated and constructed to deflect the remaining negatively charged particles prior to entering the CSR. This electrostatic element allows the neutral atom beam to pass unhindered, while the anions are steered by an electrical field set up between parallel plates and subsequently dumped into a Faraday cup. This setup thus yields a pure, neutral, atomic beam which can be injected into the CSR and merged with the stored ion beam.

9.1 Photodetachment efficiency

The photodetachment (PD) probability η of a negatively charged particle passing through a laser field can be given by

$$\eta = 1 - \exp \int_{-\infty}^{+\infty} -\sigma_{\mathrm{PD}} \Phi(t) dt \,, \tag{9.1}$$

where σ_{PD} denotes the wavelength-dependent PD cross section and Φ the photon flux, integrated over the interaction time t[166]. Eq. 9.1 assumes that the laser beam crosses the ion beam with an angle of 90° and that the ion beam height is smaller than that of the laser beam. For continuous beams and an ion beam with a constant velocity v_{ion} in x-direction, the integration over the interaction time t in Eq. 9.1 can be substituted by $dt = \frac{1}{v} dx$, leading to

$$\eta(y,z) = 1 - \exp \left[-\frac{\sigma_{\mathrm{PD}}}{v_{\mathrm{ion}}} \int_{-\infty}^{+\infty} \Phi(x,y,z)\, dx \right] . \tag{9.2}$$

Assuming that the laser beam propagates in z-direction and has a Gaussian profile (the beam width w is defined by two standard deviations), the photon flux can be

represented by

$$\Phi(x,y) = \frac{2\,P}{h\nu\pi w^2} \exp\left[-\frac{2(x^2+y^2)}{w^2}\right], \tag{9.3}$$

where P denotes the laser power and $h\nu$ represents the photon energy. Using Eq. 9.3 in Eq. 9.2 and solving the integral, leads to

$$\eta(y) = 1 - \exp\left[-\sqrt{\frac{2}{\pi}}\frac{\sigma_{\mathrm{PD}}}{v_{\mathrm{ion}}}\frac{P}{h\nu w}\exp\left(-\frac{2y^2}{w^2}\right)\right]. \tag{9.4}$$

Assuming a PD operation below the saturation regime, the exponential in Eq. 9.4 can be approximated using the series expansion ($e^x = 1 + x + ...$), yielding

$$\eta(y) \approx \sqrt{\frac{2}{\pi}}\frac{\sigma_{\mathrm{PD}}}{v_{\mathrm{ion}}}\frac{P}{h\nu w}\exp\left(-\frac{2y^2}{w^2}\right). \tag{9.5}$$

The effective PD efficiency for a laser beam crossing an ion beam at an angle of 90°, where the laser beam size is larger than the size of the ion beam, can be approximated by averaging Eq. 9.5 over the ion beam profile along the y direction. The resulting PD efficiency is inversely proportional to the beam width w of the laser. To optimize the total PD efficiency for a given ion beam, it is beneficial to roughly match the vertical (y) laser beam size to size of the crossed ion beam.

The photodetachment efficiency can be amplified by reducing the angle between the crossing laser and ion beam to $< 90°$, leading to an increase of the effective overlap length. Assuming a constant laser beam profile in the overlap region, this effective overlap length is increased by a factor $1/\sin\Theta$. The resulting PD efficiency is then given by

$$\eta(y) \approx \frac{1}{\sin\Theta}\sqrt{\frac{2}{\pi}}\frac{\sigma_{\mathrm{PD}}}{v_{\mathrm{ion}}}\frac{P}{h\nu w}\exp\left(-\frac{2y^2}{w^2}\right). \tag{9.6}$$

Introducing an angle $\theta = 30°$ between the laser and the ion beam would double the PD efficiency compared to an angle of 90°. The photodetachment section (discussed in Sec. 9.3) is designed to create an angle θ of ≈2.7°. In this case, the PD efficiency is increased by a factor of 21.2, provided that the laser beam profile is constant in the interaction region.

In order to estimate the actual PD efficiency of negatively charged particles merged by a laser field, the knowledge of both beam profiles at each position in the interaction region is essential.

9.2 Laser system

The heart of the photodetachment section is a high-power (2 kW), continuous wave (cw) diode laser system. This laser system (manufactured by DILAS Inc.) operates at a fixed wavelength, centered at $\lambda_{ph} = 808$ nm. The schematic of the laser head, as shown in Fig. 9.2, consists of two water-cooled, vertically stacked diode bar arrays. Both arrays possess 15 diode bars, which in turn have 19 individual emitters each. These two stacks are optically superimposed by a set of refractive elements, yielding a single beam. This laser beam is thus a rectangular matrix of 19 $\times$ 30 individual beamlets, which are collimated via micro-optical lenses. The entire beam is further shaped and focused by a series of standard optical elements, as shown in Fig. 9.2. The diode output is varied via the supplied current. This system is capable of delivering up to 2.0 kW of continuous wave (cw) laser power at the exit window for an 85 A supply current.

Direct diode laser arrays are advantageous, compared with other laser systems, in that they are compact and can reliably deliver a continuous high power output beam. These diode arrays typically can run maintenance-free for more than 10000 h, with an electro-optical power conversion ratio of ~45% under typical operating conditions. The laser stacks (shown in Fig. 9.2) are driven by currents up to 85 A and voltages of ~40 V, using a power supply (manufactured by Amtron GmbH). This power supply allows for reasonably fast switching the laser beam, with rise and fall times on the order of ~20 μs. A shortcoming of diode laser arrays is the poor laser beam quality, as they often emit a highly divergent, elliptical, and astigmatic laser beam [174].

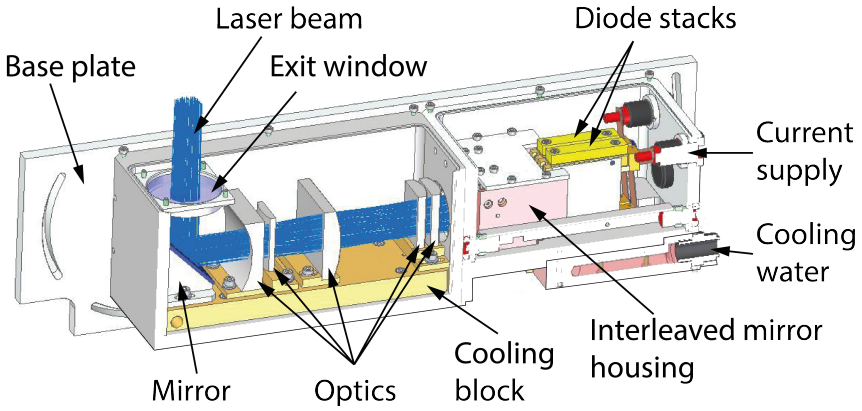

Figure 9.2: Schematic of the laser head (DILAS 808-nm).

9.2.1 Measurement of the laser profile

As previously described, the resulting laser beam is composed of an array of collimated individual beamlets, that can be modelled as an incoherent bundle of Gaussian beams [174]. As the laser beam propagates, the highly divergent beamlets superimpose to form the laser beam. It is for this reason, that the resulting beam shape appears box-like in the near field and becomes Gaussian-like near and beyond the focus.

To characterize the laser beam, the beam profiles at different positions along the propagation direction were recorded. The size and shape of the laser beam is determined using the knife-edge method [175]. A metal plate is mounted on a stepper motor, which scans the horizontal (x) and vertical (y) plane in steps of 0.1 mm, independently of each other. The transmitted laser beam is monitored by a powermeter (Coherent Power-head PM150-50C) as a function of the metal plate position. Using this method, the laser beam profiles at 10 distances z_{laser} relative to the output

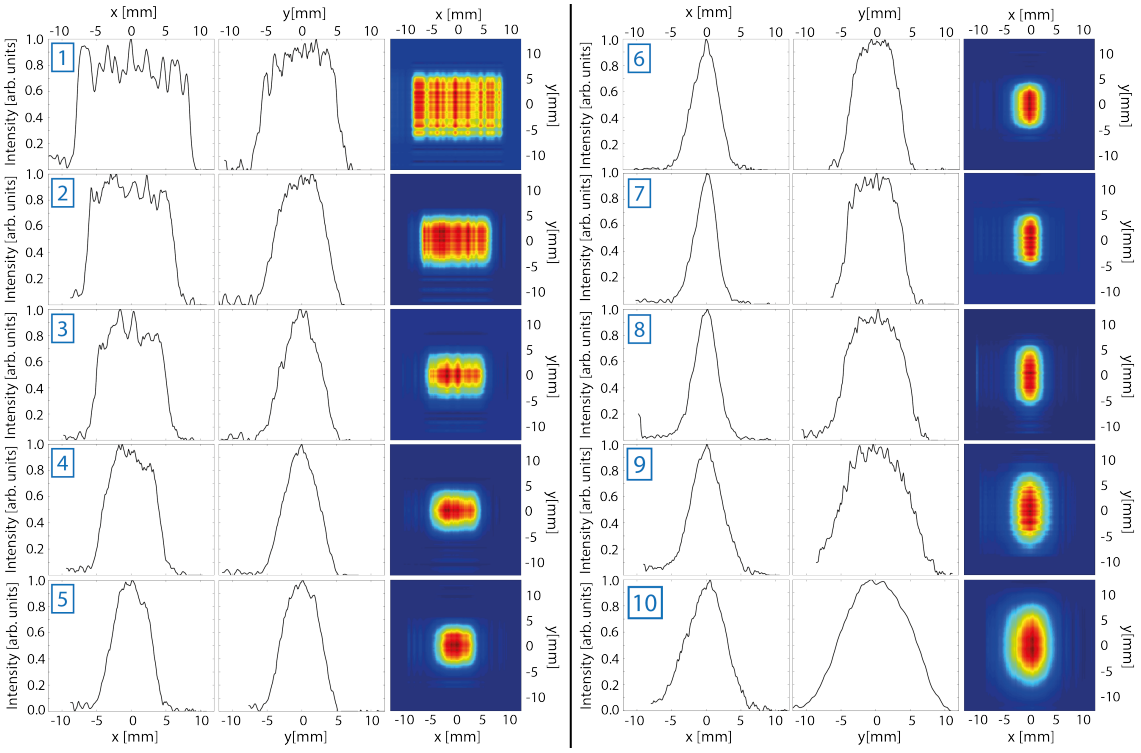

Figure 9.3: Measured spatial laser beam profiles at distances relative to the output window of the laser head. The horizontal (x) and vertical (y) laser beam profiles of 10 different positions along the laser beam path was recorded. These positions together the horizontal and vertical beam widths are listed in Tab. 9.1.

window of the laser head were recorded, shown in Fig. 9.3. In these measurements, the total laser output power is constantly held at 50 W for all profile scans. For each measured beam intensity profile, the horizontal (x) and vertical (y) beam widths (defined by a 90 % transmission power) are determined. In Tab. 9.1, the resulting beam widths $x_{90\%}$ and $y_{90\%}$ (radii which encompasses 90% of the laser power) are listed, together with the distances z_{laser}, relative to the output window of the laser head.

The measured beam widths $x_{90\%}$ and $y_{90\%}$ as a function z_{laser} can be used to determine the quality of the laser beam by the Gaussian beam quality factor M^2. The laser beam width of a laser with a Gaussian intensity profile can be described by [174]

$$w\left(z_{\text{laser}}\right) = w_0 \sqrt{1 + \left[\frac{M^2 \lambda \left(z_{\text{laser}} - z_0\right)}{\pi w_0^2}\right]^2}, \tag{9.7}$$

where λ denotes the laser wavelength and w_0 represents the width in the beam waist, which is located at z_0 with respect to the laser exit window. The measured horizontal and vertical beam widths along the propagation axis are plotted in Fig. 9.4, together with a fit using Eq. 9.7. Assuming independent diffractive propagation in the horizontal and vertical direction, both fits show an overall good agreement

Profile	z_{laser} [m]	$x_{90\%}$ [mm]	$y_{90\%}$ [mm]
1	0.063	5.2	7.5
2	0.313	4.2	5.7
3	0.463	3.7	4.9
4	0.588	3.6	4.2
5	0.713	3.5	3.6
6	0.838	3.6	3.2
7	0.988	4.0	2.9
8	1.162	4.9	3.2
9	1.363	6.0	4.4
10	1.488	7.4	4.9

Table 9.1: Measured horizontal ($x_{90\%}$) and vertical ($y_{90\%}$) laser beam widths (that includes 90% of the total laser power) at distances (z_{laser}) relative to the laser head. The corresponding recorded spatial laser beam profiles are illustrated in Fig. 9.3.

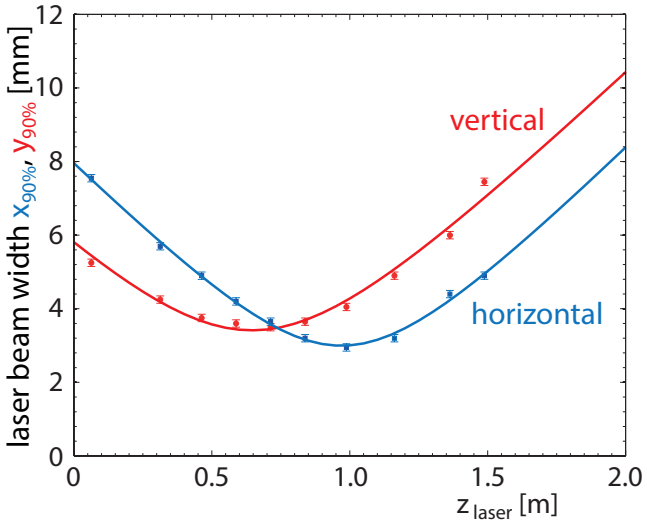

Figure 9.4: Measured horizontal ($x_{90\%}$) and vertical ($y_{90\%}$) laser beam widths as a function of the distance z_{laser} relative to the laser output window.

	w_0 [mm]	M^2	z_0 [m]
Horizontal	3.0	88	0.97
Vertical	3.4	97	0.65

Table 9.2: Horizontal and vertical laser beam parameters, which have been derived using Eq. 9.7.

with the recorded data sets. The beam parameters, derived from these two fits are summarized in Tab. 9.2. Horizontally, the laser beam forms a beam waist in a distance of ∼1 m from the laser head. In this focal point, the horizontal beam width (containing 90% of the total laser power) is measures as $x_{90\%} = 3$ mm. In the vertical direction, the beam waist is created at a distance of 0.65 m, with a beam width of $y_{90\%} = 3.4$ mm. The expected poor beam is quantified by $M^2 \sim 100$.
It should be noted that these measurements, which characterized the emitted laser beam, were performed at a relatively low total output power (50 W) and that the divergence of the resultant laser beam increases at high power operation due to thermal effects. These thermal effects result in a drop in the overall beam quality. As a consequence, the emitted beam may overfill the collimating optics. Thus, a fraction of the photons can miss the microlenses and end up outside the nominal beam. At continuous operation at maximum power, up to 15% of the laser power dissipates in so-called side lobes [166].

9.3 Photodetachment chamber

To photodetach an ion beam and fly the resultant neutral beam along the CSR transfer line, the laser beam (previously described in Sec. 9.2) has to be coupled into a vacuum chamber. A vacuum chamber was designed and constructed to permit the merging of the laser beam with the transported ion beam at a shallow angle of $\Theta \sim 2.7°$, thus increasing the effective photodetachment efficiency. This photodetachment (PD) chamber with a total length of ∼2 m, as depicted in Fig. 9.5, consists of two DN160CF vacuum pipes each with a length of ∼0.8 m and a six-way cross. This six-way cross (DN160CF), placed at the center of the PD chamber, permits attachment of a turbomolecular pump (TMP) while providing access to the laser beam path for alignment. The laser beam is guided through a laser windows integrated in a custom-built reducer flange (DN160-DN40) at both the entrance and exit of the vacuum chamber. To achieve a high laser beam transmission, these windows are anti-reflection (AR) coated on both sides, reducing the reflection to $< 0.3\%$ for lasers operating at wavelengths of 800±30 nm. After passing through the system and exiting the second laser window, the laser beam is then dumped in a power meter (Coherent Power-head PM3K), which continuously monitors the laser power. The ion beam, which propagates along the central axis of the PD chamber, is vertically

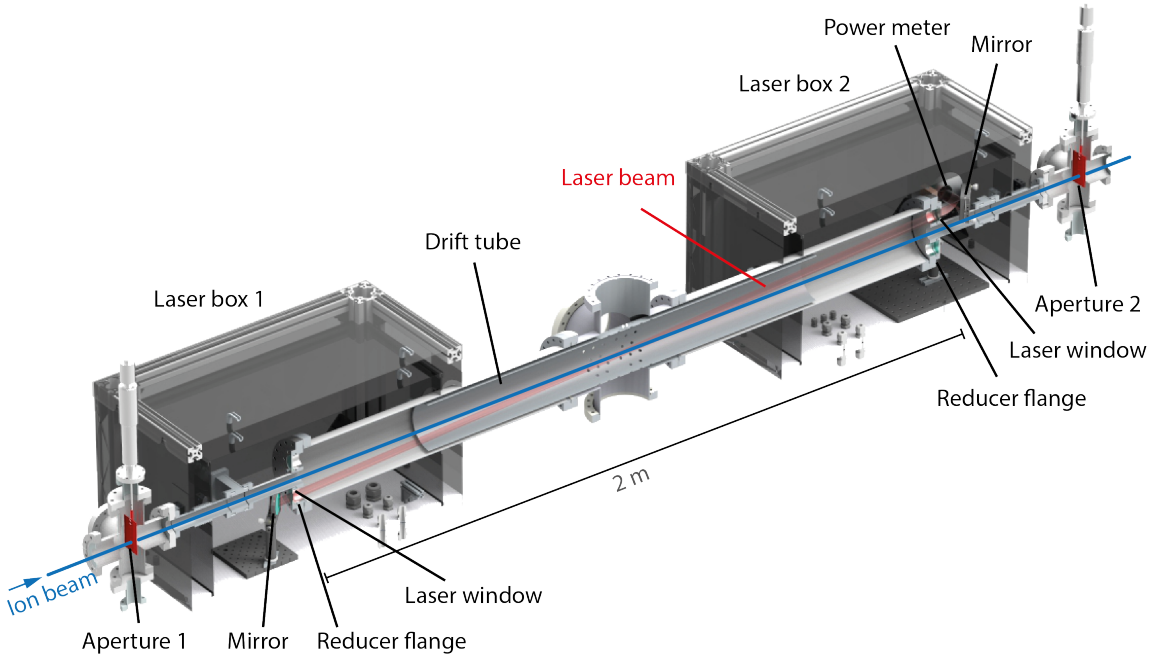

Figure 9.5: Schematic overview of the photodetachment chamber.

crossed by the laser beam at an angle of 2.7°. On entering and exiting the PD chamber the ion beam passes two circular apertures, separated by a distance of 2.9 m. For merged beams experiments, to restrict and define the center-of-mass collision energy, it is desirable to minimize the relative collision angle, thus the apertures are employed to collimate the neutral beam. This beam emittance cut limits the horizontal and vertical displacement (x,y), and the maximum angles (x′,y′) of the transported beam. The transmitted fraction of beam's phase space can be determined by the size of the utilized apertures at these positions. For a diameter of 4.5 mm for both apertures (a diameter proposed for first experiments), the maximum beam displacement relative to the central path is limited to 2.25 mm at these two positions, confining the maximum angle of the transmitted particles to $\frac{4.5\ \text{mm}}{2900\ \text{mm}} \approx 1.5$ mrad. As a result, the maximum area in phase space, that is transmitted through these apertures, can be calculated to $A = \pi\epsilon = 6.75$ mm mrad. For a better understanding of this emittance restriction, a simulation is presented in Fig. 9.6. Starting with a converging particle beam, which forms a beam waist at the midpoint of the two apertures, the beam's phase space is limited by the two apertures (d = 4.5 mm). The horizontal and ver-

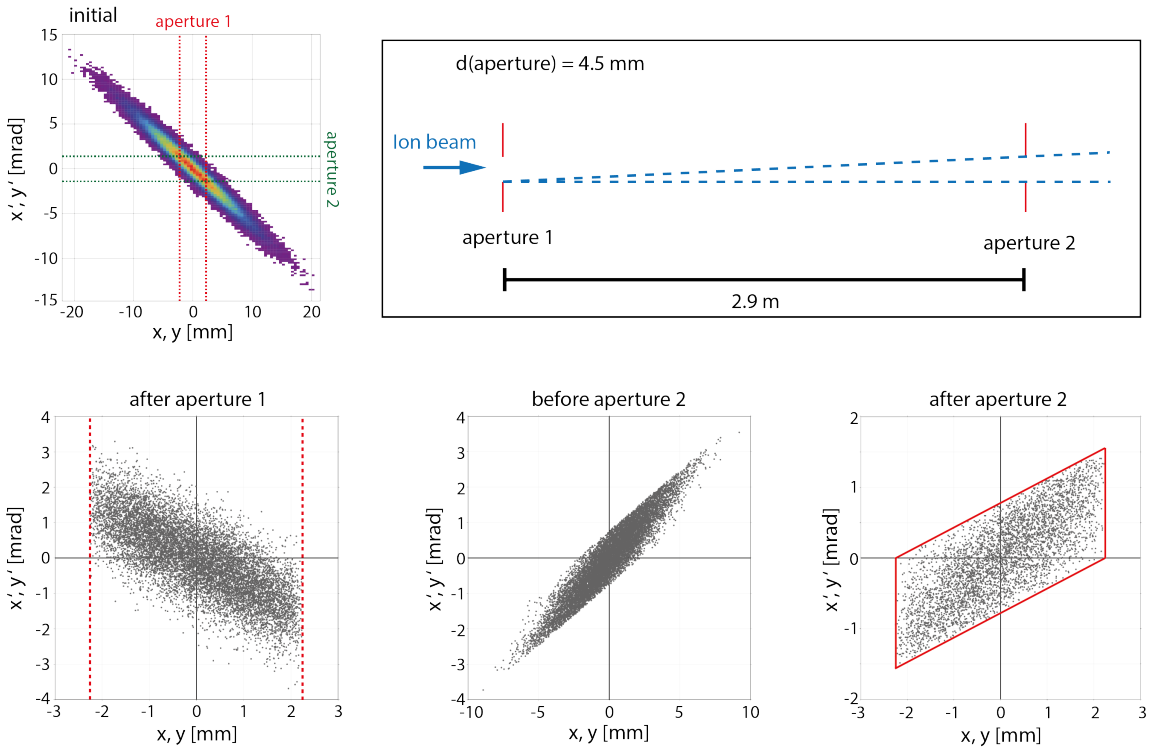

Figure 9.6: Simulation of a particle beam, which is collimated by two apertures, 4.5 mm in diameter, placed at a distance of 2.9 m.

tical distribution in x,y and x′,y′ are both mapped to a Gaussian distribution with a beam emittance of $\epsilon^{90\%} = 14.4$ mm mrad, as illustrated in Fig. 9.6. Aperture 1 transmits only particles which have a displacement smaller than 2.25 mm relative to the central beam path. This spatial limitations are indicated by the red dashed lines. In the following drift section, the particle beam propagates ballistically. After passing its focal point the beam size increases towards aperture 2. This diverging beam is then limited by aperture 2, resulting in a phase space distribution which is bounded by a parallelogram, as indicated by the red solid lines in Fig. 9.6. This area reflects the maximum emittance that is transmitted through both apertures.
The kinetic energy of the neutral beam, to be injected into the CSR, is determined by the kinetic energy of the photodetached anions. To perform velocity-matched merged-beams experiments, the kinetic energy of the two particle beams, produced on either the 60kV or 300kV ion source platform, are scaled to each other with the ratio of their masses. To fine-tune and scan the relative collision energy between the stored ion beam and the neutral beam injected into the CSR, a so-called drift tube is implemented in the center of the PD chamber, as shown in Fig. 9.5. By applying a constant voltage, this drift tube allows a fine variation of the kinetic energy of the generated neutral particle beam. Due to the electrostatic field, set up inside the tube, a negatively charged ion beam undergoes a decceleration (acceleration) at the entrance and an acceleration (decceleration) at the exit of the drift tube by applying a negative (positive) voltage. As the neutral particles are photodetached at the center of the drift tube, they posses the same kinetic energy as the decellerated (accelerated) parent anion. However, on exiting the drift tube the neutral particle beam is no longer influenced by the retarding (accelerating) electric field. Thus, the neutral particles kinetic energy will remain lower (higher) after passing the drift tube, while the kinetic energy of the ions is set back to their original value.
As not to negatively influence the neutral particle's energy distribution, it is essential that in the laser interaction region, the electric field set up inside the drift tube is uniform. This fundamental requirement in the design of the drift tube, must also be compatible with providing sufficient clearance for the laser beam to pass unhindered through the drift region. In the final design of the drift tube, a length of 1.2 m and inner diameter of 125 mm was chosen. To examine the ion-optical operation, a simulation of charged particles, propagating through the drift tube, was performed. In this SIMION simulation, a singly negatively charged particle with a kinetic energy of 30 keV is guided along the central path through the drift tube, which is held at

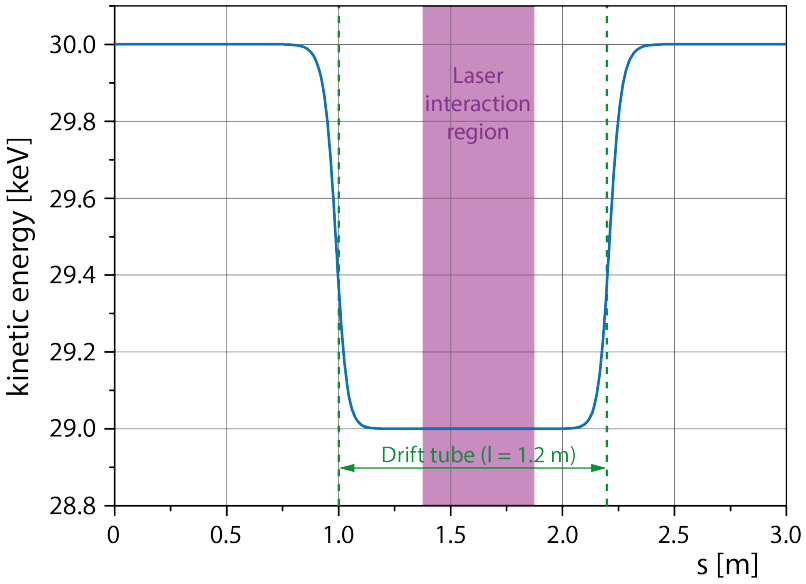

Figure 9.7: Kinetic energy E_{kin} of a singly negatively charged particle as a function of the flight path s. Propagating along the central path, the kinetic energy of the particle is manipulated via a drift tube, held at a potential of -1 kV. The geometrical position of the tube (which has an inner diameter of 125 mm and length of 1.2 m) is indicated by the green dashed line. The position of the laser interaction region, relative to the drift tube, is represented by the purple area.

a potential of -1 kV. To determine the region in which the ion reaches a constant kinetic energy inside the drift tube, the kinetic energy E_{kin} of the particle is recorded over the flight path s. As shown in Fig. 9.7, the singly negatively charged particle with an initial kinetic energy of 30 keV is first decelerated by the electric field of the drift tube, reaching a minimum kinetic energy of 29 keV, and is again accelerated to its original kinetic energy after passing the tube. The geometrical position of the entrance and exit of the drift tube is indicated by the green dashed line. A broad plateau in the kinetic energy curve as a function of the flight path is formed around the center of the drift tube, which encompasses the length of the laser interaction region in its entirety (indicated by the purple area in Fig. 9.7). Thus, all neutral particles, which are photodetached from the parent anion beam, will possess a kinetic energy of 29 keV.

In the physical design, the drift tube is comprised of a stainless steel pipe, which has an inner diameter of 125 mm and a wall thickness of 2 mm. To ease the mounting of the photodetachment section, the drift tube (total length of 1.2 m) is split into two pipes, each with a length of 0.6 m. With an outer diameter of 129 mm, each pipe is mounted on four small half spheres with a thickness of 10.5 mm, resulting in

an axially centered position inside the DN160 vacuum pipe (with an inner diameter of 150 mm). These half spheres are produced of a machinable ceramic (Macor), to electrically insulate the drift tube from the grounded vacuum pipe. Placed in their final position inside the photodetachment section, the two pipes are connected via a sheet-metal ring surrounding the gap between the two pipes. Via this metal ring, a potential of up to ±1 kV can be applied to the drift tube.

9.4 Beam cleaner

As previously discussed, only a fraction of the anions, transported through the PD chamber, are photodetached by the laser beam. This results in a particle beam consisting of a superposition of neutral atoms and anions leaving the PD chamber. In order to inject a pure neutral atomic beam into the CSR, the remaining anions have to be first removed using either an electric or magnetic fields. During experimental measurements, the CSR transfer line must ultimately cycle between transportation of ions into the CSR and then photodetachment of anions from the second platform for the production of a neutral beam. To this end, each ion-optical element (including the beam cleaner) must be capable of fast switching ($\sim \mu$s) the applied potentials. Given the relative simplicity and robustness, an electrostatic parallel-plate deflector was selected and subsequently designed, simulated and constructed to separate the anion beam from the neutral beam after the PD process. This parallel-plate deflector, the so-called beam cleaner, deflects the anions into a Faraday cup (see Sec. 8.3.2), where the beam current is monitored. The equation of motion for a particle in a uniform

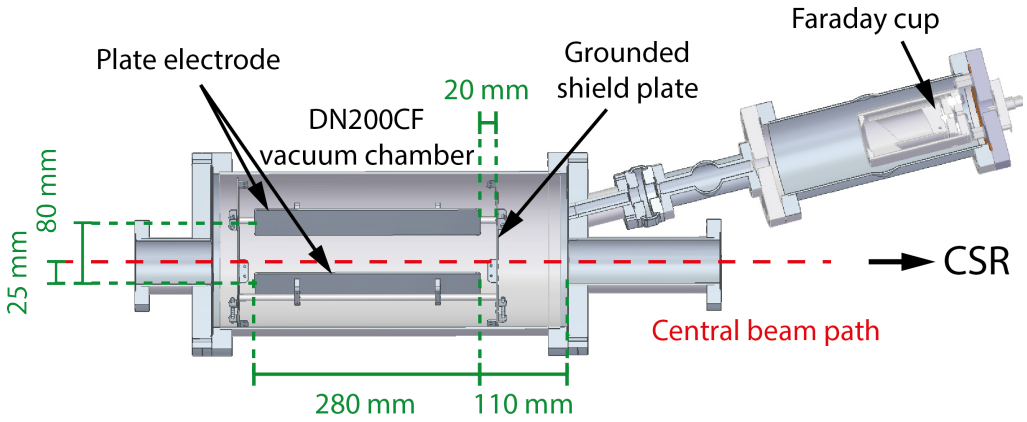

Figure 9.8: Schematic overview of the beam cleaner.

electric field, generated between two parallel plate electrodes, is well known [176]. To define a suitable geometry for the beam cleaner, a simple numerical simulation was employed. By limiting the maximum plate potential to ±20 kV (due to electrical breakdown design requirements), the optimal plate configuration, which allows a 50 mm clearance of the transported ion beam (at a maximum kinetic energy of 300 keV), was found to have a 80 mm plate separation with a horizontally offset of 25 mm relative to the beam path, as illustrated in Fig. 9.8. The two electrodes of the beam cleaner, formed from 2 mm sheet metal (stainless steel), have a height of 130 mm and a length of 280 mm. Grounded shield plates are placed at a distance of 20 mm from the entrance and exit of the parallel plates, as shown in Fig. 9.8. These shield plates, which reduce the fringing field of the beam cleaner, have a rectangular aperture of 70 mm × 90 mm, permitting both beams (the neutral and the deflected beam) to pass the deflector.

For a more in-depth verification of this geometry configuration, a simulation of the beam cleaner was performed using SIMION. In this simulation (see Fig. 9.9), a collimated particle beam with a maximum horizontal and vertical displacement of 15 mm is guided through the beam cleaner. This particle beam contains neutral and singly negatively charged particles, both possessing a kinetic energy of 300 keV. With a potential of ±20 kV, applied to the electrodes of the beam cleaner (highlighted in red), the anion beam is deflected by 14.5° relative to the central beam path. The neutral beam (highlighted in blue), unaffected by the electric field, propagates ballistically.

For this configuration, the beam cleaner assembly was designed to fit a DN200CF vacuum pipe. In Fig. 9.8, the custom-built vacuum chamber is depicted. The

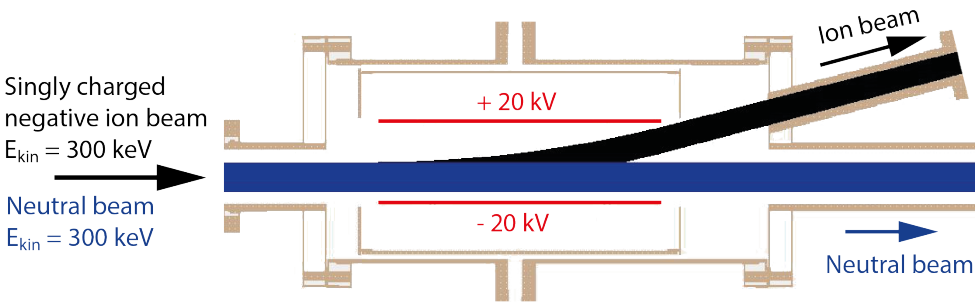

Figure 9.9: Ion-optical simulation of a collimated particle beam (30 mm in diameter), consisting of neutral and singly negatively charged particles with a kinetic energy of 300 keV, passing the beam cleaner. By applying a potential of ±20 kV to the electrodes, the ion beam is deflected by 14.5°, while the neutral particles continue unaffected.

deflector plates, housed in the DN200CF vacuum pipe, are positioned at a distance of 110 mm towards the exit of this pipe. The back of the deflector chamber is closed, using a reducer flange, on which two vacuum pipe nipples are mounted. A DN63CF pipe is mounted parallel to the beam axis, transporting the beam particles into the CSR and a DN40CF pipe is mounted at an angle of 14.5° to the beam axis, through which the deflected ion beam is guided onto the attached Faraday cup. The assembled beam cleaner was finally electrically tested in vacuum and successfully held a potential of ±20 kV applied to the plate electrodes.

Chapter 10

Final design of the CSR transfer line

In this chapter, an overview of the CSR transfer line, comprised of the previously discussed ion optical steering and diagnostic elements, is presented. To ensure that the vacuum requirements of the CSR transfer line were met, vacuum simulations of the CSR transfer line were performed. To meet the required residual gas pressure target, in the range of 10^{-11} mbar, inside the final chamber of the CSR transfer line, the injection chamber design is presented here along with the measured vacuum conditions. In this chapter, the baseline residual gas pressure as a function of the beamline path is estimated using the VakTrak simulation software [157], in Sec. 10.1, while Sec. 10.2 outlines the design of the final CSR transfer line.

10.1 Vacuum simulations

Using several turbo molecular pumps (TMP) situated along each of the two beamlines, which are built of stainless steel vacuum chambers (mainly sealed via copper gaskets), a residual gas pressure in the order of 10^{-9} mbar can be expected. To fulfill the required vacuum conditions in the final chamber of the transfer line, a differential pumping vacuum system, suitable for undergoing a bake-out of temperatures of $\sim$ 200° C, is needed to minimize the outgassing rate of the chamber. Dependent on the pumping time, the outgassing rate for stainless steel can be effectively reduced from $\sim 10^{-10}$ l s^{-1} cm^{-2} to $\sim 10^{-12}$ l s^{-1} cm^{-2} by the bake-out process [177]. TMPs are particularly suited to pump heavier gas species, e.g. N_2, O_2 and Ar, but the ultimate pressure which they can achieve is limited by their compression ratio. To achieve residual gas pressures down to 10^{-11} mbar, where the predominant gas species is H_2, getter pumps in combination with titanium-sublimation pumps are preferable.

A titanium-sublimation pump (TSP) coats the inner surface of the surrounded vacuum chamber with titanium, which is thermionically ejected from a filament. Chemically active gas molecules combine with this evaporated titanium layer. Despite the relatively high pumping rate of several $\mathrm{l\,s^{-1}\,cm^{-2}}$ of exposed surface, inert gases (e.g. noble gases) are not pumped at all. Therefore, TSP are typically used in conjunction with ion-getter pumps (IGP). In these pumps, residual gas particles are ionized via electron impact. The resulting positively charged particles are then accelerated via an electrical field towards the cathode, where they are captured in its surface. The combination of the high pumping speed of H_2 provided by the TSP and the pumping of inert gases from a IGP is suitable for generating residual gas pressures down to the 10^{-11} mbar regime.

The final chamber, known as the injection chamber in the CSR transfer line is comprised of two distinct differential pumping sections, shown in Fig. 10.1. The first section of the injection chamber, which also houses the quadrupole triplet QP4, is pumped by a TMP (Pfeiffer TMU 521 YP, CF160), backed by a fore-line scroll pump (Edwards nXDS10i). This section is bounded by two small diameter tubes, which limit the gas conductance between the three regions and thus, creating differential pumping between these sections. In the direction of the ion source, the vacuum pipe system is reduced to a DN40CF for a length of $\sim$ 200 mm, and towards the second section of the injection chamber an internal pipe system with an inner diameter of 40 mm and a length of 200 mm is attached. As shown in Fig. 10.1, this differentially pumped section is connected to the two TSP and IGP before being finally connected via DN40CF vacuum pipes (length of 300 mm) to the external wall of the CSR. Ion beam simulations were employed to determine the minimum size for the inner diameter of these tubes, as discussed in Sec. 8.2. To avoid further beam losses in the CSR transfer line, due to the differential pumping section, the minimum clearance can be calculated relative to the acceptance of the beamlines (according to Eq. 8.6 or Eq. 8.8). The second section is equipped with a combination of two TSP (Pfeiffer USP 035) and an IGP (Agilent VacIon Plus 75). Each of the two titanium filaments (TSP) are surrounded by DN160 vacuum pipes of $\sim$ 500 mm in length.

The vacuum conditions in the two beamlines are simulated using the VakTrak simulation software [157]. As shown in Fig. 10.2, these simulations indicate that this system is suitable in achieving residual gas pressures $< 10^{-9}$ mbar in the first section and $< 10^{-10}$ mbar in the second section of the injection chamber, after bake-out. In initial beamline tests, using a selection of ion sources on the source platform, gas

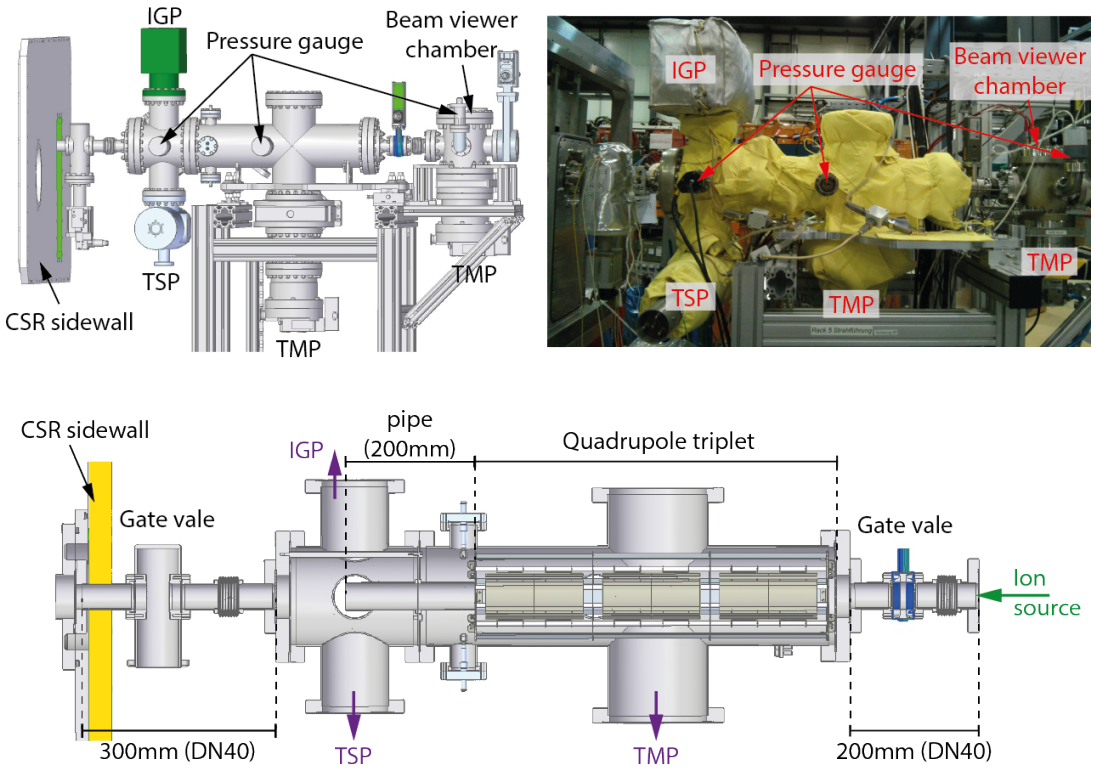

Figure 10.1: CAD drawing and photograph of the sideview of the injection chamber, illustrating the layout of the vacuum system. The top two pictures show the injection chamber, implemented in the CSR transfer line, between beam viewer and CSR. The photograph shows the entire injection chamber wrapped in insulation for bake-out. On the left-hand side, a CAD drawing of the injection chamber is shown, using the same perspective. The CAD drawing in the bottom picture shows a vertical cut through the injection chamber, illustrating the internal structure of the differential pumping system. Using a turbo molecular pump (TMP), ion-getter pump (IGP) and titanium sublimation pump (TSP), a residual gas pressure in the 10^{-11} mbar regime is maintained in the last section of the injection chamber.

pressures of $\leq 10^{-5}$ mbar were measured at the vacuum chamber in front of the first quadrupole triplet of the 60kV beamline and directly after the 300kV ion source platform. Using this value as an upper limit for the starting parameter in a vacuum simulation, the baseline residual gas pressure can be estimated as a function of the paths along each of the two beamlines, as shown in Fig. 10.2. In these simulations, the predominant residual gas species is assumed to be H_2, which represents the worst case scenario, as the conductance of the vacuum pipes decreases for gas species with higher masses [178]. In addition, the utilized TMPs pump H_2 less efficiently than heavier species. Therefore, the resulting residual gas pressures (indicated by the red line in Fig. 10.2) represent an upper limit for the first part of the transfer line. Us-

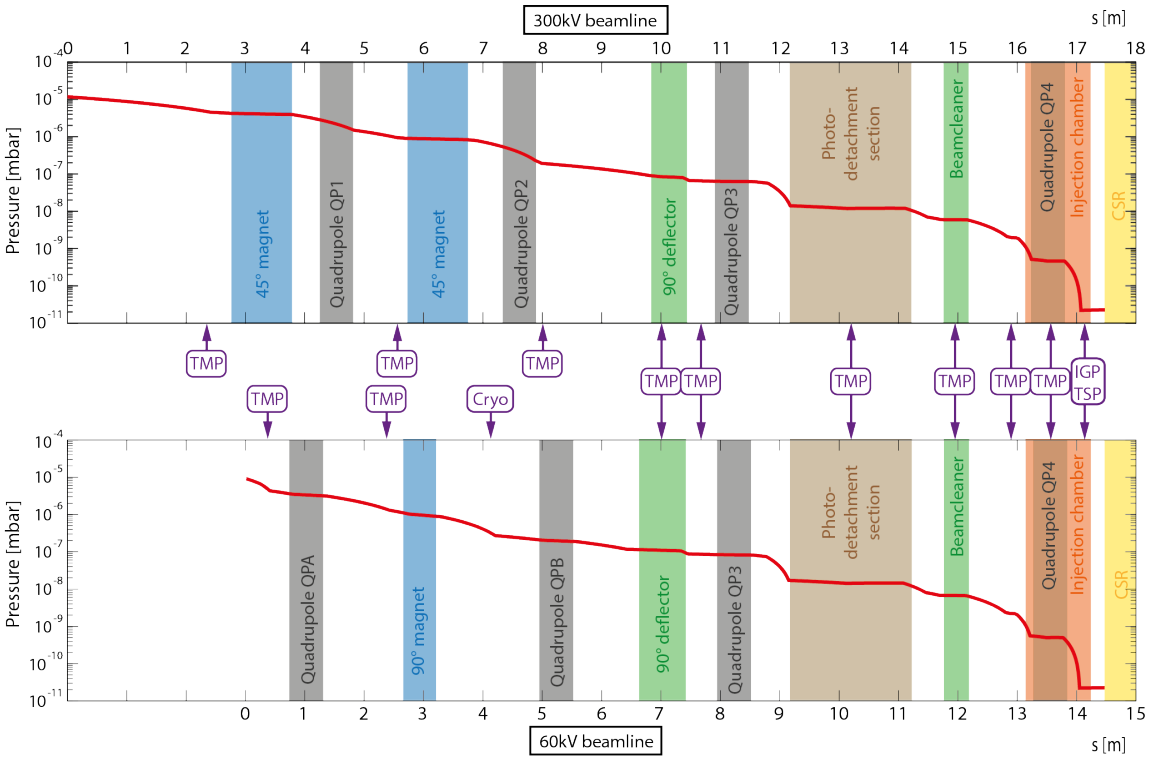

Figure 10.2: Vacuum simulation of the 300kV (top diagram) and 60kV beamline (bottom diagram) using the VakTrak simulation software [157], in order to estimate the baseline residual gas pressure as a function of the paths along each of the two beamlines. The locations of the utilized vacuum pumps are indicated by the purple arrows. For better orientation, the individual sections of the beamlines are highlighted.

ing solely stainless steel vacuum chambers, the outgassing rate for unbaked systems can be estimated as 10^{-10} l s^{-1} cm^{-2}, and for baked systems as 10^{-12} l s^{-1} cm^{-2} [177]. The pumping speed of the vacuum pumps are adopted from the respective manuals, which specify pumping speeds in the region of ∼200 - 550 l s^{-1} for TMP [179, 180, 181, 182], 50 l s^{-1} for the IGP [183] and 3 l s^{-1} cm^{-2} for the ISP [184]). As the vacuum system of the two beamlines are connected by the 90° deflector chamber, an appropriate mutual gas load is considered in the two VakTrak simulations. The vacuum simulations, demonstrated in Fig. 10.2, show that the targeted residual gas pressure of $< 10^{-10}$ mbar in front of the CSR can be satisfied, using the presented vacuum system.

This differential pumping section of the injection chamber has been implemented and tested in the CSR transfer line. The entire injection chamber was baked for one week at 200° C and subsequently leak-checked. A leak rate $< 5{\cdot}10^{-12}$ l s^{-1} cm^{-2} was observed. Using a cold-cathode ionization gauge (Edwards WRG-S DN40CF), the

gas pressure was measured to be $\sim 2 \cdot 10^{-9}$ mbar in the vacuum chamber of the beam viewer (see Fig. 10.1). After activation of the titanium-sublimation pumps and the subsequent pumping of the injection chamber for a week, a residual-gas pressure of $\sim 5 \cdot 10^{-11}$ mbar was observed (using a hot-cathode vacuum gauge (Leybold IE 414)). These measurements, which are in reasonable agreement with the estimates obtained from the VakTrak simulations (shown in Fig. 10.2), demonstrate a suitable residual gas pressure.

10.2 Overview of the CSR transfer line

The layout of the CSR transfer line is shown in Fig. 10.3. Starting on either the 60kV or 300kV ion source platform, the ion beam is transported via the ion-optical elements, as presented in Sec. 8.2 (see Fig. 8.3 and Fig. 8.6). In both beamlines, dipole magnets (labeled in blue in Fig. 10.3) are used to select only a specific ion beam species, as discussed in Sec. 8.3.1. These two beamlines are merged together using the 90° deflector with hole (discussed in Sec. 8.3.4) and are comprised of the elements presented in the previous Chap. 8. After careful design, simulation and testing, the CSR transfer line successfully meets all the stringent requirements placed upon it. A photodetachment section is embedded in the transfer line to generate a fast neutral atom beam (discussed in Chap. 9), which is subsequently merged to the ions stored in the CSR. Fast ($\sim \mu$s) switching of the potentials applied to the 90° deflector and all subsequent ion-optical elements of the transfer line allows the interchange between ion beams generated on either the 60kV or the 300kV source platform. The positioning of the photodetachment section after the merging section facilitates the neutral beam production via photodetachment from either beamline. To prevent the remaining negatively charged particles, which are not photodetached by the laser photons, from entering the CSR, they are deflected via the subsequent beam-cleaner. Using a Faraday cup to dump these particles, the ion current can be detected to monitor the beam stability during experiments. The structure of the injection chamber (discussed in Sec. 10.1) reduces the residual gas pressure to a final range of 10^{-11} mbar, to maintain the vacuum conditions of the cryogenic storage ring. The final quadrupole triplet (QP4) of the CSR transfer line, which is integrated in the injection chamber, is employed to match the twiss parameters of the injected beam to the CSR machine parameters, as discussed in Sec. 8.2.

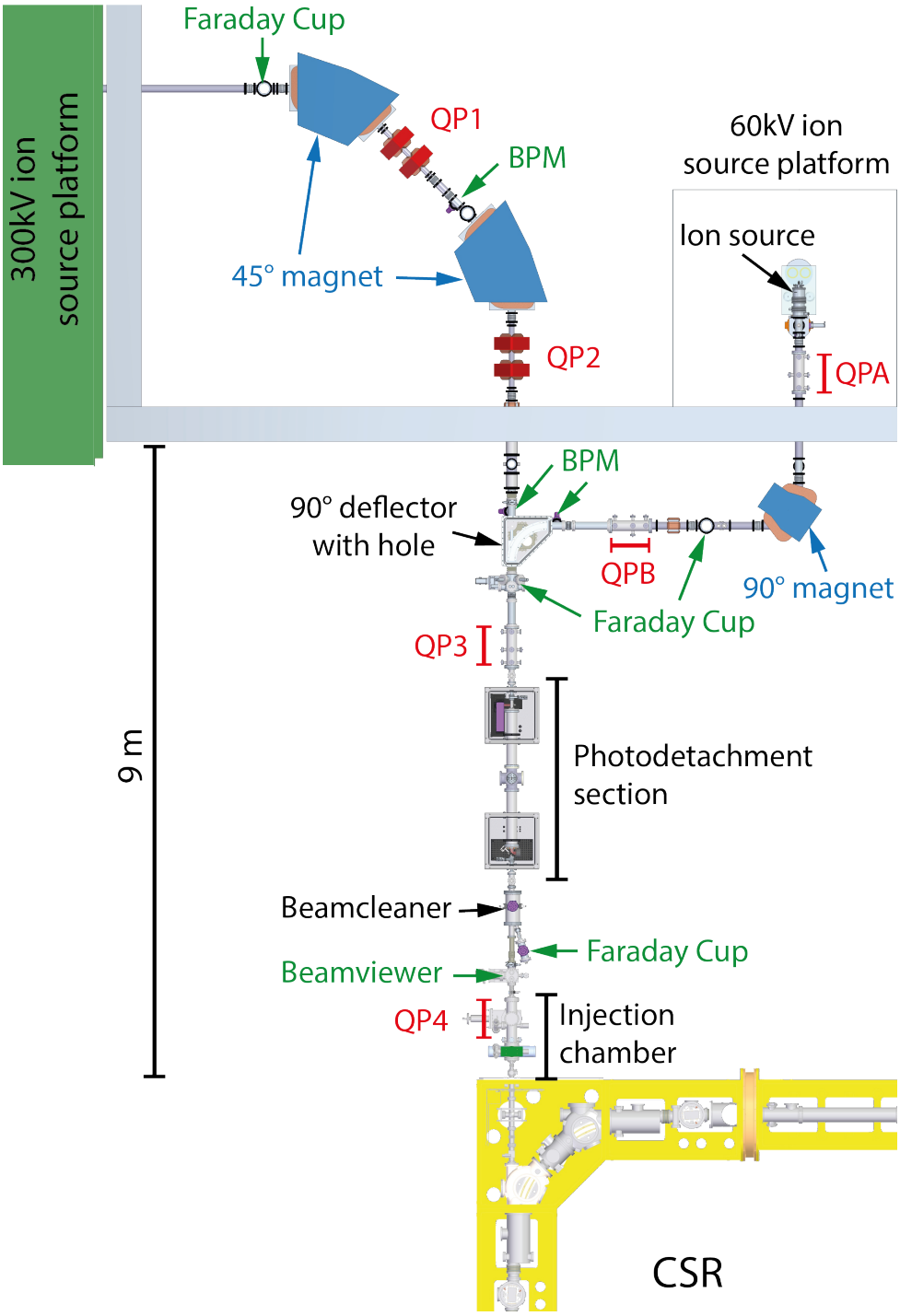

Figure 10.3: Overview of the final CSR transfer line. The ion beams, generated on either the 300kV or the 60kV source platform, are selected by the mass-to-charge ratio using dipole magnets (blue labels). The quadrupole elements (labeled in red), which focus the ion beam, have the same nomenclature used in the ion-optical simulations, shown in Sec. 8.2. The monitors (discussed in Sec. 8.3.2), which are implemented for beam diagnostics are labeled in green. The two beamlines are merged via an electrostatic 90° deflector with a hole, which enables a fast switching of the transported ion beam species. In the subsequent photodetachment section, a fraction of the negatively charged ion beam can be neutralized using a high-power diode laser. After removing the remaining charged particles via the beam cleaner, the generated neutral beam travels along the first straight section of the CSR, and subsequently are superimposed to the stored ion beam.

Chapter 11

Test measurements

In Sec. 10.2, the ultimate layout of the CSR transfer line was presented. Prior to construction of this final CSR transfer line, a test beamline was assembled to perform tests of the vacuum system, the ion beam transport and the photodetachment efficiency. The layout of this test beamline, shown in Fig. 11.1, allows the continued use of the 300kV beamline for the commissioning of the CSR, while the 60kV beamline can be used independently to perform benchmark measurements of the ion beam transport and the photodetachment.

In a first measurement, the transverse emittance of an ion beam transported along the 60kV beamline was determined using the quadrupole variation method. In this method (discussed in Sec. 11.1.1), the twiss parameters of the guided ion beam are determined at a particular position. Feeding these experimentally obtained beam parameters back into the transport matrix simulations helps to verify and optimize the ion beam transport.

To test the functionality of the photodetachment section (discussed in Chap. 9), it was first installed on the test beamline to conducted benchmark measurements. Using the setup shown in Fig. 11.1, preliminary measurements of the photodetachment efficiency have been performed. Merging a high-power (2 kW) laser beam (λ_{ph} = 808 nm) with a well-defined, negatively charged ion beam (C^-, O^-), the neutralized particles (C, O) were measured as a function of the laser power. In these measurements, the absolute photodetachment efficiency was derived for various ion beam kinetic energies.

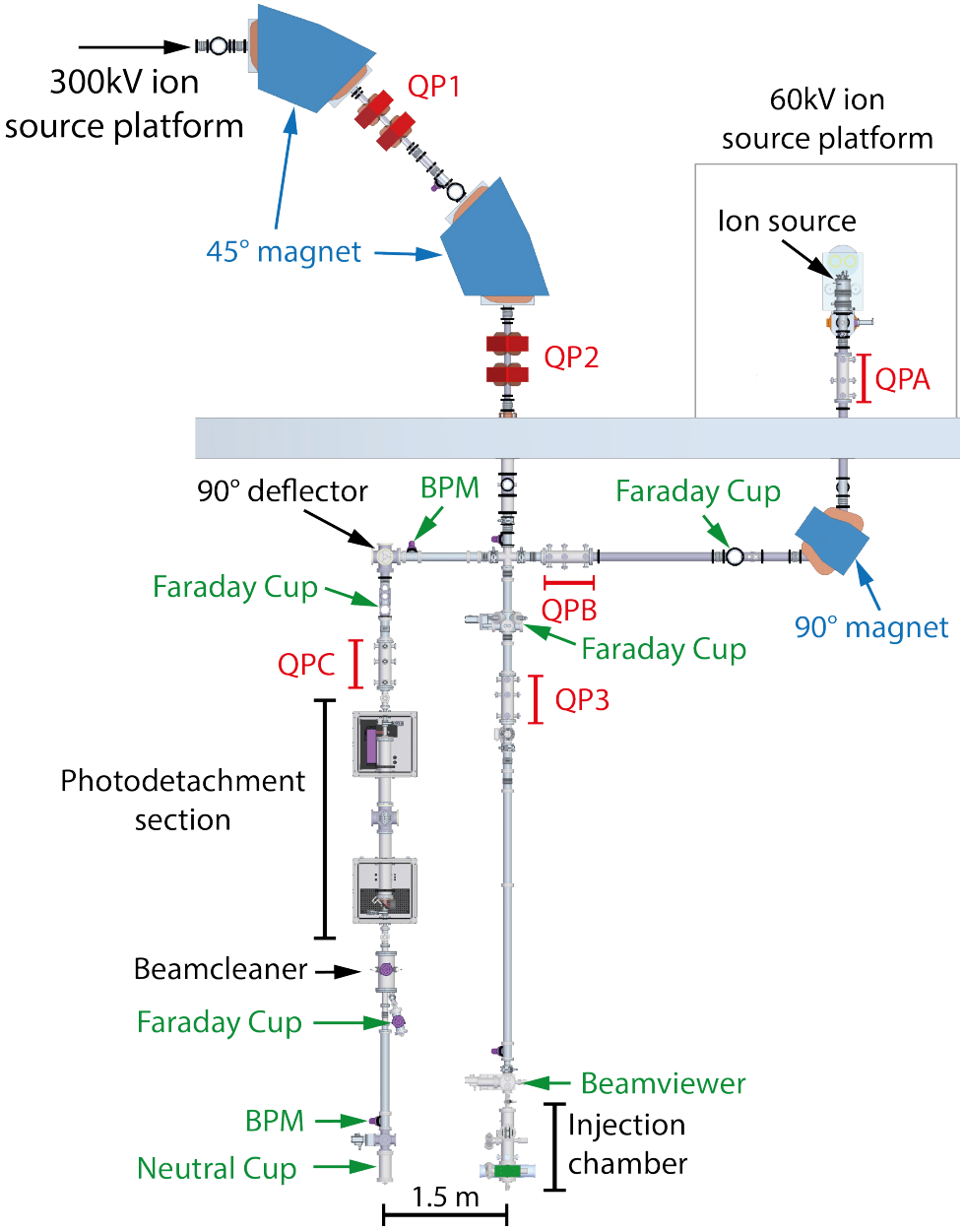

Figure 11.1: Layout of the test beamline. This beamline was used to perform test measurements on the 60kV beamline, while keeping the option to inject ion beams into the CSR via the 300kV beamline. Compared to the design of the CSR transfer line, shown in Fig. 10.3, the positions of the ion-optical elements and monitors of the 300kV beamline are identical. The 90° deflector with a hole, the photodetachment section and the beam cleaner are replaced by vacuum tubes. The 60kV beamline is slightly modified, in that the straight section after the 90° magnet crosses the 300kV beamline. The ions, created on the 60kV ion source platform, are deflected by a simple 90° deflector into the photodetachment section aligned parallel to the 300kV with at a distance of ∼1.5 m.

11.1 Beam emittance measurement

To gain information of the ion beam quality along the CSR transfer line, the transverse beam emittance is experimentally determined using the quadrupole variation method [185]. This method allows for the determination of the beam's twiss parameters α, β and the emittance ϵ at a particular position, using only the beam profile monitor already implemented in the beamline. Varying the strength K of a quadrupole lens that focuses an ion beam, affects the size of the beam at a particular distance from the quadrupole lens. Using the transport matrix formalism, this correlation can be utilized to determine the transverse phase space ellipses of the beam in front of the quadrupole lens (discussed further in Sec. 11.1.1).
In Fig. 11.2, the setup for the beam emittance measurement is illustrated. An ion source generates either a positively or negatively charged ion beam, which is then mass selected via a 90° magnet. The beam current of the selected ion species can be measured using a Faraday cup (see Sec. 8.3.2), placed after the magnet. The subsequent electrostatic quadrupole triplet QPB focuses the ion beam horizontally and vertically onto a beam profile monitor (BPM). This BPM, which is placed in a distance of $L_D = 1.57$ m from the exit of QPB, and measures the horizontal and vertical spatial distribution of the ion beam, as discussed in Sec. 8.3.2. The beam size at this position (pos. B) can be adjusted by varying the strength of the third quadrupole lens (QPB-3) in QPB. Measuring the horizontal and vertical beam width as a function of the quadrupole strength K in QPB-3, allows the calculation of the transverse phase space ellipses of the beam before entering QPB-3 (pos. A). Measuring the resulting beam widths in pos. B for a minimum of three quadrupole strengths K, the beam parameters α, β and ϵ can be determined at pos. A.

11.1.1 Quadrupole variation method

In the quadrupole variation method, illustrated in Fig. 11.2, the ion beam transport system consists of the quadrupole lens QPB-3 with a length L_Q and a drift section of a length L_D. As discussed in Sec. 6.2, this ion-optical system can then be described by the transport matrix R,

$$R = R_{\text{Drift}} \cdot R_{\text{Quad}} \,, \tag{11.1}$$

where R_{Drift} and R_{Quad} represent the transport matrices for a drift section and a quadrupole, respectively. In this ion-optical system, the horizontal and vertical mo-

tion of the particles are uncoupled, which allows to separate the transverse sections of the transport matrix in two 2×2 sub-matrices. The horizontal (x) and vertical (y) transfer matrix (see Appendix C) of the drift section are both given by

$$R_{x,\mathrm{Drift}} = R_{y,\mathrm{Drift}} = \begin{pmatrix} 1 & L_D \\ 0 & 1 \end{pmatrix} . \tag{11.2}$$

A quadrupole lens defocuses an ion beam in one transverse direction, while focusing in the other direction. Therefore, the horizontal and vertical sub-matrix of the

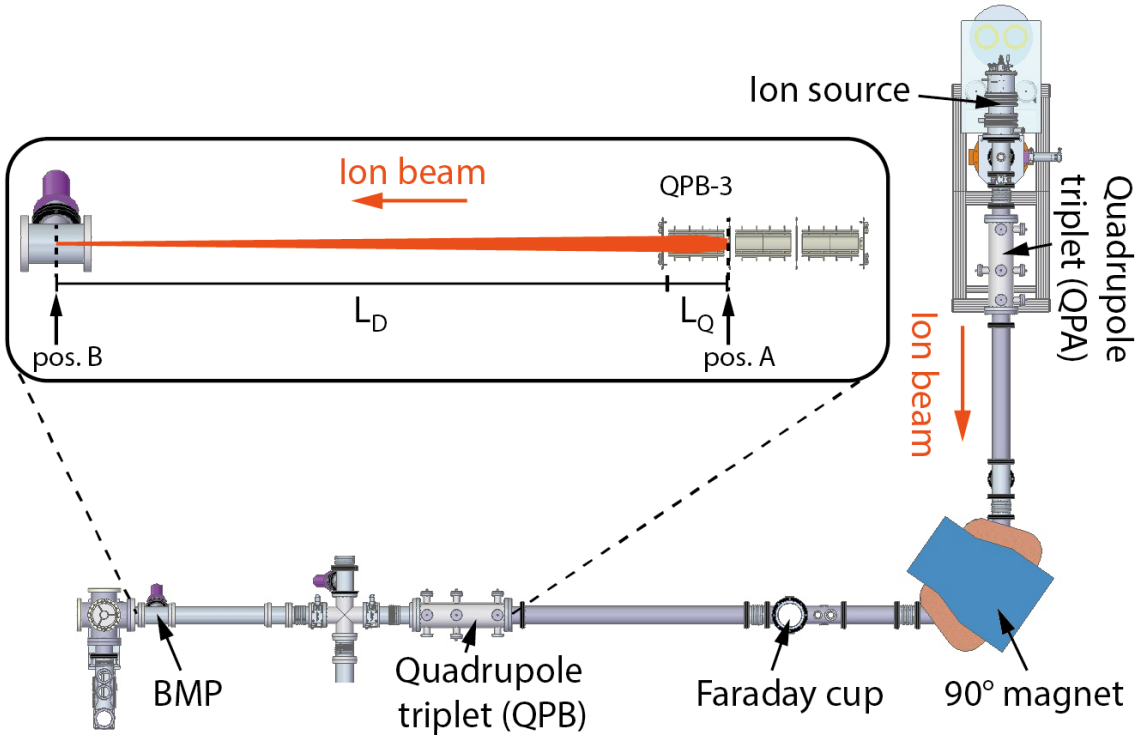

Figure 11.2: Setup for the ion beam emittance measurement, using the quadrupole variation method. Generated in an ion source, the ion beam is mass selected via the 90° magnet. The current of this ion beam is then measured using a Faraday cup, before entering the quadrupole triplet QPB. Using this quadrupole triplet QPB, the ion beam is horizontally and vertically focused onto a beam profile monitor (BPM). For different strengths applied to the third quadrupole lens (QPB-3), the beam profiles are recorded at pos. B. The measurement of the beam profiles for at least three different quadrupole settings allows the determination of the beam's twiss parameter at the entrance of the varied quadrupole lens QPB-3 (pos. A).

transport matrix R_{Quad} in Eq. 11.1 are either given by

$$R_{\mathrm{Quad,F}} = \begin{pmatrix} \cos\left(\sqrt{K}L_Q\right) & \frac{1}{\sqrt{K}}\sin\left(\sqrt{K}L_Q\right) \\ -\sqrt{K}\sin\left(\sqrt{K}L_Q\right) & \cos\left(\sqrt{K}L_Q\right) \end{pmatrix} , \tag{11.3}$$

or

$$R_{\mathrm{Quad,DF}} = \begin{pmatrix} \cosh\left(\sqrt{K}L_Q\right) & \frac{1}{\sqrt{K}}\sinh\left(\sqrt{K}L_Q\right) \\ \sqrt{K}\sinh\left(\sqrt{K}L_Q\right) & \cosh\left(\sqrt{K}L_Q\right) \end{pmatrix} , \tag{11.4}$$

where $R_{\mathrm{Quad,F}}$ and $R_{\mathrm{Quad,DF}}$ represent a focusing and a defocusing quadrupole lens with the strength K and length L_Q.
Assuming a horizontally defocusing quadrupole lens, the total ion-optical system of the quadrupole variation method, which is represented by Eq. 11.1, can be given as

$$R_x = \begin{pmatrix} R_{11} & R_{12} \\ R_{21} & R_{22} \end{pmatrix} = R_{\mathrm{x,Drift}} \cdot R_{\mathrm{Quad,DF}} \, , \tag{11.5}$$

and

$$R_y = \begin{pmatrix} R_{33} & R_{34} \\ R_{43} & R_{44} \end{pmatrix} = R_{\mathrm{y,Drift}} \cdot R_{\mathrm{Quad,F}} \, . \tag{11.6}$$

As discussed in Sec. 6.3, the phase space of a particle beam can be described by the σ-matrix. Using the twiss parameter notation, the horizontal and vertical phase space of the uncoupled particle beam is defined by

$$\sigma_x = \begin{pmatrix} \sigma_{11} & \sigma_{12} \\ \sigma_{21} & \sigma_{22} \end{pmatrix} = \epsilon_x \cdot \begin{pmatrix} \beta_x & -\alpha_x \\ -\alpha_x & \gamma_x \end{pmatrix} , \tag{11.7}$$

and

$$\sigma_y = \begin{pmatrix} \sigma_{33} & \sigma_{34} \\ \sigma_{43} & \sigma_{44} \end{pmatrix} = \epsilon_y \cdot \begin{pmatrix} \beta_y & -\alpha_y \\ -\alpha_y & \gamma_y \end{pmatrix} , \tag{11.8}$$

respectively. Assuming, that the horizontal and vertical phase space of the ion beam at pos. A (see Fig. 11.2) are represented by the σ-matrices σ_x(pos.A) and σ_y(pos.A), the beam propagation through the ion-optical system, shown in Fig. 11.2, to pos. B, can be calculated via [137]

$$\sigma_x(\mathrm{pos.B}) = R_x \cdot \sigma_x(\mathrm{pos.A}) \cdot R_x^T \, , \tag{11.9}$$

$$\sigma_y(\mathrm{pos.B}) = R_y \cdot \sigma_y(\mathrm{pos.A}) \cdot R_y^T \, . \tag{11.10}$$

Using the horizontal and vertical transport matrix R_x (Eq. 11.5) and R_y (Eq. 11.6) together with their transposed counterparts R_x^T and R_y^T in Eq. 11.9 and Eq. 11.10, respectively, the σ-matrix in pos. B can be determined for a given σ-matrix in pos. A. These systems of equations form the basis of the beam emittance measurement via the quadrupole variation method. In pos. B, the horizontal and vertical beam widths $x_{\max}$ and $y_{\max}$, which are given by

$$x_{\max}(\text{pos.B}) = \sqrt{\epsilon_x \beta_x(\text{pos.B})} = \sqrt{\sigma_{11}(\text{pos.B})}\,, \tag{11.11}$$

$$y_{\max}(\text{pos.B}) = \sqrt{\epsilon_y \beta_y(\text{pos.B})} = \sqrt{\sigma_{33}(\text{pos.B})}\,, \tag{11.12}$$

are measured as a function of the quadrupole strength K(QPB-3). In Fig. 11.3, the horizontal ion beam propagation through transport system of the quadrupole variation method is presented for three different quadrupole strengths K(QPB-3). Starting with the same beam parameters at pos. A, the beam size in pos. B varies with the applied quadrupole strength. The σ-matrix in pos. A, which remains constant during the measurement, is transformed via the transport matrix R for different values of K(QPB-3). The matrix elements σ_{11}(pos.B) and σ_{33}(pos.B), which repre-

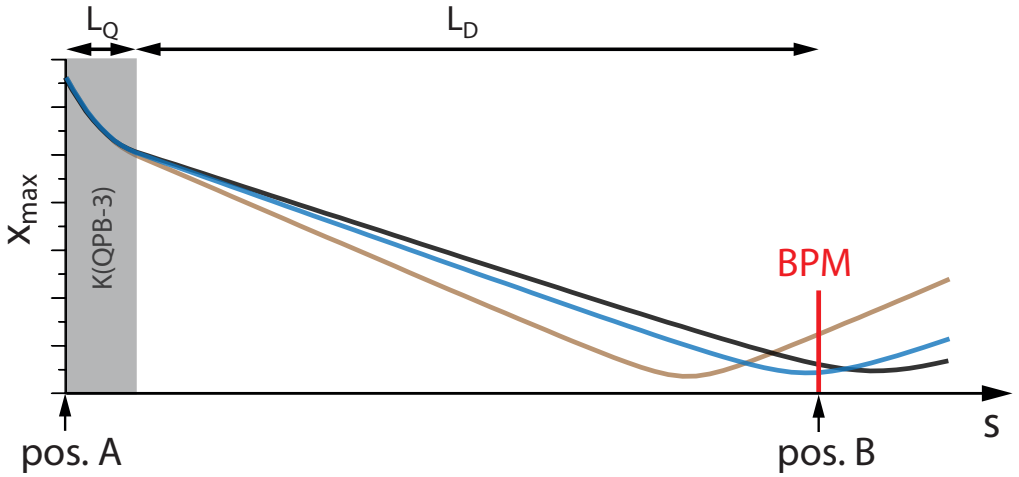

Figure 11.3: Simulated ion beam propagation to illustrate the quadrupole variation method using linear transport matrices. x_{max} represents the horizontal beam width. Starting with identical beam parameters in pos. A, the ion beam transport is shown for three different quadrupole strengths K(QPB-3). In this example, a horizontally converging beam is defocused by QPB-3 with K(QPB-3) = -14.7 m^{-2} (brown line), K(QPB-3) = -15.4 m^{-2} (blue line) and K(QPB-3) = -15.7 m^{-2} (black line), creating different beam widths in pos. B. The knowledge of the ion-optical transport system, together with the detected beam widths (x_{max}), allows to determine the beam parameters in pos. A, according to Eq. 11.13.

sent the square of the transverse beam widths, can be derived from the expansion of Eq. 11.9 and Eq. 11.10, respectively, leading to

$$x^2_{\max}(\text{pos.B}) = R^2_{11}\sigma_{11}(\text{pos.A}) + 2R_{11}R_{21}\sigma_{21}(\text{pos.A}) + R^2_{21}\sigma_{22}(\text{pos.A})\,, \qquad (11.13)$$

$$y^2_{\max}(\text{pos.B}) = R^2_{33}\sigma_{33}(\text{pos.A}) + 2R_{33}R_{43}\sigma_{43}(\text{pos.A}) + R^2_{43}\sigma_{44}(\text{pos.A})\,. \qquad (11.14)$$

The elements of the transfer matrix R are determined by the constant drift length L_D and quadrupole length L_Q, and the variable quadrupole strength K. The measurement of the horizontal and vertical width ($y_{\max}$(pos.B) and $y_{\max}$(pos.B)) for at least three different settings of K, allows then to determine all elements of σ_x(pos.A) and σ_y(pos.A) via Eq. 11.13 and Eq. 11.14, respectively.

11.1.2 Analysis

Using the setup of the 60kV test beamline, shown in Fig. 11.2, the transported transverse emittances ϵ_x and ϵ_y of a D^- beam with a kinetic energy of 35 keV, was measured. After its generation in a Cs-sputter source [186, 187], the ion beam is accelerated and subsequently guided via the quadrupole triplet QPA and the mass selective 90° magnet onto a Faraday Cup. In this measurement, the source was operated with an emphasis on stability and longevity, i.e. minimizing current fluctuations and allowing the source to run for weeks without maintenance. Using the Faraday cup after the 90° magnet, the D^- beam current was measured to $\sim$4 μA. This ion beam is then focused onto the BPM in pos. B (see Fig. 11.2) using the quadrupole triplet QPB.

For 16 different potentials applied to the third quadrupole lens of this triplet (QPB-3), the horizontal and vertical beam profiles were recorded using the BPM, as discussed in Sec. 8.3.2. The resulting beam profiles are shown in Fig. 11.4, represented by the blue lines. Both the horizontal (x) and vertical (y) beam profiles are fitted with a Gaussian distribution, indicated by the red line. A single standard deviation (1σ) is utilized as the beam width of these recorded profiles. The resulting beam widths $x_{1\sigma}$ and $y_{1\sigma}$ of the profiles 1 - 16 are listed in Tab. 11.1, together with the potential U(QPB-3) applied to the quadrupole lens QPB-3. These potentials can be converted to a quadrupole strength K(QPB-3), according to Eq. 8.13. The negative values in the quadrupole strength K(QPB-3) indicate that this quadrupole lens focuses in the vertical direction and defocuses in the horizontal. The square of the measured beam widths ($x^2_{1\sigma}$, $y^2_{1\sigma}$), also given in Tab. 11.1, are plotted as a function

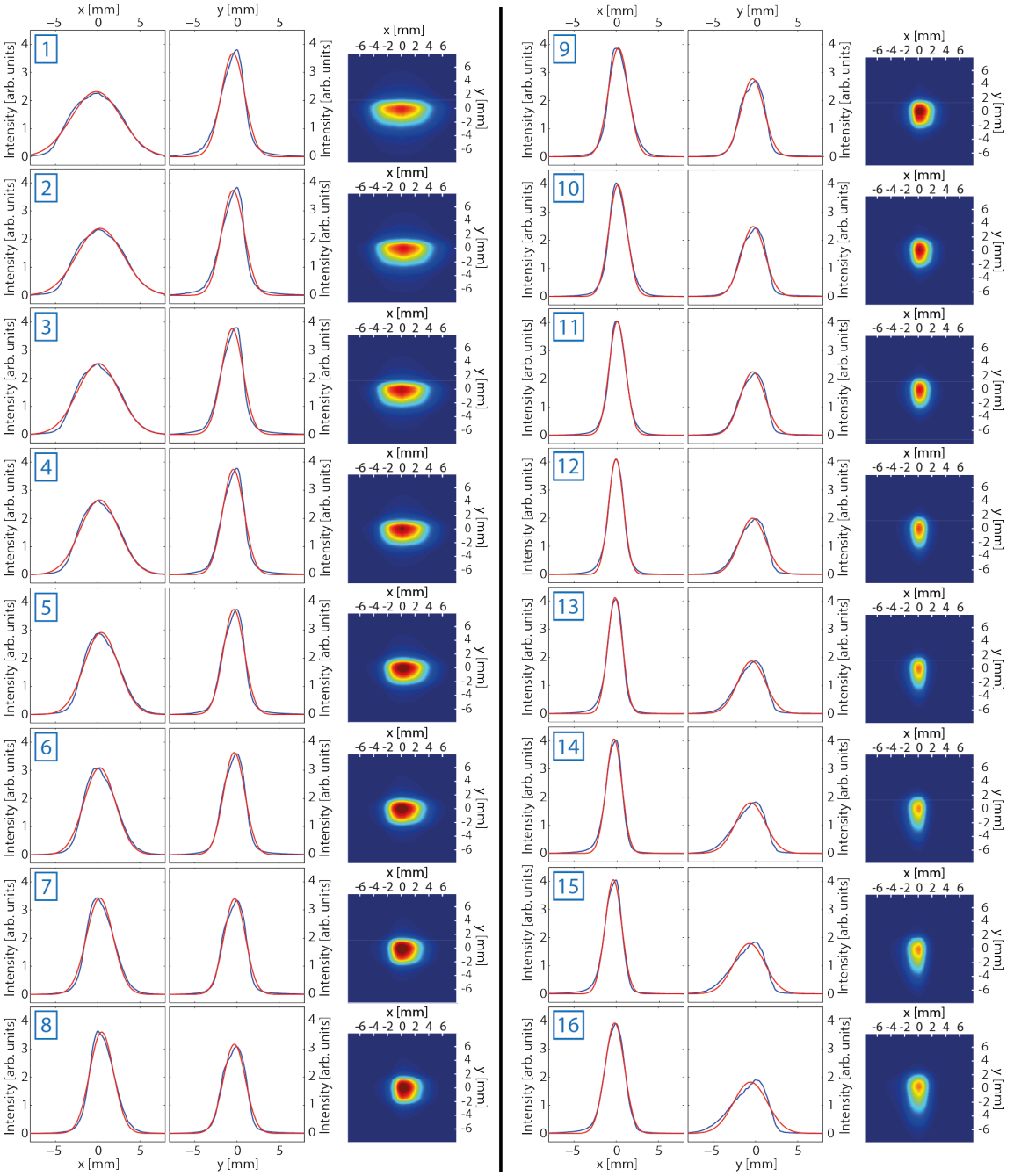

Figure 11.4: Measured transverse beam profiles at pos. B of a D^- beam with a kinetic energy of 35 keV, propagating along the CSR beamline. The horizontal and vertical beam profile is recorded for 16 different potentials, applied to the third quadrupole lens of QPB. These recorded horizontal (x) and vertical (y) spatial distributions, which are represented by the blue line, are fitted by Gaussian profiles, indicated by the red line. The settings of the varied quadrupole lens QPB-3, together with the resulting horizontal and vertical beam widths are listed in Tab. 11.1 for each recorded profile.

Profile	U(QPB-3) [V]	K(QPB-3) [m^{-2}]	$x_{1\sigma}$ [mm]	$y_{1\sigma}$ [mm]	$x^2_{1\sigma}$ [mm^2]	$y^2_{1\sigma}$ [mm^2]
1	±458.0	-14.54	2.94±0.02	1.39±0.01	8.65±0.10	1.93±0.04
2	±460.0	-14.60	2.74±0.02	1.34±0.01	7.52±0.09	1.79±0.04
3	±463.0	-14.70	2.48±0.01	1.28±0.01	6.13±0.07	1.63±0.03
4	±465.0	-14.76	2.29±0.01	1.27±0.01	5.24±0.06	1.62±0.03
5	±468.0	-14.86	2.03±0.01	1.25±0.01	4.11±0.05	1.56±0.02
6	±470.0	-14.92	1.86±0.01	1.26±0.01	3.45±0.05	1.59±0.02
7	±473.0	-15.02	1.57±0.01	1.27±0.01	2.48±0.04	1.62±0.03
8	±475.0	-15.08	1.41±0.01	1.31±0.01	2.00±0.03	1.72±0.03
9	±478.0	-15.18	1.19±0.01	1.36±0.01	1.41±0.02	1.85±0.03
10	±480.0	-15.24	1.07±0.01	1.41±0.01	1.14±0.01	1.98±0.03
11	±482.0	-15.30	0.98±0.01	1.46±0.01	0.95±0.01	2.14±0.04
12	±485.0	-15.40	0.89±0.01	1.55±0.02	0.79±0.01	2.41±0.05
13	±487.0	-15.46	0.88±0.01	1.63±0.02	0.77±0.01	2.65±0.06
14	±490.0	-15.56	0.93±0.01	1.76±0.02	0.87±0.01	3.09±0.08
15	±492.0	-15.62	0.99±0.01	1.84±0.02	0.98±0.01	3.38±0.09
16	±495.0	-15.71	1.15±0.01	2.00±0.03	1.32±0.01	4.00±0.12

Table 11.1: Recorded spatial beam profiles at position B, dependent on the voltage applied to the quadrupole lens QPB-3, as shown in Fig. 11.2. A single standard deviation of the Gaussian fits, shown in Fig. 11.4, are utilized as the horizontal and vertical beam widths, σ_x and σ_y, respectively.

of the quadrupole strength K(QPB-3) in Fig. 11.5 (represented by the blue dots). Fitting Eq. 11.13 and Eq. 11.14 to this data set using a least squares method, the matrix elements σ_{11}, σ_{21} and σ_{22} and σ_{33}, σ_{43} and σ_{44} are obtained. These fits are plotted in Fig. 11.5, indicated by the red line. Using Eq. 11.7 and Eq. 11.8, the horizontal and vertical twiss parameters prior to the quadrupole lens QPB-3 (pos. A) and the beam emittance are extracted from the fits. The resulting horizontal and vertical phase space ellipses, together with the derived twiss parameters (α_x, β_x, α_y, β_y), representing the ion beam at pos. A, are shown in Fig. 11.6. The horizontal and vertical 1σ-emittance that is transported through the beamline as shown in Fig. 11.2, is determined to $\epsilon_x^{1\sigma} = 5.4$ mm mrad and $\epsilon_x^{1\sigma} = 5.9$ mm mrad, respectively. In addition to the information of the beam quality, these parameters can be utilized to calculate the transport of the ion beam, propagating through the beamline. The

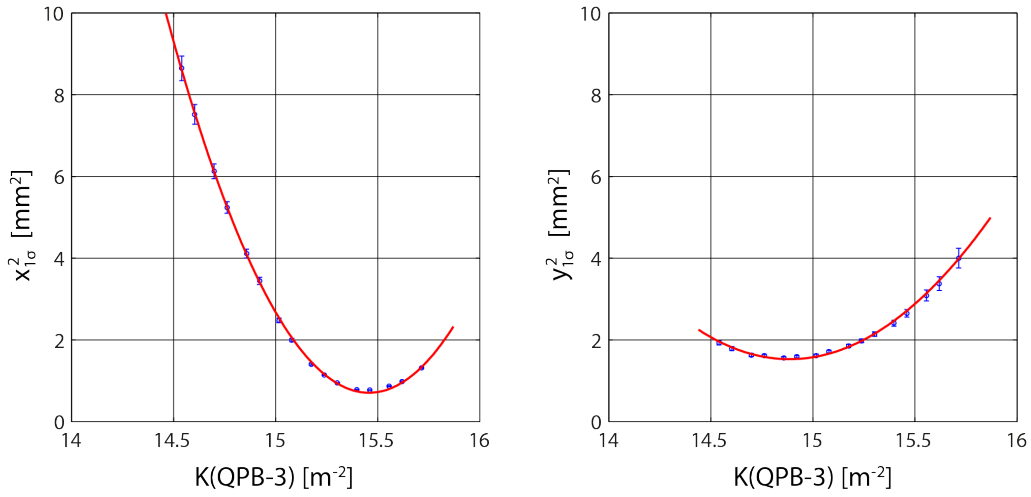

Figure 11.5: The square of the beam width as a function of the quadrupole strength K. The blue dots represent the measurements of the beam profile, as listed in Tab. 11.1. The red line indicates the fit according to Eq. 11.13 and Eq. 11.14, respectively, which yields the twiss parameters of the beam at the entrance of quadrupole lens QPB-3.

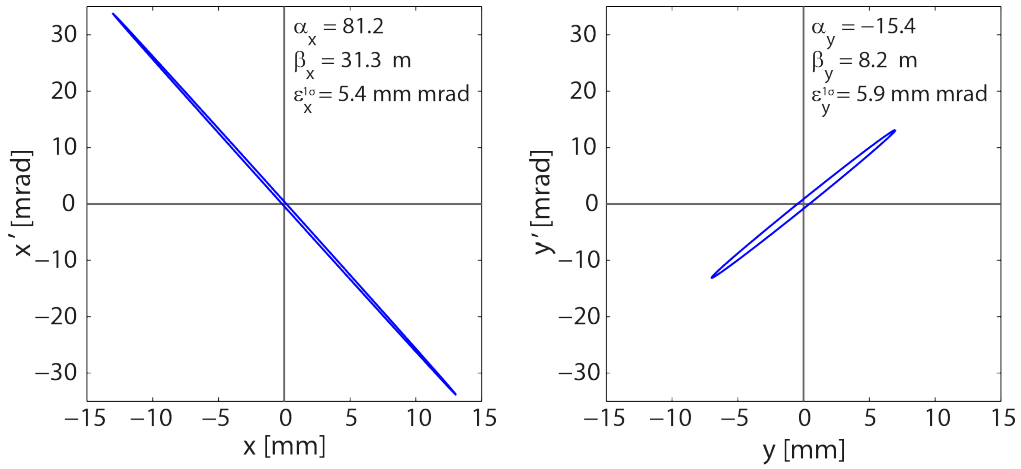

Figure 11.6: Horizontal and vertical phase space of the D^- beam directly in front of the quadrupole lens QPB-3 (pos.A in Fig. 11.3).

knowledge of the twiss parameter α, β at one reference point provides the determination of α and β at every location in a well-defined ion-optical system. Using the measured beam parameters as starting values, MAD X simulations can serve as a feedback for the ion-optical settings, in order to optimize the beam transport. On the other hand, the evolution of an ion beam along the beamline can be determined for a given set of adjusted ion-optical elements.

The quadrupole variation method is a relatively simple technique to estimate the transverse emittance of a transported ion beam, relying on the conservation of the

emittance during the variation of the quadrupole strength. Despite this advantage, this method is limited in its accuracy, as the algorithm that is employed uses linear transport matrices (discussed in Sec. 11.1.1), where non-linear effects are neglected. Higher order effects introduced by ion-optics or space charge effects are not taken into account. As a result, only elliptical shaped phase spaces can be obtained in this method.
A more accurate determination of the transported transverse beam emittance would require additional analyzing instruments (e.g. slit-grid [188], Pepper-Pot [189]).

11.2 Photodetachment measurements

To benchmark the apparatus' capabilities of producing fast, neutral-beams via photodetachment (PD), a series of preliminary measurements were performed on C^- and O^- ion beams. These measurements were taken using the test beamline setup, as depicted in Fig. 11.1, prior to its integration into the CSR injection beamline. To provide a quantitative measure of the neutral particle flux that is created by PD for the parent anion beam, a method to calibrate the utilized neutral cup detector is presented (see Sec. 11.2.2). The procedure used to measure the PD efficiency is briefly outlined in Sec. 11.2.3, after which initial measurements of the C^- and O^- PD efficiency are shown and compared to a simple model.

11.2.1 Measurement overview

The PD measurements were performed using either a C^- or O^- ion beam. Generated in a Cs-sputter source [186, 187], these beams were extracted from the 60kV source platform. Selected by its mass-to-charge ratio using a 90° bending magnet, the anion beam is guided along the test beamline, as shown in Fig. 11.1. After the second quadrupole triplet (QPB), the beam is deflected using a simple double-focusing electrostatic 90° deflector, as described in detail in [190]. Capable of applying up to ±9 kV to the inner and outer electrode, respectively, this 90° deflector limits the maximum kinetic energy to 35 keV for the transport of singly charged ions along the test beamline. Now flying parallel to the CSR injection beamline, the ion beam undergoes final focusing and steering in quadrupole triplet QPC and is then passed through the PD section, as depicted in Fig. 11.7. After passing a 4.5 mm aperture, the beam continues to fly near ballistically for approximately 2.9 m, before

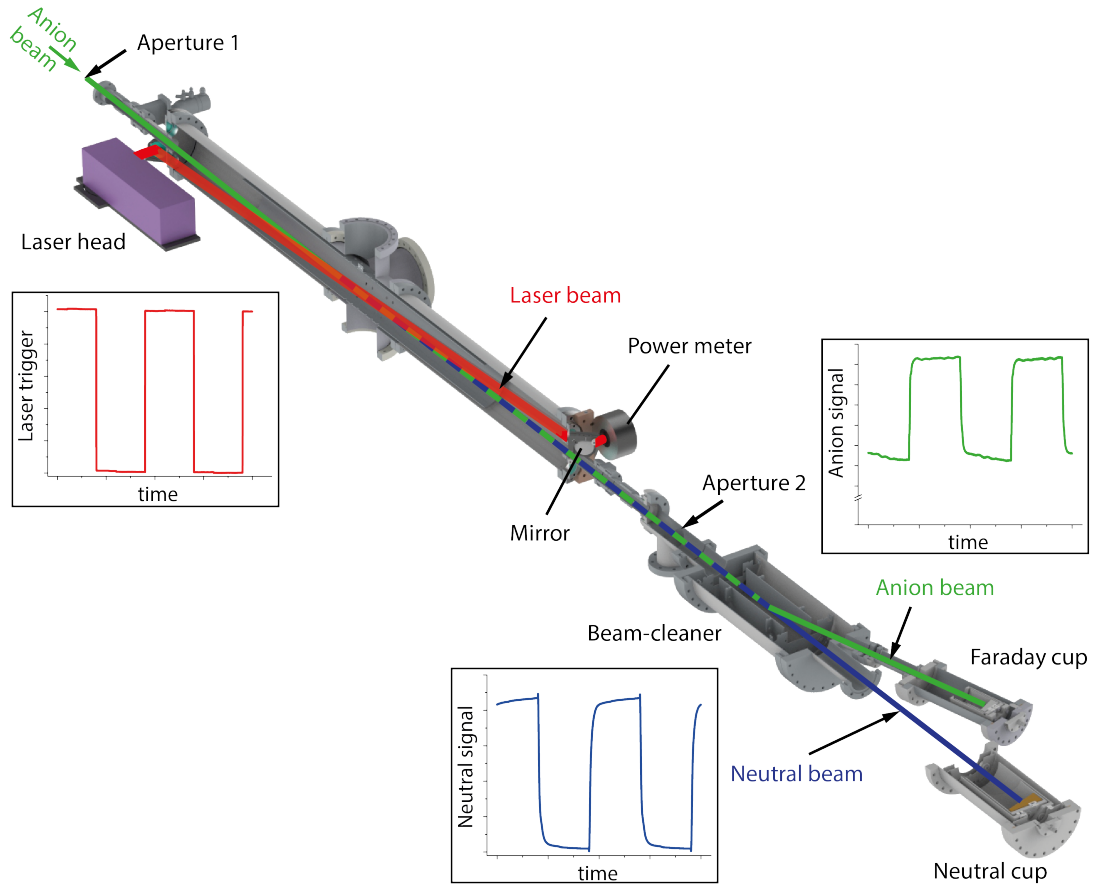

Figure 11.7: Overview of the PD test measurement scheme. The inlaid graphs represent a relative measurements of the neutral and ion signal, while gating the laser.

passing a second 4.5 mm aperture. This aperture pairing limits the maximum area in phase space of ballistic beams transmitted through the PD section to A = $\pi\epsilon \approx$ 6.75 mm mrad, as demonstrated in Sec. 9.3.

In the PD section, the ion beam is crossed with an 808 nm direct diode laser (described in Sec. 9.2), which crosses the ion beam with an angle of $\sim 2.7°$. As the laser energy is higher than the binding energy of the outermost electron of both the C^- and O^- anion, a fraction of the parent ion beam is photodetached in the laser interaction region.

The resulting superposition of a fast neutral and parent anion beams continue ballistically until a parallel plate deflector, the so-called beam cleaner (see Sec. 9.4), is reached. With the correct potentials applied, the ion beam undergoes a deflection of 14.5° and is guided into a Faraday cup. The neutral beam, unaffected by the electrostatic field, continues its ballistic trajectory. The resulting fast, pure, atomic,

neutral-beam continues for $\sim$ 2 m, after which the neutral flux is measured in a neutral cup, described in Sec. 11.2.2. The neutral cup provides a measure of the neutral beam flux via the secondary electron emission current induced from particle impacts. A similar detection system is described by [191, 123].
During the PD benchmarking measurements, the ion current and neutral flux are measured as a function of the ion-beam kinetic energy over a range of laser powers. To determine the absolute photodetachment efficiency, the average secondary electron yield per neutral atom impact (γ), must be first evaluated. The γ factor for a metal target has been shown to possess a dependence on the projectile atomic number, velocity, charge, angle of incidence, target material, target surface roughness, and surface contamination [192, 193, 194]. Given γ's sensitivity to both the incident particle parameters and the condition of the target surface, a relatively simple and reliable method for determining γ is required.

11.2.2 Neutral flux measurement

To determine the absolute neutral particle flux, a custom neutral cup was designed to measure the secondary electron emission induced from incident keV atomic particles. A schematic overview of this design is shown in Fig. 11.8. The layout of this cup is similar to that of a traditional Faraday cup, described previously in Sec. 8.3.2, and commonly utilized for ion beam measurements.
The neutral cup consists of a copper target, slightly angled toward the incident parti-

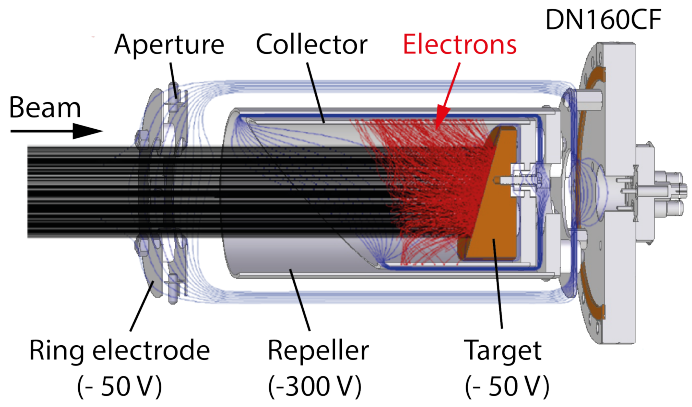

Figure 11.8: Schematic of the neutral cup, overlaid with a SIMION simulation of the secondary electron trajectories induced by keV neutral particle collisions with the Cu target surface.

cle beam. The target is enclosed within, but electrically isolated from a stainless-steel cylindrical electrode (with a diameter of 97 mm), known as the collector. The collector, in turn, is nested concentrically within a larger electrode, denoted the repeller. The repeller is electrically insulated from both the target and the collector. The target, collector, and repeller are mounted, via a series of ceramic shoulder bushings, to ensure the arrangement remains electrically insulated, to a base plate that is mounted to a CF160 to CF40 reducer flange. To prevent any neutral particles striking any cup elements except the target surface, an aperture with an bore diameter of 75 mm is mounted directly in front of the cup arrangement. In front of this aperture, mounted towards the incoming beam, a ring electrode is attached. Applying a potential of $\sim$ -50 V, this electrode serves to repel free electrons in the vacuum system from entering the cup.
Biasing the copper target with a negative potential of $\sim$ -50 V, ensures that the slow secondary electrons (kinetic energy of typically a few eV [193]) are repelled from the target surface, reducing surface recombination. The surrounding collector electrode, as the name suggests, can then collect the secondary electrons. The generated signal is subsequently measured via a fast-current amplifier (FEMTO DLPCA-200).
To further enhance the electron collection efficiency, the surrounding repeller electrode is negatively biased to $\sim$ -300 V, guiding the secondary electrons to the collector surface. This effect is magnified by an angular cut in the collector surface. This angling, with a normal opposing that of the target normal, aids the leakage of repeller potential field into the collector volume, thus creating a potential gradient which steers the electrons towards the grounded, longer-arm of the collector (see Fig. 11.8). The entire cup arrangement is designed to fit within a standard CF160 nipple, which provides an outer grounding volume to the housed electrodes.
During experimental measurements, secondary electron currents down to few pA were measured, this limit was due to, predominantly, environmental electrical noise. To absolutely measure the incident particle flux, the secondary electron emission per particle impact must first be determined. In this context, it is convenient to define the neutral flux in terms of an effective current.

Gamma determination

To provide a reliable and repeatable measure of the γ factor (secondary electron yield per particle), a technique that is compatible with the stringent operating demands

of the CSR transfer line was required. Previous experiments relied on a He-gas cell to strip a parent negative ion beam in order to calibrate a similar neutral cup [123]. Simultaneously measuring the parent ion current transmitted through the gas cell and the double-stripped positive ion current in a Faraday cup, while monitoring the effective neutral current in the neutral cup, a value for γ could be determined. Such a gas cell usually requires narrow, confining apertures/channels to minimize the conducted gas load into the surrounding vacuum system. Such apertures would severely limit the beam transport into the CSR, discussed in Sec. 8.2, whereas without the apertures, the gas pressure would exceed the beamline's design requirements.
A simple method to calibrate the neutral cup is the use of a pilot ion beam. This method assumes that the secondary electron emission for a negatively charged particle is approximately equal to that of its neutral counterpart [193], when the addition charge of the ion beam is taken into account. For such a measurement, the neutral cup is first configured to its Faraday cup mode by electrically coupling the target and collector. In this mode the neutral cup can give an absolute measurement of the pilot ion beam current, as the secondary electrons are recaptured by the collector and thus only the beam current is measured (cup mode). To measure the electron loss from the target, the neutral cup is reconfigured, in that the target is electronically disconnected from the collector. By applying a positive potential ($\sim$ 300 V) to the collector and measuring the ion current on the target, allows to measure the secondary electron loss from the target (loss mode). Finally, to cross-check the measurement, the actual configuration of the neutral cup, as denoted in Fig. 11.8, is applied. The target of the neutral cup is biased with -50 V and the secondary electron emission is detected on the collector (gain mode).
Measuring the ion current (in cup mode), I_{beam}, and the secondary electron current (in either the loss or gain mode), I_{electron}, induced by a stable ion beam that impinges on the target surface, allows to determine the γ factor via

$$\gamma = \frac{I_{\mathrm{electron}}}{I_{\mathrm{beam}}} - n\,, \tag{11.15}$$

where n denotes a compensation value for the additional electron brought into the system by the detected anions (0 for loss mode, and 1 for gain mode). The electron to anion current ratio yields the number of electrons measured per particle impact. To account for the additional electron brought by the negative charged ion, this ratio must be subtracted by 1 to yield the γ factor.
Tab.11.2 shows a sample measurement utilizing the three discussed neutral cup con-

Ion current (cup mode) [nA]	Ion current (gain mode) [nA]	Ion current (loss mode) [nA]	derived γ (gain mode)	derived γ (loss mode)
50.8	244.5	193.5	3.81	3.80
52.6	241.4	189.0	3.58	3.59

Table 11.2: Typical γ measurement for C^- at 25 keV, with the cup configured in cup mode, gain mode, and loss mode.

figurations for C^- ions at a kinetic energy of 25 keV. The two neutral cup configurations to measure the current of the secondary electrons were found to be in good agreement. Using Eq. 11.15, the calculation of γ within the individual measurements were consistent.

For both C^- and O^- beams, measurements were taken to determine the γ factor for kinetic energies ranging between 10 and 35 keV, in 5 keV steps. In Fig. 11.9, the resulting γ as a function of the ion velocity are presented. The γ factor for both the C^- and O^- ion beams, are shown to increase in an approximately linear fashion with ion beam velocity. This is in general agreement with data presented in [193, 194], which suggest that the secondary electron emission coefficient follows a linear relationships for impact velocities in the region of 2 to $20{\cdot}10^7$ cm s^{-1}.

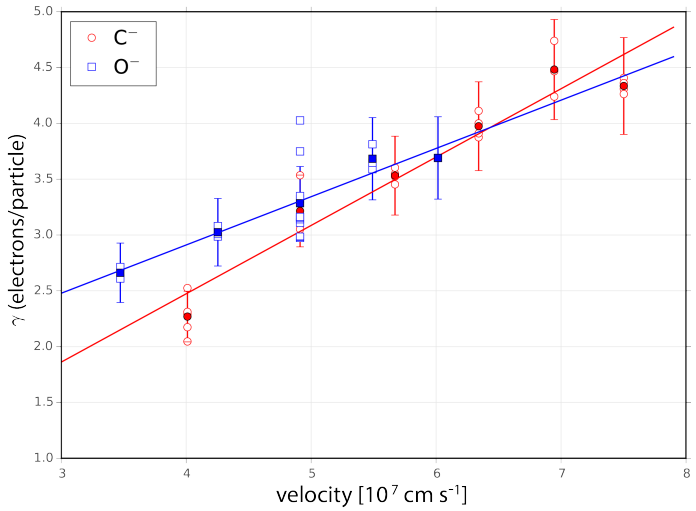

Figure 11.9: Gamma measurements derived from measurements on C^- (open circles) and O^- (open squares) ion plotted against their respective velocities, for parent beams with energies ranging from 10 to 35 keV. The average of measurements at a given velocity are shown by the filled markers. A linear fit for each of the data sets is also shown.

Independent measurements of the γ factor over a period of days, demonstrated a repeatable accuracy in the region of 10 %, with the exception of the multiple measurements of the γ factor in the O^- data, obtained for velocities $\sim 5\times10^7$ cm s^{-1}. This series of measurements were taken after venting of the system to atmosphere, suggesting that the large variation was due to surface contamination which can dramatically affect the secondary electron emission coefficient [193]. This effect highlights the need for regular calibration of the γ factor prior to each experimental measurement.

11.2.3 Photodetachment efficiency

PD efficiency measurements were taken for a C^- and O^- parent anion beam at kinetic energies ranging from 10-35 keV for C^- and 10-30 keV for O^-. Due to facility maintenance, the vacuum system was vented for a period of two days between subsequent O^- measurements, this venting greatly affected the γ factor and introduced a large uncertainty as the neutral cup target was gradually surface cleaned by the ion beam via surface sputtering. After optimizing the beam transport, the γ factor was first measured (previously discussed in Sec.11.2.2) prior to beginning the PD efficiency measurement. According to the measurement scheme, illustrated in Fig. 11.7, the PD efficiency for C^- and O^- was measured using laser drive currents ranging from 10-85 A (corresponding to laser powers ranging from $\sim$ 0.1-1.6 kW). With the laser off, the parent ion current is first measured as a benchmark. In a next step, the laser is cycled on and the laser parameters are recorded (e.g. current, voltage, output power, temperature). The power meter, on which the laser power is recorded, requires a short period to thermally stabilize. In this time period, the ion current and the laser-induced neutral current are detected, after which finally the laser output power is measured. The laser is then cycled off, the drive current incremented and the process started again. It is essential to record the ion current with the laser off for each measurement step to account for any current drift throughout the measurement.
A sample measurement shown in Fig. 11.10, illustrates a typical measurement, whilst also highlighting the effect of a $\approx$ 6 nA current drift on the parent beam (the laser power is iteratively increased for each measurement). The ion beam currents detected for laser off (red circles) and for laser on (green squares), together with the secondary electron currents (blue triangles) induced by the generated neutral beam,

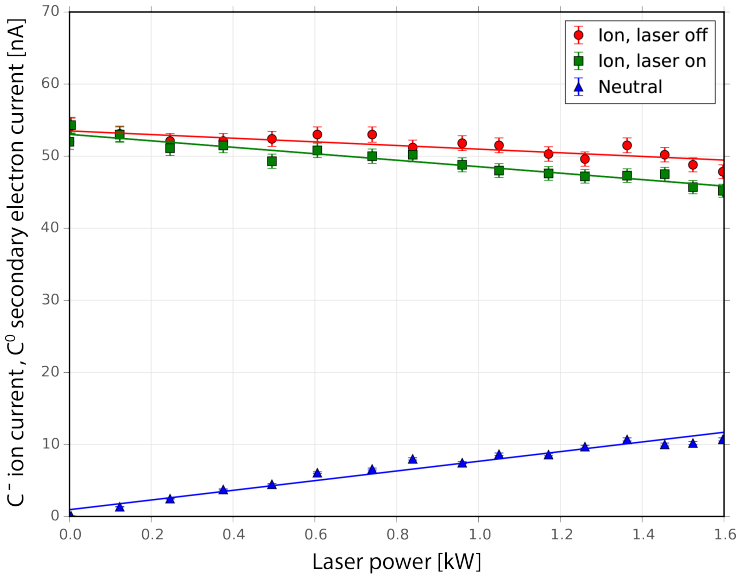

Figure 11.10: Sample of the ion currents, laser on (green squares), laser off (red circles) and the measured, uncalibrated secondary electron current due to neutral impacts (blue triangles) for a range of applied laser powers. Measurements shown are recorded for a C^- parent ion beam at 25 keV.

are measured as a function of the laser power.
Utilizing the γ factor measurements, derived in the previous section (see Fig. 11.9), the detect beam currents (measured at a specific laser power), allow to determine the PD efficiency η by

$$\eta = \frac{I_{\text{neutral}}}{I_{\text{ion}}} = \frac{I_{\text{electrons}}}{\gamma} \cdot \frac{1}{I_{\text{ion}}}\,, \tag{11.16}$$

where $I_{\text{electrons}}$ denotes the secondary electron current, yielded by the corresponding neutral beam current I_{neutral}. I_{ion} represents the parent ion beam current, detected via the Faraday cup when the laser beam is switch off. Using Eq. 11.16, the derived PD efficiencies in the measurements, performed for C^- (red circles) and O^- (blue squares) ion beams with kinetic energies ranging from 10-35 keV and 10-30 keV, respectively, are shown in Fig. 11.11. For all measurements, the PD efficiency is observed to linearly increase with the laser power until approximately 1.2 kW. This observation is in agreement with Eq. 9.6 (see Sec. 9.1), where the predicted PD efficiency is approximated by

$$\eta(y) \approx \frac{1}{\sin\Theta}\sqrt{\frac{2}{\pi}}\frac{\sigma_{\text{PD}}}{v_{\text{ion}}}\frac{P}{h\nu w}\exp\left(-\frac{2y^2}{w^2}\right), \tag{11.17}$$

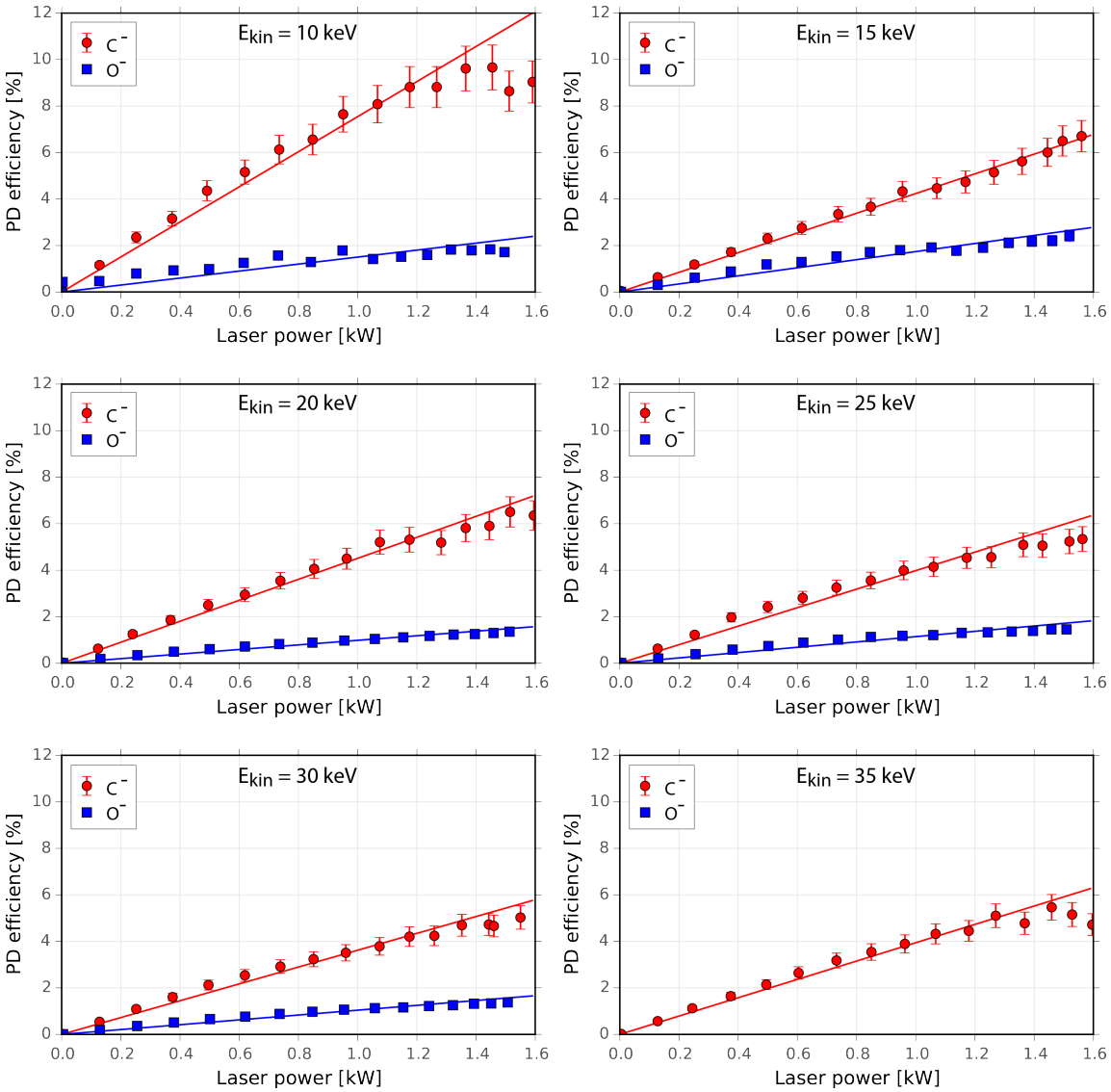

Figure 11.11: PD efficiency measurements for a C^- (red circles) and O^- (blue squares) ion beams as a function of laser power, for a range of ion beam energies. The errorbars represent ≈10 % uncertainty which are dominantly propagated from the γ measurement error. The solid curves are a straight line fit from 0 to 1.4 kW with the intercept fix to 0.

indicating that the PD efficiency η scales linearly with the laser power P. Operating the diode laser system at higher powers (beyond a laser power of ∼1.2 kW) leads to a degradation in the laser beam quality, as previously described in Sec. 9.2. Due to an increasing thermal load on the diode stacks, the divergence of the resultant laser beam increases, which leads to an increase of the laser beam width w in the PD interaction region. As a result, the increase in PD efficiency with laser power slows, at these higher powers (see Fig. 11.11).

Taking the C^- and O^- PD efficiency measurements (from Fig. 11.11) performed at maximum laser power, the relationship between PD efficiency and the kinetic energy of the parent ion beam can be investigated. From Eq. 11.17, the PD efficiency (η) should be inversely proportional to the velocity of the parent ion beam (v_{ion}). In Fig. 11.12, the experimentally measured PD efficiency for both C^- and O^- ion beams are shown to reasonably follow this inverse dependence, $\eta \propto 1/v_{\text{ion}}$.

In this section, test measurements of the PD efficiency of C^- and O^- anions were presented. After calibrating a neutral particle detector, the neutral flux generated via photodetachment from a parent anion beam was measured. These test measurements demonstrated photodetachment efficiencies ranging between ≈ 9 % to 4.7 % for C^- anions possessing kinetic energies of 10 to 35 keV, respectively and similarly for O^-

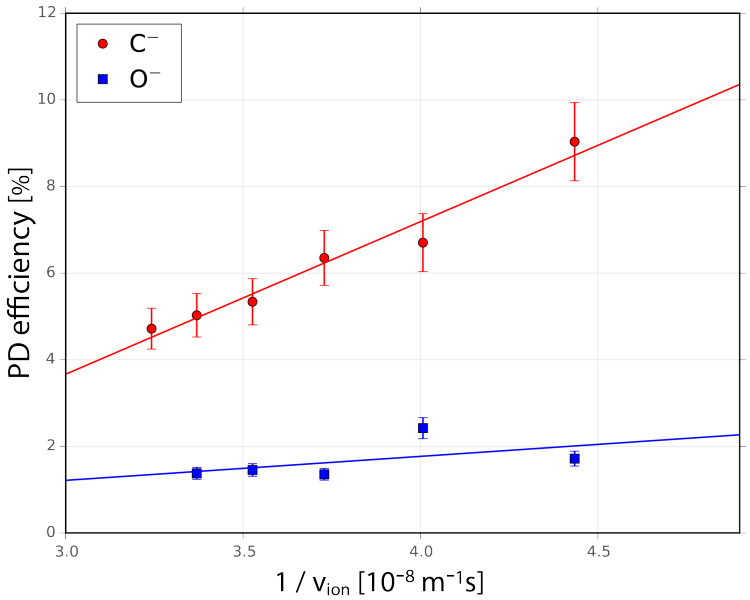

Figure 11.12: Laser photodetachment efficiency, at full laser power, for C^- (red circles) and O^- ions (blue squares), plotted against $1/v_{\text{ion}}$. The lines represent a linear fit of the data.

anions, ≈ 1.7 % to 1.4 % with the corresponding kinetic energies of 10 to 30 keV. For the continuous, stable operation of the ion source for several weeks without maintenance, a moderate ion beam current was produced ($\sim \mu$A) and transported through the PD setup. With a parent beam current of ∼10-70 nA (dependent on the anion species and its kinetic energy) transmitted through both 4.5 mm apertures, fast neutral atom beams were generated of 1-3 nA (C) and 300-900 pA (O).

Chapter 12

Summary and Perspectives

Ion-neutral reactions play a pivotal role in the cosmic chemistry of interstellar clouds, representing approximately 2/3 of all reactions in current gas-phase models [195, 196]. Despite the importance of ion-neutral reactions in astrochemistry, discrepancies remain in the reaction rates of the chemical network. As these destruction and formation rates determine the relative cosmic abundances, they are critical for the complete understanding of interstellar chemistry.

Traditionally, preparation of an internally and translationally cold molecular ion beam and superimposing it with a ground-state atomic beam, presented a significant barrier in experimental studies. In this work, an apparatus surpassing these limitations was introduced. This apparatus is capable of preparing a cold molecular ion beam and subsequently merging it with an atomic neutral beam at low ($\sim$ meV) center-of-mass collision energies. This apparatus' design, simulation and construction of individual components were described and discussed in detail.

Ions formed in traditional ion sources tend to have high degrees of internal excitation, with internal temperatures often of a few thousand Kelvin, e.g. [197]. To accurately investigate ion-neutral chemistry at astrophysically relevant temperatures, these ions must first be internally and translationally cooled. To this end, ions are first stored in the Heidelberg Cryogenic Storage Ring (CSR), where they can radiatively couple to the surrounding 10 K radiation field. Also, currently under construction at the CSR is an electron-cooler which will provide translationally cold stored ion beams [143, 151]. Following a brief introducing of the CSR's design principles and experimental capabilities, the requirements of a transfer line were discussed. To efficiently couple a well-defined ion beam for storage in the CSR, while minimizing both the induced thermal and gas load, an efficient transfer line was designed, matching the

CSR machine parameters. Two distinct ion source platforms, supplied by a potential of up to ±300 kV and ±60 kV, respectively, were combined via an electrostatic 90° deflector with a hole. The transport of charged particles through both the 300kV and 60kV beamline were optimized via MADX simulations. In these simulations, the ion-optical system was calculated using the linear matrix formalism. To also account for higher order effects and provide a more in-depth description of individual components of the CSR transfer line, the ion beam transport through the designed models were simulated using SIMION. In these simulations, particle beam trajectories were tracked through the ion-optical elements and the resulting phase space distributions were analyzed. In this manner, the validity of the linear approximation utilized in the previous MADX simulations were examined.

A crucial component of the CSR transfer line for merged beams experiments is the photodetachment apparatus. In this section, a fraction of the anion beam is photodetached and thus, a keV energy, neutral, atomic beam is generated. In a brief description of the photodetachment process, it was shown that the photodetachment efficiency can be optimized by minimizing the overlap angle between the ion and laser beam (thus maximizing the overlap length). In a series of laser profile measurements the high-power (2 kW) continuous wave laser system was characterized, after which an optimized design of the photodetachment chamber permits a shallow angle (2.7°) of incidence between the two beams. To inject a pure, neutral atom beam, the remaining anions must first be cleaned from the system. To this end, the design and simulation of a parallel-plate deflector, denoted the beam cleaner, which removes the remaining anion particles, were presented.

Taking into account all of the design considerations from Chap. 8 and 9, an overview of the final CSR transfer line design was presented. To ensure that the injection beamline could meet the stringent vacuum criteria demanded by the CSR, VacTrak vacuum simulations were performed and the various vacuum pumping and optimization methods briefly discussed (e.g. baking).

Finally a test beamline was constructed and assembled in the experimental hall prior to conducting a series of preliminary test measurements. This test beamline also successfully provided the first cold commissioning phase of the CSR [151]. To confirm the functionality of the beamlines, a series of test measurements were performed to determine the beam twiss parameters, emittance of a transported ion beam and the photodetachment capabilities of the PD section. Following that, the methods and results of these measurements were presented and their implications discussed.

In the Summer of 2015, during the course of this work, the CSR itself was commissioned, and under cold conditions a series of experimental measurements were obtained. In these measurements, both negatively and positively charged ions ranging from simple atoms, e.g. Ar^+, to clusters, e.g. Co_3^-, with energies in the region of $\sim$ 60 keV, were successfully stored [151]. Being almost fully-electrostatic, the injection beamline and CSR potentials were scaled to a range of injection energies, for example during the CH^+ photodissocation measurements [198]. These measurements demonstrated that the stored CH^+ ions cool down in internal temperature to regions of 20 K. In the CSR, storage times on the scale of $\sim$ 1000 s, for $\sim 10^8$ stored ions were observed, from which equivalent residual gas pressures below 10^{-14} mbar were deduced. Thus confirming both the successful design of the CSR's vacuum system and the low conductance of the injection beamline into the CSR.
The demonstrated storage times, residual gas and thermal conditions are favorable for conducting ion-neutral merged-beams experiments, as they permit stable conditions in which replicate those found in interstellar environments. To conduct these experiments, a combination of detectors mounted inside the CSR and external energy analyzers will be employed. In the upcoming beamtime, the first series of ion-neutral merged-beams experiments will be performed at the CSR. These measurements will focus on the charge exchange reaction between atomic and molecular hydrogen

$$H_2^+ + H \rightarrow H^+ + H_2\,,$$
$$HD^+ + H \rightarrow H^+ + HD\,.$$

This reaction represents a potential destruction pathway for interstellar H_2^+ ions, a competitive pathway for H_3^+ formation reaction:
$H_2^+ + H_2 \rightarrow H_3^+ + H$.
Other reaction systems of interest include the water formation, deuterium fractionation or the synthesis of organic molecules initiated by ion-neutral reactions with H_3^+ in interstellar space. These reaction pathways (depicted in Fig. 2.7 in Sec. 2.3), can

be investigated in ion-neutral collision experiments involving H_3^+, e.g.

$$\begin{aligned} H_3^+ + O &\rightarrow OH^+ + H_2 \\ &\rightarrow OH_2^+ + H\,, \\ &\rightarrow OH_3^+. \\ H_3^+ + D &\rightarrow HD^+ + H_2 \\ &\rightarrow H_2D^+ + H\,, \\ H_3^+ + C &\rightarrow CH^+ + H_2 \\ &\rightarrow CH_2^+ + H \\ &\rightarrow CH_3^+\,. \end{aligned}$$

Due to the lack of a permanent dipole moment, H_3^+ can not undergo efficient radiative cooling while being stored inside the CSR. To circumvent this barrier, the H_3^+ ions can be pre-cooled in a 22 pole trap, mounted to either ion source platform, prior to extraction and injection into the CSR. As demonstrated in Part I of this work, the 22 pole trap is capable of producing internally cold ions, via buffer gas cooling, e.g H_3^+. The combination of these two laboratory instruments forms a versatile experimental tool which, for the first time, is capable of investigating neutral molecular-ion reactions at true astrophysical temperatures.

Appendix A

Statistical nuclear spin configurations of the reaction $H_3^+ + H_2$

High temperature statistical model by Oka

The resulting nuclear spin configurations of the (o/p)-H_3^+ + (o/p)-H_2 complex can be derived for high temperatures, using nuclear spin selection rules. The values in the statistical limit for the reaction pathways of $H_3^+ + H_2$ have been derived by T. Oka [76] and are summarized in Tab. A.1 and A.2. At low temperatures (10 - 160 K), the nuclear spin selection rules, alone, are insufficient to describe the resulting nuclear spin configurations of H_3^+ and H_2. Therefore, Park and Light developed a microcanonical statistical model which also account for the conservation of the angular momentum, energy and parity [79]. The calculated probabilities for the resulting nuclear spin (ortho / para) configurations at the high temperature limit, 80K and 10K are summarized in Tab. A.3.

Table A.1: The nuclear spin configurations with their values in the statistical limit for the three reaction pathways (identity, proton hop, exchange) and their sum (total) of $H_3^+ + H_2$ [76]. The rows of the tables represent the nuclear spin configuration of the reactant and the columns of the tables represent the nuclear spin configuration of the product.

identity	weight	(o-H_3^+, o-H_2)	(o-H_3^+, p-H_2)	(p-H_3^+, o-H_2)	(p-H_3^+, p-H_2)
(o-H_3^+, o-H_2)	12	6/5	0	0	0
(o-H_3^+, p-H_2)	4	0	2/5	0	0
(p-H_3^+, o-H_2)	12	0	0	6/5	0
(p-H_3^+, p-H_2)	4	0	0	0	2/5

proton hop	weight	(o-H_3^+, o-H_2)	(o-H_3^+, p-H_2)	(p-H_3^+, o-H_2)	(p-H_3^+, p-H_2)
(o-H_3^+, o-H_2)	12	12/5	0	6/5	0
(o-H_3^+, p-H_2)	4	0	0	6/5	0
(p-H_3^+, o-H_2)	12	6/5	6/5	3/5	3/5
(p-H_3^+, p-H_2)	4	0	0	3/5	3/5

exchange	weight	(o-H_3^+, o-H_2)	(o-H_3^+, p-H_2)	(p-H_3^+, o-H_2)	(p-H_3^+, p-H_2)
(o-H_3^+, o-H_2)	12	19/5	1	8/5	4/5
(o-H_3^+, p-H_2)	4	1	3/5	4/5	0
(p-H_3^+, o-H_2)	12	8/5	4/5	19/5	1
(p-H_3^+, p-H_2)	4	4/5	0	1	3/5

total	weight	(o-H_3^+, o-H_2)	(o-H_3^+, p-H_2)	(p-H_3^+, o-H_2)	(p-H_3^+, p-H_2)
(o-H_3^+, o-H_2)	12	37/5	1	14/5	4/5
(o-H_3^+, p-H_2)	4	1	1	2	0
(p-H_3^+, o-H_2)	12	14/5	2	28/5	8/5
(p-H_3^+, p-H_2)	4	4/5	0	8/5	8/5

Table A.2: The probabilities for the resulting nuclear spin configurations of the $H_3^+ + H_2$ reaction [76]. The rows of the tables represent the nuclear spin configuration of the reactant and the columns of the tables represent the nuclear spin configuration of the product.

total	(o-H_3^+, o-H_2)	(o-H_3^+, p-H_2)	(p-H_3^+, o-H_2)	(p-H_3^+, p-H_2)
(o-H_3^+, o-H_2)	37/60	1/12	7/30	1/15
(o-H_3^+, p-H_2)	1/4	1/4	1/2	0
(p-H_3^+, o-H_2)	7/30	1/6	7/15	2/15
(p-H_3^+, p-H_2)	1/5	0	2/5	2/5

Mircocanonical statistical model by Park & Light

Table A.3: The probabilities for the resulting nuclear spin configurations derived from state-to-state reaction rate coefficients assuming complete proton scrambling [79]. The rows of the tables represent the nuclear spin configuration of the reactant and the columns of the tables represent the nuclear spin configuration of the product.

high temp	(o-H_3^+, o-H_2)	(o-H_3^+, p-H_2)	(p-H_3^+, o-H_2)	(p-H_3^+, p-H_2)
(o-H_3^+, o-H_2)	0.62	0.08	0.23	0.07
(o-H_3^+, p-H_2)	0.25	0.25	0.5	0
(p-H_3^+, o-H_2)	0.23	0.17	0.47	0.13
(p-H_3^+, p-H_2)	0.2	0	0.4	0.4

80 K	(o-H_3^+, o-H_2)	(o-H_3^+, p-H_2)	(p-H_3^+, o-H_2)	(p-H_3^+, p-H_2)
(o-H_3^+, o-H_2)	0.66	0.05	0.23	0.06
(o-H_3^+, p-H_2)	0.05	0.84	0.11	0
(p-H_3^+, o-H_2)	0.24	0.14	0.49	0.13
(p-H_3^+, p-H_2)	0.02	0	0.06	0.92

10 K	(o-H_3^+, o-H_2)	(o-H_3^+, p-H_2)	(p-H_3^+, o-H_2)	(p-H_3^+, p-H_2)
(o-H_3^+, o-H_2)	0.68	0.05	0.22	0.05
(o-H_3^+, p-H_2)	0	1	0	0
(p-H_3^+, o-H_2)	0.02	0.19	0.62	0.17
(p-H_3^+, p-H_2)	0	0	0	1

Appendix B

Estimated reaction rates inside the 22 pole trap

The reaction rates for the gas species, which are present inside the 22 pole trap during the experiments can be estimated via a calibrated measurement using a pressure gauge or via measuring the lifetimes of certain reactions.
Three different gas species are fed directly into the cold 22 pole trap. The pressure gauge (Pfeiffer IKR270) is placed on the outer vacuum chamber of the 22 pole trap. Therefore, it measures only the room temperature gas pressure surrounding the trap. But the gas pressure inside the trap p_{gauge} can be approximated according to

$$p_{\text{trap}} \approx k \cdot c \cdot p_{\text{gauge}} \cdot \sqrt{\frac{T_{\text{trap}}}{300}}\,, \tag{B.1}$$

where p_{gauge} denotes the gas pressure measured at the outer vacuum chamber and T_{trap} represents the nominal trap temperature. The parameters k and c represent the scaling factors based on the pressure gauge and the conductance of the trap, respectively. Both scaling factors depend on the gas species. The values for scaling factor k (taken from its data sheet [112]) for the gas species, which are present in

Gas species	He	Ar	H_2	N_2
k	5.9	0.8	2.4	1
c	71	22	100	

Table B.1: Scaling factor k for the gas species in the 22 pole, taken from [112] and calculated scaling factor c for the gas species, which are fed into the 22 pole.

the 22 pole are listed in Tab. B.1. The values for scaling factor c (also listed in Tab. B.1) have been calculated, based on a calibration adjustment using a capacitance pressure gauge (Baratron).
In a next step, the number densities $n(X)$ of the gas species X are approximated by the ideal gas law. The number of collisions with an ion that is stored in the 22 pole trap can be inferred using the Langevin rate coefficient, which is given in practical units (polarizability α in Å^3, reduced mass μ in amu) by [58]

$$k_L = 2.342\sqrt{\frac{\alpha}{\mu}} \cdot 10^{-9}\, cm^3 s^{-1}\,. \tag{B.2}$$

The calculated Langevin rate coefficients for the ion-neutral collisions that occur inside the 22 pole trap, H_3^+ + X (X = He, Ar, H_2, N_2) are listed in Tab. B.2. Furthermore, the collision rates R_L are determined by

$$R_L = k_L \cdot n(X)\,, \tag{B.3}$$

where $n(X)$ denotes the number densities of the gas species X.
Another approach in order to estimate the number densities $n(X)$ and derive the reaction rates R_L is to exploit the lifetimes of ions stored in the 22 pole trap. The destruction of the stored H_3^+ ions proceeds via the exothermic reaction

$$H_3^+ + N_2 \rightarrow N_2H^+ + H_2\,, \tag{B.4}$$

gas species X	p_{trap}(X) [mbar]	n_{trap}(X) [cm^{-3}]	α(X) [Å^3]	μ [amu]	$k_L(H_3^+ + X)$ [10^{-9} cm^3 s^{-1}]	R_L [s^{-1}]
He	$9.1 \cdot 10^{-4}$	$1 \cdot 10^{14}$	0.208	1.71	0.82	$8.2{\cdot}10^5$
Ar	$5.4 \cdot 10^{-6}$	$5.9 \cdot 10^{11}$	1.664	2.79	1.81	$1.1{\cdot}10^4$
H_2	$1.5 \cdot 10^{-6}$	$1.6 \cdot 10^{11}$	0.787	1.20	1.90	$3.0{\cdot}10^2$
N_2	$< 2.7 \cdot 10^{-9}$	$< 3 \cdot 10^8$	1.710	2.71	1.86	$< 5.6{\cdot}10^{-1}$

Table B.2: List of gas species present inside the trap volume. The estimated gas pressures p_{trap} are determined via Eq. B.1 and converted to number densities n_{trap} using the ideal gas law. The Langevin rate coefficients k_L of the gas species colliding with H_3^+ are calculated via Eq. B.2, in which the polarizability α(X) is taken from [59]. The collision rates R_L of H_3^+ + X are determined by Eq. B.3.

in which the residual gas N_2 collide with H_3^+. The measured lifetime ($\tau_{H_3^+}$) of H_3^+ stored in the trap is typically ~ 5 s. The back reaction of previously excited H_3^+ ions, that reacted with Ar at the beginning of the trap storage time, can be exploited in order to derive the number density of H_2 inside the trap volume. In reaction

$$ArH^+ + H_2 \rightarrow H_3^+ + Ar\,, \tag{B.5}$$

the ArH^+ ions form again H_3^+ via collisions with H_2. In the study, the number density $n(H_2)$ in the 22 pole trap causes an ArH^+ lifetime of $\tau_{H_3^+} = 10$ ms. The number density $n(X)$ can then be determined by

$$n(X) = \frac{1}{k_L \cdot \tau}, \tag{B.6}$$

where τ denotes the lifetime of the stored ions and k_L denotes the Langevin rate coefficient in reaction B.4 and B.5, respectively. The number densities n of H_2 and N_2 (Eq. B.6) and their reaction rates R_L with H_3^+ (Eq. B.3), using Langevin rate coefficients are summarized in Tab. B.3.

Tab. B.2 and B.3 show estimations for the number densities of the gas species, which are present inside the trap volume. Their collision rates with H_3^+ were inferred using the Langevin rate coefficient. In Tab. B.2, the number densities n_{trap}(X) were derived from an indirect gas pressure measurement. In Tab. B.2, the number densities n_{trap}(X) were derived from lifetime measurements of ions stored in the trap together and Langevin rate coefficients. Both methods are inherently limited due to the accuracy of the pressure gauge ($\pm$ 30%) and the Langevin rate coefficient. In most cases the Langevin rate coefficient describes only an upper limit for the physical rate coefficient. Since the experiments were performed at temperatures ranging from 45 to 100 K and rate coefficients tend to posses a temperature dependence, the

gas species X	n_{trap}(X) [cm^{-3}]	α(X) [Å^3]	μ [amu]	$k_L(H_3^+ + X)$ [10^{-9} cm^3 s^{-1}]	R_L [s^{-1}]
H_2	$6.6 \cdot 10^{10}$	0.787	1.20	1.90	$1.3{\cdot}10^2$
N_2	$1.1 \cdot 10^8$	1.710	2.71	1.86	$2.0{\cdot}10^{-1}$

Table B.3: List of gas species and their estimated number densities n_{trap}(X) inside the trap volume. The estimations were derived from lifetime measurements of stored ions, using calculated Langevin rate coefficients.

reaction rates may be overestimated. In conclusion, while both methods posses inaccuracies, in estimating the trap number densities and reaction rates, they can provide a reasonably good approximation.

Appendix C

Transfer matrices in linear approximation

Drift

$$R_{\text{Drift}} = \begin{pmatrix} 1 & s & 0 & 0 & 0 & 0 \\ 0 & 1 & 0 & 0 & 0 & 0 \\ 0 & 0 & 1 & s & 0 & 0 \\ 0 & 0 & 0 & 1 & 0 & 0 \\ 0 & 0 & 0 & 0 & 1 & s/\gamma^2 \\ 0 & 0 & 0 & 0 & 0 & 1 \end{pmatrix}, \tag{C.1}$$

where s denotes the length of the drift section [137].

Quadrupole

Horizontal focusing

$$R_{\text{FQP}} = \begin{pmatrix} \cos\left(\sqrt{K}s\right) & \frac{1}{\sqrt{K}}\sin\left(\sqrt{K}s\right) & 0 & 0 & 0 & 0 \\ -\sqrt{K}\sin\left(\sqrt{K}s\right) & \cos\left(\sqrt{K}s\right) & 0 & 0 & 0 & 0 \\ 0 & 0 & \cosh\left(\sqrt{K}s\right) & \frac{1}{\sqrt{K}}\sinh\left(\sqrt{K}s\right) & 0 & 0 \\ 0 & 0 & \sqrt{K}\sinh\left(\sqrt{K}s\right) & \cosh\left(\sqrt{K}s\right) & 0 & 0 \\ 0 & 0 & 0 & 0 & 1 & s/\gamma^2 \\ 0 & 0 & 0 & 0 & 0 & 1 \end{pmatrix}. \tag{C.2}$$

s denotes the length of the quadrupole section and K denotes the quadrupole strength [137].

Vertical focusing

$$R_{\mathrm{DQP}} = \begin{pmatrix} \cosh\left(\sqrt{K}s\right) & \frac{1}{\sqrt{K}}\sinh\left(\sqrt{K}s\right) & 0 & 0 & 0 & 0 \\ \sqrt{K}\sinh\left(\sqrt{K}s\right) & \cosh\left(\sqrt{K}s\right) & 0 & 0 & 0 & 0 \\ 0 & 0 & \cos\left(\sqrt{K}s\right) & \frac{1}{\sqrt{K}}\sin\left(\sqrt{K}s\right) & 0 & 0 \\ 0 & 0 & -\sqrt{K}\sin\left(\sqrt{K}s\right) & \cos\left(\sqrt{K}s\right) & 0 & 0 \\ 0 & 0 & 0 & 0 & 1 & L/\gamma^2 \\ 0 & 0 & 0 & 0 & 0 & 1 \end{pmatrix}. \tag{C.3}$$

s denotes the length of the quadrupole section and K denotes the quadrupole strength [137]. In linear approximation the transfer matrix of a magnetic and electrostatic quadrupole is identical. The quadrupole strength K is given by

$$K = \frac{|B_0|}{R_0}\frac{1}{(B\rho)_0}, \tag{C.4}$$

for a magnetic quadrupole, where B_0 denotes the magnetic field at the pole tip, R_0 is the radial distance from the central axis to the pole tip and $(B\rho)_0$ represents the magnetic rigidity.
The strength K for an electrostatic quadrupole is given by [137]

$$K = \frac{2|V_0|}{R_0^2}\frac{1}{(E\rho)_0}, \tag{C.5}$$

where V_0 denotes the electric potential at the pole tip, R_0 is the radial distance from the central axis to the pole tip and $(E\rho)_0$ represents the electric rigidity.

Electrostatic deflector

Cylindrical

$$R_{\mathrm{cDefl}} = \begin{pmatrix} \cos\left(\frac{\sqrt{2}}{\rho_0}s\right) & \frac{\rho_0}{\sqrt{2}}\sin\left(\frac{\sqrt{2}}{\rho_0}s\right) & 0 & 0 & 0 & \rho_0\left(1-\cos\left(\frac{\sqrt{2}}{\rho_0}s\right)\right) \\ -\frac{\sqrt{2}}{\rho_0}\sin\left(\frac{\sqrt{2}}{\rho_0}s\right) & \cos\left(\frac{\sqrt{2}}{\rho_0}s\right) & 0 & 0 & 0 & \sqrt{2}\sin\left(\frac{\sqrt{2}}{\rho_0}s\right) \\ 0 & 0 & 1 & s & 0 & 0 \\ 0 & 0 & 0 & 1 & 0 & 0 \\ -\sqrt{2}\sin\left(\frac{\sqrt{2}}{\rho_0}s\right) & \rho_0\cos\left(\frac{\sqrt{2}}{\rho_0}s\right) & 0 & 0 & 1 & -s+\sqrt{2}\rho_0\sin\left(\frac{\sqrt{2}}{\rho_0}s\right) \\ 0 & 0 & 0 & 0 & 0 & 1 \end{pmatrix}, \quad \text{(C.6)}$$

where s and ρ_0 denote the length and the radius of the deflector, respectively [137]. The horizontal and the vertical motion of particles, transported by the electrostatic deflector, given the transport matrix C.6, are uncoupled. In the vertical plane, this ion-optical element acts as a drift section. In the horizontal plane, the charged particle beam is focused and deflected by the angle $\phi = s/\rho_0$.
The imaging properties are defined by the ion-optical system, which can be represented by the transport matrix. Considering an ion-optical system, that consists of a drift, a cylindrical deflector and a drift, the transport matrix is given by

$$R_T = R_{\mathrm{Drift2}} \cdot R_{\mathrm{cDefl}} \cdot R_{\mathrm{Drift1}} \,. \quad \text{(C.7)}$$

For particles, that start from a point object at the ion-optical axis ($x_1 = 0$) with an arbitrary angular coordinate x_1', their transport through R_T is determined by

$$\begin{pmatrix} x_2 \\ x_2' \end{pmatrix} = R_T \cdot \begin{pmatrix} 0 \\ x_1' \end{pmatrix}, \quad \text{(C.8)}$$

with the final coordinates x_2 and x_2'. To determine the longitudinal position, where the horizontal beam profile is mapped from image point 1 to image point 2, Eq. C.8 has to be solved for $x_2 = 0$, in which the two drift sections are equal ($R_{\mathrm{Drift1}} = R_{\mathrm{Drift2}}$). Using $s = \rho_0 \cdot \phi$ in matrix C.6 and l for the drift length in matrix C.1, this condition leads to

$$2l\cos(\sqrt{2}\phi) + \frac{\rho_0}{\sqrt{2}}\sin(\sqrt{2}\phi) - \frac{\sqrt{2}}{\rho_0}l^2\sin(\sqrt{2}\phi) = 0 \,. \quad \text{(C.9)}$$

Solving the quadratic Eq. C.9 for l, the positive solution is given by

$$l = \frac{\rho_0}{\sqrt{2}} \cot \frac{\phi}{\sqrt{2}} \,. \tag{C.10}$$

At this distance l from the entrance and exit of the cylindrical deflector, the horizontal beam profiles are mapped. For a cylindrical 90° deflector ($\phi = \pi/2$), with a central path radius of $\rho_0 = 500$ mm, l is ≈ 175 mm.
The required angle (ϕ) of a cylindrical deflector, to create the horizontal image point at the entrance and exit, can be calculated via Eq. C.9 using $l = 0$, leading to $\phi \approx 127.3°$.

Sector dipole magnet

$$R_{\text{Dipole}} = \begin{pmatrix} \cos\left(\frac{s}{\rho_0}\right) & \rho_0 \sin\left(\frac{s}{\rho_0}\right) & 0 & 0 & 0 & \rho_0\left(1-\cos\left(\frac{s}{\rho_0}\right)\right) \\ -\frac{1}{\rho_0}\sin\left(\frac{s}{\rho_0}\right) & \cos\left(\frac{s}{\rho_0}\right) & 0 & 0 & 0 & \sin\left(\frac{s}{\rho_0}\right) \\ 0 & 0 & 1 & s & 0 & 0 \\ 0 & 0 & 0 & 1 & 0 & 0 \\ -\sin\left(\frac{s}{\rho_0}\right) & -\rho_0\left(1-\cos\left(\frac{s}{\rho_0}\right)\right) & 0 & 0 & 1 & -s+\rho_0\sin\left(\frac{s}{\rho_0}\right)+s/\gamma^2 \\ 0 & 0 & 0 & 0 & 0 & 1 \end{pmatrix}, \tag{C.11}$$

where s and ρ_0 denote the length and the radius of the dipole magnet, respectively. The transfer matrix C.11 represents only the hard-edge model. The vertical direction is represented by a drift section. In fact, the dipole magnet focuses the ion beam in the vertical plane due to edge focusing. The focal strength depends on the angle and the form of the pole shoe [137].

Appendix D

Ion-optical simulation of the 90° deflector without shielding tube

In this simulation the 90° deflector with a 30 mm hole in its outer electrode is simulated via SIMION [156]. Using the same deflector geometry, as presented in Sec. 8.3.4, the designed 90° deflector is simulated without the shielding tube. This simulation uses the same ion beam parameters and conditions than for the previous simulation, shown in Sec. 8.3.4 (see Fig. 8.17). The only difference is the absence of the shielding tube, attached to the hole in the outer electrode.
In Fig. D.1, the horizontal (x) and vertical (y) phase space distributions of the propagating ion beam are shown for the positions A - E along the beam path. The hole in the outer electrode does not introduce any filamentation, but leads to an additional focusing effect in the horizontal and vertical plane. This effect is demonstrated by comparing the resulting twiss parameters α and β of this SIMION simulation to the MAD X simulations, as shown in Fig. 8.19 and Tab. 8.6. Furthermore, the recorded horizontal phase space distributions, shown in Fig. D.1, indicate an increasing displacement in the beam position as the angle of the beam deviates from 90°.

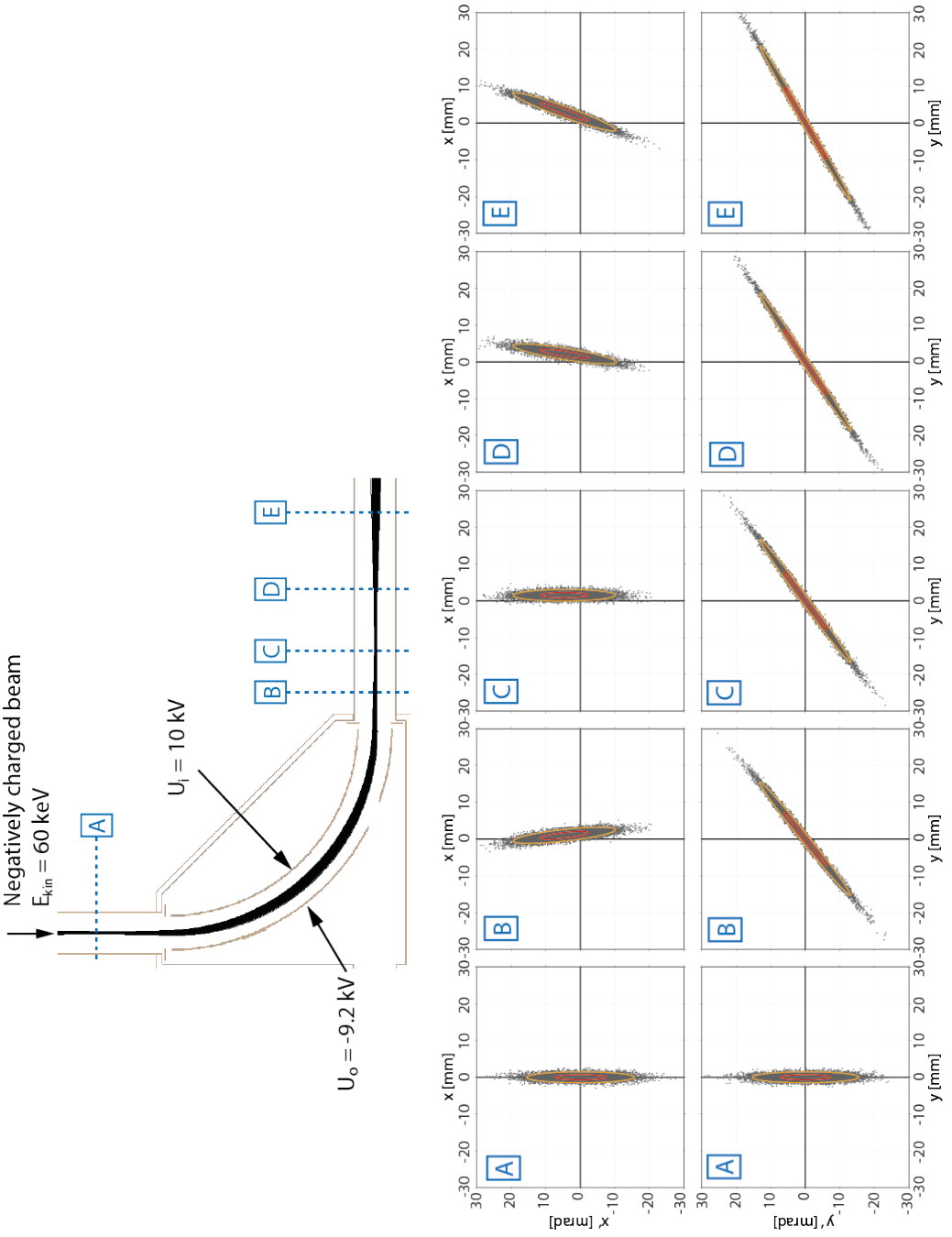

Figure D.1: Simulation of a negatively charged ion beam with an kinetic energy of 60 keV, deflected by an electrostatic 90° deflector with hole. At the positions A - E, along the beam path, the horizontal (x) and vertical (y) phase space distributions are recorded.

Bibliography

[1] The cologne database for molecular spectroscopy. `http://www.cdms.de/`. Online; accessed 10 March 2016.

[2] Pilbratt, G. L., Riedinger, J. R., Passvogel, T., Crone, G., Doyle, D., Gageur, U., Heras, A. M., Jewell, C., Metcalfe, L., Ott, S., and Schmidt, M. Herschel Space Observatory - An ESA facility for far-infrared and submillimetre astronomy. *A&A*, 518:L1, 2010.

[3] R. D. Gehrz, T. L. Roellig, M. W. Werner, G. G. Fazio, J. R. Houck, F. J. Low, G. H. Rieke, B. T. Soifer, D. A. Levine, and E. A. Romana. The nasa spitzer space telescope. *Review of Scientific Instruments*, 78(1), 2007.

[4] E. T. Young, E. E. Becklin, P. M. Marcum, T. L. Roellig, J. M. DeBuizer, T. L. Herter, R. Güsten, E. W. Dunham, and P. Temi et al. Early Science with SOFIA, the Stratospheric Observatory For Infrared Astronomy. *The Astrophysical Journal Letters*, 749(2):L17, 2012.

[5] Alwyn Wootten. Atacama Large Millimeter Array (ALMA). *Proc. SPIE*, 4837:110–118, 2003.

[6] Eric Herbst and William Klemperer. The formation and depletion of molecules in dense interstellar clouds. *Astrophysical Journal*, 185:505–534, 1973.

[7] E. E. Ferguson, F. C. Fehsenfeld, and A. L. Schmeltekopf. *Ion-Molecule Reaction Rates Measured in a Discharge Afterglow*, chapter 7, pages 83–91.

[8] N.G. Adams and D. Smith. The selected ion flow tube (SIFT); a technique for studying ion-neutral reactions. *International Journal of Mass Spectrometry and Ion Physics*, 21(3 - 4):349 – 359, 1976.

[9] R. Plasil, T. Mehner, P. Dohnal, T. Kotrik, J. Glosik, and D. Gerlich. Reactions of cold trapped CH^+ ions with slow H atoms. *The Astrophysical Journal*, 737(2):60, 2011.

[10] J. J. Thomson. Rays of positive electricity. *Philosophical Magazine*, 21:225, 1911.

[11] J. J. Thomson. Further experiments on positive rays. *Philosophical Magazine*, 24:209, 1912.

[12] J. J. Thomson. *Rays of Positive Electricity and their Application to Chemical Analysis*. Longmans, Green and Co. (1st edn. London), 1913.

[13] J. J. Thomson. *Rays of Positive Electricity and their Application to Chemical Analysis*. Longmans, Green and Co. (2nd edn. London), 1921.

[14] J. J. Thomson. Heavy hydrogen. *Nature*, 133:280–281, 1934.

[15] Harold C. Urey, F. G. Brickwedde, and G. M. Murphy. A hydrogen isotope of mass 2. *Physical Review*, 39(1):164, 1932.

[16] A. J. Dempster. LII. the ionization and dissociation of hydrogen molecules and the formation of H3. *Philosophical Magazine Series 6*, 31(185):438, 1916.

[17] T. R. Hogness and E. G. Lunn. The ionization of hydrogen by electron impact as interpreted by positive ray analysis. *Physical Review*, 26(1):44, 1925.

[18] C. A. Coulson. The electronic structure of H_3^+. *Mathematical Proceedings of the Cambridge Philosophical Societys*, 31(2):244–259, 1935.

[19] J. Hirschfelder, H. Eyring, and N. Rosen. I. calculation of energy of H_3 molecule. *The Journal of Chemical Physics*, 4(2):121, 1936.

[20] J. Hirschfelder, H. Eyring, and N. Rosen. II. calculation of energy of H_3^+ ion. *The Journal of Chemical Physics*, 4(2):130, 1936.

[21] J. Hirschfelder, H. Diamond, and H. Eyring. Calculation of the energy of H_3 and of H_3^+. III. *The Journal of Chemical Physics*, 5(9):695, 1937.

[22] David Stevenson and Joseph Hirschfelder. The structure of H_3, H_3^+, and of H_3^-. IV. *The Journal of Chemical Physics*, 5(12):933, 1937.

[23] Joseph O. Hirschfelder. The energy of the triatomic hydrogen molecule and ion, v. *The Journal of Chemical Physics*, 6(12):795, 1938.

[24] M. Gaillard, D. Gemmell, G. Goldring, I. Levine, W. Pietsch, J. Poizat, A. Ratkowski, J. Remillieux, Z. Vager, and B. Zabransky. Experimental determination of the structure of H_3^+. *Physical Review A*, 17:1797–1803, 1978.

[25] Harold Conroy. Potential energy surfaces for the H_3^+ molecule-ion. *The Journal of Chemical Physics*, 40:603, 1964.

[26] Harold Conroy. Molecular Schrödinger Equation. IV. Results for One- and Two-Electron Systems. *The Journal of Chemical Physics*, 41:1341, 1964.

[27] Ralph E. Christoffersen. Configuration-Interaction study of the ground state of the H_3^+ molecule. *The Journal of Chemical Physics*, 41(4):960, 1964.

[28] D. W. Martin, E. W. McDaniel, and M. L. Meeks. On the possible occurence of H_3^+ in interstellar space. *The Astrophysical Journal*, 134:1012, 1961.

[29] William D. Watson. The rate of formation of interstellar molecules by ion-molecule reactions. *The Astrophysical Journal*, 183:L17, 1973.

[30] G. D. Carney and R. N. Porter. H_3^+: Ab initio calculation of the vibration spectrum. *The Journal of Chemical Physics*, 65(9):3547–3565, 1976.

[31] T. R. Geballe and T. Oka. Detection of H_3^+ in interstellar space. *Nature*, 384(6607):334–335, 1996.

[32] B. J. McCall, T. R. Geballe, K. H. Hinkle, and T. Oka. Detection of H_3^+ in the diffuse interstellar medium toward cygnus ob2 no. 12. *Science*, 279:1910–1913, 1998.

[33] T. R. Geballe. H_3^+ at UKIRT – a saga of discovery. *UKIRT Newsletter*, (24):7–10, Spring 2009.

[34] T. Oka. My 45 years of astrochemistry: Memoirs of Takeshi Oka. *The Journal of Physical Chemistry A*, 117:9308 – 9313, 2013.

[35] T. R. Geballe and T. Oka. An infrared specroscopic search for the molecular ion H_3^+. *The Astrophysical Journal*, 342:855–859, 1989.

[36] P. Drossart, J.-P. Maillard, J. Caldwell, S. J. Kim, J. K. G. Watson, W. A. Majewski, J. Tennyson, S. Miller, S. K. Atreya, J. T. Clarke, J. H. Waite, and R. Wagener. Detection of H_3^+ on jupiter. *Nature*, 340(6234):539–541, 1989.

[37] T. Oka and T. R. Geballe. Observations of the 4 micron fundamental band of H_3^+ in jupiter. *The Astrophysical Journal*, 351:L53–L56, 1990.

[38] T. R. Geballe, M.-F. Jagod, and T. Oka. Detection of H_3^+ infrared emission lines in saturn. *The Astrophysical Journal*, 408:L109, 1993.

[39] Liesl Neale, Steven Miller, and Jonathan Tennyson. Spectroscopic properties of the H_3^+ molecule: A new calculated line list. *Astrophysical Journal*, 464:516, 1996.

[40] Christopher P. Morong, Jennifer L. Gottfried, and Takeshi Oka. H_3^+ as the benchmark for rigorous ab initio theory. *Journal of Molecular Spectroscopy*, 255(1):13–23, 2009.

[41] J. Mikosch, H. Kreckel, R. Wester, R. Plasil, J. Glosik, D. Gerlich, D. Schwalm, and A. Wolf. Action spectroscopy and temperature diagnostics of H_3^+ by chemical probing. *The Journal of Chemical Physics*, 121(22):11030–11037, 2004.

[42] Annemieke Petrignani, Max H. Berg, Florian Grussie, Andreas Wolf, Irina I. Mizus, Oleg L. Polyansky, Jonathan Tennyson, Nikolai F. Zobov, Michele Pavanello, and Ludwik Adamowicz. Communication: Visible line intensities of the triatomic hydrogen ion from experiment and theory. *The Journal of Chemical Physics*, 141(24), 2014.

[43] Michele Pavanello, Ludwik Adamowicz, Alexander Alijah, Nikolai F. Zobov, Irina I. Mizus, Oleg L. Polyansky, Jonathan Tennyson, Tamás Szidarovszky, Attila G. Császár, Max Berg, Annemieke Petrignani, and Andreas Wolf. Precision measurements and computations of transition energies in rotationally cold triatomic hydrogen ions up to the midvisible spectral range. *Phys. Rev. Lett.*, 108:023002, 2012.

[44] Robert Röhse, Werner Kutzelnigg, Ralph Jaquet, and Wim Klopper. Potential energy surface of the H_3^+ ground state in the neighborhood of the minimum with microhartree accuracy and vibrational frequencies derived from it. *The Journal of Chemical Physics*, 101(3):2231–2243, 1994.

[45] Alexander Alijah. Accurate calculations and assignments of above-barrier states of h_3^+ up to 15 300 cm^{-1}. *Journal of Molecular Spectroscopy*, 264(2):111–119, 2010.

[46] Jonathan Tennyson. Spectroscopy of H_3^+: planets, chaos and the universe. *Reports on Progress in Physics*, 58(4):421–476, 1995.

[47] F.-S. Pan and T. Oka. Calculated forbidden rotational spectra of H_3^+. *The Astrophysical Journal*, 305:518, 1986.

[48] James K.G. Watson. Forbidden rotational spectra of polyatomic molecules. *Journal of Molecular Spectroscopy*, 40(3):536 – 544, 1971.

[49] Gerhard Herzberg. *Molecular Spectra and Molecular Structure*, volume II. Krieger, Malabar, Florida, 1991.

[50] C.Michael Lindsay and Benjamin J. McCall. Comprehensive evaluation and compilation of H_3^+ spectroscopy. *Journal of Molecular Spectroscopy*, 210(1):60–83, 2001.

[51] Jon T. Hougen. Classification of rotational energy levels for Symmetric-Top molecules. *The Journal of Chemical Physics*, 37(7):1433, 1962.

[52] Benjamin J. McCall. *Spectroscopy of H_3^+ in Laboratory and Astrophysical Plasmas.* PhD thesis, University of Chicago, 2001.

[53] Per Jensen Philip R. Bunker. *Molecular Symmetry and Spectroscopy.* NRC Research Press, Ottawa, 1998.

[54] E.P. Hunter and S.G. Lias. Nist chemistry webbook, nist standard reference database number 69. `http://webbook.nist.gov`. Online; accessed 26 June 2015.

[55] Charles J. Lada, Edwin A. Bergin, Jo ao F. Alves, and Tracy L. Huard. The Dynamical State of Barnard 68: A Thermally Supported, Pulsating Dark Cloud. *The Astrophysical Journal*, 586(1):286, 2003.

[56] Paul Langevin. A fundamental formula of kinetic theory. *Annales de chimie et de physique*, 5:245–288, 1905.

[57] George Gioumousis and D. P. Stevenson. Reactions of Gaseous Molecule Ions with Gaseous Molecules. V. Theory. *The Journal of Chemical Physics*, 29(2):294–299, 1958.

[58] Oskar Asvany and Stephan Schlemmer. Numerical simulations of kinetic ion temperature in a cryogenic linear multipole trap. *International Journal of Mass Spectrometry*, 279(2-3):147–155, 2009.

[59] Russell D. Johnson III, editor. *NIST Chemistry WebBook, NIST Standard Reference Database Number 101.* 2013.

[60] Roger P. Clow and Jean H. Futrell. Ion-molecule reactions in isotopic hydrogen by ion cyclotron resonance. *International Journal of Mass Spectrometry and Ion Physics*, 8(2):119 – 142, 1972.

[61] David L. Smith and Jean H. Futrell. Ion-molecule reactions in the CO_2/H_2 system by ion cyclotron resonance. *International Journal of Mass Spectrometry and Ion Physics*, 10(4):405 – 418, 1973.

[62] Lowell P. Theard and Wesley T. Huntress. Ion-molecule reactions and vibrational deactivation of H_2^+ ions in mixtures of hydrogen and helium. *The Journal of Chemical Physics*, 60(7):2840–2848, 1974.

[63] A. Dalgarno. The galactic cosmic ray ionization rate. *Proceedings of the National Academy of Sciences*, 103(33):12269–12273, 2006.

[64] Nick Indriolo and Benjamin J. McCall. Investigating the cosmic-ray ionization rate in the galactic diffuse interstellar medium through observations of H_3^+. *The Astrophysical Journal*, 745(1):91, 2012.

[65] Takeshi Oka. Interstellar H_3^+. *Proceedings of the National Academy of Sciences*, 103(33):12235–12242, 2006.

[66] B. J. McCall, A. J. Huneycutt, R. J. Saykally, N. Djuric, G. H. Dunn, J. Semaniak, O. Novotny, A. Al-Khalili, A. Ehlerding, F. Hellberg, S. Kalhori, A. Neau, R. D. Thomas, A. Paal, F. Österdahl, and M. Larsson. Dissociative recombination of rotationally cold H_3^+. *Phys. Rev. A*, 70:052716, Nov 2004.

[67] Viatcheslav Kokoouline and Chris H. Greene. Unified theoretical treatment of dissociative recombination of D3h triatomic ions: Application to H_3^+ and D_3^+. *Physical Review A*, 68(1):012703, 2003.

[68] Samantha Fonseca dos Santos, Viatcheslav Kokoouline, and Chris H. Greene. Dissociative recombination of H_3^+ in the ground and excited vibrational states. *The Journal of Chemical Physics*, 127(124309), 2007.

[69] Theodore P. Snow and Veronica M. Bierbaum. Ion chemistry in the interstellar medium. *Annual Review of Analytical Chemistry*, 1(1):229–259, 2008. PMID: 20636080.

[70] F. Bertoldi and B.T. Draine. Nonequilibrium photodissociation regions: Ionization dissociation fronts. *The Astrophysical Journal*, 458(1):222–232, 1996.

[71] H. H. Lee, R. P. A. Bettens, and E. Herbst. Fractional abundances of molecules in dense interstellar clouds: A compendium of recent model results. *Astronomy and Astrophysics Supplement*, 119:111–114, 1996.

[72] J. A. Cardelli, D. M. Meyer, M. Jura, and B. D. Savage. The abundance of interstellar carbon. *The Astrophysical Journal*, 467:334–340, 1996.

[73] Ulysses J. Sofia, Jason A. Cardelli, Kenneth P. Guerin, and David M. Meyer. Carbon in the diffuse interstellar medium. *The Astrophysical Journal Letters*, 482(1):L105, 1997.

[74] Martin Quack. Detailed symmetry selection rules for reactive collisions. *Molecular Physics*, 34(2):477–504, 1977.

[75] M. Cordonnier, D. Uy, R. M. Dickson, K. E. Kerr, Y. Zhang, and T. Oka. Selection rules for nuclear spin modifications in ion-neutral reactions involving H_3^+. *The Journal of Chemical Physics*, 113(8):3181–3193, 2000.

[76] Takeshi Oka. Nuclear spin selection rules in chemical reactions by angular momentum algebra. *Journal of Molecular Spectroscopy*, 228:635–639, 2004.

[77] Kyle N. Crabtree, Brian A. Tom, and Benjamin J. McCall. Nuclear spin dependence of the reaction of H_3^+ with H_2. I. kinetics and modeling. *The Journal of Chemical Physics*, 134(194310), 2011.

[78] Kyle N. Crabtree, Carrie A. Kauffman, Brian A. Tom, Eftalda Beçka, Brett A. McGuire, and Benjamin J. McCall. Nuclear spin dependence of the reaction of H_3^+ with H_2. II. experimental measurements. *The Journal of Chemical Physics*, 134(194311), 2011.

[79] Kisam Park and John C. Light. Microcanonical statistical study of ortho-para conversion in the reaction $H_3^+ + H_2 \rightarrow (H_5^+)^* \rightarrow H_3^+ + H_2$ at very low energies. *The Journal of Chemical Physics*, 126(4):–, 2007.

[80] Kyle N. Crabtree, Nick Indriolo, Holger Kreckel, Brian A. Tom, and Benjamin J. McCall. On the ortho:para ratio of H_3^+ in diffuse molecular clouds. *The Astrophysical Journal*, 729(1):15, 2011.

[81] Lyman Spitzer and William D. Cochran. Rotational excitation of interstellar H_2. *The Astrophysical Journal*, 186:L23–L28, 1973.

[82] A. Dalgarno, J. H. Black, and J. C. Weisheit. Ortho-para transitions in H_2 and the fractionation of HD. *Astrophysical Letters*, 14:77–79, 1973.

[83] B. D. Savage, R. C. Bohlin, J. F. Drake, and W. Budich. A survey of interstellar molecular hydrogen. I. *The Astrophysical Journal*, 216:291–307, 1977.

[84] Brian L. Rachford, Theodore P. Snow, Jason Tumlinson, J. Michael Shull, William P. Blair, Roger Ferlet, Scott D. Friedman, Cecile Gry, Edward B. Jenkins, Donald C. Morton, Blair D. Savage, Paule Sonnentrucker, Alfred Vidal-Madjar, Daniel E. Welty, and Donald G. York. A far ultraviolet spectroscopic explorer survey of interstellar molecular hydrogen in translucent clouds. *The Astrophysical Journal*, 577(1):221, 2002.

[85] Kyle N. Crabtree and Benjamin J. McCall. The ortho : para ratio of H_3^+ in laboratory and astrophysical plasmas. *Philosophical Transactions of the Royal Society of London A: Mathematical, Physical and Engineering Sciences*, 370(1978):5055–5065, 2012.

[86] T. Albertsson, N. Indriolo, H. Kreckel, D. Semenov, K. N. Crabtree, and Th. Henning. First time-dependent study of H_2 and H_3^+ ortho-para chemistry in the diffuse interstellar medium: Observations meet theoretical predictions. *The Astrophysical Journal*, 787(1):44, 2014.

[87] Benjamin J. McCall, Kenneth H. Hinkle, Thomas R. Geballe, and Takeshi Oka. H_3^+ in dense and diffuse clouds. *Faraday Discuss.*, 109:267–280, 1998.

[88] B. J. McCall, A. J. Huneycutt, R. J. Saykally, T. R. Geballe, N. Djuric, G. H. Dunn, J. Semaniak, O. Novotny, A. Al-Khalili, A. Ehlerding, F. Hellberg, S. Kalhori, A. Neau, R. Thomas, F. Osterdahl, and M. Larsson. An enhanced cosmic-ray flux towards ζ persei inferred from a laboratory study of the H_3^+-e^- recombination rate. *Nature*, 422(6931):500–502, 2003.

[89] E. L. Gibb, S. D. Brittain, T. W. Rettig, M. Troutman, Theodore Simon, and C. Kulesa. CO and H_3^+ toward MWC 1080, MWC 349, and LkHα 101. *The Astrophysical Journal*, 715(2):757, 2010.

[90] Dieter Gerlich. *Inhomogeneous RF Fields: A Versatile Tool for the Study of Processes with Slow Ions*. Wiley, New York, 1992.

[91] E. Fischer. Die dreidimensionale Stabilisierung von Ladungsträgern in einem Vierpolfeld. *Zeit*, 156:1–26, 1959.

[92] Dieter Gerlich. Ion-neutral collisions in a 22-pole trap at very low energies. *Physica Scripta*, T59:256–263, 1995.

[93] J. D. Prestage, A. Williams, L. Maleki, M. J. Djomehri, and E. Harabetian. Dynamics of charged particles in a Paul radio-frequency quadrupole trap. *Phys. Rev. Lett.*, 66:2964–2967, Jun 1991.

[94] Wolfgang Demtröder. *Molekülphysik*. Oldenburg Wissenschaftsverlag, 2003.

[95] Alain Campargue, Samir Kassi, Krzysztof Pachucki, and Jacek Komasa. The absorption spectrum of H2: CRDS measurements of the (2-0) band, review of the literature data and accurate ab initio line list up to 35 000 cm-1. *Phys. Chem. Chem. Phys.*, 14:802–815, 2012.

[96] Dennis Bing. Kontrollierte Parawasserstofferzeugung zur Untersuchung der Spinsymmetrie bei gespeicherten Wasserstoffmolekülen . Master's thesis, Ruprecht Karls Universität Heidelberg, 2006.

[97] Wolfgang Demtröder. *Laserspektroskopie*. Springer, 2007.

[98] D.A. Long. *The Raman Effect*. John Wiley & Sons, 2002.

[99] Annette Svendsen, Ulrich J. Lorenz, Oleg V. Boyarkin, and Thomas R. Rizzo. A new tandem mass specrometer for photofragment spectroscopy of cold, gas-phase molecular ions. *Rev. Sci. Instrum.*, 81(073107), 2010.

[100] W. Paul, S. Schlemmer, B. Lücke, and D. Gerlich. Deuteration of positive hydrogen cluster ions H_5^+ to H_{17}^+ at 10 K. *Chemical Physics*, 209(2 - 3):265 – 274, 1996. Structure and Reactivity of Molecular Ions.

[101] S. Trippel, J. Mikosch, R. Berhane, R. Otto, M. Weidemüller, and R. Wester. Photodetachment of cold OH- in a multipole ion trap. *Physical Review Letters*, 97(19):193003, 2006.

[102] Holger Kreckel. *Internal Excitations of Stored Triatomic Hydrogen Molecular Ions*. PhD thesis, Ruprecht Karls Universität Heidelberg, 2003.

[103] E. Teloy and D. Gerlich. Integral cross sections for ion–molecule reactions. I. the guided beam technique. *Chemical Physics*, 4(3):417–427, 1974.

[104] R. Disch. Diplomarbeit, 1987.

[105] W. Paul, H. P. Reinhard, and U. Zahn. Das elektrische massenfilter als massenspektrometer und isotopentrenner. *Zeitschrift für Physik*, 152(2):143–182, 1958.

[106] N. R. Daly. Scintillation type mass spectrometer ion detector. *Review of Scientific Instruments*, 31(3):264, 1960.

[107] H. C. Bourne, R. W. Cloud, and J. G. Trump. Role of positive ions in high-voltage breakdown in vacuum. *Journal of Applied Physics*, 26(5):596–599, 1955.

[108] L. Ricci, M. Weidemüller, T. Esslinger, A. Hemmerich, C. Zimmermann, V. Vuletic, W. Kónig, and T.W. Hánsch. A compact grating-stabilized diode laser system for atomic physics. *Optics Communications*, 117(5-6):541 – 549, 1995.

[109] M. Puchalski, D. Kedziera, and K. Pachucki. D_1 and D_2 lines in ^{6}Li and ^{7}Li including qed effects. *PRA*, 87(3):032503, March 2013.

[110] J T Knudtson and E M Eyring. Laser-induced chemical reactions. *Annual Review of Physical Chemistry*, 25(1):255–274, 1974.

[111] S. Schlemmer, T. Kuhn, E. Lescop, and D. Gerlich. Laser excited N_2^+ in a 22-pole ion trap: Experimental studies of rotational relaxation processes. *International Journal of Mass Spectrometry*, 185-187:589–602, April 1999.

[112] Pfeiffer Vacuum. *Operating manual: Compact Cold Cathode Gauge IKR270.*

[113] Susanna L. Widicus Weaver, David E. Woon, Branko Ruscic, and Benjamin J. McCall. Is HO_2^+ a detectable interstellar molecule? *The Astrophysical Journal*, 697(1):601, 2009.

[114] Lars Kluge, Sabrina Gärtner, Sandra Brünken, Oskar Asvany, Dieter Gerlich, and Stephan Schlemmer. Transfer of a proton between H_2 and O_2. *Philosophical Transactions of the Royal Society of London A: Mathematical, Physical and Engineering Sciences*, 370(1978):5041–5054, 2012.

[115] Kyle N. Crabtree. private communication.

[116] F. Grussie, M. H. Berg, K. N. Crabtree, S. Gärtner, B. J. McCall, S. Schlemmer, A. Wolf, and H. Kreckel. The low-temperature nuclear spin equilibrium of H_3^+ in collisions with H_2. *The Astrophysical Journal*, 759(1):21, 2012.

[117] Dieter Gerlich, Eric Herbst, and Evelyne Roueff. $H_3^+ + HD \leftrightarrow H_2D^+ + H_2$: low-temperature laboratory measurements and interstellar implications. *Planetary and Space Science*, 50(12 - 13):1275 – 1285, 2002. Special issue on Deuterium in the Universe.

[118] Edouard Hugo, Oskar Asvany, and Stephan Schlemmer. $H_3^+ + H_2$ isotopic system at low temperatures: Microcanonical model and experimental study. *The Journal of Chemical Physics*, 130(16):164302, 2009.

[119] Michal Hejduk, Petr Dohnal, Peter Rubovič, Ábel Kálosi, Radek Plašil, Rainer Johnsen, and Juraj Glosík. Flowing-afterglow study of electron-ion recombination of para-H_3^+ and ortho-H_3^+ ions at temperatures from 60 K to 300 K. *The Journal of Chemical Physics*, 143(4):–, 2015.

[120] Brian A. Tom, Vitali Zhaunerchyk, Michael B. Wiczer, Andrew A. Mills, Kyle N. Crabtree, Magdalena Kaminska, Wolf D. Geppert, Mathias Hamberg, Magnus af Ugglas, Erik Vigren, Wim J. van der Zande, Mats Larsson, Richard D. Thomas, and Benjamin J. McCall. Dissociative recombination of highly enriched para-H_3^+. *The Journal of Chemical Physics*, 130(3):031101–4, 2009.

[121] Holger Kreckel, Oldřich Novotný, Kyle N. Crabtree, Henrik Buhr, Annemieke Petrignani, Brian A. Tom, Richard D. Thomas, Max H. Berg, Dennis Bing, Manfred Grieser, Claude Krantz, Michael Lestinsky, Mario B. Mendes, Christian Nordhorn, Roland Repnow, Julia Stützel, Andreas Wolf, and Benjamin J. McCall. High-resolution storage-ring measurements of the dissociative recombination of H_3^+ using a supersonic expansion ion source. *Physical Review A*, 82(4):042715, 2010.

[122] I. Savić, I. Čermák, and D. Gerlich. Reactions of C_n (n = 1-3) with ions stored in a temperature-variable radio-frequency trap. *International Journal of Mass Spectrometry*, 240(2):139 – 147, 2005.

[123] A. P. O'Connor, X. Urbain, J. Stützel, K. A. Miller, N. de Ruette, M. Garrido, and D. W. Savin. Reaction studies of neutral atomic C with H_3^+ using a merged-beams apparatus. *The Astrophysical Journal Supplement Series*, 219(1):6, 2015.

[124] McGowan J. W. Brouillard, F. *Physics of Ion-Ion and Electron-Ion Collisions*. Number ISBN 978-1-4613-3545-0. Springer US, 1 edition, 1983.

[125] R. A. Phaneuf, C. C. Havener, G. H. Dunn, and A. Müller. Merged-beams experiments in atomic and molecular physics. *Rep. Prog. Phys.*, 62:1143 – 1180, 1999.

[126] A. Rostagni. Untersuchungen über langsame Ionen und Neutralstrahlen. *Zeitschrift für Physik*, 88(1-2):55–75, 1934.

[127] Rodman Smythe and James W. Toevs. Collisional electron detachment from hydrogen atoms and negative hydrogen ions between 4 and 18 MeV. *Phys. Rev.*, 139:A15–A18, Jul 1965.

[128] B. Van Zyl, N. G. Utterback, and R. C. Amme. Generation of a fast atomic hydrogen beam. *Review of Scientific Instruments*, 47(7):814–819, 1976.

[129] C. C. Havener, M. S. Huq, H. F. Krause, P. A. Schulz, and R. A. Phaneuf. Merged-beams measurements of electron-capture cross sections for O^{5+} + H at electron-volt energies. *Phys. Rev. A*, 39:1725–1740, Feb 1989.

[130] T. Andersen. Atomic negative ions: structure, dynamics and collisions. *Phys. Rep.*, 394:157–313, 2004.

[131] H. Bruhns, H. Kreckel, K. Miller, M. Lestinsky, B. Seredyuk, W. Mitthumsiri, B. L. Schmitt, M. Schnell, X. Urbain, M. L. Rappaport, C. C. Havener, and D. W. Savin. A novel merged beams apparatus to study anion-neutral reactions. *Review of Scientific Instruments*, 81(1), 2010.

[132] H. Bruhns, H. Kreckel, K. A. Miller, X. Urbain, and D. W. Savin. Absolute energy-resolved measurements of the $H^- + H \rightarrow H_2 + e^-$ associative detachment reaction using a merged-beam apparatus. *Phys. Rev. A*, 82:042708, Oct 2010.

[133] A.R.P. Rau. The negative ion of hydrogen. *Journal of Astrophysics and Astronomy*, 17(3-4):113–145, 1996.

[134] N. de Ruette, K. A. Miller, A. P. O'Connor, X. Urbain, C. F. Buzard, S. Vissapragada, and D. W. Savin. Merged-beams reaction studies of $O + H_3^+$. *The Astrophysical Journal*, 816(1):31, 2016.

[135] Michael Scheer, René C. Bilodeau, Cicely A. Brodie, and Harold K. Haugen. Systematic study of the stable states of C^-, Si^-, Ge^- and Sn^- via infrared laser spectroscopy. *Phys. Rev. A*, 58:2844–2856, Oct 1998.

[136] C. Blondel, W. Chaibi, C. Delsart, C. Drag, F. Goldfarb, and S. Kröger. The electron affinities of O, Si, and S revisited with the photodetachment microscope. *Eur. Phys. J. D*, 33:335–342, 2005.

[137] Frank Hinterberger. *Physik der Teilchenbeschleuniger und Ionenoptik*. Springer-Verlag Berlin Heidelberg, 2008.

[138] Helmut Wiedemann. *Particle Accelerator Physics*. Springer-Verlag, 2007.

[139] E.D Courant and H.S Snyder. Theory of the alternating-gradient synchrotron. *Annals of Physics*, 3(1):1 – 48, 1958.

[140] Florian Fellenberger. *Aufbau und Charakterisierung der ersten Ecke des kryogenen elektrostatischen Speicherrings CSR*. PhD thesis, Ruprecht-Karls-Universität, Heidelberg, Germany, 2012.

[141] R. von Hahn, V. Andrianarijaona, J. R. Crespo López−Urrutia, H. Fadil, M. Grieser, Ch. Haberstroh, V. Mallinger, D. A. Orlov, H. Quack, M. Rappaport, C. D. Schröter, D. Schwalm, J. Ullrich, T. Weber, A. Wolf, and D. Zajfman. Cryogenic concept for the low−energy electrostatic cryogenic storage ring (csr) at mpik in heidelberg. *AIP Conference Proceedings*, 823(1):1187–1193, 2006.

[142] Andrey Shornikov. *An electron cooler for ultra-low energy cryogenic operation*. PhD thesis, Ruprecht-Karls-Universität, Heidelberg, Germany, 2012.

[143] Stephen Vogel. *Developments at an Electrostatic Cryogenic Storage Ring for Electron-Cooled keV Energy Ion Beams*. PhD thesis, Ruprecht-Karls-Universität, Heidelberg, Germany, 2016.

[144] C. Krantz, F. Berg, K. Blaum, F. Fellenberger, M. Froese, M. Grieser, R. von Hahn, M. Lange, F. Laux, S. Menk, R. Repnow, A. Shornikov, and A. Wolf. The cryogenic storage ring and its application to molecular ion recombination physics. *Journal of Physics: Conference Series*, 300(1):012010, 2011.

[145] Arno Becker. *Imaging of Neutral Fragmentation Products from Fast Molecular Ion Beams: Paving the Way for Reaction Studies in Cryogenic Environment.* PhD thesis, Ruprecht-Karls-Universität, Heidelberg, Germany, 2016.

[146] Kaija Spruck. *Dielectronic Recombination Experiments with Tungsten Ions at the Test Storage Ring and Development of a Single-Particle Detector at the Cryogenic Storage Ring.* PhD thesis, Justus-Liebig-Universität, Gießen, Germany, 2015.

[147] Felix Laux. *Entwicklung von kapazitiven Positions-, Strom- und Schottkysignal-Messsystemen für den kryogenen Speicherring CSR.* PhD thesis, Ruprecht-Karls-Universität, Heidelberg, Germany, 2011.

[148] T. Sieber, K. Blaum, M. Grieser, M. Lange, F. Laux, Tobias Sorg, R. von Hahn, and A Wolf. Beam diagnostics for the prototype of the Cryogenic Storage Ring CSR. In *Proceedings of EPAC2008*, pages 1287–1289, Genoa, Italy, 2008.

[149] J. Ullrich, R. Moshammer, A. Dorn, R. Dörner, L. P. H. Schmidt, and H. Schmidt-Böcking. Recoil-ion and electron momentum spectroscopy: reaction-microscopes. *Reports on Progress in Physics*, 66(9):1463, 2003.

[150] R. Moshammer, M. Unverzagt, W. Schmitt, J. Ullrich, and H. Schmidt-Böcking. A 4π recoil-ion electron momentum analyzer: a high-resolution microscope for the investigation of the dynamics of atomic, molecular and nuclear reactions. *Nuclear Instruments and Methods in Physics Research Section B: Beam Interactions with Materials and Atoms*, 108(4):425 – 445, 1996.

[151] R. von Hahn, A. Becker, F. Berg, K. Blaum, C. Breitenfeldt, H. Fadil, F. Fellenberger, M. Froese, S. George, J. Göck, M. Grieser, F. Grussie, E. A. Guerin, O. Heber, P. Herwig, J. Karthein, C. Krantz, H. Kreckel, S. Kumar, M. Lange, F. Laux, S. Lohmann, S. Menk, C. Meyer, P. M. Mishra, O. Novotný, A. P. O'Connor, D. A. Orlov, M. L. Rappaport, R. Repnow, S. Saurabh, S. Schippers, C. D. Schröter, D. Schwalm, L. Schweikhard, T. Sieber, A. Shornikov, K. Spruck, J. Ullrich, X. Urbain, S. Vogel, P. Wilhelm, A. Wolf, and D. Zajfman. The Cryogenic Storage Ring CSR. *submitted to Review of Scientific Instruments*, 2016.

[152] H. Grothe and F.C. Iselin. *MAD 8 - Methodical Accelerator Design.* CERN.

[153] Vector Fields Limited, 24 Bankside, Kidlington, Oxford OX5 1JE, England. *Opera-3D reference manual*, 2004.

[154] T. Roberts. *G4beamline User's Guide 2.16*, 2013.

[155] Frank Schmidt. *MAD X - Methodical Accelerator Design*. CERN.

[156] David J. Manura and David A. Dahl. *SIMION 8.0 User Manual*, 2007.

[157] Volker Ziemann. Vacuum tracking. In *Proceedings of the Particle Accelerator Conf., Washington, D.C.*, 1992.

[158] Felix A. Berg. Diplomarbeit, 2011.

[159] Roland Repnow. private communication.

[160] D.G. Seely, H. Bruhns, D.W. Savin, T.J. Kvale, E. Galutschek, H. Aliabadi, and C.C. Havener. Rotating dual-wire beam profile monitor optimized for use in merged-beams experiments. *Nuclear Instruments and Methods in Physics Research Section A: Accelerators, Spectrometers, Detectors and Associated Equipment*, 585(1 - 2):69 – 75, 2008.

[161] *National Electrostatics Corporation Instruction Manual for Model BPM80 Beam Profile Monitor*.

[162] P. Van den Bergh, M. Huyse, K. Krouglov, P. Van Duppen, and L. Weissman. The rex-isolde beam diagnostic system. *AIP Conference Proceedings*, 576(1):235–238, 2001.

[163] Kurt Stiebing (University of Frankfurt). private communication.

[164] Mikhail Yavor. Chapter 6 electrostatic energy analyzers. In *Optics of Charged Particle Analyzers*, volume 157 of *Advances in Imaging and Electron Physics*, pages 213 – 258. Elsevier, 2009.

[165] T. Andersen, H. K. Haugen, and H. Hotop. Binding energies in atomic negative ions: Iii. *J. Phys. Chem. Ref. Data*, 28(6):1511–1533, 1999.

[166] A. P. O'Connor, F. Grussie, H. Bruhns, N. de Ruette, T. P. Koenning, K. A. Miller, D. W. Savin, J. Stützel, X. Urbain, and H. Kreckel. Generation of neutral atomic beams utilizing photodetachment by high power diode laser stacks. *Review of Scientific Instruments*, 86(11), 2015.

[167] Stephen J. Smith and David S. Burch. Photodetachment Cross Section of the Negative Hydrogen Ion. *Phys. Rev. Lett.*, 2:165–166, 1959.

[168] M. Génévriez and X. Urbain. Animated-beam measurement of the photodetachment cross section of H^-. *Physical Review A*, 91(3):033403, 2015.

[169] M. Venuti and P. Decleva. Convergent multichannel continuum states by a general configuration interaction expansion in a b-spline basis: application to IMG photodetachment. *J. Phys. B: At. Mol. Opt. Phys.*, 30(21):4839, 1997.

[170] D. Feldmann. Infrared photodetachment measurements near thresholds of C^-. *Chem. Phys. Lett.*, 47:338–340, April 1977.

[171] Michael L. Seman and Lewis M. Branscomb. Structure and Photodetachment Spectrum of the Atomic Carbon Negative Ion. *Phys. Rev.*, 125:1602–1608, Mar 1962.

[172] L. M. Branscomb, S. J. Smith, and G. Tisone. Oxygen Metastable Atom Production Through Photodetachment. *J. Chem. Phys.*, 43:2906–2907, October 1965.

[173] P. Hlavenka, R. Otto, S. Trippel, J. Mikosch, M. Weidemüller, and R. Wester. Absolute photodetachment cross section measurements of the O^- and OH^- anion. *J. Chem. Phys.*, 130(6):061105, February 2009.

[174] Haiyin Sun. *A practical guide to handling laser diode beams.* SpringerBriefs in Physics, Dordrecht, Heidelberg, New York, London, 2015.

[175] Gerald F Marshall and Glenn E Stutz. *Handbook of optical and laser scanning.* CRC Press, 2011.

[176] Miklos Szilagyi. *Electron and Ion Optics.* Plenum Press, New York, 1988.

[177] R.J. Elsey. Outgassing of vacuum materials-II. *Vacuum*, 25(8):347 – 361, 1975.

[178] Karl Jousten, editor. *Handbook of Vacuum Technology.* WILEY-VCH, 2008.

[179] Pfeiffer Vacuum. *Operating IInstruction: Turbomolecular Drag Pumps TMU 261.*

[180] Agilent Technologies. *Agilent TwisTorr 304 FS.*

[181] Edwards Vacuum. *Instruction Manual nEXT Turbomolecular Pumps, nEXT400.*

[182] Pfeiffer Vacuum. *Operating IInstruction: Turbomolecular Drag Pumps TMU 521.*

[183] Agilent Technologies. *Instruction Manual VacIon Plus 75.*

[184] Pfeiffer Vacuum. *Betriebsanleitung Titan-Sublimator USP 035.*

[185] M. C. Ross, N. Phinney, G. Quickfall, H. Shoaee, and J. C. Sheppard. Automated emittance measurements in the SLC. In *Washington PAC*, 1987.

[186] R. Middleton and Charles T. Adams. A close to universal negative ion source. *Nuclear Instruments and Methods*, 118(2):329 – 336, 1974.

[187] G.T. Caskey, Ross A. Douglas, H.T. Richards, and H. Vernon Smith Jr. A simple negative-ion sputter source. *Nuclear Instruments and Methods*, 157(1):1 – 7, 1978.

[188] T. Ludwig, K. Volk, W. Barth, and H. Klein. Quantization error of slit-grid emittance measurement devices. *Review of Scientific Instruments*, 65(4):1462–1464, 1994.

[189] Y. Yamazaki, T. Kurihara, H. Kobayashi, I. Sato, and A. Asami. High-precision pepper-pot technique for a low-emittance electron beam. *Nuclear Instruments and Methods in Physics Research Section A: Accelerators, Spectrometers, Detectors and Associated Equipment*, 322(2):139 – 145, 1992.

[190] H. Kreckel, H. Bruhns, K. A. Miller, E. Wahlin, A. Davis, S. Hockh, and D. W. Savin. A simple double-focusing electrostatic ion beam deflector. *Rev. Sci. Instrum.*, 81(6):063304, 2010.

[191] Kenji Morita, Hideo Akimune, and Tokuo Suita. Secondary electron emission type neutral particle detector. *Japanese Journal of Applied Physics*, 5(6):511, 1966.

[192] D. Hasselkamp, K.G. Lang, A. Scharmann, and N. Stiller. Ion induced electron emission from metal surfaces. *Nuclear Instruments and Methods*, 180(2):349 – 356, 1981.

[193] N. Benazeth. Review on kinetic ion-electron emission from solid metallic targets. *Nuclear Instruments and Methods in Physics Research*, 194(1):405 – 413, 1982.

[194] P.C. Zalm and L.J. Beckers. Ion-induced secondary electron emission from copper and zinc. *Surface Science*, 152:135 – 141, 1985.

[195] Woodall, J., Agúndez, M., Markwick-Kemper, A. J., and Millar, T. J. The umist database for astrochemistry 2006. *A&A*, 466(3):1197–1204, 2007.

[196] V. Wakelam and the Kida team. Kinetic database for astrochemistry. *European Astronomical Society Publications Series*, 58:287–290, 1 2012.

[197] E. Heinicke, K. Bethge, and H. Baumann. A universal ion source for tandem accelerators. *Nuclear Instruments and Methods*, 58(1):125 – 133, 1968.

[198] A. P. O'Connor, A. Becker, K. Blaum, C. Breitenfeldt, S. George, J. Göck, M. Grieser, F. Grussie, E. A. Guerin, R. von Hahn, U. Hechtfischer, P. Herwig, J. Karthein, C. Krantz, H. Kreckel, S. Lohmann, C. Meyer, P. M. Mishra, O. Novotný, R. Repnow, S. Saurabh, D. Schwalm, K. Spruck, S. Sunil Kumar, S. Vogel, and A. Wolf. Photodissociation of an internally cold beam of ch^+ ions in a cryogenic storage ring. *Phys. Rev. Lett.*, 116:113002, 2016.

Danksagung

An dieser Stelle möchte ich mich bei allen bedanken, die mich persönlich und fachlich in den letzten Jahren begleitet und unterstützt haben. Mein besonderer Dank gilt:

Holger Kreckel für die Möglichkeit als Teil seiner Nachwuchsgruppe an interessanten und lehrreichen Projekten zu arbeiten, für die Betreuung und Unterstützung der letzten Jahre und das Ermöglichen von selbstständigem Arbeiten. Danke für die schöne Zeit.
André Schöning für die freundliche Übernahme des Zweitgutachtens.
Aodh O'Connor for a great time, the weeks of assembling the beamlines, the support, for reading and correcting my thesis, and especially for being a pleasant office colleague.
Manfred Grieser für die unzähligen sehr hilfreichen Diskussionen rund um Beschleunigerphysik. Er hatte immer eine offene Tür und Zeit um alle anfallenden Fragen zu besprechen.
Der Beschleunigerwerkstatt, ehemals unter der Leitung von Karl Hahn, jetzt Max Falckenthal, für die Unterstützung und Fertigung von allen benötigten Bauteilen. Besonderer Dank gilt Christian Kaiser für die schnellen, unkomplizierten Hilfestellungen beim Aufbau der CSR Beamline.
Den Operateuren um Roland Repnow und Manfred König für die viele Unterstützung rund um die Beamline und Ionenquelle.
Dirk Kaiser für seine Hilfsbereitschaft und Anpassung von Bauteilen, auch spät abends.
Der Elektronikabteilung: Peter Werle, Oliver Koschorreck und Rolp Epking für die freundliche Unterstützung bei allen technischen Fragen.
Der Hauptwerkstatt unter der Leitung von Thorsten Spranz für ihre professionelle Arbeit und dass immer eine Lösung gefunden wurde.
Gernot Vogt für die sehr schnelle Beschaffung von Publikationen und Büchern.
Dem kompletten (ehemalige und derzeitige) CSR-Team unter der Leitung von Robert von Hahn, Klaus Blaum und Andreas Wolf für die angenehme Arbeitsatmosphäre und erfolgreiche Zusammenarbeit.
Meiner Familie für die Unterstützung, inbesondere während meines Studiums.
Meiner Freundin Ina für ihre grenzenlose Geduld und den Rückhalt. Vielen Dank für alles!